Heterogeneous Nucleation of Anisotropic Particles

Dissertation
zur Erlangung des akademischen Grades eines
Doktors der Naturwissenschaften
(Dr. rer. nat.)

vorgelegt von

Ann-Kathrin Johanna Göppert

an der

Universität Konstanz

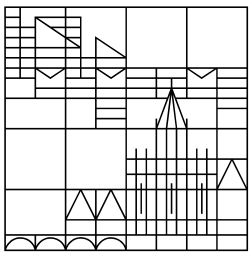

Mathematisch-Naturwissenschaftliche Sektion

Fachbereich Chemie

Konstanz, 2022

Tag der mündlichen Prüfung: 25.11.2022

1. Referent/Referentin: Professor Dr. Cölfen

2. Referent/Referentin: Professorin Dr. Peter

DANKESWORT

Viele Menschen hatten auf ganz unterschiedliche Art Weise Anteil an dieser Doktorarbeit. Ohne sie wäre das Erstellen der Arbeit nicht möglich gewesen und ich möchte mich an dieser Stelle von ganzem Herzen bei ihnen bedanken.

An erster Stelle gilt mein großer Dank dir Helmut. Du hast mir nicht nur das vielseitige Thema und eine Stelle in deiner Arbeitsgruppe angeboten, sondern diese Arbeit auch mit vielen Diskussionen und kreativen Ideen vorangebracht. Ich möchte mich vor allem für die unterstützenden Gespräche und deinen Optimismus während den Durstphasen der Arbeit bei dir bedanken. Deine Tür stand immer offen und beim Schreiben von Papern und anderen Anliegen kamen deine Antworten sagenhaft schnell. Vielen herzlichen Dank, dass du auch wenn dein Tagespensum meist mehr als voll war mit so viel Leidenschaft und Engagement mit mir an meinem Projekt gearbeitet hast. Dein Optimismus und deine unübertroffen gute Laune werden mir immer ein Vorbild sein.

Liebe Frau Peter, Ihnen ein herzliches Dankeschön für die Übernahme des Zweitgutachtens, die konstruktiven und angenehmen Gespräche während der Doktorarbeit und Ihre tolle Arbeit in der IRTG.

Ein weiteres großes Dankeschön dir, lieber Guillermo. Mit dem Schwenk auf das Goldnanopartikelsystem und deiner Expertise in diesem Gebiet hast du die Arbeit ein großes Stück vorangebracht. Ich habe von dir nicht nur sehr viel über die praktische Arbeit im Labor gelernt, sondern auch über die Planung von Versuchen, die Kommunikation von Ergebnissen und das wissenschaftliche Schreiben. Vielen Dank für die tolle Zusammenarbeit bei unseren Veröffentlichungen, die Korrektur dieser Arbeit und deine uneingeschränkte Unterstützung.

Der Deutschen Forschungsgemeinschaft danke ich für die finanzielle Unterstützung dieser Arbeit (SFB 1214). Euch, Felizitas Kirner, Sebastian Theiß und Michael Voggel möchte ich danken für die Synthese und den unkomplizierten, schnellen Nachschub der Nanopartikel, die ich in dieser Arbeit in rauen Mengen verwendet habe. Vielen Dank an das BIC-Team der Universität Konstanz, insbesondere an Martin Stöckl und Carolin Bottling, für die kompetente Hilfe rund um die Lichtmikroskopie und Bildauswertung. Bei eurer tollen Organisation liefen die stundenlangen Versuche am Lichtmikroskop zumindest technisch immer einwandfrei. Ein weiterer Dank gilt Brigitte Bössenecker und dem PAC der Universität Konstanz für die Möglichkeiten der Partikelanalyse und die immer gute Laune sowie Matthias Hagner, Marina Krumova, dem Nanolab der Universität Konstanz und Michael Laumann für die Unterstützung bei der Elektronenmikroskopie. Hier habe ich viel von euch gelernt. Danke euch, Jennifer Knaus und Philipp Graus für die Unterstützung bei den AFM Messungen. Außerdem möchte ich mich bei Jonathan Avaro für die Hilfe bei IR Messungen und Thomas Diemant von der Universität Ulm für die XPS Messungen bedanken.

Weiterhin hatte ich die Möglichkeit, mit verschiedenen tollen Studenten an meinem Projekt zu arbeiten. Hier konnte ich nicht nur selbst viel zum Thema Mitarbeiterführung lernen, sondern habe kompetente und

gute Beiträge zu meiner Arbeit erhalten. Vielen lieben Dank dafür an Anna Khudyshkina, Yanna Piccini, Tristan Steegemans und vor allem für die sehr lange und gute Arbeit, Simon Schnitzlein.
Neben der direkten Hilfe und Mitarbeit am Projekt hat auch die Einbettung in den SFB und die IRTG viel zum Gelingen der Arbeit beigetragen. Daher möchte ich mich bei allen Mitgliedern ganz herzlich für die guten Diskussionen, Ideen und Hilfestellungen bedanken. Auch der Einblick in andere Forschungsthemen auf unseren Veranstaltungen war sehr interessant für mich und hat geholfen, den Blick etwas vom eigenen Projekt zu weiten. Dies gilt auch für die gesamte AG Cölfen, der ich von Herzen danken möchte. Nicht nur für die tolle Aufnahme in die Gruppe, die gute Zusammenarbeit im Labor und die Hilfe bei der Arbeit, sondern auch dafür, dass ihr die Jahre der Doktorarbeit für mich unvergesslich gemacht habt. Ich habe hier Freunde fürs Leben gewonnen, Menschen aus aller Welt kennengelernt und konnte einzigartige Momente mit euch erleben. Diese Unterstützung hat geholfen, auch in stressigen Phasen nicht den Kopf hängenzulassen und nur Kleinigkeiten wie das pünktliche Mittagessen um 11 Uhr waren ein wichtiger Ankerpunkt für mich.
Auch beim Schreibprozess der Arbeit habe ich viel Unterstützung erhalten und möchte mich für die hilfreichen Korrekturen und Anregungen bei Sascha Keßler, Christian Jennewein, Dominik Gruber, Cathrin Kronenbitter, Andreas Spinnrock, David Schupp, Lisa Fuhrer, Julian Konsek, Masoud Farhadi-Khouzani, Michael King, Michael Seybold, Julian Schlotheuber, Cristina Ruiz-Agudo, Jonathan Avaro und Thomas Gießl bedanken.
Ganz besonders möchte ich meiner Familie für die finanzielle, aber vor allem für die bedingungslose Unterstützung während dieser Zeit danken. Danke, dass ihr mir dieses spannende Studium, die Doktorarbeit und die tollen Jahre an der Universität Konstanz ermöglicht habt, mir in den stressigen Phasen den Rücken gestärkt und mir zu Hause einen schönen Zufluchtsort geboten habt. Und dir lieber Michael möchte ich von ganzem Herzen für deine Hilfe danken. Einmal für die langen wissenschaftlichen Gespräche, die ich dir aufgenötigt habe, die kreativen Ideen und die praktische Hilfe im Labor. Aber vor allem dafür, dass wir diese Jahre gemeinsam mit allen Höhen und Tiefen erleben durften, dass du mich, wenn nötig, aufgemuntert, mir Selbstvertrauen und Zuversicht gegeben hast und wir unsere Erfolge gemeinsam feiern konnten.

TABLE OF CONTENTS

LIST OF ABBREVIATIONS

General Abbreviations

E_A	effective activation barrier
E_λ	extinction
g_{bulk}	bulk enthalpy
$g_{surface}$	surface enthalpy
k_B	Boltzmann constant
x	concentration of nanoparticles
x^*	concentration of nanoparticles in a saturated dispersion
Δg_n^*	nucleation barrier at the point of the critical radius r*
μ	chemical potential
Abs	absorption
c	concentration
CNT	classical nucleation theory
d	nanoparticle diameter
D_H	volume-based hydrodynamic radii
DLVO	Boris Derjaguin and Lev Landau, Evert Verwey, and Theodoor Overbeek
et al.	and others
F	surface area of the newly formed surface
f	numerical factor that depends on the nucleus geometry
J_n	nucleation rate
LSPRs	located surface plasmon resonances
M_W	mass average molar mass
n	number of atoms
OWRK	Owens, Wendt, Rabel and Kaelble
PDI	polydispersity index
pH	potential of hydrogen (historical)
pK_S	negative decadic logarithm of the acid constant
r	nucleus radius
r*	critical radius
R^2	Coefficient of determination
R_a	surface roughness value $R_{max}/4$
R_{ms}	root mean square of the roughness height

RT	room temperature
T	temperature
V_M	volume of one atom, molecule or building block
α	interfacial energy
α_{lc}	interfacial tension between the nuclei and the surrounding parent phase
α_{ls}	interfacial tension between the surface and the surrounding parent phase
α_{sc}	interfacial tension between the nuclei and the surface
Δg_n	nucleation barrier
σ	supersaturation
K	scatter coefficient
f	numerical factor
Θ	contact angle
σ	supersaturation
τ	turbidity

Compounds

CPC	hexadecylpyridinium chloride
CTAB	hexadecyl(trimethyl)ammonium bromide
DIPEA	1,1-Diisopropylethylamine
DMTMM	4-(4,6-dimethoxy-1,3,5-triazin-2-yl)-4-methyl-morpholinium chloride
DNA	deoxyribonucleic acid
P3P	polyglyceryl-3-polyricinoleate
PAA	polyacrylic acid
PEG	polyethylene glycol
PMMA	polymethylmethacrylate
PSS	polystyrene sulfonate

Units

%	percent
°	degree
°C	degree centigrade
µl	microliter

µm	micrometer
a.u.	arbitrary unit
cm	centimeter
eV	electron volt
kHz	kilohertz
kV	kilovolt
l	liter
m	meter
M	molar
mΩcm	mega ohm-meter (electrical resistivity)
min	minute
ml	milliliter
mm	millimeter
mm^2	square millimeter
mN	millinewton
mol	amount of substance
mV	millivolt
N	newton
N	equivalent concentration (normality)
nm	nanometer
nm^3	cubic nanometer
rpm	rotations per minute
s	seconds
vol.-%	percentage by volume
W	watt
wt.-%	percentage by mass

Instruments and Methods

AFM	atomic force microscopy
ATR-IR	attenuated total reflection infrared spectroscopy
AUC	analytical ultracentrifugation
DLS	dynamic light scattering
EDX	energy-dispersive X-ray spectroscopy
EXAFS	extended X-ray absorption fine structure
FFT	fast Fourier transform

HR-TEM	high-resolution transmission electron microscopy
LC-TEM	liquid cell transmission electron microscopy
NIR	near-infrared
SAXS	small-angle X-ray scattering
SEM	scanning electron microscopy
STORM	stochastic optical reconstruction microscopy
TEM	transmission electron microscopy
TGA	thermogravimetric analysis
UV-vis	ultraviolet-visible
WAXS	wide-angle X-ray scattering
XANES	X-ray absorption near edge structure
XPS	x-ray photoelectron spectroscopy

1 Introduction

1.1 General Introduction

.

„Und jedem Anfang wohnt ein Zauber inne“ – Hermann Hesse[1]

Nucleation – this term refers to the very first phase of a particle’s life. Nucleation surrounds us every day all around the world and amazes us consistently with the formation of beautiful ice crystals on windows, the impressive constructions we can build with cement, or even the pleasant mouthfeel of ice cream. In our everyday life, we are in constant contact with the products of nucleation, but the actual nucleation process remains mostly hidden. The formation of a new particle often takes place within a few millions of a second and the newly formed particle usually consists of a few molecules or atoms and exhibits a size of ten-thousandths of a hair.[2] Doubtless, nucleation takes a great effort to remain hidden. To unravel the secrets of nucleation means to better understand processes in our environment. In addition, a more detailed understanding allows targeted intervention and opens access to create functional materials with tailor-made properties. Therewith the wish to understand nucleation better unites scientists of various fields from biologists over chemists to engineers.[2]

This thesis promotes the understanding of nucleation by utilizing anisotropic nanoparticles as a model system to study heterogeneous nucleation. This idea implies that instead of atoms or molecules nucleating into larger structures, particles are used as building blocks and nucleate into larger superstructures comparable to building with Lego bricks. That brings the system to a larger scale and thus simplifies the analysis of the nucleation process. To avoid misunderstandings, the term nucleation of nanoparticles refers to nanoparticles as building blocks nucleating into larger superstructures and not to the formation of the nanoparticle itself. The thesis deals explicitly with heterogeneous nucleation as this is the nucleation that dominates in most systems. And this aspect also leads to the anisotropic particles, which are used since anisotropic building blocks are omnipresent in nature and industry instead of isotropic particles commonly utilized for nucleation experiments.

The following introduction will explain the theoretical background for this thesis starting with nucleation in general, followed by the special case of heterogeneous nucleation and the analytical challenges encountered in analyzing nucleation processes. In the second part, the introduction will elaborate nucleation phenomena with particles as building blocks. Subsequently, Chapter 2 will explain the scope of this thesis in more detail before Chapters 3 - 7 show the results of this thesis. To provide more information, the appendix and experimental part will follow directly after the results of each chapter. The thesis ends with a summary of the presented results and an outlook on what will be interesting for further research in this field.

Parts of this thesis have been already published in publications and to keep clarity own content and citations are not marked. This considers the publication „Microscopic Analysis of Heterogeneous Nucleation of Nanoparticle Superstructures"[3] which mainly deals with the content of Chapter 5. Further, the publication „Influence of Anisotropy on Heterogeneous Nucleation of Gold Nanorod Assemblies"[4] deals with the impact of particle anisotropy on heterogeneous nucleation which is primarily content in Chapter 7. But now, we want to dive into the fascinating world of nucleation with a closer look at the theoretical background.

1.2 Nucleation

Nucleation is a ubiquitous phenomenon relevant to many aspects of everyday life.[5-10] One impressive example of nucleation shows up in the sky with the formation of clouds through condensation of water vapor into liquid droplets (Figure 1 A). Despite of being intensively investigated for more than a century, there are still many unanswered questions regarding nucleation processes.[11-17] Studying the nucleation mechanisms behind phenomena like the formation of clouds helps to understand and to possibly influence them.[8, 9] In another fascinating example from nature, the nucleation processes direct the formation of complex biomineral structures, giving them outstanding properties (Figure 1 B).[18-23] It is well known that materials with the same structural components can show different properties depending on the final arrangement of their building blocks. One outstanding example constitutes carbon: an arrangement in a diamond structure makes it the hardest material on earth, while the same atomic building block arranged in the graphite structure can be used for writing since layers are abraded easily.[24] Also, the structures and properties of most artificial materials are influenced by their nucleation processes such as concrete or pharmaceutical drugs. Controlling the nucleation of those systems can potentially allow to tune their structure and thereby improve their properties or even create new ones.[25, 26] However, nucleation can also pose problems when it is related to the unwanted deposition of minerals in water-handling equipment. Often calcification of washing machines or formation of mineral scale in industrial pipelines is troubling and understanding the formation of those scale-forming minerals can help to prevent them (Figure 1 C).[25] After all these vivid examples for nucleation, the question arises: What exactly is nucleation?

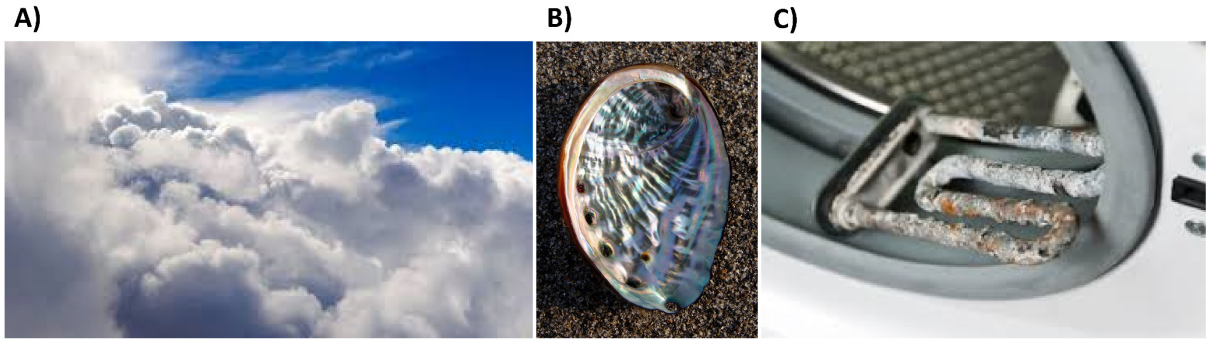

Figure 1. Examples of Nucleation. A) The formation of clouds through condensation of water vapor into liquid droplets.[27] B) A nacre outer shell composed of calcium carbonate and chitin.[28] C) The calcification of washing machines.[29]

1.2.1 Nucleation Theory

Nucleation is defined as the first step in the formation of a distinct new thermodynamic phase which can be augmented by a growth process.[8-10] Josiah Willard Gibbs (1839-1903), an American scientist, realized first that the formation of a distinct new thermodynamic phase requires the appearance of small clusters formed from atoms or molecules in the supersaturated volume of the surrounding phase.[30] These small clusters were called nuclei, and Gibbs estimated them to have the same properties as their corresponding bulk phase and only differ by their size.[30] This picture may be oversimplified but has been a very important step towards the understanding of nucleation processes. The theory of the formation of a new phase was further developed by many different scientists such as Gibbs[14], Volmer[11, 31], Farkas[12], and others and is known as capillary or classical nucleation theory (CNT).[13, 16, 32] CNT describes the formation of nuclei inside a supersaturated solution as a statistical process characterized by the stochastic collision of the building blocks like atoms, ions, or molecules that eventually form a nucleus. Based on CNT, the nucleation process is governed by two different energy contributions related to the newly created bulk material and its surface (Figure 2). The formation of a nucleus has a favorable bulk enthalpy if the new thermodynamic phase is more stable than the initial surrounding phase (1):

$$\Delta g_{bulk} = -n * \Delta\mu \tag{1}$$

with n being the number of atoms and Δμ being the chemical potential (Figure 2 dashed grey line). On the contrary, the formation of a nucleus automatically entails the formation of a new surface, which is energetically unfavorable (2):

$$\Delta g_{surface} = \alpha * F \tag{2}$$

with α being the interfacial tension between the newly formed surface and the surrounding phase and F being the surface area of the newly formed surface (Figure 2 dashed black line). The blue line in Figure 2 shows the resulting free enthalpy of the nucleus formation dependent on the nucleus radius r (3):

$$\Delta g_n = -n * \Delta\mu + F * \alpha = -\frac{4}{3}\frac{\pi r^3}{V_M} * \Delta\mu + 4\pi r^2 * \alpha \tag{3}$$

assuming a spherical nucleus with the radius r and V_M being the volume of one atom or molecule. At small radii, the surface contribution predominates, while at higher radii the energy gain of the bulk contribution predominates making the formation of a nucleus favorable. Therefore, the nucleus can grow or disappear, depending on its size and this process is controlled by the free energy of the nucleus. In order to create a stable nucleus, it is necessary to overcome an energy barrier or the so-called nucleation barrier. The nucleation barrier of a system depends strongly on the supersaturation and the temperature. While a metastable system may not nucleate in years, just a small change in the system can trigger the nucleation process immediately. The radius of the nucleus at the maximum of the nucleation barrier r* is called the

critical germ radius and illustrates a point of inflection in the free energy change of the system. If the radius of a nucleus is smaller than the critical radius r*, the further growth of the nucleus is energetically not favorable, and it will most likely dissolve. If the radius of a nucleus is larger than the critical radius r*, the further growth is energetically favorable and the tendency to grow will prevail without further limit if the corresponding constituent units are provided.[30]

The corresponding critical free energy Δg_n^* at the critical radius r* (r = r*) can be calculated by setting to zero the first derivation of Δg_n to find the maximum of the blue curve in Figure 2. If the assumption of a spherical nucleus is not considered, one can describe the nucleation barrier at the point of the critical radius r* in a general form (4):

$$\Delta g_n^* = f\alpha^3 \left(\frac{V_M}{k_B T \sigma}\right)^2 = B\,\frac{\alpha^3}{\sigma^2} \tag{4}$$

with f being a numerical factor that depends on the nucleus geometry and σ being the supersaturation.[26]

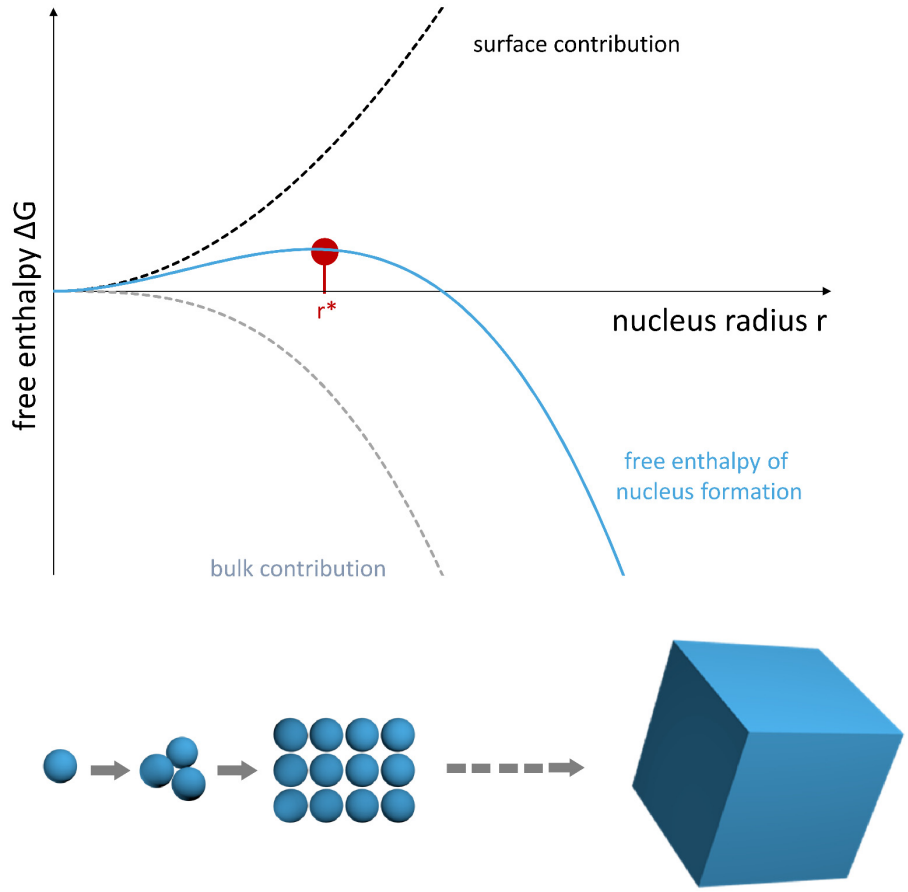

Figure 2. Classical nucleation theory. The diagram shows the free enthalpy of nucleus formation Δg_n dependent on the nucleus radius r (blue). The free enthalpy of nucleus formation depends on the unfavorable formation of a new surface (black) and the favorable transition from the metastable phase into the new stable phase, referred to as bulk contribution (grey). At small nucleus radii, the surface contribution dominates the resulting free enthalpy, making the growth of the nucleus unfavorable. Therefore, nuclei with a radius smaller than r* tend to decay. At higher nucleus radii, the bulk

contribution dictates the resulting free enthalpy making the growth of a nucleus favorable and it can grow without further limit.

While CNT allows a good qualitative description of nucleation processes, the obtained quantitative values have high degrees of error.[33-35] One source of error in quantitative descriptions is the capillary assumption. This assumption is based on the idea that small clusters exhibit the same properties as their corresponding bulk material.[36] However, it is already shown for the example of nanomaterials, which are - compared to nuclei - bigger, that the properties of a nanomaterial differ distinctly from the properties of the corresponding bulk phase. Such differences can be explained by the large ratio of surface atoms in nanomaterials compared to their corresponding bulk material, which results in deviating properties such as enhanced catalytic activity, magnetism, or solubility for instance.[37-42] Examples related to nanomaterials will be discussed more in detail in Chapter 1.3. However, the difference between nano and bulk material makes it questionable to base predictions about nucleation behavior on the capillary assumption. To compensate for this drawback, corrections for the size dependency of the respective energies can be applied.[43-45] Unfortunately, for sizes in the range of typical critical germ radii, correct values are inaccessible these days.[26, 36, 46]

By taking a closer look at the nucleation process at the atomic or molecular level, it becomes clear that nucleation is a random process, meaning the transition from a metastable system to a new stable thermodynamic phase or structure is initiated by random fluctuations. This dependency on random fluctuations often causes a so-called induction period in nucleation experiments and makes predicting single nucleation times challenging. Therefore, statistics are essential and multiple repetitions of the same experiment conditions can lead to good statistical results. Furthermore, due to the randomness of many nucleation processes, the number of nuclei formed in a time interval is an arbitrary quantity. Therefore, it is necessary to determine the average value of nuclei formed in a time interval to characterize the kinetics of a nucleation process. This value, the average number of nuclei formed per unit time and volume of the ambient phase, is called nucleation rate J_n and can be described as (5):[30]

$$J_n = A\, e^{\frac{-E_A}{k_B T}} e^{\frac{-\Delta g_n}{k_B T}} = A\, e^{\frac{-E_A}{k_B T}} e^{\frac{-B\alpha^3}{\sigma^2}} \tag{5}$$

The equation of the nucleation rate is composed of a kinetic energy barrier, the activation energy for diffusion, and a thermodynamic energy barrier, the nucleation energy. The kinetic term includes the effective activation barrier E_A, which describes, for example, the attachment of the forming nucleus and structural rearrangements.[26] The parameter A is a complicated function of the molecular-level parameters depending on features of the accepted model, which are difficult to verify experimentally.[47] k_B is the Boltzmann constant and T the temperature. The thermodynamic energy barrier for the formation of a critical nucleus depends on the interfacial tension and the supersaturation of the system as described above. The nucleation

rate depends directly on the probability of the existence of a critical germ and further on the probability of attachment of another building block and thereby the growth of the nucleus.

The nucleation type we have dealt with so far is called homogeneous nucleation, where the formation of the nuclei occurs throughout the parent phase. However, interfaces like air bubbles, dust particles or reaction vessels are present in most real systems.[25, 30] The nucleation processes taking place at those interfaces differ from the homogeneous nucleation. They are described as heterogeneous nucleation and shall be discussed in more detail now.

1.2.2 Heterogeneous Nucleation

The formation of a nucleus at a surface is called heterogeneous nucleation and, compared to homogeneous nucleation, it is a surface catalyzed or assisted process. The presence of a favorable interface reduces the effective surface energy and, as a result, the energy barrier for the nucleation (Figure 2 blue line) is decreased. For heterogeneous nucleation the form of the nuclei is estimated as a drop on a surface (Figure 3), while for homogeneous nucleation, the form of the nuclei was estimated as a sphere (equation 3).

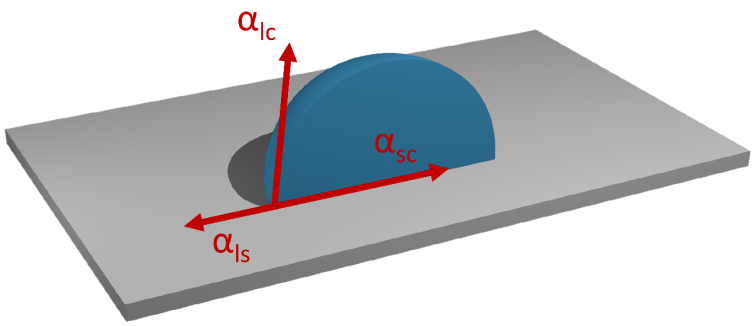

Figure 3. Heterogeneous nucleation. Scheme of a growing nucleus (blue) on a substrate (grey) surrounded by the parent phase. The red arrows illustrate the different surface tensions: between the nuclei and the surrounding parent phase α_{lc}, between the nuclei and the surface α_{sc}, and between the surface and the surrounding parent phase α_{ls}.

With this estimation, the resulting free enthalpy of the nucleus formation dependent on the nucleus radius r for heterogeneous nucleation can be written as (6):

$$\Delta g_n = -\frac{2}{3}\frac{\pi r^3}{V_M} * \Delta\mu + 4\pi r^2 * \alpha \qquad (6)$$

The red color highlights the differences compared to the free enthalpy of nucleus formation in homogeneous nucleation (equation (3)). For the heterogeneous nucleation, the interfacial tension α has to be adapted since different contributions to the interfacial tension α have to be considered. Besides the initial interfacial tension between the nuclei and the surrounding parent phase α_{lc}, the interfacial tensions between the nuclei and the surface, α_{sc}, and between the surface and the surrounding parent phase, α_{ls}, come into play (7):

$$\alpha = \alpha_{lc}\left(\frac{1-(\alpha_{ls}-\alpha_{sc})}{2\alpha_{lc}}\right) \quad (7)$$

A reduction of the energetically unfavorable newly formed surface is possible when $\alpha_{ls} > \alpha_{sc}$ and leads to the lowered energy barrier of heterogeneous nucleation. As a result, heterogeneous nucleation tends to occur at faster rates, lower degrees of supersaturation, and more often than homogeneous nucleation.[7, 48] Examples of heterogeneous nucleation run through our everyday life. The before-mentioned formation of clouds through condensation of water vapor into liquid droplets, which takes place mostly on dust particles, or the formation of mineral scale in washing machines or pipelines are some examples.[8, 9, 25] Here, the presence of a suitable surface might reduce the interfacial energy due to the minimization of lattice strain (since the structure of the substrate matches a particular plane of the nucleating phase) or by allowing strong bonding to the nucleus.[18, 49, 50] In this context, understanding heterogeneous nucleation processes is of major importance to influence or mimic them. One example out of the industry is the additive X-SEED® by BASF that enhances the hardening and strength development of concrete. The additive, as a suitable substrate, is triggering heterogeneous nucleation of calcium silicate hydrates (the main binding phase in cement), acting as seeding material, and thereby speeding the original nucleation kinetics.[51] Going one step further, controlling heterogeneous nucleation can be beneficial for the properties and quality of products in the pharmaceutical, agriculture, or food industry.[9, 25] The presence of a surface could be used to gain more control over nucleation. Due to the influence of a template on the nucleating crystallographic plane, the development into specific orientations can be favored.[26, 52-56] Hence, templates can be used to control the orientation of the resulting crystal and achieve directed growth like in the matrix-mediated biomineralization processes.[26] Despite the importance of nucleation processes, the reduced dimension of the critical nuclei and the sensitivity to small changes in the system make their analysis highly challenging which will be discussed in the following section.

1.2.3 Analytical Challenges

One of the most severe difficulties in observing nucleation in situ is the required spatial resolution since the critical germ size ($n < 100$) is starting on the atomic scale (Figure 4).[18] In the case of heterogeneous nucleation, experimental investigations have shown that the number of atoms constituting the critical nucleus can be even smaller, and for some systems, they start with the first attachment of a single atom.[30, 57-60] Another difficulty in analyzing nucleation is the coexistence of multiple species, like nuclei with different numbers of atoms and morphologies, which makes size and shape distributions a major influencing factor. Besides the spatial resolution, another challenge is affording sufficient temporal resolution to observe the highly dynamic nucleation processes. We lack analytical methods that can address all of the described characteristics of nucleation processes at once.[7, 26] One potential strategy to address this issue could be the combination of various state-of-the-art analytical techniques, which can then cover the different morphological, kinetic, and thermodynamic aspects of heterogeneous nucleation processes.

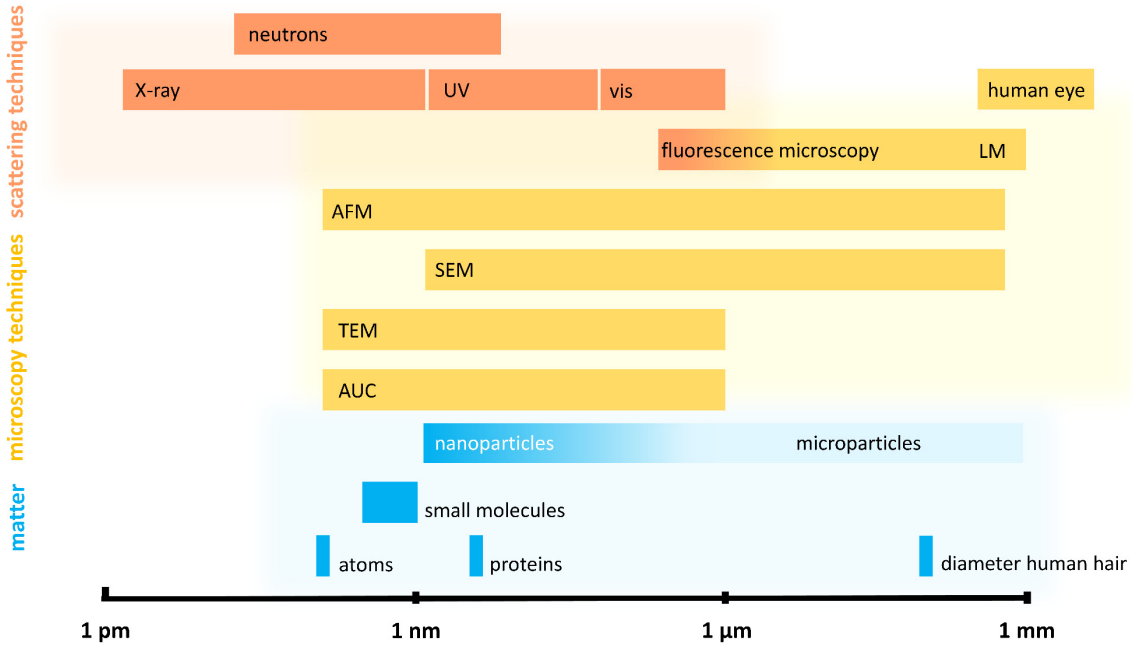

Figure 4. Typical length scales of matter and analytical techniques.

A short overview shall be given depicting examples for suitable analytical methods, which can address the individual aspects of nucleation processes. In context of the required high spatial resolution, Figure 4 shows the typical length scales of matter and analytical techniques. X-ray-based spectroscopies like extended X-ray absorption fine structure (EXAFS) spectroscopy or X-ray absorption near edge structure (XANES) spectroscopy can be used to investigate the local environment around elements, their oxidation states, or the formation or breakage of chemical bonds.[61] X-ray-based spectroscopy is, therefore, suitable to provide information about chemical speciation in nucleation and growth processes. A pair distribution function analysis can further reveal quantitative information on bond lengths, as demonstrated in the case of gold[62] or platinum[63] nanoparticle nucleation processes. In this sense, titration methods can also give information about chemical speciation. Furthermore, simple ultraviolet-visible (UV-vis) spectroscopy is especially suitable for investigating the early stages of metal or semiconductor nanoparticle nucleation and growth.[64] In some cases, UV-vis spectroscopy provides information about the size, shape, and crystallinity during the nucleation process. For example, Pong *et al.* used UV-vis spectroscopy to detect the formation of gold nanowires during the synthesis of gold nanospheres (Figure 5).[65] The gold nanowires nucleating and growing at the initial synthesis stages showed a broad surface plasmon band in the absorption spectra, while the defined sphere-like gold particles at the end of the growth process displayed a distinct narrow plasmon band with higher intensity (Figure 5 A). The size and morphological evolution of the gold nanoparticles could be determined by the combination with transmission electron microscopy (TEM) (Figure 5 B).

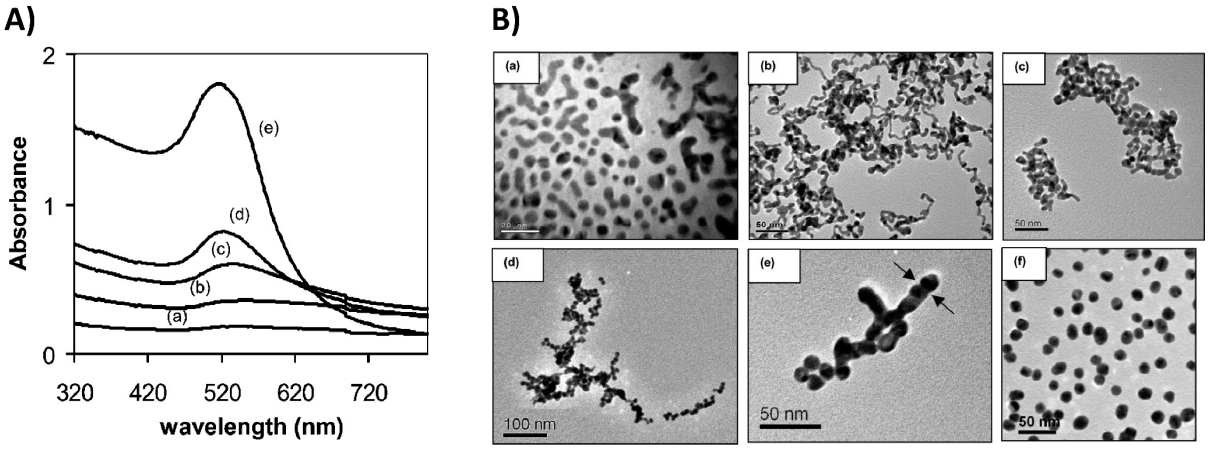

Figure 5. Investigation of the early stages of gold nanoparticle formation. A) UV−vis spectra of colloidal solutions that show the color change as the reaction progressed from colorless to ruby-red. B) TEM images show the progress in the formation of gold nanoparticles. At the beginning of the reaction, the colorless solution contained small nanoclusters. As the solution turned dark blue, an extensive network of Au nanowires was formed, which broke up in the further course, and spherical particles between 10 and 13 nm in diameter began to cleave off from the nanowires when the color of the reaction turned purple. Reprinted with permission.[65]

Other interesting techniques are free jet small-angle X-ray scattering (SAXS) and wide-angle X-ray scattering (WAXS) which are convenient for analysis with a high temporal resolution going down to the microsecond domain.[66] However, they lack sufficient size resolution since they detect particle sizes as an average. Analytical ultracentrifugation (AUC) on the other hand is a slow technique but stands out due to its extremely high particle size resolution in the angstrom range.[67] It can even detect single ions or molecules and therefore lends itself to analyzing multiple species occurring during the nucleation process.[68] Additionally, in situ atomic force microscopy (AFM) can measure growth step velocities and structural details during nucleation processes and thereby delivers thermodynamic and kinetic aspects of nucleation and growth processes.[69-71] Here, frequency-modulated AFM even allowed atomic resolution on surfaces for the cases of brookite titanium dioxide[72], calcite[73, 74], and sodium chloride[75]. Nevertheless, the disadvantage of AFM is that the scanning speed either limits the spatial or temporal resolution. Liquid cell transmission electron microscopy (LC-TEM) has emerged as a valuable tool for in situ investigation of nucleation due to its atomic resolution, enabling the direct observation of the nuclei formation in solution or on substrates.[5, 26, 76-79] For instance, Radisic *et al.* observed the deposition of copper clusters onto a gold electrode by combining a miniaturized electrochemical cell within a TEM microscope.[77] With this combination, they analyzed the effect of surface adsorption on the cluster density and the growth rates during electrodeposition.

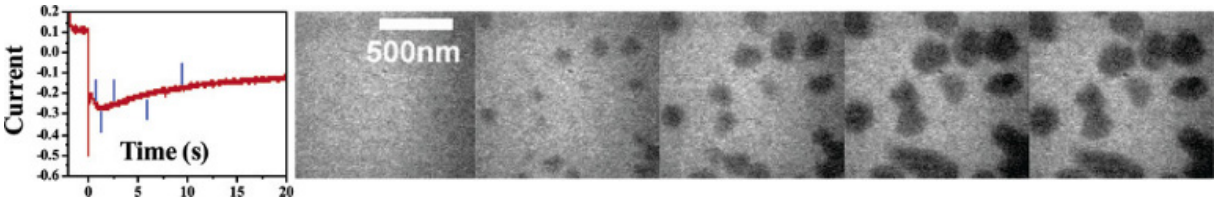

Figure 6. Nucleation of copper observed by TEM. (left) „Current transient recorded during the deposition of copper on polycrystalline gold." (right) „Five images extracted from a video recorded simultaneously with the current transient. The times corresponding to the images are indicated by vertical marks on the current-time curve. (…) The scale bar is 500 nm." Reprinted with permission.[77]

Additionally, LC-TEM allows element detection and electron diffraction and with its high spatial resolution, the identification of crystalline and amorphous phases is possible. However, the analysis with LC-TEM is limited because of the small volume used for the nucleation experiments, which reduces the nuclei number and mobility and limits the growth process.[5, 80] Moreover, the electron beam can affect the nucleation process influencing the kinetics, and the high resolution of TEM comes at the cost of poor statistics as only a few particles can be observed at the same time.[5]

Overall, this short overview of the most significant analytical methods currently used to characterize nucleation processes suggests that only a combined approach of the different techniques can give a complete insight into nucleation phenomena. Additionally, it is problematic that most of the discussed characterization techniques are elaborate and expensive. These drawbacks could be partly circumvented, if instead of investigating nucleation from ions or molecules particles are used as building blocks. The assembly of particles into larger superstructures is comparable to nucleation processes and can therefore serve as a model system for nucleation.

1.3 Nucleation with Particles as Building Units

The previous chapter showed that the analysis of nucleation remains challenging due to the required high temporal and spatial resolution. One approach to overcome this drawback is to go to a larger scale by using dispersed particles as a model system for nucleation.[81-84] But before taking a closer look at the utilization of particles in nucleation experiments, first, the definition of particles and nanoparticles shall be clarified briefly.

1.3.1 Particles and Nanoparticles

There is no distinct definition for the term particle regarding size concepts. Depending on the discipline, the term particle ranges from subatomic particles like electrons, up to atoms, nano- and microparticles, and can even end with planets that can be considered as particles as well. Relevant in terms of nucleation are atoms, molecules, and ions that exhibit sizes of less or equal to 1 nm, and nano-, and microparticles that are in a size range of about 1 nm to 1 mm. These nano- and microparticles are referred to as particles in the

thesis. A possible definition of a particle would be „an aggregation of sufficiently many atoms or molecules that it can be assigned macroscopic properties such as volume, density, pressure, and temperature".[85] Most of the time, colloidal particles are considered pieces of solid materials suspended within a liquid or gaseous phase. However, particles can also exhibit other aggregation states, for example, liquid droplets or bubbles. Further, particles can consist of any material or a combination of different ones, for instance: metals, semiconductors, ceramics, or polymers or examples from nature like sand, fog, and smoke, or even biological particles like proteins or viruses.[86]

Within this vast field of particles, nanoparticles play a special and increasingly important role in science and technology. As a definition for nanoparticles, Goesmann and Feldmann suggested that at least one of the dimensions of the particle must be smaller than 100 nm.[87] The exact size definition is more or less arbitrary, however, it is in the nanometer range where many exciting size-dependent properties emerge. These size-dependent properties of nanoparticles constitute in three different facets.[87] First, the surface-to-volume ratio increases, leading to a high number of surface atoms compared to bulk atoms. This high surface ratio implies why surface-dependent properties like catalysis are highly enhanced in the case of nanoparticles.[88-90] Second, some size-dependent properties manifest at a certain size, for example the superparamagnetism of magnetite nanoparticles at around 30 nm.[91-94] Third, in some materials, the electron confinement and surface effect give rise to unique interactions with light. A vivid example constitutes the extinction behavior of gold nanoparticles, which arise in different colors depending on their size (Figure 7).[95]

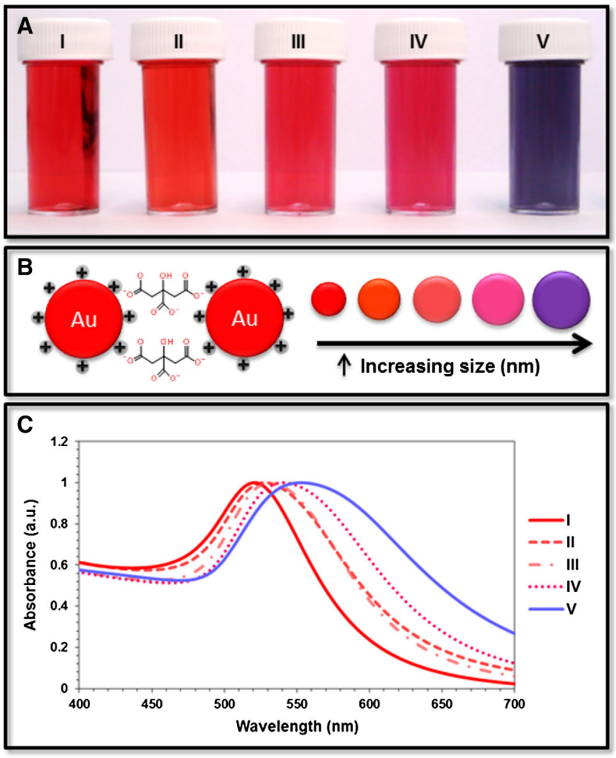

Figure 7. Absorbance behavior of gold nanoparticles. A) Image of colloidal gold nanoparticles with increasing sizes exhibiting different colors. B) The stability of the gold nanoparticles is achieved through electrostatic stabilization with citrate ions. C) The varying size and with it, the color of the gold

nanoparticle dispersions reveals in differently located LSPRs bands in the UV–vis spectra. Reprinted with permission.[96]

The characteristic colorful appearance of gold and other metal nanoparticles with sizes of 2 to 100 nm can be explained by the formation of localized surface plasmon resonances (LSPRs) (Figure 8). The conduction electrons of gold constitute a cloud moving collectively behind a background of positively charged core atoms. A LSPRs occurs when this cloud of conduction electrons is excited by electromagnetic radiation resulting in collective oscillation.[97, 98] When the frequency of the incident radiation is above that of the electron cloud, regions with positive and negative net charges appear at the interface between the metal and the surrounding dielectric medium.[99] Due to the displacement of the electron cloud, light is absorbed and scattered. [100] The nature of the LSPRs strongly depends on the size and the form of the nanoparticle and the dielectric constant of the metal as well as the surrounding medium.[97, 101-103] Moreover, the presence of another plasmonic nanoparticle in the vicinity also influences the LSPRs, due to the formation of new resonance modes. This property of plasmonic nanoparticles can be highly beneficial for monitoring nucleation processes using UV-vis-NIR spectroscopy.

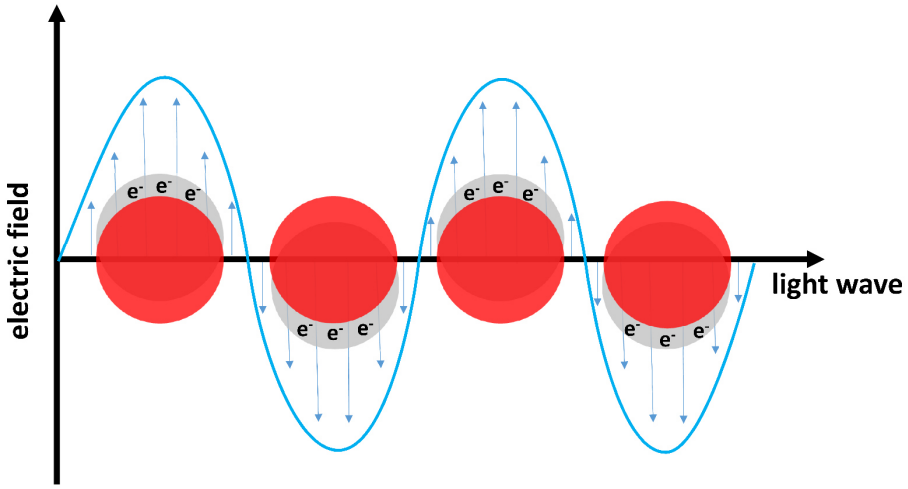

Figure 8. Surface plasmon resonance. Scheme of the induction of surface plasmon resonance in metal nanoparticles. The electromagnetic radiation of a light wave (blue) induces a collective oscillation in a metal nanoparticle (red). The negative charge (grey) is concentrated on one side of the metal nanoparticle and the electron cloud oscillates with the frequency of the electromagnetic radiation resulting in a specific color of the metal nanoparticle.

After this excursion into the field of particles, it shall be outlined how one can use these particles as building blocks in nucleation experiments.

1.3.2 Particles as Model System for Nucleation

As previously introduced, one approach to study nucleation more easily is to use particles as a model system for nucleation.[81-84, 104, 105] Here, the particles serve as building blocks, similar to atoms or molecules, building

up into superstructures.[106-108] These superstructures might be amorphous or crystalline, analog to classical nucleation and growth.

In this sense, nature provides abundant examples of such superstructures: biominerals. They exhibit complex hybrid compositions of inorganic minerals as nanoparticle building blocks and soft organic components, for instance, in bone hard tissue[19, 109], sea urchin spine[20, 110], nacre[21, 111], corals[22, 112] or egg shells[23].[107, 108, 113, 114] Inspired by nature, biomimetic structures have been developed in the lab.[115-117] Furthermore, the use of colloidal particles[118, 119] is of interest for developing new materials such as photonic bandgap materials[120, 121] or optical filters[122] formed by self-assembly processes. The term self-assembly process is often used to describe a superstructure formation out of colloidal particles that corresponds to their nucleation and subsequent growth. However, in general, self-assembly describes a process by which individual components arrange themselves into an ordered structure.[123] The building blocks are not linked together via covalent bonds but ordered through weak forces, such as van der Waals forces, hydrogen bonding, or hard-particle interactions.[123] Next to particles, a variety of materials can be self-assembled into superstructures, for example, DNA[124], proteins[125], lipid vesicles[126], or block copolymer melts[127]. Thus, self-assembly processes are at the core of the use of nanoparticles as model systems to investigate nucleation processes.

Amongst self-assembled superstructures built out of particles, the mesocrystals stand out because these crystalline nanostructured materials combine properties of the nanoparticles themselves with properties on the macroscopic length scale. A mesocrystal, per definition, includes a three-dimensional assembly of monocrystalline particles exhibiting the same orientation and sizes of 1 up to 1000 nm.[20, 128] Herein, the building blocks of a mesocrystal must feature certain structural properties: crystalline nanoparticles and a nanoparticle packing exhibiting a crystallographic orientation.[114] These oriented subunits differ a mesocrystal from a randomly oriented polycrystal, while the identifiable building blocks on the nanoscale differ it from a single crystal that contains impurities.[20, 128] This construction principle gives mesocrystals a tremendous diversity with possible variations in chemical composition, particle size, or particle shape.[109] Equally diverse are the potential applications of these new materials, for instance, in catalysis[129, 130], optoelectronic applications[131-133], electrodes[134], or biomedical applications[132] to only name a few of them. In the sense of nucleation, mesocrystalline structures revealed similar growth mechanisms or the presence of defects (Figure 9) as classical crystals obtained by using atoms or molecules as building blocks.[135-138] However, the formation mechanism of superstructures from their nanoparticle constituents like the mesocrystals is not yet fully understood. Further studies in this field are of interest to understand and control this process and, therefore, the resulting properties of the nanoparticle superstructures.

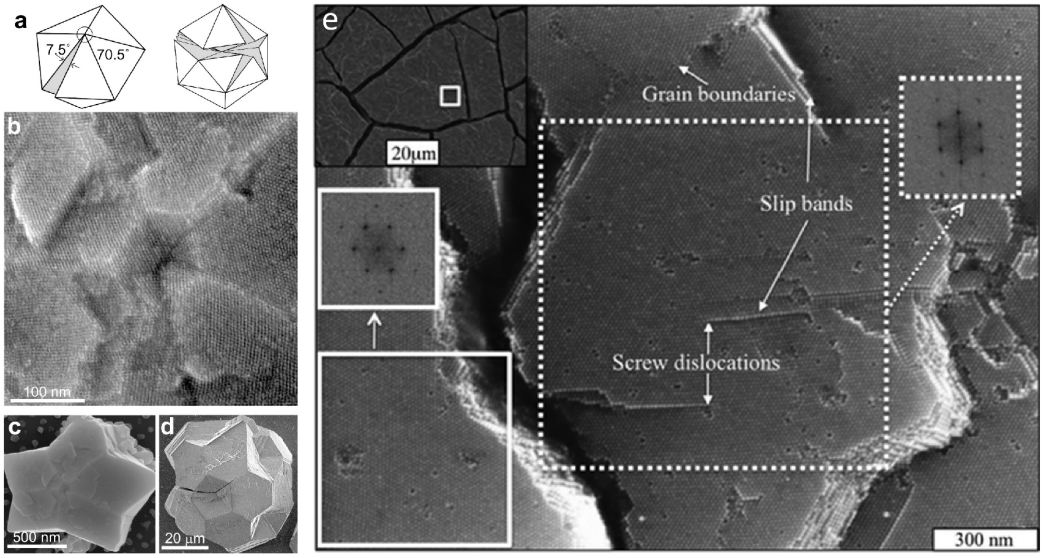

Figure 9. Crystalline defects in mesocrystals. The left images (a-d) show twinning observed in lead (II) sulfide mesocrystals and the right image shows different crystal defects in iron (III) oxide mesocrystal. a) „Solid angle deficiency in multiply twinned nanocrystal superlattices leads to elastic strain proportional to volume of the superlattice. b) High-resolution SEM image taken along the five-fold axis of the multiply twinned superlattice shown in panel (c). d) Removal of the occluded solvent molecules increases the shear modulus of the superlattice, which can relax by opening a gap as shown in panel (a)." Reprinted with permission[138].e) Field emission gun SEM „image of the top surface corresponding to the square shown in insets (SEM image). Point defects, grain boundaries, slip bands and dislocations are observed. Insets: Fourier transforms of areas delimited by solid and dashed lines." Reprinted with permission.[135]

The example of mesocrystals indicates that colloidal particles show an analogous phase behavior to atoms or molecules and they, therefore, stand as a suitable model system to study nucleation.[48, 139, 140] Furthermore, they allow to analyze nucleation phenomena easier than nucleation from atoms or molecules. One big advantage of colloidal systems is their larger size and the consequent lower diffusion coefficient.[7, 141-145] These characteristics provide good experimental accessibility and the possibility to observe nucleation with particles as building units directly with light microscopy.[48, 141] In this field Gasser *et al.* were the first to follow a nucleus growing and overcoming the nucleation barrier.[141] Herein, they observed the nucleation and growth of nearly hard-sphere colloidal polymethylmethacrylate (PMMA) crystals with laser scanning confocal microscopy ((Figure 10). In addition, Bergström *et al.*, for example, investigated the growth of ordered arrays of iron oxide nanocubes.[146-148]

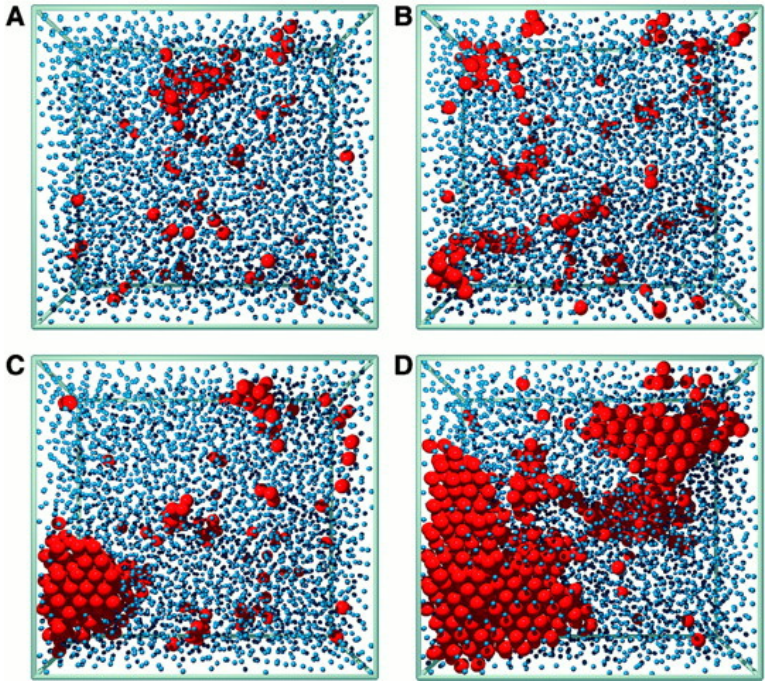

Figure 10. Nucleation and growth of nearly hard-sphere colloidal crystals. Fast laser scanning confocal microscope images show „four snapshots during crystallization of a sample (…). The red spheres are drawn to scale and represent particles that were identified as crystal-like. The particles in the metastable liquid state are shown by the blue spheres, reduced in size for clarity. (**A**) Time t = 20 min (…) (**B**) t = 43 min, (**C**) t = 66 min, and (**D**) t = 89 min." Reprinted with permission from AAAS. [141]

Another advantage of using colloidal particles is the possibility of controlling the interparticle potentials by tuning the particles themselves.[7, 48, 143, 149-151] This particle tuning can be done for instance by changing the electrical or magnetic properties of the particles or their morphology.[48, 140] Thereby, it is possible to adjust the interactions of the particles and induce the formation of different superstructures.[123, 152, 153] This opportunity, to control the interaction potential in colloidal systems, additionally facilitates a comparison of the experimental results with simulation and theory.[7, 84, 154]

Nevertheless, drawbacks exist when using colloidal particles as a model system for nucleation. Polydispersity is probably the most significant one, as particles are no discrete systems in contrast to molecules or atoms with a nearly perfect size distribution. Studies showed that with a polydispersity greater than 5 %, the crystallization and phase behavior of particles is significantly affected. [48, 154] First, a fractionation between the particles of different sizes has to take place before nucleation, which leads to an accumulation of nucleation events at different points in time.[155] Second, the barrier for nucleation can increase rapidly due to an increase in the energy cost of the liquid-solid interface in polydisperse systems.[48] Third, particles exhibit long-range hydrodynamic interactions similar to atoms or molecules. But with the larger size, the density of the particles is much lower. As a consequence the total interaction energy between particles is low and freezing and melting in a particle system can happen without a change of temperature.[48]

Additionally, micron-sized particles are subject to gravity and do not show diffusion as atoms or molecules do.

An opportunity to approach the atomic or molecular system would be to use nanoparticles instead of micron-sized particles. Due to their small size and the consequently higher ratio of surface to bulk atoms, nanoparticles behave differently than their bulk material and they are closer to the behavior of atoms or molecules compared to micron-sized particles.[87] Small nanoparticles do not sediment due to gravity and show a diffusion behavior like atoms or molecules. Furthermore, nanoparticles have the advantage (depending on their properties) that the analysis of them nucleating to bigger structures can be facilitated. One of the examples are the already mentioned gold nanoparticles: their LSPRs not only allows to detect different particle sizes but additionally the aggregation of two or more gold nanoparticles to small clusters. Hence, it is possible to monitor the early stages of particle nucleation into superstructures with UV-vis spectroscopy.[152, 156, 157] Based on the above-mentioned, nanoparticles may close the gap between atoms or molecules and micron-sized particles for investigating nucleation processes. They show diffusion comparable to atoms and molecules but their nucleation into superstructures is easier to analyze due to their bigger size and further special properties. The massive improvement of chemical methods in the last years allows the preparation of nanoparticles with nearly uniform size and controllable morphologies.[123, 158] With those improvements, the number of nanoparticles suitable for nucleation experiments increased tremendously. Particularly promising would be any findings about the nucleation of anisotropic particles into superstructures, which is explained in more detail in the following.

1.3.3 Anisotropic Particles

One can differ between isotropic and anisotropic particles. Isotropic particles exhibit uniformity in all directions such as spherical particles. For nucleation experiments, hard spherical particles as building units are the simplest system. Today, we have a relatively good understanding of the nucleation of hard spherical particles into superstructures using computer simulations[159, 160] and experiments with, for example, spherical PMMA particles.[48, 161-165] Although most work on nucleation and crystallization typically focuses on isotropic particles, systems with anisotropic particles are of greater importance to investigate many nucleation phenomena.[48, 166, 167] For example, crystal formation in concrete proceeds through the nucleation and growth of the anisotropic calcium silicate hydrate platelets to superstructures which in turn brings high mechanical stability to the system.[166, 167] Concrete is the second most widely used material on earth, and its vast carbon dioxide emission urges us to develop greener alternatives such as magnesium silicate-based concrete.[168] The challenge regarding these alternative materials is to direct their nucleation and crystal growth towards a similar structure to existing concrete systems, giving them similar mechanical properties. Understanding and manipulating the nucleation process in these anisotropic systems can thus potentially help to improve the properties of magnesium silicate-based or alternative concretes, allowing a partial replacement of calcium silicates. Proteins are another prominent example, as they can also exhibit

anisotropic forms. Today, X-ray crystallography remains the gold standard for the determination of the macromolecular structure of proteins.[169] However, the crystallization of proteins, which is needed for the analysis with X-ray crystallography, is extremely challenging. Also, in this example, a better understanding of the nucleation of proteins can bring us to a more controlled crystallization of proteins and thus simplify their analysis enormously.

Moreover, anisotropic nanoparticles have direction-dependent properties like different shapes or surface chemistry. Via the shape of a particle, the properties of the single-particle such as electronic[170], catalytic[171], or magnetic[172, 173] properties can be influenced. [174] Further, the break in the symmetry of anisotropic particles can induce remarkable physical properties.[175] For instance, in gold nanorods the shape anisotropy leads to unique optical properties.[176] An isotropic gold nanosphere possesses a single LSPR, as already discussed above (Chapter 1.3.1). In comparison, a gold nanorod exhibits two distinct LSPRs: one longitudinal and one transversal for the two different axes of the gold nanorod. By changing the aspect ratio, meaning the ratio of the length to width of the gold nanorod, one can tune the location of these LSPRs bands.[177] With the discovery of shape-dependent properties of nanoparticles, the synthesis of various shapes was initiated, for example, rods, plates, triangles, and even stars, or flowers.[178-185] Moreover, anisotropy is not limited to the particle shape but can be caused by the chemical composition of the particle. One example would be the so-called Janus particles.[186] Janus particles are typically spherical nanoparticles whose hemispheres differ in chemical compositions. Beyond their special properties, anisotropic particles cannot only self-assemble to simple closest packings, like isotropic spherical particles. Further, they can self-assemble into a rich variety of structures, ranging from different closest packings to lamellar and liquid crystal phases.[109, 187-189] Figure 11 shows the example of truncated cubic-shaped iron oxide nanoparticles assembling into superstructures with varying structure and morphogenesis.[190] Furthermore, the nanoparticle-based superstructure eventually determines its macroscopic properties.[106, 107, 109, 113]

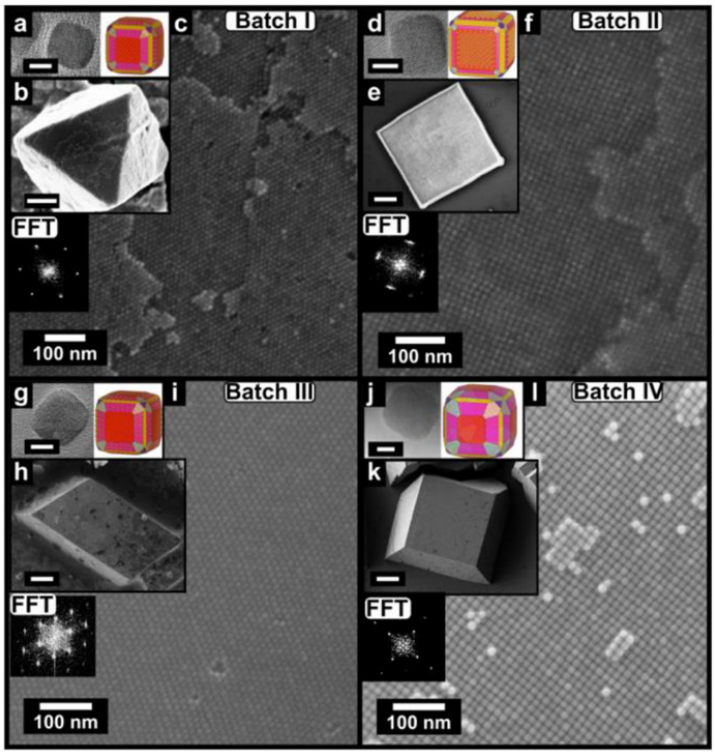

Figure 11. Influence of particle anisotropy on the structure of the resulting superstructures. HR-TEM images (insets, scale bars = 5 nm) and models of the corresponding nanocube building blocks. (b, e, h, k) Mesocrystals self-assembled from the nanoparticles showing different morphologies (inset, scale bar = 10 µm). (c, f, i, l) HR-SEM images and corresponding FFT of the projected mesocrystals faces showing the packing of the nanocubes. Reprinted with permission.[190]

Comprising, anisotropic building units from molecules to particles are not only common in nature but additionally open the possibility to design new material properties resulting from a variation in the assembly structures.[123] However, in many cases, it is yet unclear how the shape of the building units influences the nucleation processes.

1.3.4 Interparticle Interactions

In general, the nucleation and growth of nanoparticle superstructures is a process that depends on diverse parameters on different size scales: the particle composition, the particle size and shape, the layer of surfactant ligands that colloidally stabilizes the particle, the surrounding medium, and the stimuli used to trigger the self-assembly.[123]

The formation of superstructures via self-assembly brings the particles from a diluted state to a state where the particles are close to each other and interact with their nearest neighbor. Here, a great variety of particle-particle interactions have to be considered, whose combination is commonly described as an effective interparticle pair interaction.[123] Van der Waals forces are generally responsible for attractive interaction between particles, while steric and electrostatic interactions are typically utilized to ensure sufficient repulsive forces to maintain colloidal stability. Thus, particles can be stabilized either sterically using hydrocarbon

surfactants or neutral polymers or electrostatically via charged species. The two fundamentally different cases of particle stabilization can be combined by using polymeric chains with ionizable groups, so-called polyelectrolyte ligands, resulting in an electrosteric stabilization.

The combination of different particle-particle interactions is commonly described in a pair potential. The particles are colloidally stable and remain dispersed as long as the pair potential is dominantly repulsive (Figure 12A, light red). To destabilize such a particle dispersion, one can use different approaches depending on the particles and their stabilizing ligands: increasing the particle concentration by removing the solvent, adding a nonsolvent, cooling the solution, and changing the pH or the ionic strength of the solvent.[123] With the starting destabilization, the particle-particle interaction changes from repulsive to attractive (Figure 12A, dark red), and the particles might end up in a potential well from where they cannot escape with the thermal energy k_BT of the system.[123] The total interaction potential of particles is often described with the Boris Derjaguin and Lev Landau, Evert Verwey, and Theodoor Overbeek (DLVO)-theory. It combines the long-range attractive van der Waals forces between particles and the short-range repulsive electrostatic forces of the particles themselves or the double layer of counter ions around them.[191] Figure 12B shows the resulting total potential dependent on the distance between the two particles. The particles do not experience a force if they are far away from each other. By getting closer, they can run through a secondary and a primary minimum separated by an energy barrier. The primary minimum is a deep attractive potential well and the aggregation of the particles here is irreversible. If the energy barrier is too high, the particles may stay in the secondary shallow minimum. Here, the particles hold together, but more weakly compared to the primary minimum and the process is reversible. If the interparticle distance is small, a strong repulsive force from the electrostatic interactions dominates.

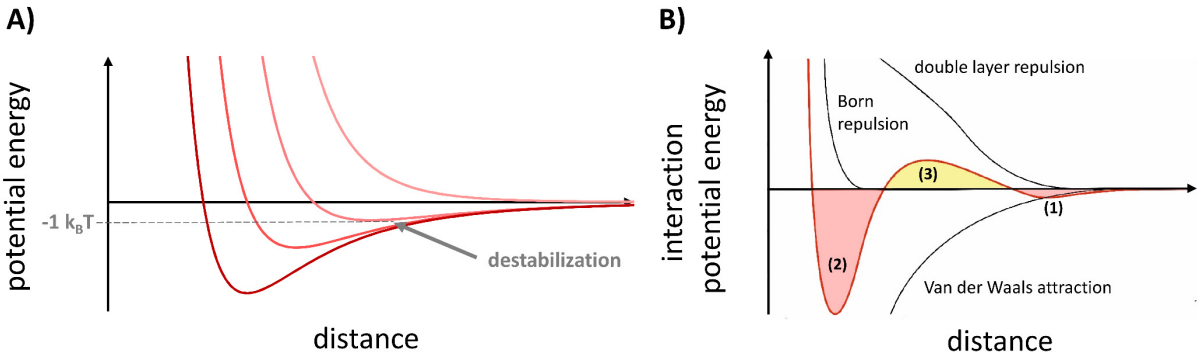

Figure 12. Pair potentials for particle-particle interaction. A) Pair potential of two particles approaching each other and the transition from a repulsive (light red) to an attractive (dark red) interaction due to destabilization of the particle solution. B) Total interaction potential from the DLVO-theory, resulting from the combination of the Born repulsion, the double layer repulsion, and the van der Waals attraction. Approaching each other, particles pass through a secondary minimum (1) where the particle-particle interaction is reversible. If the energy barrier (3) is not too high, particles might pass to a primary minimum (2), where the particle-particle interaction is not reversible.

The potential interactions between the particles are the key determinant for their assembly and the resulting superstructures. This circumstance not only applies to particles, but all size scales, thus also to atoms and molecules. However, attractive and repulsive forces acting on atoms or molecules might differ in some cases from the ones acting on particles, for example, the double-layer repulsion does not apply.[48] The DLVO-theory for particle interactions discussed above assumes an isotropic particle whose assembly results in a simple closest packing. At this point lies the chance to bring diversity to particle superstructures by inducing an anisotropic behavior or shape to the building blocks that could result in a more complex potential landscape that offers various potential wells resulting in different superstructures.

Though, the self-assembly of particles into ordered superstructures is not solely determined by their interparticle interactions but further through entropic parameters.[123] The most stable phase of a particle system corresponds to the phase maximizing the total free energy of the system. In this sense, the densest possible packing for the particle will eventually be the most stable structure since it results in the maximum entropy state.[123] There might be a configurational entropy loss due to the ordering of the mean particle positions, however, there is a predominant gain of translational and rotational entropy through the extra free volume.

1.3.5 Nanoparticle Superstructures on Substrates

The previous chapters showed that the nucleation and the resulting structure of particle assemblies are influenced by different factors, for instance, the chemical composition and the size of the particle, its' stabilization, and the surrounding medium. Further, properties like particle anisotropy can induce a variety of structures in the resulting particle assemblies. Another versatile possibility to influence the nucleation and assembly of particles is to use substrates. There are already a lot of examples of the (heterogeneous) nucleation or the assembly of nanoparticles on substrates, which play a significant role in the formation and analysis of particle superstructures. A substrate in heterogeneous nucleation, in general, can be any imaginable foreign surface, such as the reaction vessel's wall, air bubbles, or dust particles present in the system as inevitable examples.[25, 30] Continuing this thought, substrates could be used targeted in the nucleation and self-assembly of nanoparticle superstructures to direct their structural formation and with this, the properties of the resulting superstructures. Furthermore, typical subsequent characterization techniques of nanoparticle assemblies require the immobilization of the nanoparticle superstructures on a substrate. Therefore, in the synthesis of nanoparticle superstructures, such as mesocrystals, commonly smooth substrates like silicon wafers or glass slides are used. In retrospect, it can be challenging to estimate whether the superstructures formed heterogeneously on the substrate or sedimented from the solution and to measure the influence of a substrate on the superstructure formation.[123] Here, theoretical investigations can be helpful, like the example of Luedtke *et al.,* who simulated the adsorption of dodecanethiol capped gold nanoparticles on the basal plane of graphite.[192] The simulations showed a bending of the hydrocarbon chains when attaching to the substrate resulting in an edge orientation of the nanoparticles.

Next to planar substrates, textured substrates on the order of the nanoparticle diameter open the possibility of direct structural control. Certainly not all examples for textured substrates proceed over a heterogeneous nucleation mechanism but could rather be considered as a self-assembly in confinement. For instance, lithographically patterned templates can trap solvated nanoparticles via capillary forces[193-195] or periodically structured templates allowed to arrange gold nanorods to plasmonic supercrystals (Figure 13).[196] On the other hand, spherical substrates like emulsion droplets[197] or microspheres[198] can be used to control the structuring of nanoparticle assemblies. Additionally, the assembly of cadmium selenide nanoparticles to monolayers at liquid-liquid interfaces gave more insight into the formation mechanism.[199] Pendant drop tensiometry and ex situ TEM measurements showed three steps in this process: first free nanoparticle diffusion to the interface, second, a closer packing of the nanoparticles to clusters, and third, a thermally activated exchange between incoming and adsorbed nanoparticles resulting in a dense packed monolayer. Another example at liquid-liquid interfaces constitutes the assembly of tri-n-octylphosphine oxide-covered cadmium selenide nanorods.[200] The structures of these assemblies ranged from low-density smectic packings over more dense columnar ordering to crystalline-like phases. These different structures could be induced by varying the interfacial energy between the liquids and the nanorods, the nanorod concentration, or the nanorod aspect ratio.

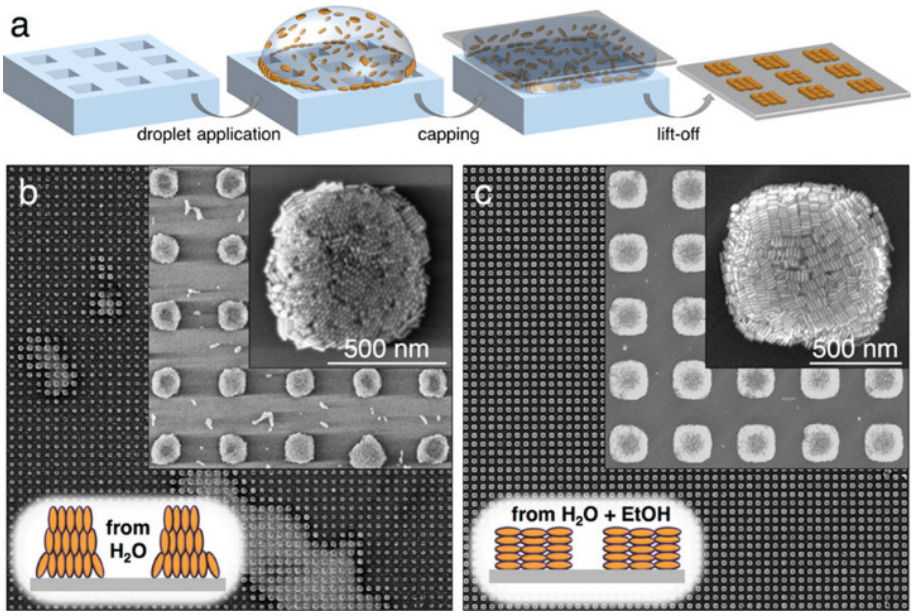

Figure 13. Arrangement of gold nanorods with periodically structures templates. a) A scheme shows „the patterning process, which comprised drying of a dispersion droplet confined between a structured soft polydimethylsiloxane stamp and a flat target substrate."[196] b) SEM images from gold nanorod arrangements originally dispersed in water. c) SEM images from gold nanorod arrangements obtained with the same particles but now dispersed in an ethanol/water mixture. Reprinted with permission.[196]

Besides the substrates' topography, its surface chemistry is crucial for the heterogeneous nucleation of nanoparticle superstructures. This idea implies that the interfacial energy between the nucleus and the

substrate can be tuned through the control over the surface charge, the hydrophobicity, the presence of different organic molecules, or its crystal lattice. For instance, when the interfacial energy decreases, the critical size of the nucleus becomes smaller, thereby favoring nucleation processes.[6, 10, 14, 156] The interfacial energy of a nucleus on a substrate might be reduced by allowing strong bonding to the nucleus or by minimizing lattice strain since the substrates' structure matches a particular plane of the nucleation phase.[18, 49] Indeed, there are various examples where the surface chemistry of substrates is used to direct the nucleation of atomic or molecular crystals.[201-205] For instance, surfaces derivatized with different functional groups can direct calcite crystal growth into specific orientations due to their impact on the nucleation plane.[52-54] However, there are fewer examples in the case of nanoparticles. For example, silver octahedral are directed into three different 2D plasmonic superlattices at liquid-liquid interfaces by systematically tuning the wettability.[206] Another example constitutes the fabrication of 2D gold nanoparticle superlattices over an area of hundreds of square micrometers. To achieve a uniform nanoparticle organization, the role played by the surface chemistry of the substrate was found to be essential. When it was tuned from hydrophilic to hydrophobic by depositing Teflon-like films onto silicon a more favorable interaction with the hydrophobic alkyl chain on the gold nanoparticle surface was observed (Figure 14).[207] In another example, the hydrothermal treatment of lead (II) titanate precursors successfully deposited a three to six millimeters thick mesocrystal layer on substrates. Herein also, the surface chemistry of the substrate was found to be crucial. The growth of the mesocrystal layer on lead (II) titanate and strontium titanate substrates was successful due to similar crystal lattices. However, when aluminum oxide was used as a substrate, no layers were observed due to crystal lattice mismatch.[208]

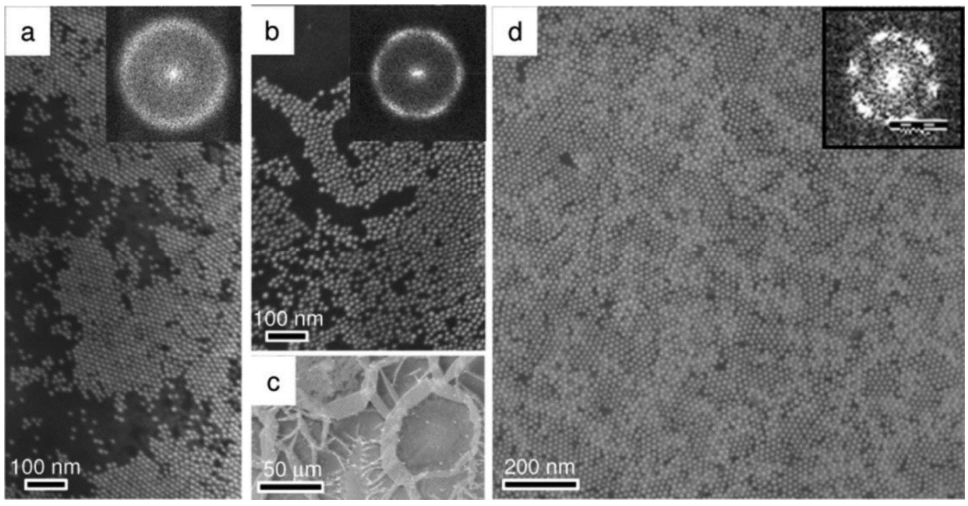

Figure 14. Gold nanoparticle superlattices on different substrates. SEM images of gold nanoparticles in nonane drop-cast on the different substrates: a) bare silicon/silicon dioxide, b, c) silicon covered with Teflon-like films (low crosslinking degree) at different magnifications, and d) silicon covered with Teflon-like films (high crosslinking degree) with the corresponding Fast Fourier transform. Reprinted with permission.[207]

The here-presented examples support the idea that using particles as a model system to study nucleation could be a promising approach to circumvent the analytical difficulties regarding the analysis of nucleation. Furthermore, this approach can help to understand the sparsely studied heterogeneous nucleation with anisotropic building blocks and allow for a closer insight into particle assembly and the formation of novel materials. The following thesis describes how this approach is used to study the heterogeneous nucleation of anisotropic nanoparticles with a focus on the impact of surface chemistry and particle anisotropy

2 Scope of the Thesis

This thesis aims to develop a model system on anisotropic particles to investigate the complex phenomena of heterogeneous nucleation. Herein, the influence of surface chemistry and particle shape on the heterogeneous nucleation into superstructures is analyzed. Heterogeneous nucleation is a common phenomenon in nature. There it vividly shows up in the formation of clouds or biominerals. However, it is no less important in industrial applications like the hardening of cement or the formation of mineral scale in pipes. Despite its relevance, until today, heterogeneous nucleation is not fully understood, in part due to the demanding analysis, which requires a high spatial and temporal resolution at the same time.

To simplify the analysis of nucleation phenomena, this thesis uses the model system of nanoparticles building up into bigger superstructures to analyze heterogeneous nucleation in more detail. Especially the impact of surface chemistry and particle shape on the nucleation of the nanoparticles into superstructures is examined. To be able to study the effect of these two parameters, first, a controlled system needs to be established according to the three aspects: 1. substrates with a defined surface chemistry where the heterogeneous nucleation of the nanoparticles takes place (Chapter 3), 2. nanoparticles with a defined surface chemistry and particle shape as building blocks for the nucleation (Chapter 4), and 3. analytical methods, which allow observing the nucleation process and measuring its kinetic behavior (Chapter 5). For a qualitative and quantitative analysis of the heterogeneous nucleation, a controlled destabilization of the nanoparticle systems and a (homogeneous) nucleation in solution is first investigated. In the next step, a substrate is introduced into the system to achieve heterogeneous nucleation on the substrate's surface. The in situ observation of this heterogeneous nucleation process is accomplished with the widely available analytical methods of light microscopy and UV-vis-NIR spectroscopy, which allow the determination of nucleation rates and further the analysis of the data with the classical nucleation theory.

When it comes to nucleation, surface chemistry is one crucial factor. Amongst others, the nanoparticles' surfaces determine the particle-particle interaction and thereby, the nucleation kinetics. A favorable attractive particle-particle interaction most likely will lead to enhanced nucleation kinetics, while an unfavorable interaction might prevent it completely. In heterogeneous nucleation processes, another surface comes into play. Now, additionally, the particle-substrate interaction impacts the nucleation process, which might lead to enhanced nucleation kinetics. This thesis investigates how nanoparticle and substrate surface chemistry impacts on nucleation of nanoparticle superstructures (Chapter 6). In this sense, two different approaches are used: tuning the surface chemistry of the substrates and modifying the surface chemistry of the nanoparticles. With this approach, it is possible to build up a library with substrates and nanoparticles that only differ in their surface functionality. In the next step, nucleation experiments can be performed with all combinations of substrates and nanoparticles to determine the influence of the surface chemistry

on the nucleation process. Next to the nucleation kinetics, the structural influence of the surface chemistry on the superstructures built up by the nanoparticles is also analyzed.

Beyond the surface chemistry, the shape of the building block plays an essential role in nucleation phenomena, as demonstrated by the nucleation of proteins. Nevertheless, most studies on nucleation focus on isotropic hard spheres. This thesis analyzes the nucleation of anisotropic nanoparticles since they are not only common in nature but additionally open the possibility to design new material properties resulting from a variation in their assembly structures (Chapter 7). For a first insight into the impact of particle anisotropy, this thesis analyzes the nucleation and assembly of nanorods with varying aspect ratios. Thereby, it reveals the influence of the aspect ratio on heterogeneous nucleation.

For both aspects, the surface chemistry and the nanoparticle anisotropy, the differences between the nanoparticle-based model system and atomic or molecular building units are revealed. Moreover, the reported experiments provide experimental data for theoretical descriptions of nucleation using non-spherical building units. To unravel the secrets of nucleation means to better understand environmental processes. Beyond that, a more detailed understanding of nucleation allows for targeted intervention and the creation of functional materials with tailor-made properties.

3 Substrates for Heterogeneous Nucleation

Substrates play a crucial role in nucleation since a favorable interaction between building blocks and substrate decreases the nucleation barrier resulting in enhanced kinetics at lower degrees of supersaturation compared to the homogeneous nucleation in dispersion.[48] Additionally, the substrate may influence the structure of the nucleating material. At the beginning, this first chapter focuses on the substrates selected for heterogeneous nucleation experiments and their functionalization to create a broad variety in surface chemistry.

3.1 Results and Discussion

For convenient analysis of heterogeneous nucleation experiments, a suitable substrate had to meet three requirements: the possibility to introduce functional groups to the surface, low roughness, and ideally transparency. First, the introduction of functional groups to the substrate's surface is essential since analyzing the influence of the substrate surface chemistry on heterogeneous nucleation displayed one main objective. With free hydroxyl groups on the surface, the three chosen substrates mica, glass, and silicon wafers were all suitable for the introduction of functional groups via a siloxane chemistry-based approach. Second, to avoid undesired and not quantifiable nucleation of nanoparticle-based superstructures induced by surface cracks or roughness, smooth substrates, such as polished silicon wafers or mica were advantageous. Third, transparency was a desirable property of suitable substrates, enabling the in situ investigation by light microscopy techniques. A transparent substrate allowed here to use transmitted-light microscopy additional to reflected light microscopy, which considerably simplified the experiment setup. Mica reconciled all mentioned crucial requirements for heterogeneous nucleation analysis and thus was chosen as the primary substrate for the experiments conducted here.

For this purpose, mica substrates were tailored in their surface chemistry by introducing different functional groups via siloxane chemistry (Chapter 3.3.3). Prior to the functionalization, the substrate surface was treated with oxygen plasma to clean the surface and maximize the number of activated hydroxyl groups.[209] The functionalization with different silanes followed the same basic principle (Figure A 1). Initially, hydrolysis of the alkoxy groups occurs, promoted by the base 1,1-Diisopropylethylamine (DIPEA). In a second step, hydrogen bonding with substrate hydroxyl groups is followed by a covalent linkage of the silane to the substrate.[210, 211] The covalent nature of the assembly process results in superior stability, allowing extensive handling and further modification steps without deterioration of the silane layer.[212] During baking of the substrates at 150 °C, the remaining hydroxyl bonds crosslink with neighbored silanes and unbound mobile silanes are incorporated into the layer, which smoothens the silane coating.[210] Performing the synthesis as a vapor phase diffusion allowed us to keep a clean substrate and to have high control over the process (Figure A 2). Thereby, basic ($-NH_2$), acidic (-COOH, $-SO_3H$), hydrophilic (-OH), and hydrophobic

(-CH_3, -CF_3) functional groups were introduced efficiently, representing a broad range of surface chemistry properties (Figure 15 A). Caution was required by introducing the hydroxyl (-OH) and carboxyl (-COOH) groups. These groups can take part in the condensation reaction by forming a bond with the hydroxyl groups of other silanes, which means they would not be available as functional groups anymore. To preserve the functional groups, the silanes had to be introduced to the mica surface with a protection group (succinic anhydride for the carboxyl group and acetyl for the hydroxyl group), followed by a deprotection step (Chapter 3.3.3). An analytical comparison between the protected and deprotected surface properties are given in Table A 1 for the carboxyl and in Table A 2 for the hydroxyl functionalization.

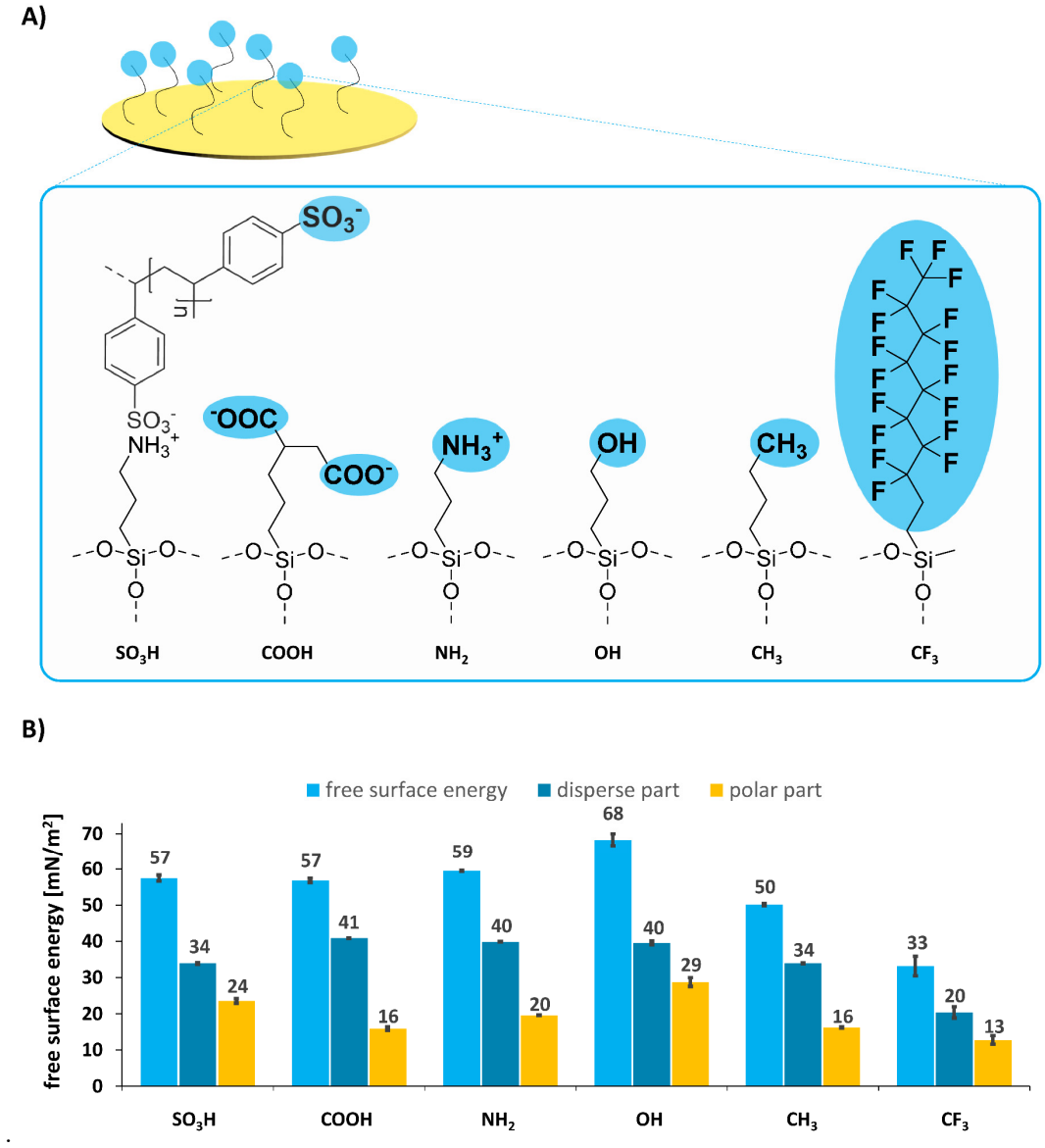

Figure 15. Different functional groups introduced to substrates. A) Scheme of a functionalized mica substrate showing the variety of introduced functional groups: sulfonate (-SO_3H), carboxyl (-COOH), amine (-NH_2), hydroxyl (-OH), alkyl (-CH_3) and fluorine (-CF_3). B) Free surface energies of the substrates (light blue) modified with the respective functional groups determined by contact angle measurements and their disperse (dark blue) and polar parts (orange).

To ensure the comparability of the coating with the different functional groups, the synthesis conditions were adapted. The coating thickness has proven to be directly depended on the reaction time, as exemplarily displayed for the amine functionalization (Figure A 3) and determined by ellipsometry measurements (Table 1, Table A 3). The thin coating thickness of about one nanometer met the crucial requirement of smooth substrates for the investigation of heterogeneous nucleation. The remaining low surface roughness of the modified mica substrates was verified by AFM (Table 1, Table A 3). While mica had a surface roughness of R_a = 0.4 nm, the different functionalizations' surface roughness was between 0.1 nm for the carboxyl group and 0.6 nm for the alkyl group.

Table 1. Silane layer characterization. Characterization of the functionalized mica substrates: surface roughness determined by AFM and layer thickness determined by ellipsometry.

	mica	**sulfonate**	**carboxyl**	**amine**	**hydroxyl**	**alkyl**	**fluorine**
roughness R_{ms} [nm](1)	0.4	0.2	0.2	0.4	0.2	0.6	0.2
roughness R_a [nm] (1)	0.3	0.3	0.1	0.3	0.2	0.5	0.2
thickness [nm](2)	-	1.94	0.94	0.96	2.06	1.34	1.12

(1) R_{ms} = root mean square of the roughness height and R_a = surface roughness value $R_{max}/4$ were determined with AFM over a surface of 1 x 1 µm.

(2) The layer thickness was determined using ellipsometry. A polished Si wafer was used as substrate since mica cannot be used in this method because of its birefringence.

The characterization of the modified substrates by using attenuated total reflection infrared spectroscopy (ATR-IR) or energy-dispersive X-ray spectroscopy (EDX) measurement was not possible, since the penetration depths of these methods are in the range of 0.5 to 2 µm.[213] Hence, the main detected signals were accorded to the mica and not to the surface functionalization. Nevertheless, the amine (Figure A 4) and fluorine (Figure A 5) functional groups were certified by X-ray photoelectron spectroscopy (XPS). The analysis with XPS was complex for the other functional groups since the carbon and oxygen signals are similar to signals of typical organic impurities during the measurement. However, the enhanced C1s peak most likely indicated a successful carboxylate functionalization (Figure A 6), while a slightly enhanced O1s peak might indicate a hydroxyl functionalization (Figure A **7**). Furthermore, signals of characteristic elements in mica like fluorine (FKLL and F1s) disappeared with the functionalization, suggesting that a certain density of silane units exists on the substrates (Figure A 8).

Due to the problematic compositional analysis of the thin layers, contact angle measurements were identified as the most significant and easy to handle analytical method to detect and characterize the different functional group-dependent surface properties. Measuring contact angles with water and diiodomethane as solvent allowed calculating the free surface energies of the here established substrates with their dispersive and polar parts (Figure 15B, Table A 4, Table A 3). The free surface energy quantifies the work for the disruption of intermolecular bonds that would occur when a new surface of the solid phase is generated and determines decisively the wettability of the surface. It can be further characterized by its dispersive and polar parts. Surfaces with a high dispersive part are mainly able to form van der Waals bonds, while for surfaces with a high polar part, polar interactions like dipole-dipole interactions or hydrogen bridge bonds prevail.[214] In the characterization of the silane coatings, polar functional groups like hydroxyl or carboxyl groups obtained high free surface energies with a large polar part, while for the apolar alkyl group the dispersive part prevailed. In contrast, the fluorine group had a low polar and dispersive part and, therefore, a resulting low free surface energy. In addition to the XPS measurements, the contact angle measurements displayed successful tailoring of the mica surface chemistry, which is determined by the introduced functional groups. Additionally, contact angle measurements allowed testing the temporal stability of the silane coatings, as shown for the hydroxyl functionalization (Figure A 9). Here the water contact angle increased by 20° in the first ten days, suggesting to use the substrates directly after the functionalization. Studies from Wasserman *et al.* exhibit that especially polar silane surfaces contaminate rapidly but can be cleaned with ethanol even after a long storage time to receive the original surface properties.[215]

Keeping the heterogeneous nucleation experiments in mind, a closer look at the basic and acidic functional groups was of interest since depending on the pH value of the solution they can be protonated or deprotonated. Thus, the basic and acidic functional groups may exhibit a charge, which crucially influences the substrates' surface chemistry. The substrates were functionalized with the base amine as well as the carboxylic (succinic) and sulfonic acid (Figure 15). While the negative decadic logarithm of the acid constant (pK_S) of the succinic acid is $pK_{s1} = 4.16$ and $pK_{s2} = 5.61$[216] the pK_S of sulfonate acids are in the range of $pK_S = -0.5 - 2$[217, 218] and the pK_S of the amine group is $pK_S = 10$[219]. That means at neutral pH the acids on our substrates were negatively charged and the amine group was positively charged. Contact angle measurements at different pH values illustrated the pH-dependent behavior as shown exemplarily for the carboxyl group (Figure A 10). Substrates with these charged acidic and basic groups had a key role in heterogeneous nucleation experiments in the combination with charged nanoparticles (Chapter 6). Here the combination of oppositely charged substrate and nanoparticles led to a highly favorable interaction, while the combination of equal charged substrate and nanoparticles led to a highly unfavorable interaction. These combinations represented the two extrema on the interaction range and with the sulfonic acid at $pK_S \sim 1$, the carboxylic acid at $pK_S \sim 4$, and the amine at $pK_S \sim 10$ a broad bandwidth could be established.

In conclusion, mica was identified as a promising substrate for the analysis of heterogeneous nucleation and a broad variety of surface chemistry properties, reaching from hydrophilic to hydrophobic as well as negatively and positively charged surface functionalizations, was achieved. Thereby, the smooth substrates' surface, the prerequisite for the investigation of heterogeneous nucleation events, was preserved. The applied functionalization reactions using silanes only depended on free hydroxyl groups on the substrates' surface. Thus, not only mica but additionally silicon and quartz were functionalized in the same way. Therewith, different substrates with a variety in surface chemistry properties were established and used in the following heterogeneous nucleation experiments depending on their advantages: silicon and mainly mica as smooth substrate and the surface of quartz cuvettes to analyze kinetics in situ.

3.2 Appendix

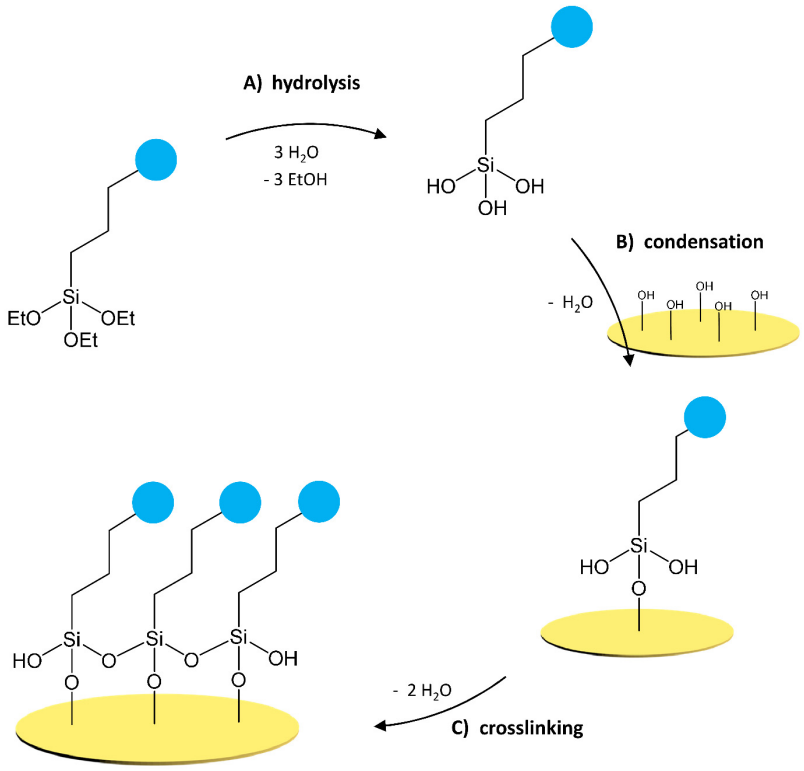

Figure A 1. Reaction mechanism of silane functionalization. A) Initially, hydrolysis of the alkoxy groups occurs in presence of water. B) Hydrogen bonding with surface hydroxyl groups is followed by a covalent linkage of the silane by condensation reaction. Usually, one bond of each silane to the substrate is present, while the other two hydroxyl groups remain. C) During baking, the remaining hydroxyl bonds crosslink with neighbored silanes accompanied with water release.

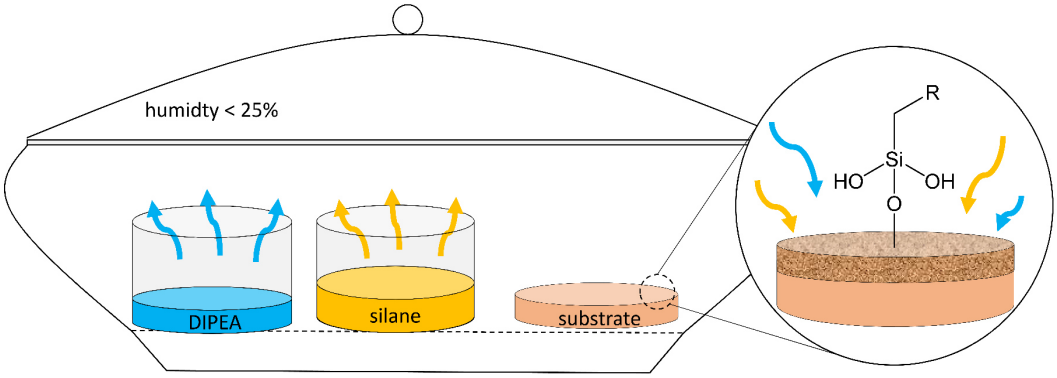

Figure A 2. Experimental setup for substrate functionalization with silanes. The reaction proceeds as vapor phase diffusion. Therefore, the humidity had to be below 25%. The substrates are placed in the desiccator next to a reservoir with the corresponding liquid silane and DIPEA. The hydrolyzed silane diffuses from the gas phase to the mica substrate and covalently links to the hydroxyl groups on the mica surface (inlay).

Table A 1. Deprotection of carboxyl groups. Characterization of mica surfaces' properties functionalized with carboxyl groups before and after the deprotection of the functional group.

	carboxyl protected	**carboxyl deprotected**
contact angle water [°]	52.25 ± 1.43	28.49 ± 0.71
contact angle diiodomethane [°]	43.00 ± 0.64	40.89 ± 0.63
free surface energy [mN/m]	55.57 ± 1.19	69.25 ± 0.70
dispersive part [mN/m]	39.07 ± 0.34	39.16 ± 0.32
polar part [mN/m]	17.50 ± 0.86	30.09 ± 0.38
thickness [nm](1)	1.13	0.94

(1) The layer thickness was determined using ellipsometry. A polished silicon wafer was used as substrate since mica cannot be used in this method because of its birefringence.

Table A 2. Deprotection of hydroxyl groups. Characterization of mica surfaces' properties functionalized with hydroxyl groups before and after the deprotection of the functional group.

	hydroxyl protected	**hydroxyl deprotected**
contact angle water [°]	68.59 ± 1.70	52.89 ± 0.85
contact angle diiodomethane [°]	36.15 ± 0.11	37.44 ± 0.18
free surface energy [mN/m]	49.04 ± 0.82	56.81 ± 0.57
dispersive part [mN/m]	41.49 ± 0.05	40.88 ± 0.09
polar part [mN/m]	7.54 ± 0.77	15.94 ± 0.48
thickness [nm](1)	1.43	2.06

(1) The layer thickness was determined using ellipsometry. A polished silicon wafer was used as substrate since mica cannot be used in this method because of its birefringence.

Table A 3. (3,3,3-trifluoropropyl)trimethoxysilane. Characterization of the (3,3,3-trifluoropropyl)-trimethoxysilane-functionalized mica surfaces with contact angles, free surface energy, surface roughness and layer thickness.

	mica	**(3,3,3-trifluoropropyl) trimethoxysilane**
contact angle water [°]	13.26 ± 0.25	65.01 ± 2.48
contact angle diiodomethane [°]	52.88 ± 0.11	65.94 ± 0.90
free surface energy [mN/m]	72.62 ± 0.14	40.93 ± 2.13
dispersive part [mN/m]	32.65 ± 0.06	25.16 ± 0.51
polar part [mN/m]	39.97 ± 0.08	15.77 ± 1.61
roughness R_{ms} [nm](1)	0.4	0.2
roughness R_a [nm] (1)	0.3	0.1
thickness [nm](2)	-	0.12

(1) R_{ms} = root mean square of the roughness height and R_a = surface roughness value $R_{max}/4$ were determined with AFM over a surface of 1 x 1 μm.

(2) The layer thickness was determined using ellipsometry. A polished silicon wafer was used as substrate since mica cannot be used in this method because of its birefringence.

Table A 4. Contact angle measurements. Characterization of the functionalized mica surfaces with contact angles for water and diiodomethane, free surface energy and its disperse and polar parts.

	mica	**sulfonate**	**carboxyl**	**amine**	**hydroxyl**	**alkyl**	**fluorine**
contact angle water [°]	13.26 ± 0.25	45.64 ± 0.98	52.89 ± 0.85	47.29 ± 0.13	30.85 ± 2.39	57.50 ± 0.31	73.71 ± 1.40
contact angle diiodomethane [°]	52.88 ± 0.11	50.67 ± 0.37	37.44 ± 0.18	39.42 ± 0.10	40.10 ± 0.97	50.62 ±0.18	74.49 ± 2.87
free surface energy [mN/m]	72.62 ± 0.14	57.46 ± 0.83	56.81 ± 0.57	59.48 ± 0.13	68.30 ± 1.68	50.15 ±0.30	33.17 ± 2.73

dispersive part [mN/m]	32.65 ± 0.06	33.90 ± 0.21	40.88 ± 0.09	39.90 ± 0.05	39.56 ± 0.49	33.93 ±0.10	20.40 ± 1.56
polar part [mN/m]	39.97 ± 0.08	23.56 ± 0.62	15.94 ± 0.48	19.58 ± 0.08	28.74 ±1.20	16.22 ±0.19	12.77 ± 1.17

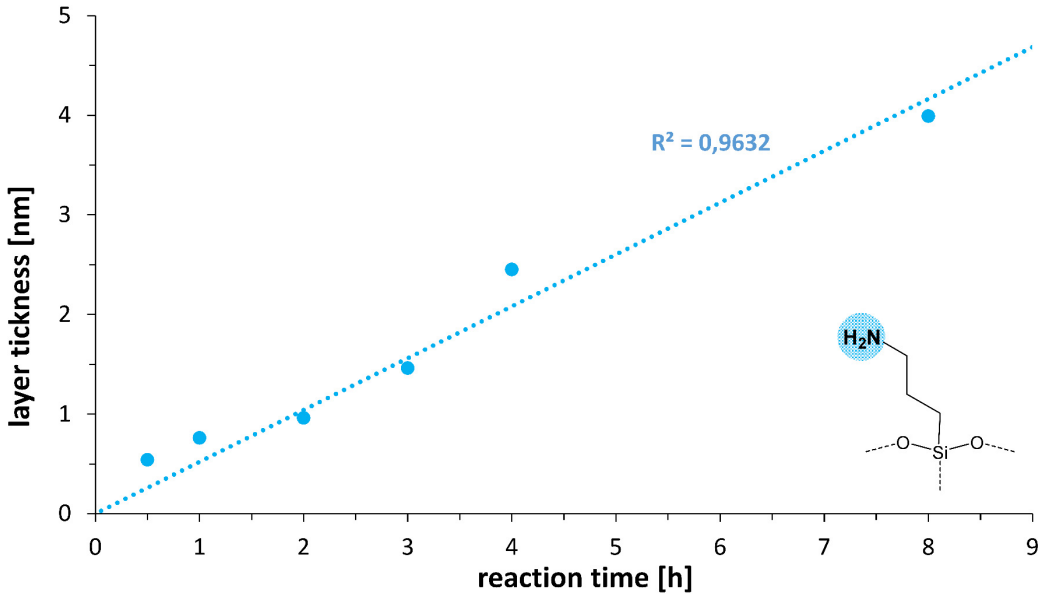

Figure A 3. Layer thickness in dependence of reaction time. Thickness of the amine functionalization layer on a silicon wafer determined by ellipsometry measurements in dependence of the reaction time during the functionalization. The layer thickness increases linearly with the reaction time. The dotted line represents the linear fit. The layer thickness was determined using ellipsometry. A polished silicon wafer was used as substrate since mica cannot be used in this method because of its birefringence.

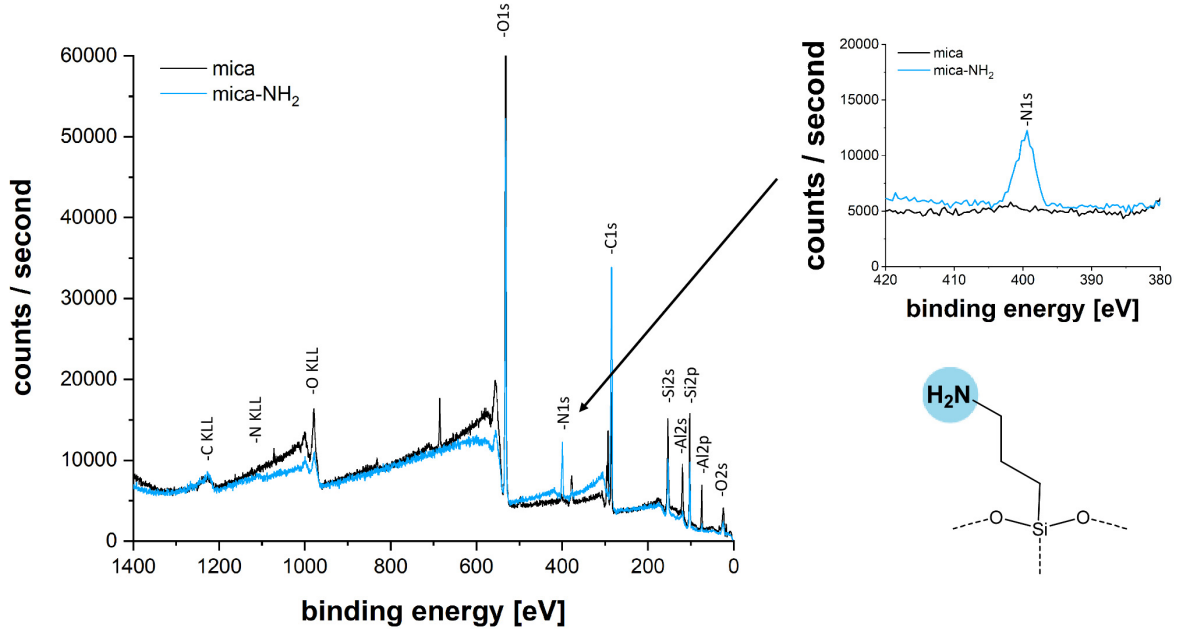

Figure A 4. XPS spectra of amine functionalization. XPS spectra of mica (black) and mica functionalized with amine groups (blue), which corresponds to the silane with the shown structure. The additional N1s peak indicates the functionalization with the amine group (inlet).

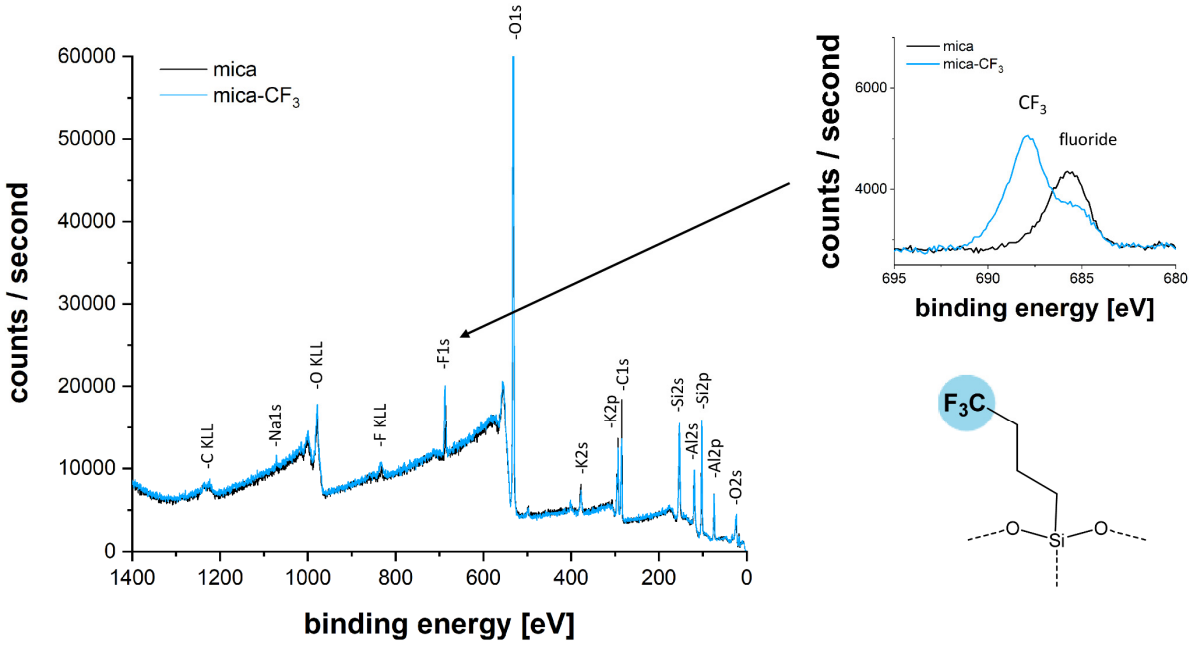

Figure A 5. XPS spectra of fluorine functionalization. XPS spectra of mica (black) and mica functionalized with fluorine groups (blue), which corresponds to the silane with the shown structure. The shifted F1s peak (inlet) indicates the functionalization with the fluorine group.

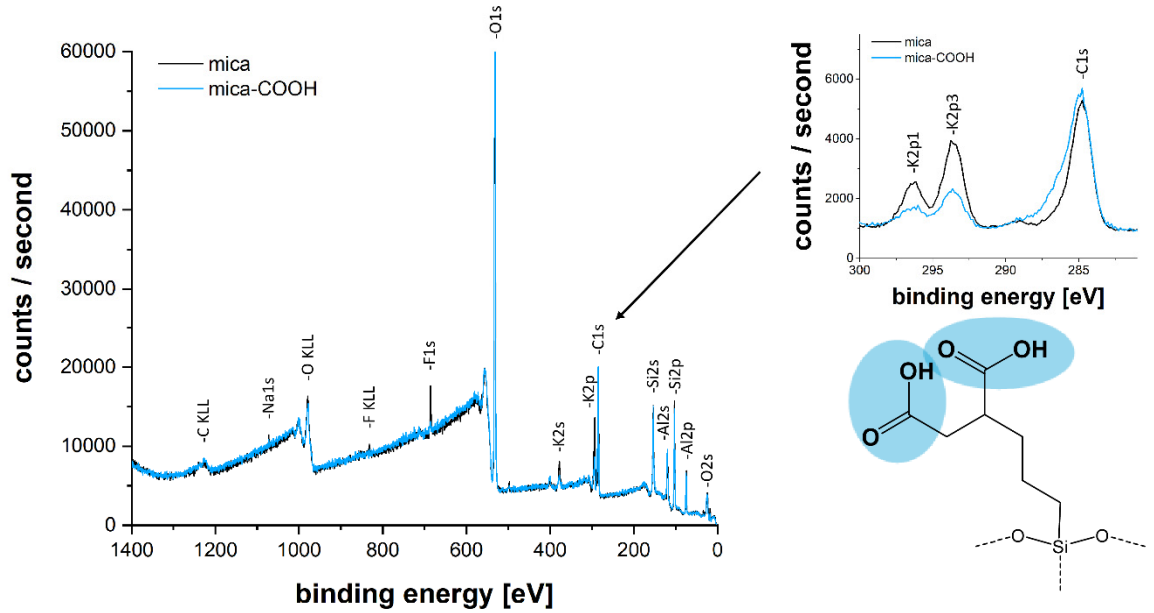

Figure A 6. XPS spectra of carboxyl functionalization. XPS spectra of mica (black) and mica functionalized with carboxyl groups (blue), which corresponds to the silane with the shown structure. The detection of the carboxyl group is complex since the carbon and oxygen signals are similar to signals of typical organic impurities during the measurement. A higher C1s peak most likely indicates the carboxyl functionalization (inlet).

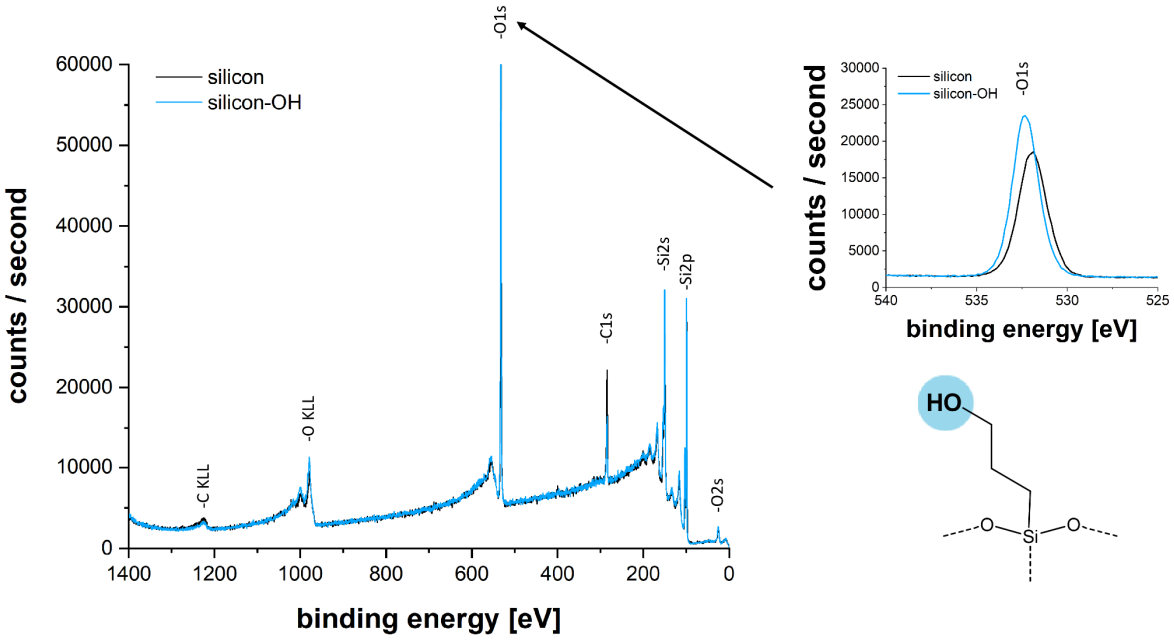

Figure A 7. XPS spectra of hydroxyl functionalization. XPS spectra of silicon (black) and silicon functionalized with hydroxyl groups (blue), which corresponds to the silane with the shown structure. The detection of the hydroxyl group is not easy since the carbon and oxygen signals are similar to signals of typical organic impurities during the measurement. A higher O1s peak could be an indication for the hydroxyl functionalization (inlet).

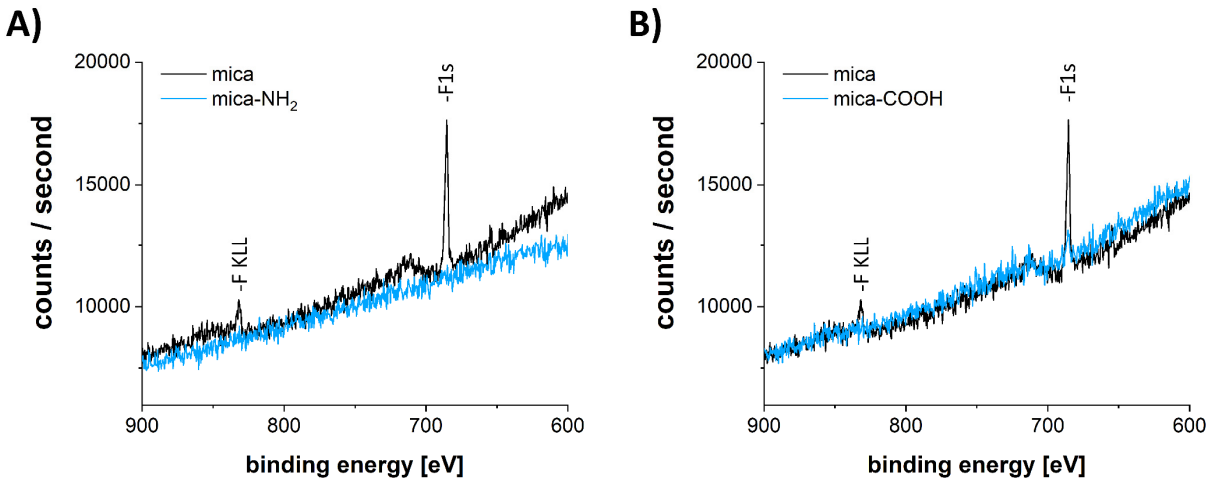

Figure A 8. XPS spectra of characteristic mica signals disappearing with functionalization. XPS spectra of mica (black) and mica functionalized (blue) with amine groups (A) and carboxyl groups (B). The characteristic FKLL and F1s signal for fluorine in mica is disappearing with functionalization indicating a successful homogeneous and continuous silane coating.

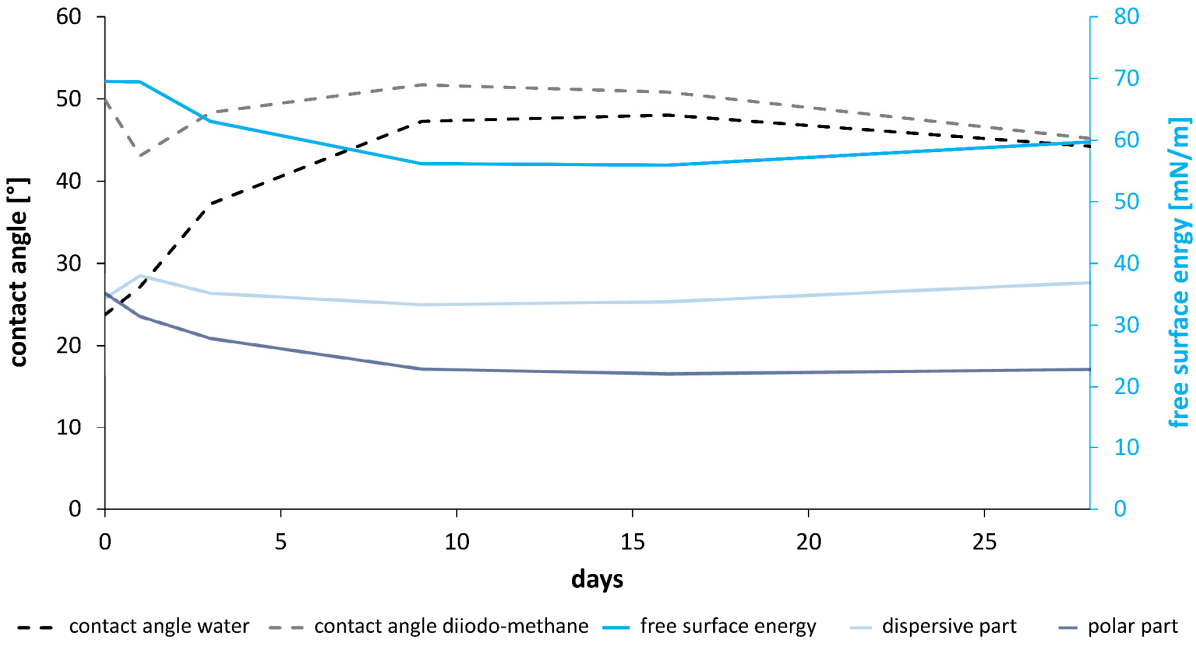

Figure A 9. Stability determined with contact angle measurements. The stability of the hydroxyl surface functionalization on mica is analyzed with contact angle measurements. The water contact angle (black dashed) increases from the first day and reaches a threshold after around 10 days, which was 20° higher than the original value. The diiodomethane contact angle (grey dashed) decreases after around 15 days. With the change of the water contact angle, the free surface energy (blue) decreases strongly within the first days. The stability test demonstrates that the functionalized substrates have to be used directly after the synthesis to guarantee the aimed properties.

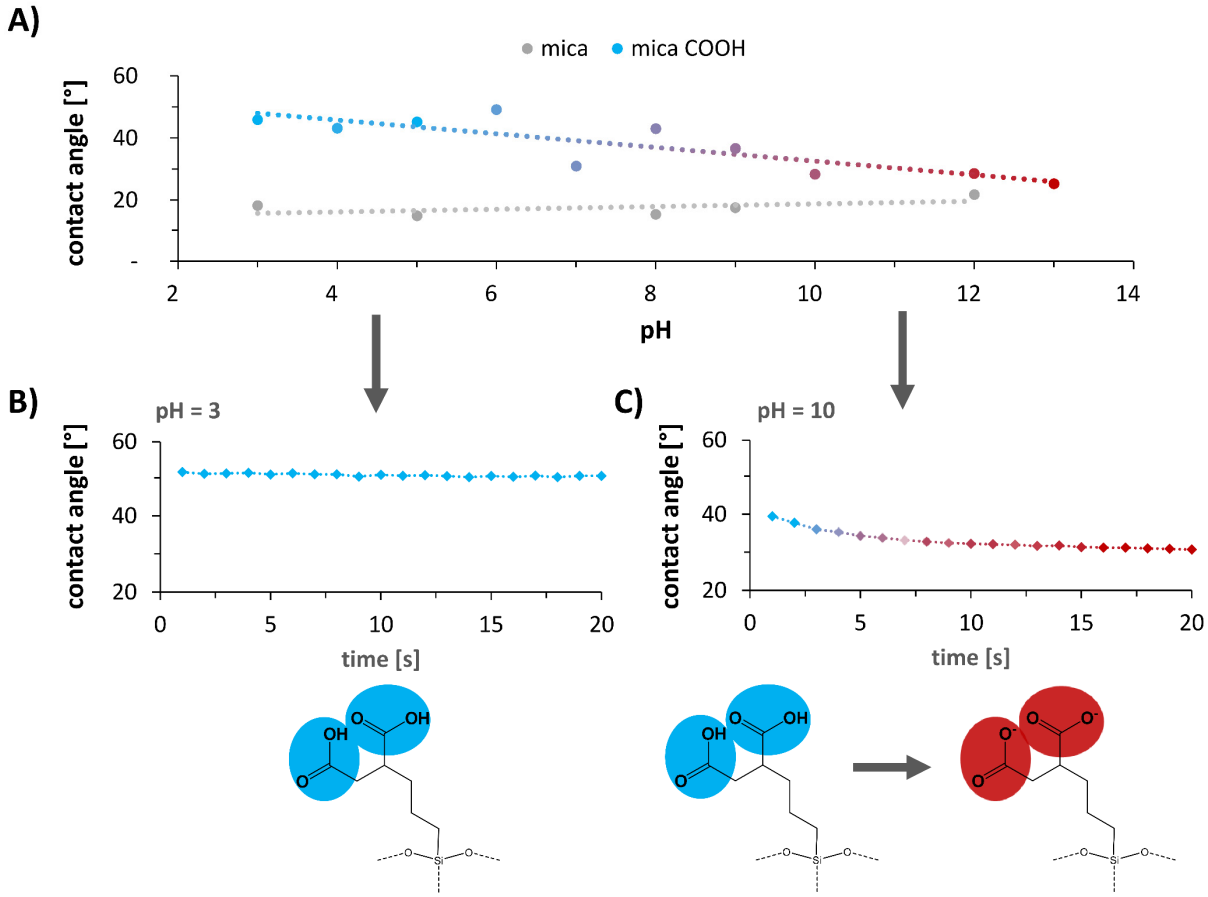

Figure A 10. pH dependent behavior of the carboxyl group. A) Contact angle measurement of a water drop on a mica surface functionalized with carboxyl groups (blue-purple). The pH of the water drop was varied between 3 and 13 and the respective contact angle was determined. With an increasing pH value, the contact angle decreases, which indicates an increasing polarity due to the deprotonation of carboxyl groups. For comparison, a bare mica surface is used as substrate (grey). B) At a pH of three, the contact angle stays constant over a time of 20 s. C) At a pH of ten, the contact angle decreases over a time of 20 s, which may be explained with a deprotonation of the carboxyl groups resulting in a more polar surface and a further wetting of the mica surface.

3.3 Materials and Methods

3.3.1 Instruments

AFM measurements were performed on a *JPK NanoWizard* instrument in the intermittent contact mode using a *Bruker* OTESPA-R3 silicon tip with a force constant of 26 N/m and a resonance frequency of about 300 kHz. Height, phase and amplitude images were recorded simultaneously.

For **contact angles** and free surface energies, the drop shape analyzer *DSA25* and the software *Advance* from *Krüss* were used. Contact angles larger than 10° were fitted with the *Ellipse (Tangent-1)* model, while contact angles smaller than 10° were fitted with the *Circle* model. The free surface energies were calculated with the contact angles from water and diiodomethane over the *Owens, Wendt, Rabel and Kaelble* (*OWRK)* model.

To determine the layer thickness with **ellipsometry** the *SENresearch 4.0* from *SENTECH* instruments GmbH was used.

For **plasma cleaning** a *Miniflecto* from *PlasmaTechnology* was used equipped with a 20-50 kHz, 80 W generator.

The **XPS** measurements were performed by Dr. Diemant from the university *Ulm (Institut für Oberflächenchemie und Katalyse)* with a *PHI 5800 MultiTechnique ESCA* System with monochromatized Al-K_α (1486.6 eV) radiation.

3.3.2 Materials

3.3.2.1 Substrates

Mica sheets were obtained from *Micro to Nano* in different shapes with a thickness of 0.15 to 0.21 mm and the highest-grade V-1 quality. For ellipsometry measurements, double polished Si wafers (Orientation [100] of 5 mm length and 7 mm width) from *Siegert Wafer* were used. For kinetic measurements in the UV-vis spectrometer, quartz cuvettes from *VWR* were used.

3.3.2.2 Chemicals

In all experiments, Milli-Q water (resistivity 18.2 MΩcm at 25 °C) was used. All chemicals were purchased and used without further purification. Propan-2-ol (C_3H_8O, ≥ 99.5%), ethanol (EtOH, ≥ 99.8%), methanol (MeOH, ≥ 99.5%), acetone (C_3H_6O, ≥ 99.5%) and hydrochloric acid (HCl, 37.0%) were purchased from *VWR*. Nitric acid (HNO_3, ≥ 65%) was purchased from *Carl Roth*. Dichloromethane (CH_2Cl_2, ≥ 99.8%) and sodium hydroxide pellets (NaOH, ≥ 98.0%) were purchased from *Merck*.

(3-aminopropyl)triethoxysilane for the amine functionalization was purchased from *Sigma-Aldrich*. 3-(Triethoxysilyl)propyl-succinic anhydride for the carboxyl functionalization, 3-acetoxypropyl-trimethoxysilane for the hydroxyl functionalization, n-butyltriethoxysilane for the alkyl functionalization and (heptadecafluoro-1,1,2,2-tetrahydrodecyl)triethoxysilane for the fluorine functionalization were purchased from *abcr*. N,N-diisopropylethylamine (DIPEA) and poly(sodium 4-styrenesulfonate) for the sulfonate functionalization with a M_w of 70 000 g/mol were purchased from *Sigma-Aldrich*.

3.3.3 Synthesis

All functionalized substrates were used in a period of one to two days after the functionalization as a stability test suggests (Figure A 9). A hydroxyl-functionalized mica substrate was stored for 28 days at RT and surface energies were determined by contact angle measurements with water and diiodomethane over the 28 days. The contact angles change from the start until they reach a constant value at around 10 days, which indicates that the functionalized substrates should be used freshly.

3.3.3.1 Cleaning of the Substrates

Different materials have been used as substrates and functionalized: mica especially for the nucleation experiments under the light microscope, silicon wafers for the ellipsometry measurements and quartz cuvettes for kinetic measurements in the UV-vis spectrometer.

Before functionalization, the different substrates were cleaned as follows. Mica substrates were freshly cleaved using a cellotape. The Si wafers were cleaned in an ultrasonic bath for 10 min each in propan-2-ol, ethanol and acetone. The quartz cuvettes were cleaned in *aqua regia* for 1 h and afterwards cleaned thoroughly with water.

3.3.3.2 Coating of the Substrates

The different substrates were treated with an oxygen plasma for 10 min at 80 W to generate free hydroxyl groups.

The surface functionalization was adapted from Crampton *et al.*[210] and was carried out using a vapor phase diffusion under a protective gas atmosphere. A 4 l desiccator was two times evacuated and flooded with nitrogen. The substrates were placed in the desiccator followed by evacuation and flooding with nitrogen for a third time to reach a humidity under 25%. The different used silanes and their respective coating conditions are shown in Table 2. 60 µl of the corresponding liquid silane and 20 µl of 1,1-Diisopropylethylamine were added to the desiccator in separate beakers. The desiccator was evacuated for 30 s, sealed afterwards and left for different timespans (depending on the used silane) at RT. Afterwards, the functionalized substrates were baked for 2 h at 150 °C under ambient conditions to ensure the homogeneous distribution of the siloxanes on the surface and a complete crosslinking of the siloxane network.

Table 2: Chemicals used for substrate functionalization. The used chemicals with their resulting functional group and the coating time in the desiccator.

chemical	functional group	coating time
polystyrene sulfonate	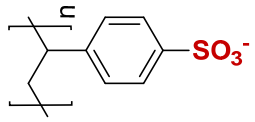	-
3-(triethoxysilyl)propyl-succinic anhydride	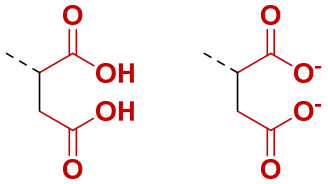	3 h
3-aminopropyltriethoxysilane	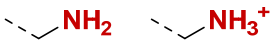	2 h
3-acetoxypropyltrimethoxysilane	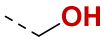	2 h
n-butyltriethoxysilane	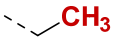	3 h
(3,3,3-trifluoropropyl)trimethoxysilane	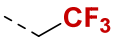	12 h
(heptadecafluoro-1,1,2,2-tetrahydrodecyl)methyldichlorosilane	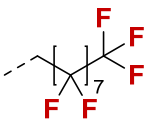	12 h

3.3.3.3 Special Treatments

For a functionalization with polystyrene sulfonate (PSS), the 3-aminopropyltriethoxysilane-functionalized substrates were given into a solution of 1 wt.-% PSS in water for 1 h. Afterwards the substrates were cleaned thoroughly with water and dried at 50 °C.

For a functionalization with carboxyl groups, the 3-(triethoxysilyl)propyl-succinic anhydride functionalized substrates were deprotected. Therefore, the substrates were given into water for 90 min at 50 °C and afterwards dried at 50 °C in a drying cabinet. With the deprotection, contact angle measurements show a decreasing water contact angle from 52.25° (±1.43) to 28.49° (±0.71) indicating the increased polar interaction through the free carboxyl groups. Table A 1 shows a comparison between the protected and deprotected carboxyl-functionalized surface characterizations with contact angles, free surface energies and the coating thickness.

For a functionalization with hydroxyl groups, the 3-acetoxypropyltrimethoxysilane-functionalized substrates were deprotected. Therefore, the substrates were given into a solution of dichloromethane and methanol in a ratio of 9:1. A solution of 2-3 N sodium hydroxide in methanol was added so that the final solution reaches a concentration of 0.1-0.2 N sodium hydroxide. The mixture was shaken overnight. Afterwards, the substrates were cleaned thoroughly with water and dried at 50 °C in a drying cabinet. With the deprotection, contact angle measurements show a decreasing water contact angle from 44.84° (± 0.50) to 30.85° (± 2.39) indicating the increased polar interaction through the free hydroxyl groups. Table A **2** shows a comparison between the protected and deprotected hydroxyl-functionalized substrate characterizations with contact angles, free surface energies and the coating thickness.

4 Nanoparticles for Heterogeneous Nucleation

The aim of this thesis is to analyze the heterogeneous nucleation of anisotropic particles into superstructures and to determine the influence of surface chemistry and particle anisotropy on this nucleation process. The first chapter focused on substrates for heterogeneous nucleation, identifying mica as a suitable substrate, and varying its surface chemistry by introducing a variety of functional groups. The following chapter will describe the establishment of nanoparticles as building blocks for heterogeneous nucleation experiments. So far, mainly isotropic hard spheres have been used for nucleation experiments in science, as they represent the simplest system. Since anisotropic particles are more interesting due to their variety in assemblies and are closer to real nucleation systems, three anisotropic nanoparticle systems were investigated in this thesis: zinc oxide nanorods, truncated gold nanocubes, and gold nanorods. For the nanoparticle field, two different influencing factors on heterogeneous nucleation were of interest: surface chemistry and anisotropy of the nanoparticles. To study the influence of surface chemistry, different functional groups were introduced to the surface of zinc oxide nanorods and gold nanocubes by exchanging the stabilizing ligand. In contrast to the mica substrates, only hydrophilic functional groups (-NH_2, -OH, -COOH, -SO_3H) were chosen to be able to disperse the nanoparticles in water and thereby ensure the comparability of subsequent nucleation approaches. To further study the influence of the nanoparticle anisotropy, gold nanorods with varying aspect ratios were provided.

4.1 Results and Discussion

4.1.1 Zinc Oxide Nanorods

Zinc oxide exhibits interesting optical and electric properties and is therefore used in numerous applications such as transistors[220], diodes[221-223], photodetectors[224], or gas sensors[225]. Nanostructured zinc oxide shows properties, which differ from its bulk material and can be synthesized in various forms like rods, springs, cages, or wires.[226, 227] The wurtzite structure of the zinc oxide nanorods results in different element compositions depending on the crystal face and, therefore, the shape of the nanoparticle has a major influence on its properties. Therefore, more knowledge and control over the nucleation of differently shaped zinc oxide nanoparticles into larger superstructures is desirable to potentially improve the interesting properties of the bulk material.[170]

For this project, zinc oxide nanorods were provided, which exhibited a hexagonal shape with a width of 15 nm and a mean length of 60 nm (Figure A 11). The zinc oxide nanorods were stabilized by the amphiphilic block copolymer polyglyceryl-3-polyricinoleate (P3P) and were soluble in unpolar organic solvents like hexane. The synthesis of the zinc oxide nanorods was described by Gerigk *et al.*.[228] To study

the influence of surface chemistry on the nucleation of the zinc oxide nanorods into larger superstructures, the surface chemistry of the zinc oxide nanorods was modified. Therefore, a ligand exchange of the stabilizer P3P with different functionalized siloxanes was required. With hydrophilic functional groups, the zinc oxide nanorods were transferred to an aqueous system and a further variation in surface chemistry could be introduced with amine (-NH_2, Figure A 12), hydroxyl (-OH, Figure A 13), and carboxyl (-COOH, Figure A 14) functionalities (Figure 16). During the ligand exchange, an excess of ligand (silane) was added to the nanoparticle dispersion, resulting in the displacement of the original ligand (P3P) on the zinc oxide nanorod surface. This ligand exchange required adjusting the concentration of silanes, zinc oxide nanorods and the amount of P3P on the rods. In addition, the cross-linking of silanes was sensitive to the amount of water in the system or the temperature used. The established experimental procedure of the ligand exchange is described in detail in Chapter 4.3.3. It was necessary to be careful when introducing the hydroxyl (-OH) and carboxyl (-COOH) groups. These functional groups can participate in the condensation reaction by forming a bond with the hydroxyl groups of other silanes, resulting in undesirable consumption of the functional groups. To preserve the functional groups, the silanes had to be introduced to the nanoparticle surface with a protection group (succinic anhydride for the carboxyl group and acetyl for the hydroxyl group), followed by a deprotection step (Chapter 4.3.3.3, Figure A 15).

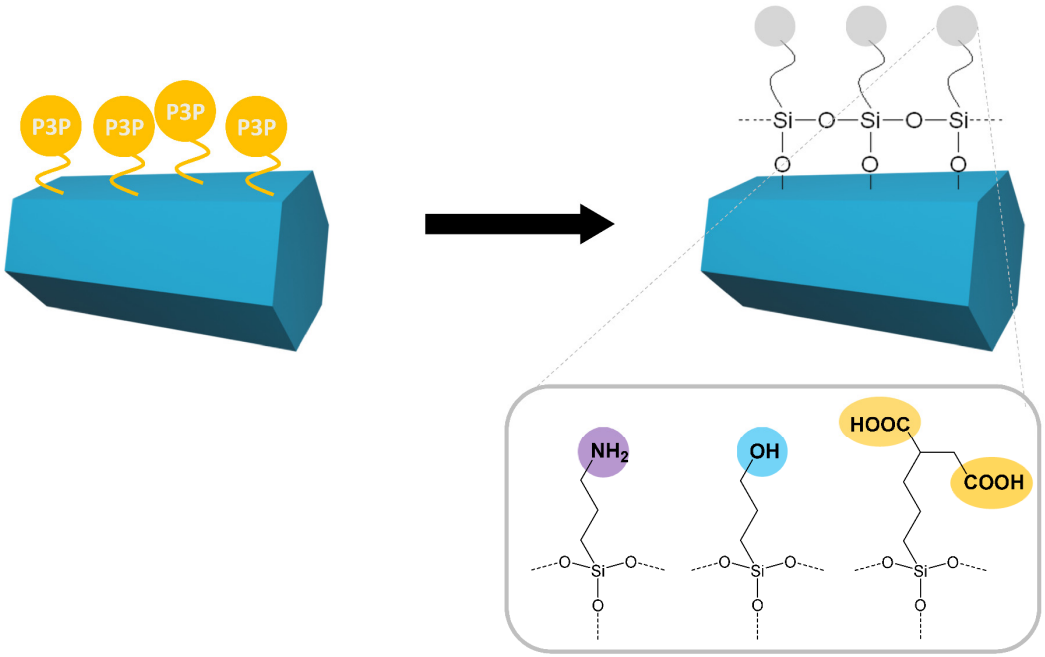

Figure 16. Ligand exchange for zinc oxide nanorods. After the synthesis, the provided zinc oxide nanorods were stabilized with the amphiphilic block copolymer P3P. The P3P was exchanged with siloxanes, which allowed the introduction of different functional groups: amine, hydroxyl, and carboxyl.

With ATR-IR spectroscopy, it was possible to detect the successful ligand exchange of P3P with the different functionalized silanes: amine (Figure 17A, Figure A 16 with peak assignment), hydroxyl (Figure A 17), and carboxyl (Figure A 18). In addition, the amine functionalization could be confirmed and quantified

by selective coupling of ninhydrin (Figure A 19), the fluorescent dye *Alexa647* for stochastic optical reconstruction microscopy (Figure A 20), and cleavable c-coumarin for quantitative fluorescent measurements (Figure A 21 and Figure A 22). Additional thermogravimetric analysis (TGA) indicated the exact determination of the quantitative fluorescent measurement (Figure A **22**). Furthermore, TGA measurements showed that the amine-functionalized zinc oxide nanorods were stabilized with only 3 wt.-% silane, while the original zinc oxide nanorods were stabilized with 61 wt.-% P3P (Figure 17B). The difference in the surface chemistry of the silane-functionalized zinc oxide nanorods was demonstrated by zeta potential measurements: amine 2.3 ± 0.9 eV, hydroxyl -30.2 ± 1.5 eV, and carboxyl -20.2 ± 0.3 eV (Figure A 23). These analytical results indicated a successful exchange of the stabilizer P3P by the three different functionalized silanes and therewith a successful tuning of the zinc oxide nanorod surface chemistry.

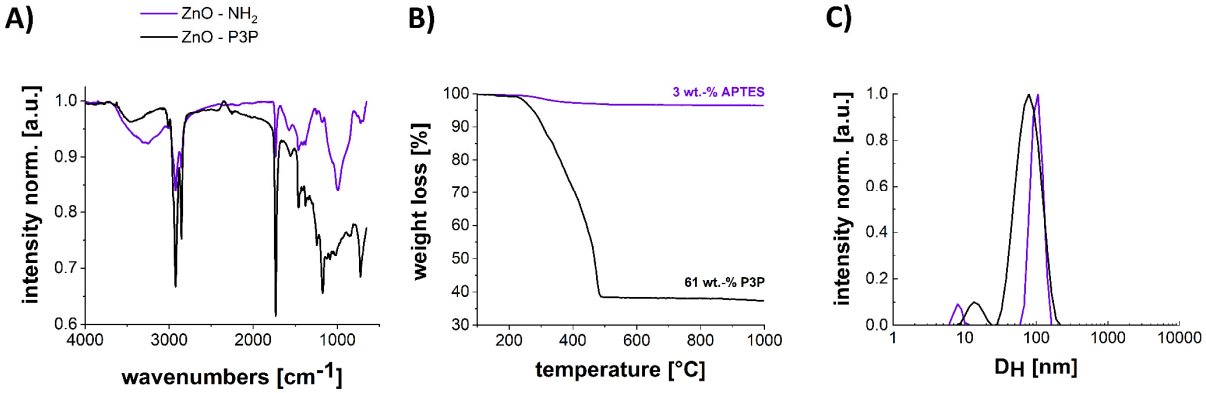

Figure 17. Characterization of zinc oxide nanorod ligand exchange. Comparison of P3P-functionalized zinc oxide nanorods (black) and amine-functionalized zinc oxide nanorods where P3P was exchanged by siloxane (purple). A) ATR-IR results indicate vanishing signals from P3P after the exchange with the siloxane and newly arising siloxane signals. B) TGA measurements exhibit that the original zinc oxide nanorods were stabilized with 61 wt.-% P3P while the functionalized zinc oxide nanorods were stabilized with around 3 wt.-% siloxane. C) DLS measurements indicate a stable particle dispersion and give volume-based hydrodynamic radii (D_H) of 117 nm (PDI 1.00) for amine zinc oxide nanorods in water and 82 nm (PDI 0.32) for P3P zinc oxide nanorods in toluene.

In addition to the exchange of P3P with functionalized siloxanes on the zinc oxide nanorods, the stability of the nanoparticles bared difficulties and was therefore subject to further investigation. Depending on the reaction conditions during the exchange process of the stabilizers, the defined rod-like particle shape was destroyed (Figure A 24 A). If the humidity was too high, the siloxane started to crosslink with itself and confined the zinc oxide nanorods in a huge siloxane network (Figure A 24 B). Furthermore, the siloxane layer had to be adjusted to the appropriate thickness, since a thin layer could not sufficiently stabilize the zinc oxide nanorods in dispersion. Nevertheless, two synthesis routes could be established introducing the siloxanes to the zinc oxide nanorods successfully: one at RT and ambient conditions and the other under inert gas atmosphere and higher temperatures (Chapter 4.3.3, Figure A 24 C). Dynamic light scattering (DLS) measurements indicated stable particle dispersions but determined slightly bigger hydrodynamic radii

(D_H) of 117 nm for amine zinc oxide nanorods (Figure 17C), 129 nm for hydroxyl zinc oxide nanorods and 264 nm for carboxyl zinc oxide nanorods (Figure A 25). With the exchange of the stabilizer, the zinc oxide nanorods also changed their self-assembling behavior. Stabilized with P3P the zinc oxide nanorods were soluble in organic solvents and arranged in a lying position on the substrate. Stabilized with the siloxanes, the zinc oxide nanorods were water-soluble and began to assemble in either a lying or standing position (Figure 18).

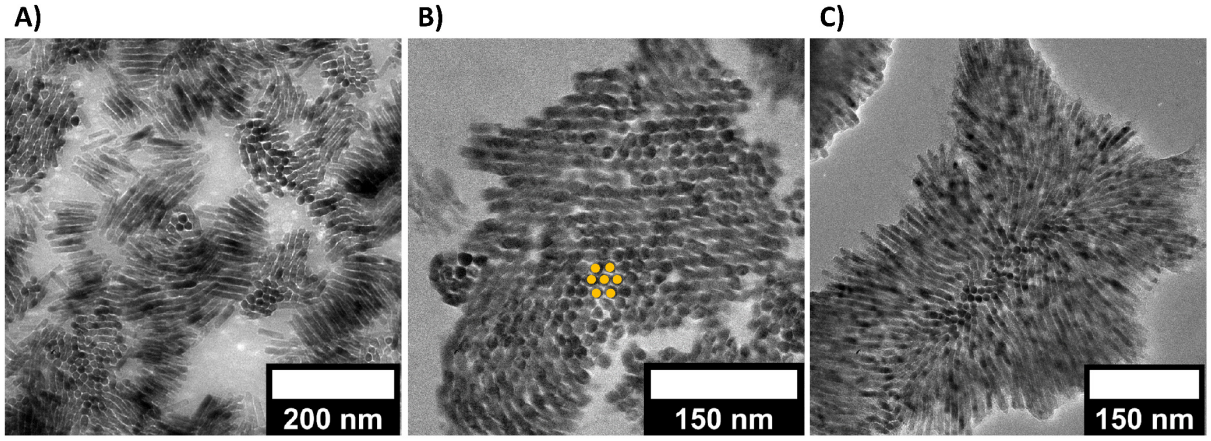

Figure 18. Assembly of amine-functionalized zinc oxide nanorods. HR-TEM images of A) amine-functionalized zinc nanorod assemblies of lying or standing rods, B) standing rods assembled in a hexagonal packing indicated through the orange spots, and C) amine-functionalized zinc oxide nanorods assembled into small islands of standing rods, which start to fall over at the side.

In conclusion, zinc oxide nanorods could be functionalized through ligand exchange with three different polar functional groups: amine ($-NH_2$), hydroxyl (-OH), and carboxyl (-COOH). Thereby, the experimental conditions were optimized to receive a desirable siloxane coating and the zinc oxide nanorods were transferred to an aqueous system. Zeta potential measurements revealed a variety in surface chemistry properties and the zinc oxide nanorods were used in the next step to establish heterogeneous nucleation experiments (Chapter 5) and to study the influence of surface chemistry on heterogeneous nucleation (Chapter 6). Previously, in addition to the zinc oxide nanorods, gold nanocubes were tuned in their surface chemistry, which will be considered in the following.

4.1.2 Gold Nanocubes

Gold nanocubes stand out due to their ease of synthesis, their low size dispersity, and their ability to self-assemble into mesocrystalline superstructures. Moreover, the strong plasmonic activity of this type of nanoparticles paired with its optical sensitivity to the aggregation state of the nanoparticle enables the use of UV-vis-NIR (ultraviolet-visible-near-infrared) spectroscopy to optimize the experimental conditions. The growth of colloidal gold nanocubes with controlled dimensions and low size dispersity can be achieved by

seed-mediated growth methods based on the spatial and temporal separation of nucleation and growth stages.[229, 230]

For this project, well-defined 23 nm gold nanocubes have been appropriated, synthesized with hexadecylpyridinium chloride (CPC), a surfactant that acts as a colloidal stabilizing agent (Figure 19).[231] The use of gold nanocubes with a size of 23 nm ensured the colloidal stability during the timespan of later nucleation experiments (Chapter 5 and 6), which was important for a homogeneous distribution in dispersion.

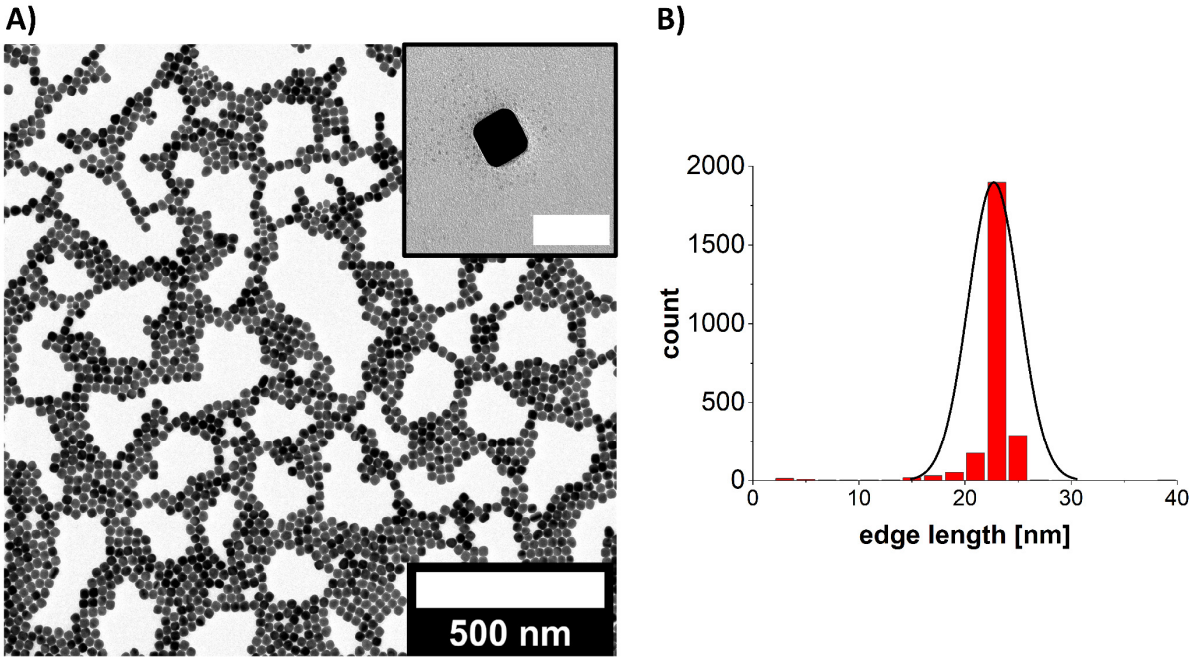

Figure 19. Characterization of gold nanocubes. A) TEM image of CPC stabilized gold nanocubes with an inlet showing one single gold nanocube. The scale bar has a size of 50 nm. B) Size distribution of the gold nanocubes with a mean size of 22.7 ± 2.4 nm measured from edge to edge.

To investigate the influence of nanoparticle surface chemistry on heterogeneous nucleation, identical nanoparticles differing only in their surface chemistry were required. Therefore, the gold nanocubes were functionalized with different chemical groups by exchanging their stabilizer CPC. Hexadecyl(trimethyl)-ammonium bromide (CTAB), polyethylene glycol (PEG), polystyrene sulfonate (PSS), and polyacrylic acid (PAA) were successfully introduced to the surface of the gold nanocubes (Figure 20). Thereby, the PEG and PAA exhibited a thiol moiety to ensure good interaction with the gold surface of the nanocubes. The CPC was exchanged with CTAB through several washing steps (Chapter 4.3.4.1) and the CTAB gold nanocubes were used to introduce the other functionalities. As for the zinc oxide nanorods, the ligand exchange was facilitated by adding an excess of new ligand to the nanoparticle dispersion resulting in the displacement of CTAB on the gold nanocube surface. Thereby, the concentration of the new ligand, the concentration of the gold nanocubes, the amount of CTAB on the gold nanocubes, the stirring speed, and the washing steps had to be adjusted for each functionalization (Chapter 4.3.4). Three different chain lengths

were introduced for the PEG stabilized gold nanocubes: 6000 g/mol (named as PEG 6000), 2000 g/mol (named as PEG), and 800 g/mol (named as PEG 800).

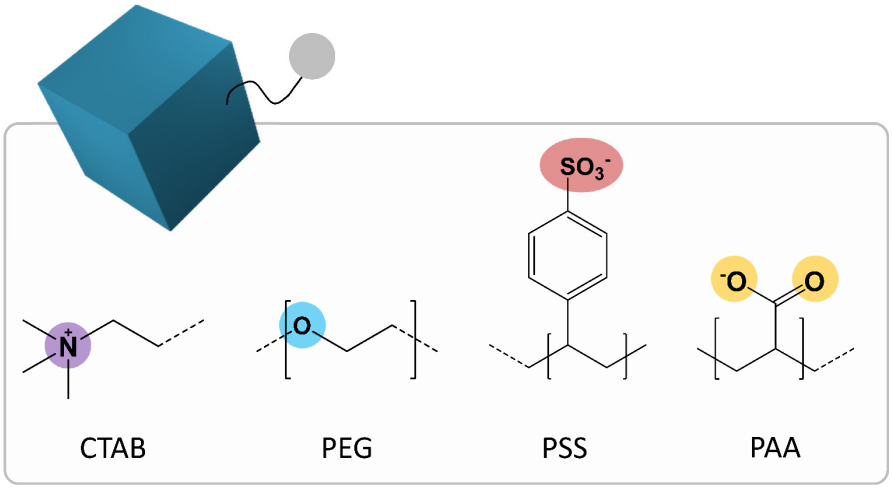

Figure 20. Different functional groups introduced to the gold nanocube surface. By exchanging the stabilizer CPC, different functional groups were introduced to the surface of the gold nanocubes: CTAB ($-N^+(CH_3)$, purple), PEG (-O-, blue), PSS ($-SO_3H$, red) and PAA (-COOH, orange).

After the ligand exchange, the stability of the gold nanocubes in dispersion was verified by UV-vis-NIR spectroscopy (Figure 21, Figure A 26). The spectra showed the typical narrow plasmonic band of single gold nanocubes centered at 523 nm indicating stable nanoparticle dispersion. One exception constituted the spectra of PEG 800 (Figure A 26C). Here the broadening of the peak to higher wavelengths indicated that some gold nanocubes aggregated to larger species. Similar results were obtained by DLS measurements (Figure A 27). The gold nanocube dispersions were stable and yielded volume-based hydrodynamic radii of 32 – 56 nm and good polydispersity indices (PDI) of 0.11 – 0.45. However, with a determined hydrodynamic radius of 248 nm, the PEG 800 gold nanocubes did not follow this trend. HR-TEM (high-resolution transmission electron microscopy) images showed as well that the gold nanocubes remained stable and additionally maintained their shape during the ligand exchange (Figure A 28), except the PEG 800 gold nanocubes. Here gold nanocubes fused into larger species fitting well the obtained UV-vis-NIR and DLS measurements. It can be concluded that the PEG chain length of 800 g/mol insufficiently stabilized the gold nanocubes, probably due to their short chain length resulting in a low steric repulsion. The corresponding samples were hence disregarded for nucleation experiments in the further course. For the PSS gold nanocubes, the ligand exchange could be adapted but was not satisfactorily reproducible over several batches. In addition, with PAA, a negatively charged acidic group could be introduced effectively, and therefore, the PSS gold nanocubes were not used for nucleation experiments either. For CTAB, PEG, PEG 6000, and PAA the functionalization of gold nanocubes was successful, easily reproducible and resulted in stable particle dispersions.

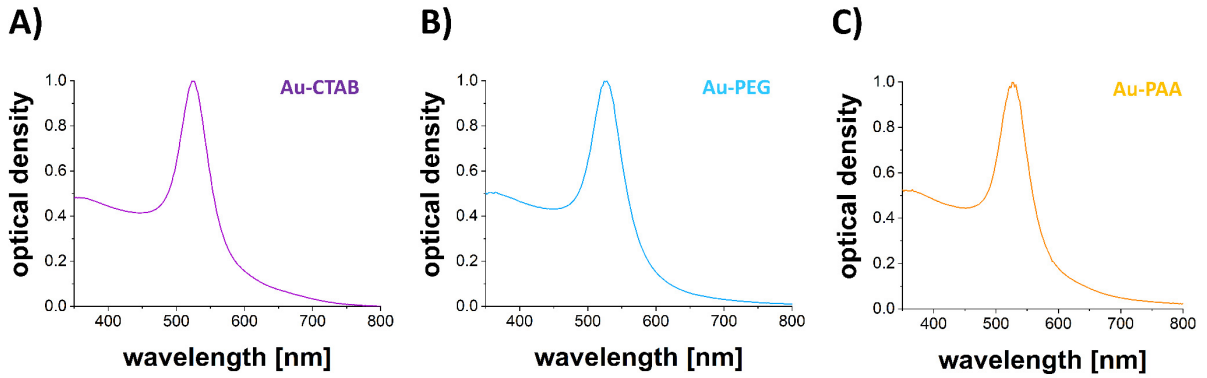

Figure 21. UV-vis-NIR spectroscopy measurements of functionalized gold nanocubes. The spectra of A) CTAB-functionalized B) PEG-functionalized and C) PAA-functionalized gold nanocubes show the typical narrow plasmonic band centered at 523 nm, which indicate that the particles were still stable after the ligand exchange.

With the four different ligands, a variety of surface functionalities could be successfully introduced to the gold nanocube surface. These findings were confirmed by zeta potential measurements revealing the surface charge of the different functionalized gold nanocubes in dispersion, ranging from positive to negative charges: CTAB (15.8 mV), PEG (-25.1 mV), PAA (-26.7 mV) (Figure 22) and PSS (-47.6 mV), PEG 6000 (-10.6 mV), and PEG 800 (-25.8 mV) (Figure A 29). Furthermore, gold substrates were functionalized analogous to the gold nanocubes giving them a comparable surface chemistry. This approach allowed determining the contact angles and therewith the free surface energies of the different functionalized substrates (Figure A 30, Figure A 31). Water contact angles ranged from hydrophilic PEG groups with contact angles of 10° to more hydrophobic CTAB groups with a contact angle of 64°.

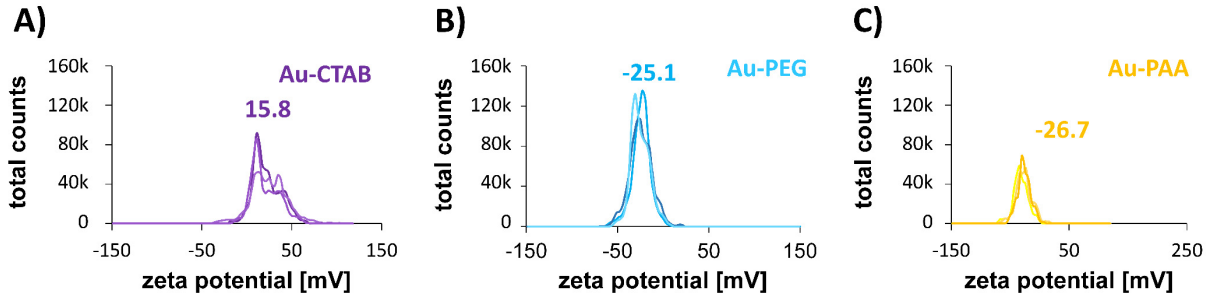

Figure 22. Zeta potential measurements of functionalized gold nanocubes. Zeta potentials of A) 15.8 mV for CTAB-functionalized B) -25.1 mV for PEG-functionalized C) -26.7 mV for PAA-functionalized gold nanocubes are shown. The shift of the zeta potential indicates a successful ligand exchange and the variety of the introduced surface functionalizations.

For the following nucleation experiments, a methodology for the controlled destabilization of the gold nanocube dispersions is necessary to perform reproducible nucleation experiments. Chapter 5 will deal with the subject of carrying out nucleation experiments and their detailed analysis. Nevertheless, the controlled

destabilization of the various functionalized gold nanocubes will already be discussed in this chapter to give a complete description of the nanoparticle systems used. In general, nanoparticle dispersions can be destabilized in a controlled manner by altering the solvent properties such as polarity, pH value, or ionic strength to achieve a poorer solubility of the stabilizing ligands or to detach the stabilizing ligands from the nanoparticle surface. For example, destabilizing the electrostatic forces of CTAB gold nanocubes through the addition of water-soluble organic solvents probably represents the most straightforward strategy.[123, 152, 232] Therefore, ethanol was chosen to destabilize the CTAB gold nanocube dispersions and to trigger the gold nanocube self-assembly into superstructures.[232] UV-Vis-NIR spectroscopy proved to be a helpful analytics in this case as the nature of the plasmonic resonances of gold nanocubes depends on the presence of other particles in the vicinity.[232] This fact opened access to characterize the self-assembly process via UV-vis-NIR spectroscopy directly in solution and to receive easily fast insights into the destabilization process.[156, 157] Thus, the self-assembly process of CTAB gold nanocubes, destabilized by ethanol could be monitored directly in solution, through the changes in the extinction band of the gold nanoparticles (Figure 23A). Initially, they exhibited a narrow plasmonic band centered at 523 nm, which decreased during the homogeneous nucleation process. New bands corresponding to the formation of aggregates emerged at longer wavelengths. These results indicated the suitability of using ethanol to trigger the aggregation of gold nanocubes stabilized by CTAB. Gold nanocubes stabilized by PEG were successfully destabilized by decreasing the pH of the dispersion with hydrochloric acid (Figure 23B). Thereby, PEG gold nanocubes with a chain length of 6000 g/mol appeared to be highly stable and could only be destabilized at a pH value below zero. While the heterogeneous nucleation of PEG gold nanocubes with a chain length of 2000 g/mol was induced at a pH value of three or less. Therefore, the PEG gold nanocubes with a chain length of 2000 g/mol were used for further nucleation experiments (Chapter 6) to ensure experimental conditions at milder pH values. For the PAA gold nanocubes, a controlled destabilization was achieved by altering the ionic strength through the addition of calcium chloride (Figure 23C). Further addition of CTAB to a destabilized gold nanocube dispersion (independent of the particle functionalization) resulted in quenching and the gold nanocube aggregates and single gold nanocubes could be stabilized again (Figure A 32). This stabilization allowed taking aliquots during experiments and greatly simplified the experimental effort. As a result, it was possible to destabilize the gold nanocubes for all three functionalizations (CTAB, PEG, and PAA) in dispersion in a controlled way and to freeze aliquots for further analysis.

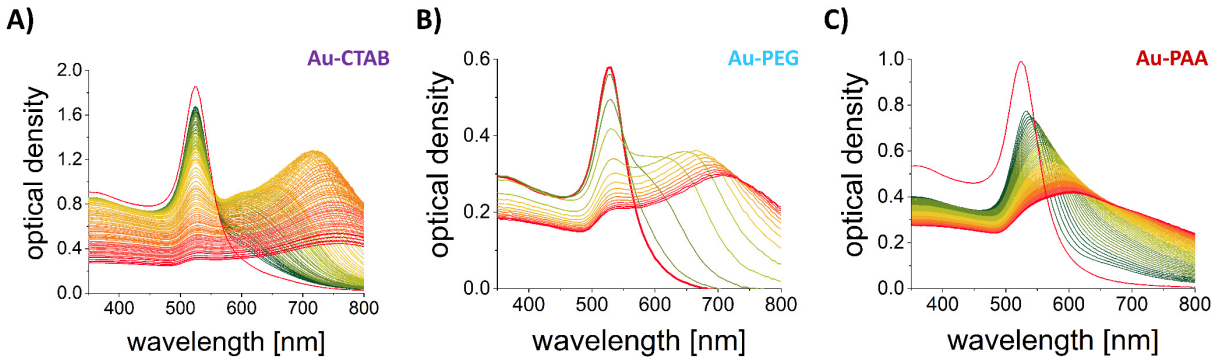

Figure 23. Controlled destabilization of gold nanocubes in dispersion. UV-vis NIR spectra of the destabilization process of gold nanocubes A) CTAB-functionalized with the addition of ethanol, B) PEG-functionalized with the addition of hydrochloric acid (to reach a pH of 0), and C) PAA-functionalized with the addition of calcium chloride. During the destabilization, the typical narrow plasmonic band centered at 523 nm of single gold nanocubes decrease while bands at longer wavelengths emerge.

In summary, gold nanocubes were functionalized successfully through a ligand exchange with five different stabilizers: CTAB (-$N^+(CH_3)_3$), PEG (-OH) with two different chain lengths, PSS (-SO_3H) and PAA (-COOH). The stability of the gold nanocubes in dispersion could be verified with UV-vis-NIR spectroscopy, DLS, and HR-TEM. Zeta potential and contact angle measurements indicated a variety in surface chemistry properties and the CTAB, PEG, and PAA gold nanocubes were used in the next step to establish heterogeneous nucleation experiments (Chapter 5) and to study the influence of the surface chemistry on heterogeneous nucleation (Chapter 6). As preliminary work for the nucleation experiments, the controlled destabilization of the three gold nanocubes was established by altering the solvent properties.

4.1.3 Gold Nanorods

Analogous to the above-discussed gold nanocubes, gold nanorods offer similar amenities. For example, the strong plasmonic activity paired with its sensitivity to the aggregation state of the nanoparticle enables the use of UV-vis-NIR spectroscopy for later nucleation experiments. Therefore, three differently shaped CTAB stabilized gold nanorods were appropriated to study the influence of the particle anisotropy on heterogeneous nucleation of anisotropic nanoparticles into superstructures. The synthesis of these colloidal gold nanorods can typically be achieved by seed-mediated growth methods based on the spatial and temporal separation of nucleation and growth stages (Chapter 4.3.5), yielding uniform gold nanorods with controlled dimensions and low size dispersity (Figure A 33, Figure A 34, and Figure A 35).[229, 230, 233] HR-TEM measurements showed gold nanorods of 40 nm in diameter and lengths of 120, 90, and 70 nm corresponding to aspect ratios of 3.00, 2.25, and 1.75. The resulting nanorods presented narrow plasmon bands ranging from 630 and 730 to 830 nm (Figure 24).

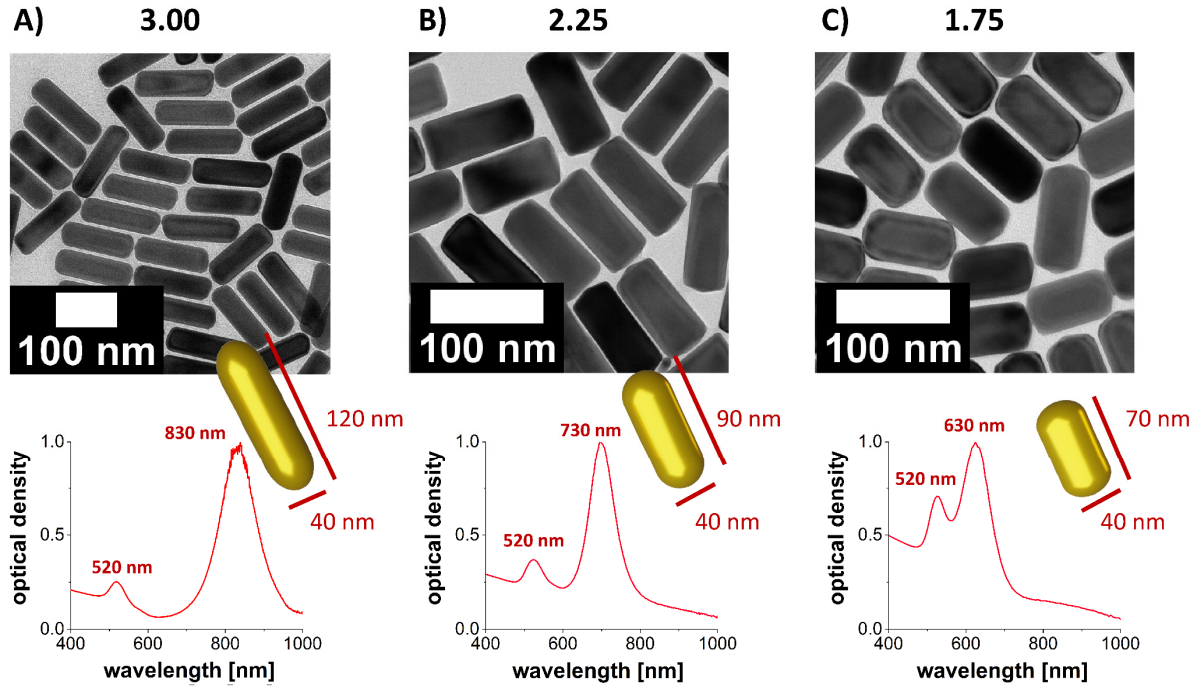

Figure 24. Gold nanorods with varying aspect ratios. The upper row shows HR-TEM images of the gold nanorods with aspect ratios of A) 3.00, B) 2.25, and C) 1.75 and the bottom row shows the corresponding UV-vis-NIR spectra and a scheme with the edge lengths of the gold nanorods.

The system of three identical gold nanorods only varying in their aspect ratio allowed studying the influence of the particle anisotropy on the heterogeneous nucleation of these gold nanorods into superstructures (Chapter 6). To investigate the heterogeneous nucleation experiments in a reproducible manner, a methodology for the controlled destabilization of the gold nanorod dispersions was first required analog to the above-described destabilization of gold nanocube dispersions. As the gold nanorods were stabilized through the adsorption of CTAB micelles on their surface, similar to the CTAB gold nanocubes (Chapter 4.1.2), ethanol allowed for a controlled destabilization, which could be monitored with UV-vis-NIR spectroscopy for the three different aspect ratios (Figure 25). The gold nanorods presented two characteristic plasmonic bands: a transversal resonance mode located at approximately 520 nm, and a longitudinal mode at longer wavelengths that depended on the aspect ratio.[234] During the nucleation and self-assembly process, a shift and broadening of the longitudinal plasmon bands for all investigated nanorod colloids were observed, meaning new bands corresponding to the formation of aggregates emerged at longer wavelengths.[235-237] Overall, these results indicated the suitability of using ethanol to trigger the aggregation of CTAB-stabilized gold nanorods.

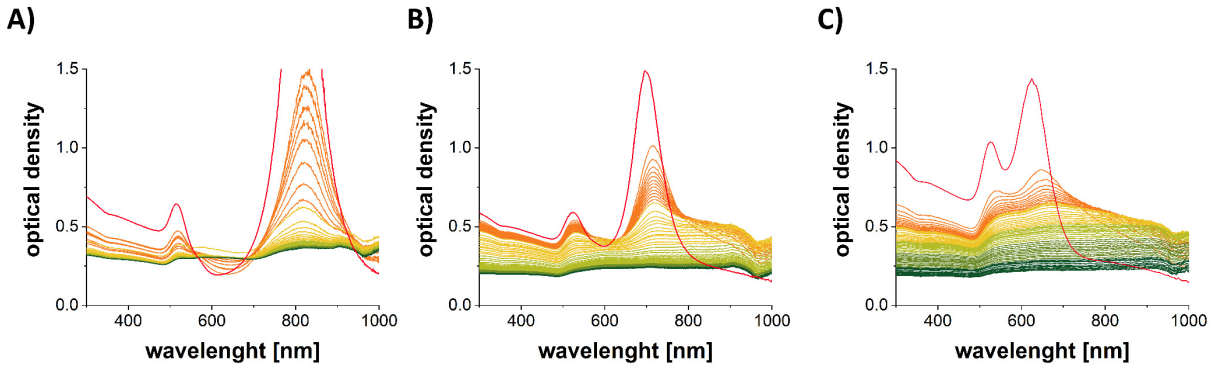

Figure 25. Controlled nucleation of gold nanorods in dispersion. UV-vis-NIR spectra of the destabilization process of gold nanorods with different aspect ratios of A) 3.00, B) 2.25, and C) 1.75. The CTAB stabilized gold nanorods can be destabilized in a controlled manner by the addition of ethanol. During the destabilization, the longitudinal plasmonic bands centered at A) 830, B) 730 nm, and C) 630 nm of single gold nanorods decrease while new bands at longer wavelengths emerge.

In summary, three different anisotropic nanoparticle systems could be established successfully for the analysis of their heterogeneous nucleation into larger superstructures. Zinc oxide nanorods were functionalized via ligand exchange with siloxanes carrying three different polar groups (-NH_2, -OH, -COOH). Furthermore, gold nanocubes were functionalized with four different polar groups (-NH_2, -OH, -SO_3H, -COOH) and their controlled destabilization by altering the solvent properties was accomplished. With these two nanoparticle systems, it was possible to analyze the influence of the surface chemistry on heterogeneous nucleation by using the same nanoparticle, which only differs in its surface chemistry, as a building block for heterogeneous nucleation (Chapter 6). To further study the influence of the nanoparticle shape (Chapter 6), three gold nanorods that differ in their aspect ratios (3.00, 2.25, and 1.75) were provided. Likewise, the controlled destabilization of the CTAB stabilized gold nanorods could be accomplished by adding ethanol and thus altering the polarity of the solvent. Hence, before the influence of the surface chemistry and the nanoparticle shape on heterogeneous nucleation could be studied it was necessary to design an appropriate experimental setup. This setup had to be able to observe the heterogeneous nucleation in situ and to quantify the nucleation process to allow a characterization and distinction between the different parameters in surface chemistry and particle shape. This difficulty and how to perform heterogeneous nucleation experiments shall be discussed in more detail in the following chapter.

4.2 Appendix

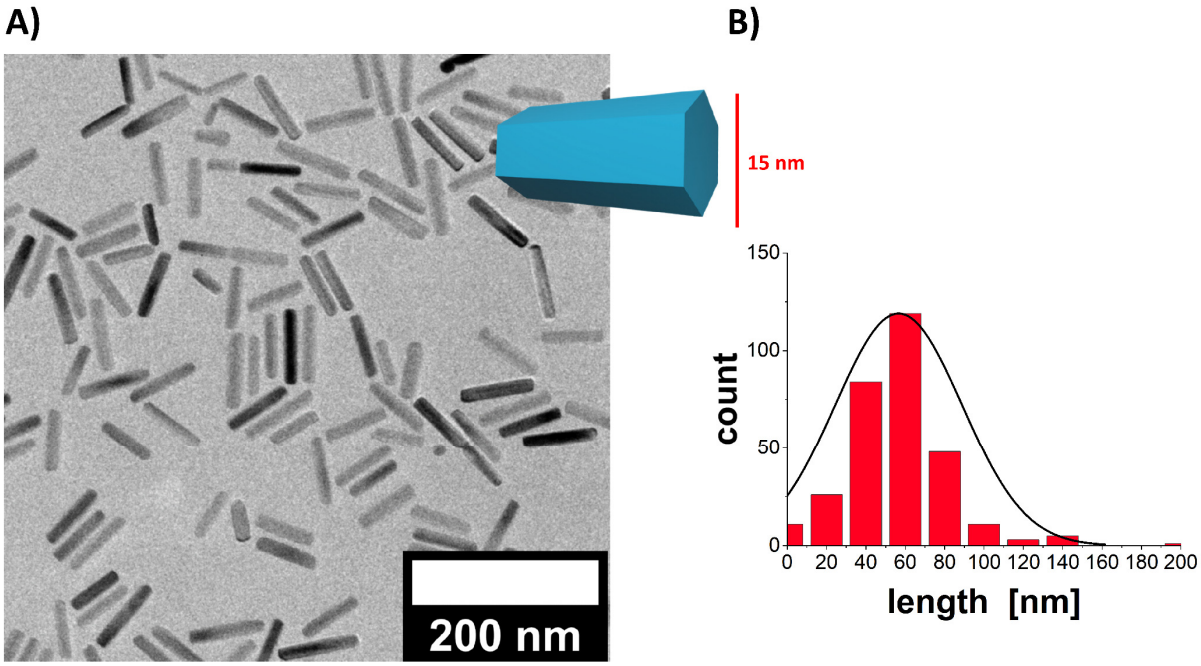

Figure A 11. P3P zinc oxide nanorods. A) HR-TEM image of P3P zinc oxide nanorods. The sketch illustrates the hexagonal form of the nanorods with a width of approximately 15 nm. B) The histogram shows the mean length of the nanorods of 57 ± 32 nm.

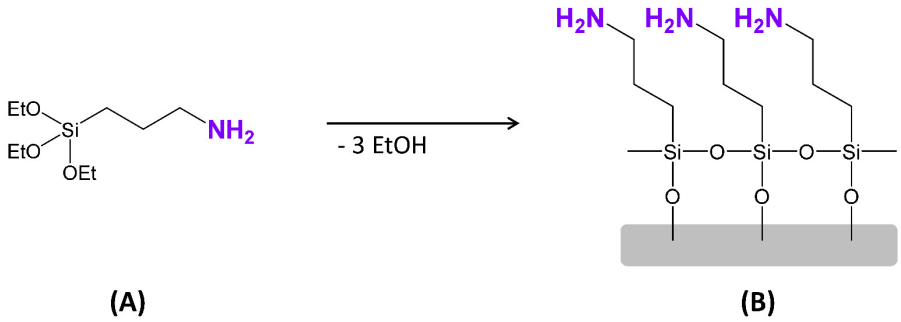

Figure A 12. Amine functionalization of zinc oxide nanorods. (3-aminopropyl)triethoxysilane was used to functionalize zinc oxide nanorods.

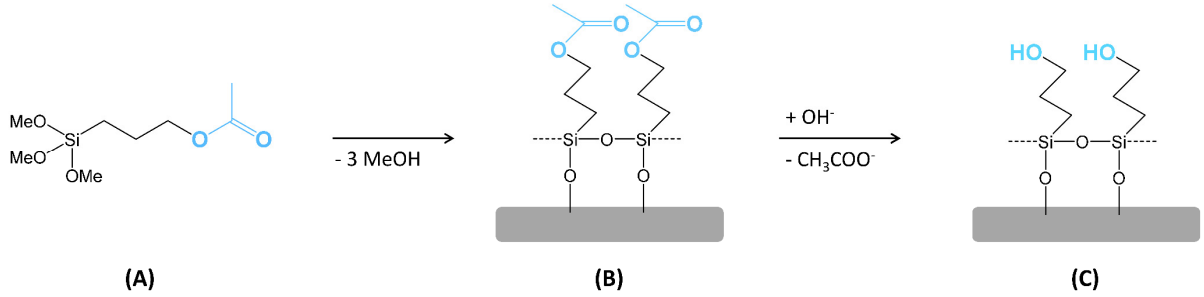

Figure A 13. Hydroxyl functionalization of zinc oxide nanorods. (A) 3-acetoxypropyltrimethoxysilane was used to functionalize zinc oxide nanorods (B). In a second step, the hydroxyl groups were deprotected (C).

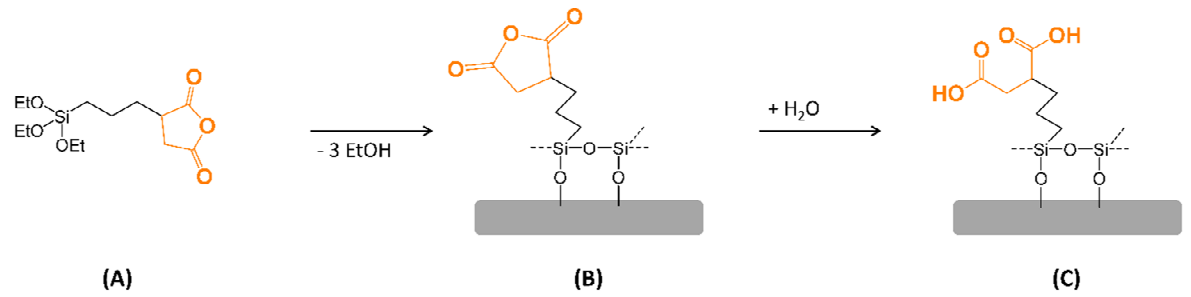

Figure A 14. Carboxyl functionalization of zinc oxide nanorods. (A) 3-(triethoxysilyl)propyl-succinic anhydride was used to functionalize zinc oxide nanorods (B). In a second step, the carboxyl groups were deprotected (C).

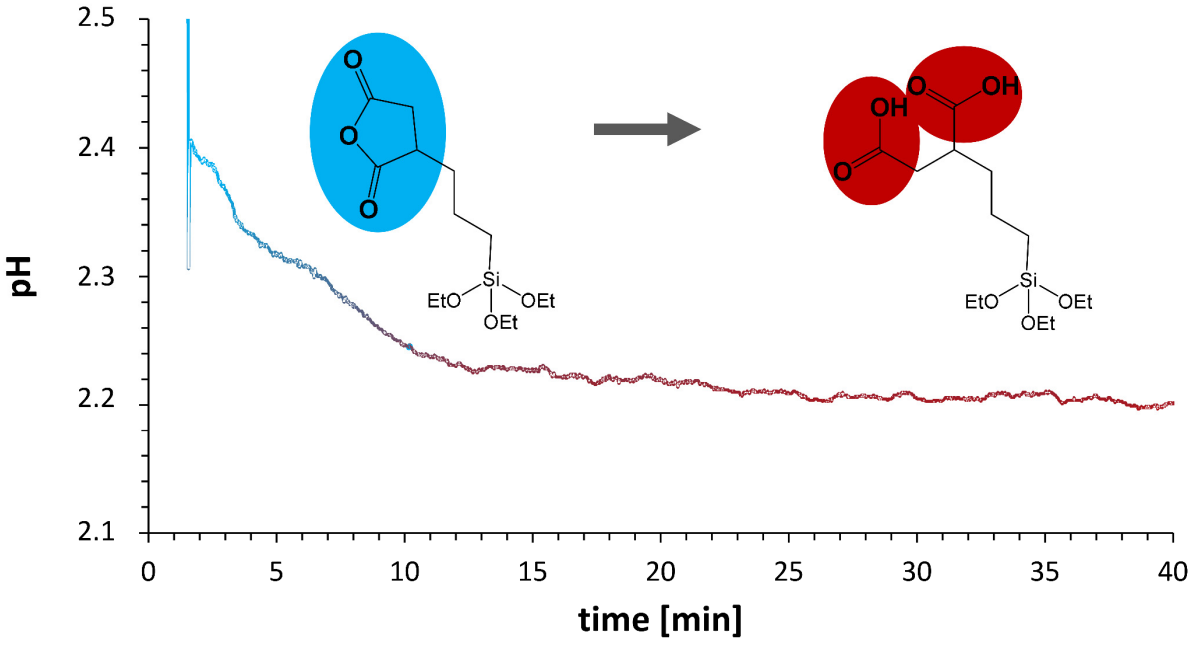

Figure A 15. Deprotection of the carboxyl functionalization. The pH of an ethanol-water (15 : 1) mixture at 70 °C was measured. 3-(triethoxysilyl)propyl-succinic anhydride was added to the mixture at

minute one. The pH decrease shows the progressing deprotection of the succinic acid. The process was finished after about 30 min.

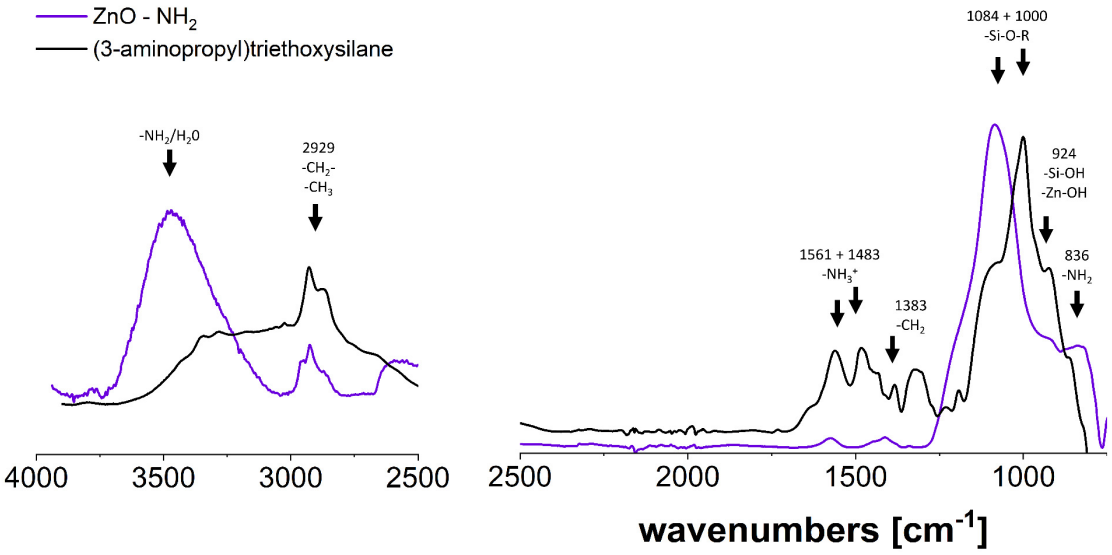

Figure A 16. ATR-IR spectra of amine-functionalized zinc oxide nanorods. ATR-IR spectra of (3-aminopropyl)triethoxysilane-functionalized zinc oxide nanorods (purple) and bare 3-aminopropythriethoxysilane (black) as a comparison, with the labeled peaks. The peaks of the amine-functionalized zinc oxide nanorods were consistent with those of the reference sample except for the –Si-O-R peak ratio at 1084 cm^{-1} and 1020 cm^{-1}. This peak ratio indicates the degree of crosslinking (1084 cm^{-1} corresponds to R-O-Si-O-R and 1000 cm^{-1} to R-Si-OH). The small degree of crosslinking for the reference sample can be explained by crosslinking at room temperature compared to 90 °C during the functionalization of the zinc oxide nanorods.

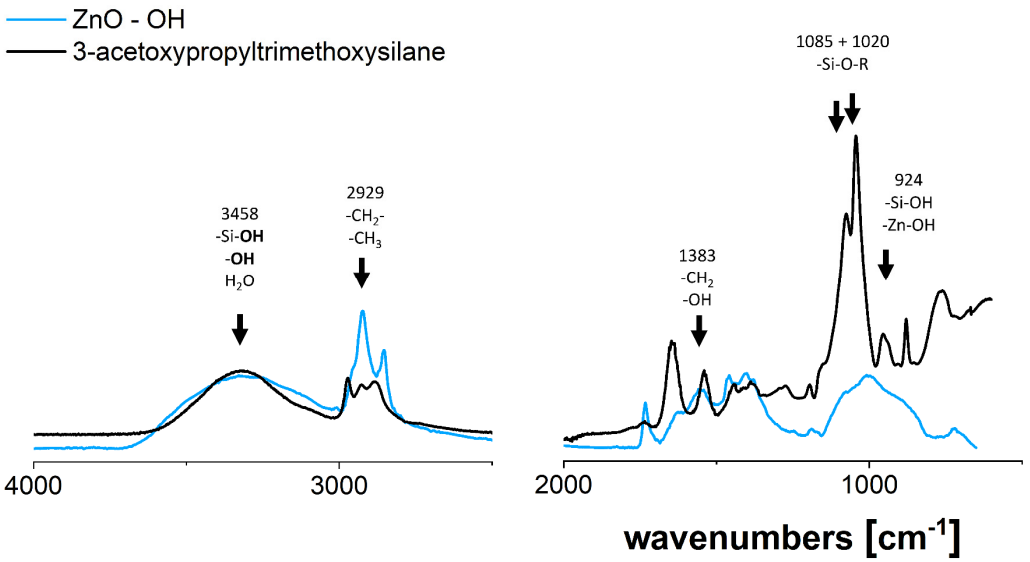

Figure A 17. ATR-IR spectra of hydroxyl-functionalized zinc oxide nanorods. ATR-IR spectra of 3-acetoxypropyltrimethoxysilane-functionalized zinc oxide nanorods (blue) and bare 3-acetoxypropyl-trimethoxysilane (black) as a comparison, with the labelled peaks. The peaks of the amine-functionalized

zinc oxide nanorods were consistent with those of the reference sample except for the –Si-O-R peak ratio at 1084 cm^{-1} and 1020 cm^{-1}. This peak ratio indicates the degree of crosslinking (1084 cm^{-1} corresponds to R-O-Si-O-R and 1000 cm^{-1} to R-Si-OH). The small degree of crosslinking for the reference sample can be explained by crosslinking at room temperature compared to 90 °C during the functionalization of the zinc oxide nanorods.

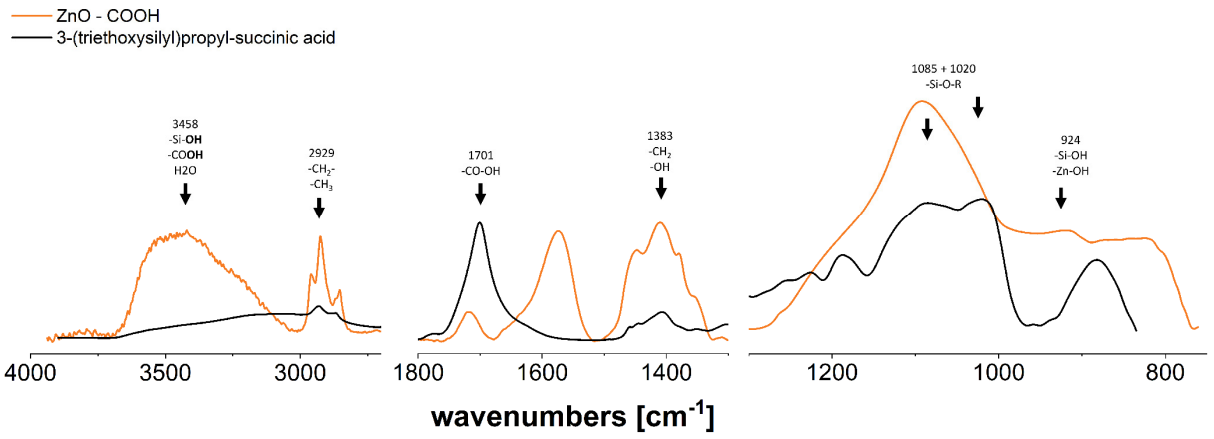

Figure A 18. ATR-IR spectra of carboxyl-functionalized zinc oxide nanorods. ATR-IR spectra of 3-(triethoxysilyl)propyl-succinic acid-functionalized zinc oxide nanorods (orange) and bare 3-(triethoxysilyl)propyl-succinic acid (black) as a comparison, with the labelled peaks. The arising –CO-OH peak at 1701 cm^{-1} indicates a successful functionalization of the zinc oxide nanorods with carboxyl groups. One difference between the spectra was the –Si-O-R peak ratio at 1084 cm^{-1} and 1000 cm^{-1}. This peak ratio indicates the degree of crosslinking (1084 cm^{-1} corresponds to R-O-Si-O-R and 1020 cm^{-1} to R-Si-OH). The small degree of crosslinking for the reference sample can be explained by crosslinking at room temperature compared to 90 °C during the functionalization of the zinc oxide nanorods.

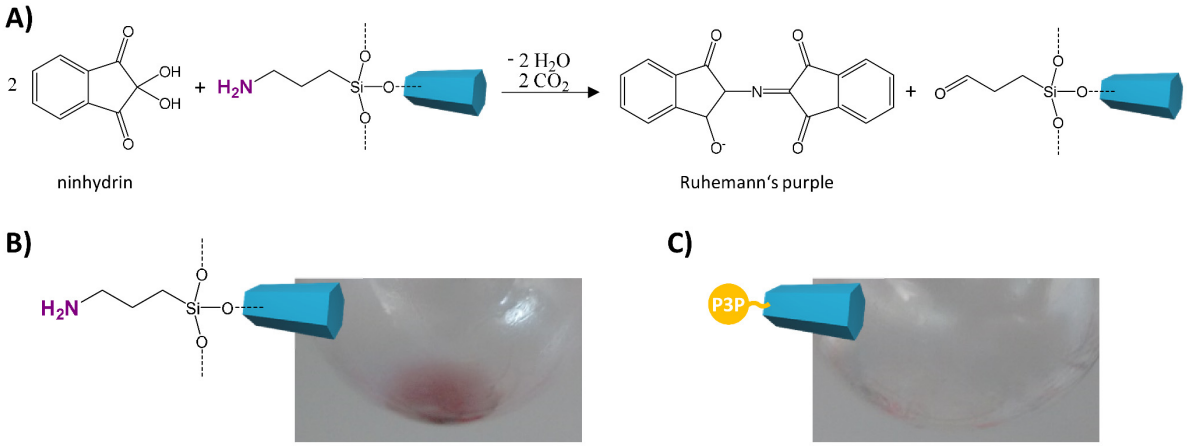

Figure A 19. Detection of the amine functionalization with ninhydrin. A) A reaction with ninhydrin and the amine group of functionalized zinc oxide nanorods produces the purple dye Ruhemann's dye. With the help of this test, amine groups can be detected. B) The positive test with amine-functionalized nanoparticles exhibits a red color. C) The negative test with P3P-functionalized nanoparticles remains colorless.

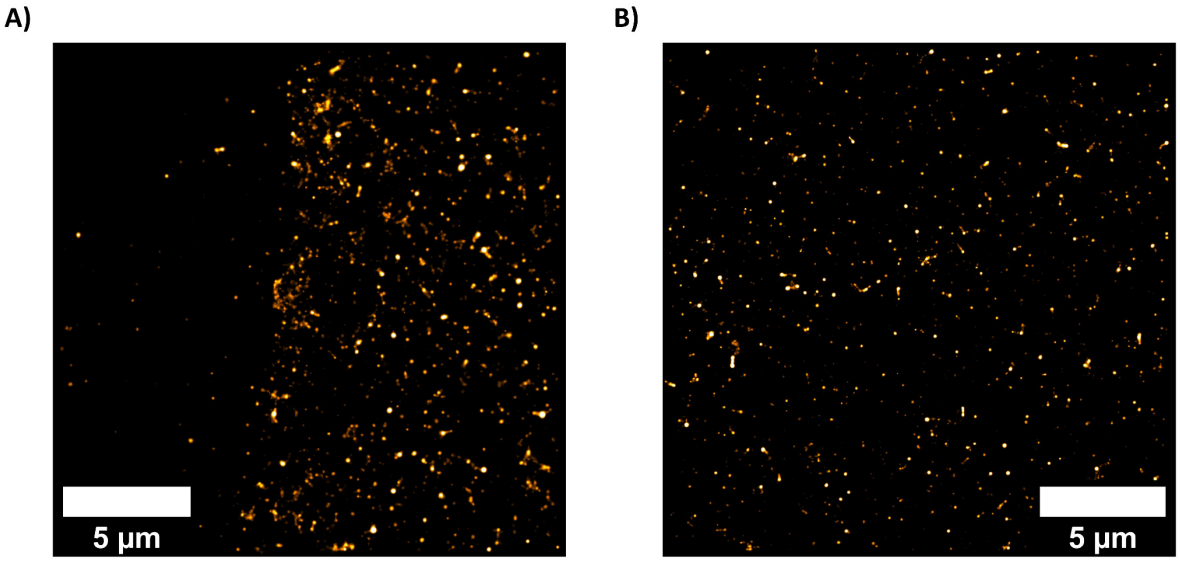

Figure A 20. Stochastic optical reconstruction microscopy (STORM) images of amine-functionalized zinc oxide nanorods. The zinc oxide nanorods were tagged with the fluorescent dye *Alexa Fluor 647* which was coupled to the amine group of the zinc oxide nanorods. A control sample with P3P-functionalized zinc oxide nanorods was treated with the fluorescent dye in the same manner and showed no signal. This observation demonstrated that the fluorescent dye was selectively coupled to the amine groups. A) The image shows the clear border of the sample indicating that the signal is directly related to the nanoparticles (right half of the image). B) Several adjacent signals indicate that the dye and thus the amine group is located on the zinc oxide nanorods.

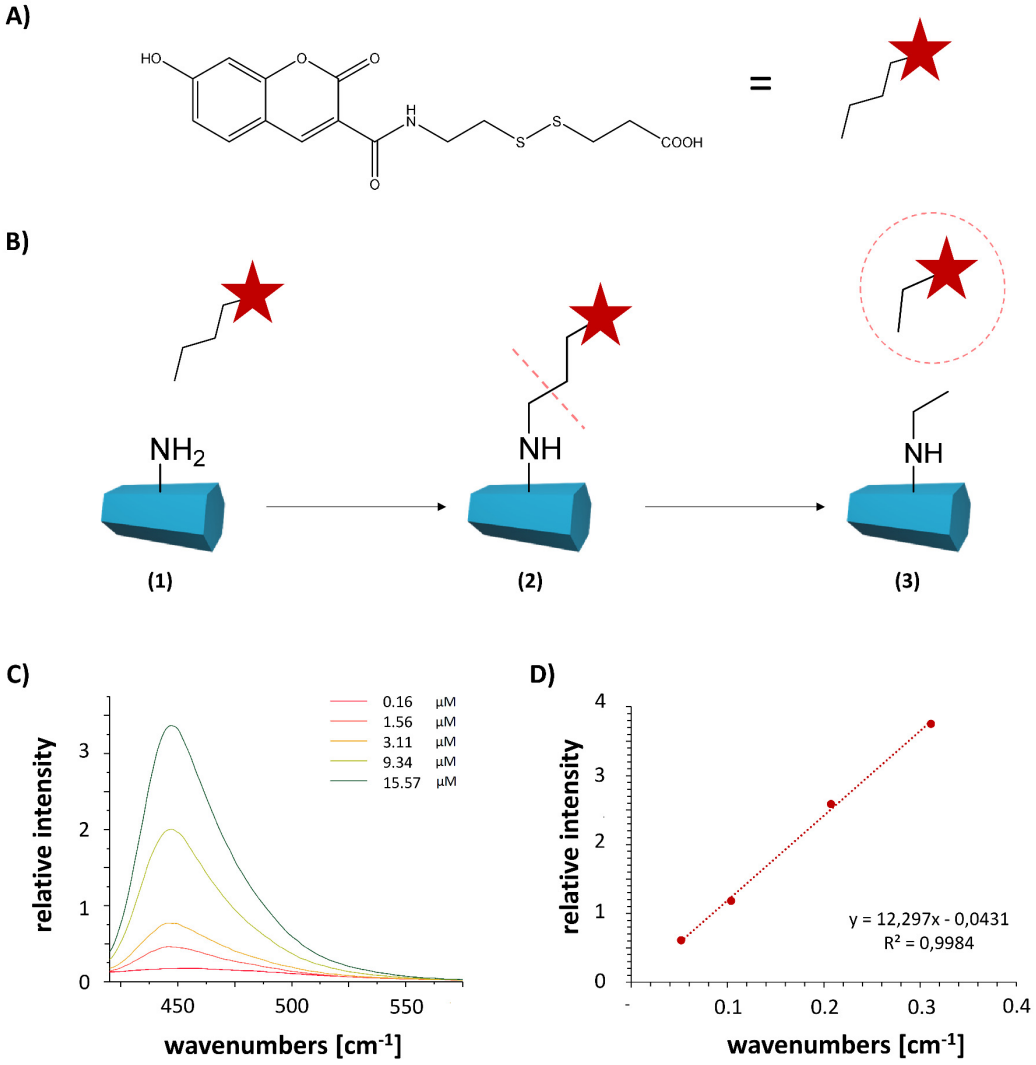

Figure A 21. Quantitative fluorescent measurement to determine the number of amine groups on a surface. A) Structure of the cleavable fluorescent compound c-coumarin. B) Principe of the method: (1) Cleavable c-coumarin was coupled selectively to the amine group on the zinc oxide nanorod surface. With several washing steps excess c-coumarin was removed, (2) c-coumarin was cleaved from the surface by opening the disulfide bridge (3) the concentration of free c-coumarin in solution could be determined over the fluorescence intensity. C) Fluorescence measurements of c-coumarin solutions with different concentrations for calibration. D) Calibration line for the measurements shown in C, connecting the c-coumarin concentration to the intensity of the fluorescent measurement. The intensity of a fluorescent measurement gives the number of c-coumarin and thus the amount of amine groups on the surface.

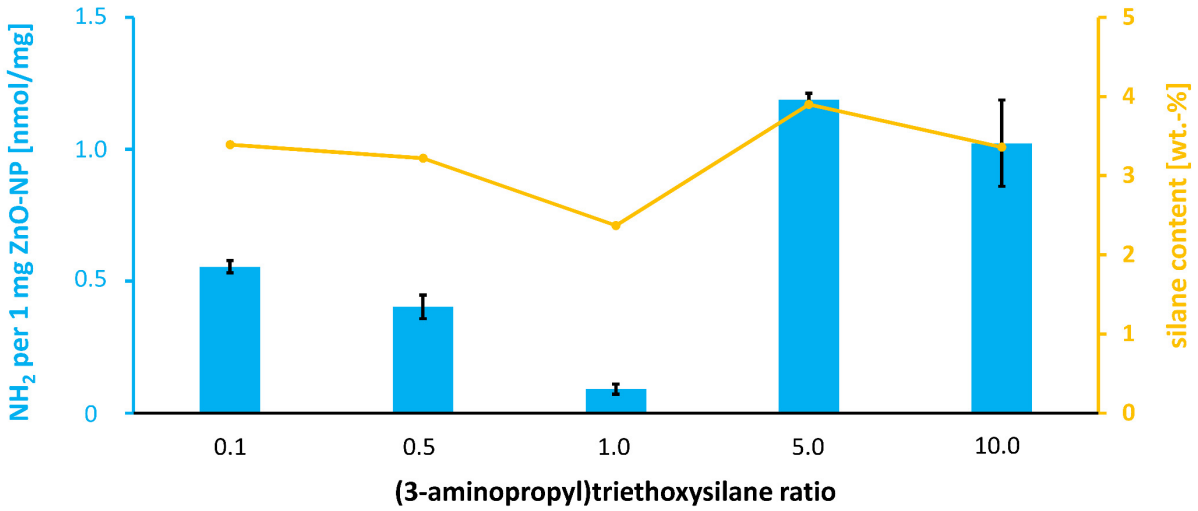

Figure A 22. Silane content respectively amount of amine groups on amine-functionalized zinc oxide nanorods. Results of quantitative fluorescent measurements (blue) giving the number of amine groups on the amine-functionalized zinc oxide nanorods per (3-aminopropyl)triethoxysilane used for the synthesis. The results of TGA analysis (yellow) show the analog siloxane content, which matches well with the results of the quantitative fluorescent measurement.

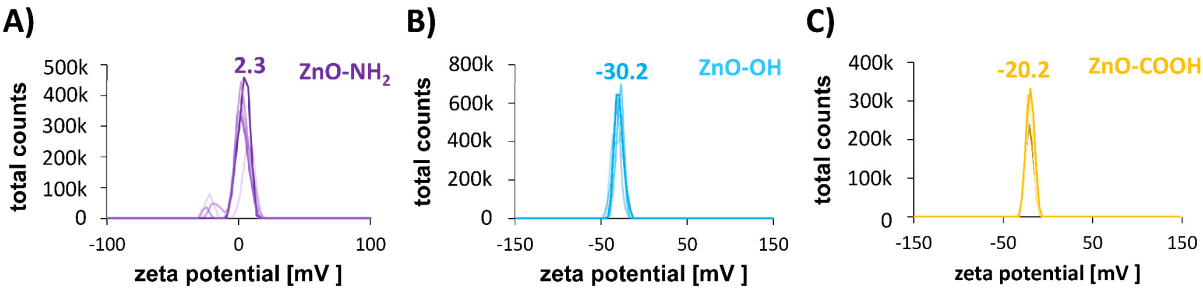

Figure A 23. Zeta potential measurements of differently functionalized zinc oxide nanorods. Zeta potential measurement of A) amine-functionalized (2.3 ± 0.9 eV), B) hydroxyl-functionalized (-30.2 ± 1.5 eV), and C) carboxyl-functionalized (-20.2 ± 0.3 eV).

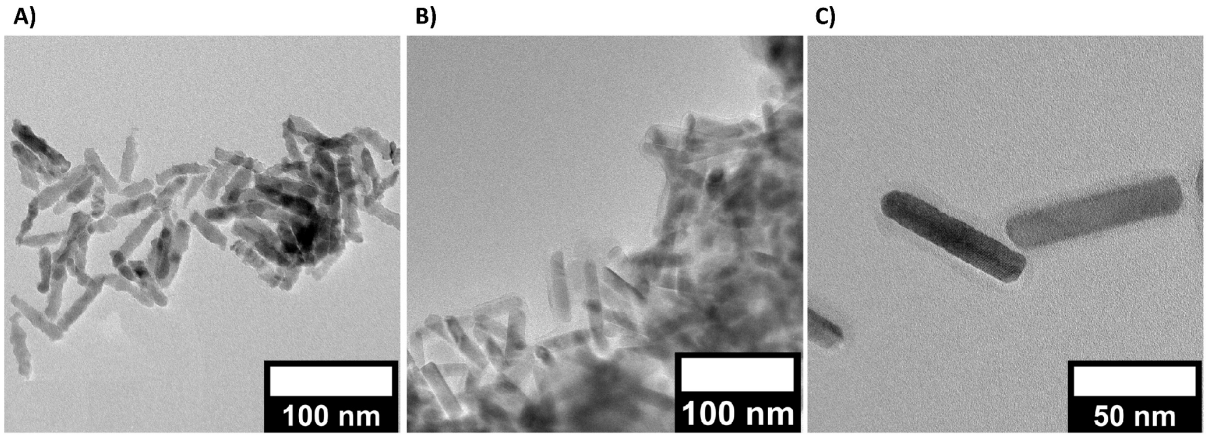

Figure A 24. Challenges during the functionalization of zinc oxide nanorods. HR-TEM images of zinc oxide nanorods after the functionalization with siloxanes. A) Zinc oxide nanorods, which lost their defined shape and exhibited tattered edges. B) Zinc oxide nanorod aggregation that is cross-linked with a huge siloxane layer. C) Zinc oxide nanorods coated with a siloxane layer that kept their form and stayed stable.

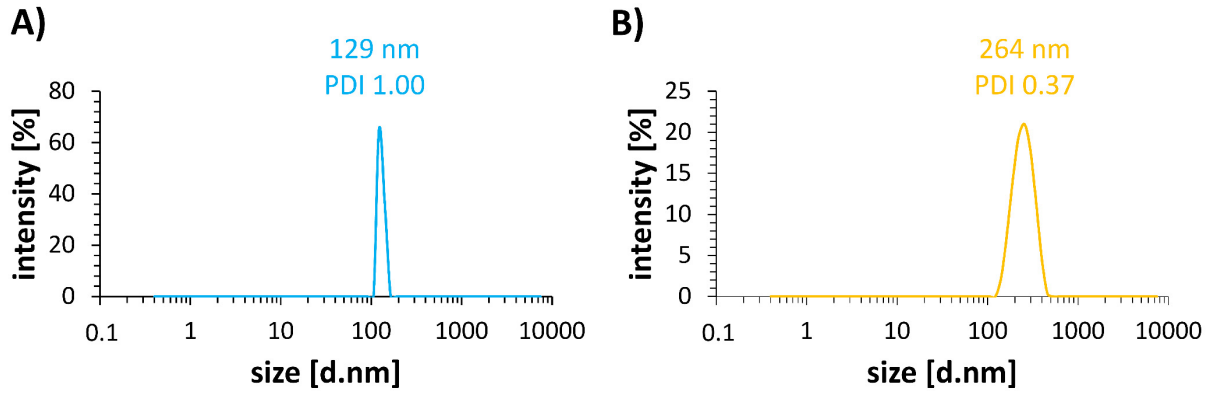

Figure A 25. DLS measurements. DLS measurements and volume based hydrodynamic radii of A) hydroxyl (129 nm, PDI 1.00) and B) carboxyl (264 nm, PDI 0.37) functionalized zinc oxide nanorods.

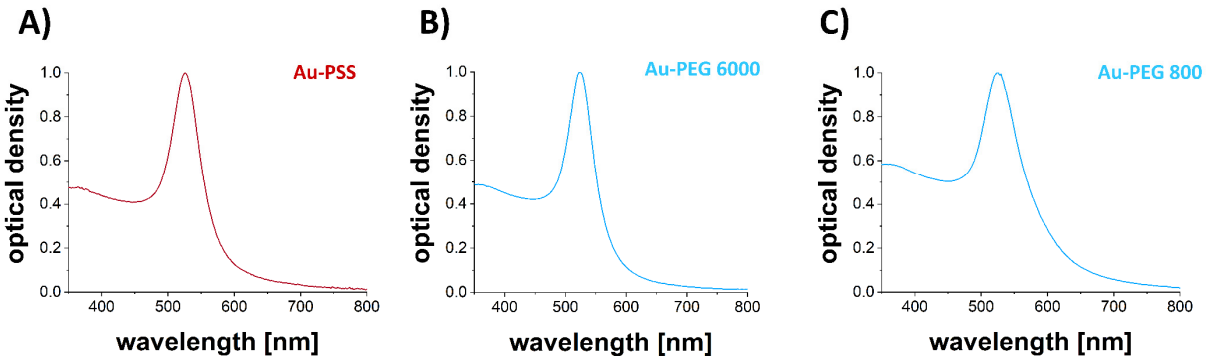

Figure A 26. UV-vis-NIR spectroscopy measurements of functionalized gold nanocubes. UV-vis-NIR spectra of A) PSS-functionalized and B) PEG 6000-functionalized gold nanocubes showing the typical narrow plasmonic band centered at 523 nm, which indicates stable particle dispersions after the ligand

exchange. The spectrum of C) PEG 800-functionalized gold nanocubes shows a broadening of the peak towards higher wavelengths indicating that some gold nanocubes aggregated to bigger structures.

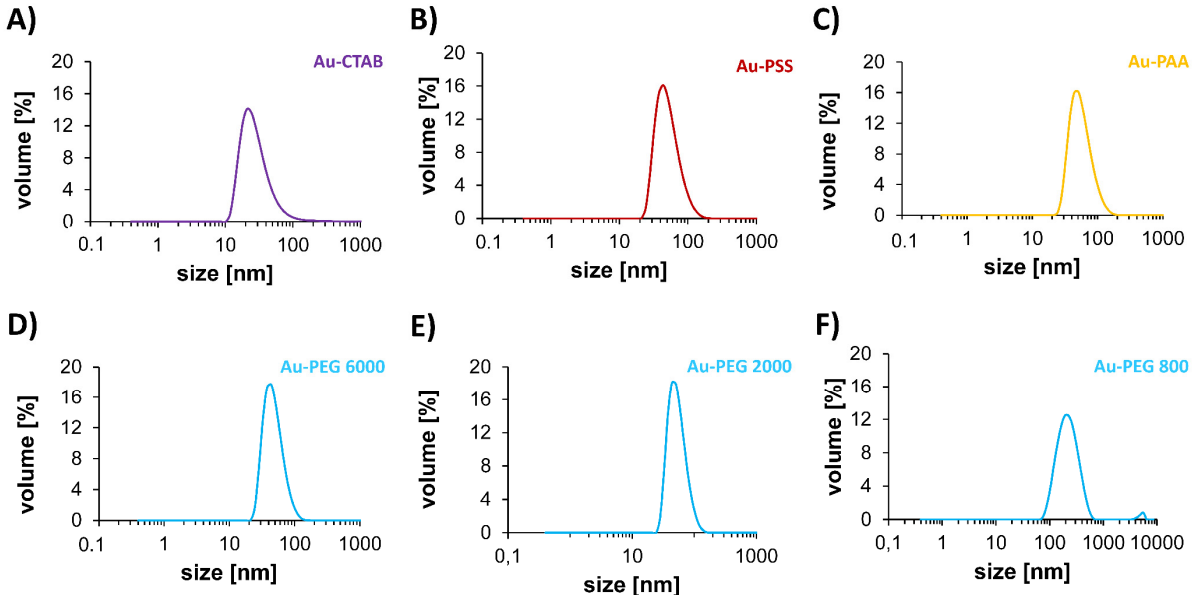

Figure A 27. DLS measurements of functionalized gold nanocubes. The volume-based size distributions for gold nanocubes functionalized with A) CTAB (32 nm, PDI 0.45) B) PSS (55 nm, PDI 0.24), C) PAA (56 nm, PDI 0.17), D) PEG 6000 (49 nm, PDI 0.11), E) PEG 2000 (55 nm, PDI 0.11) and F) PEG 800 (248 nm, PDI 0.22). The results A-E show that the different functionalized particles are still stable after the ligand exchange with the exception of F, where the measurement indicated big aggregates.

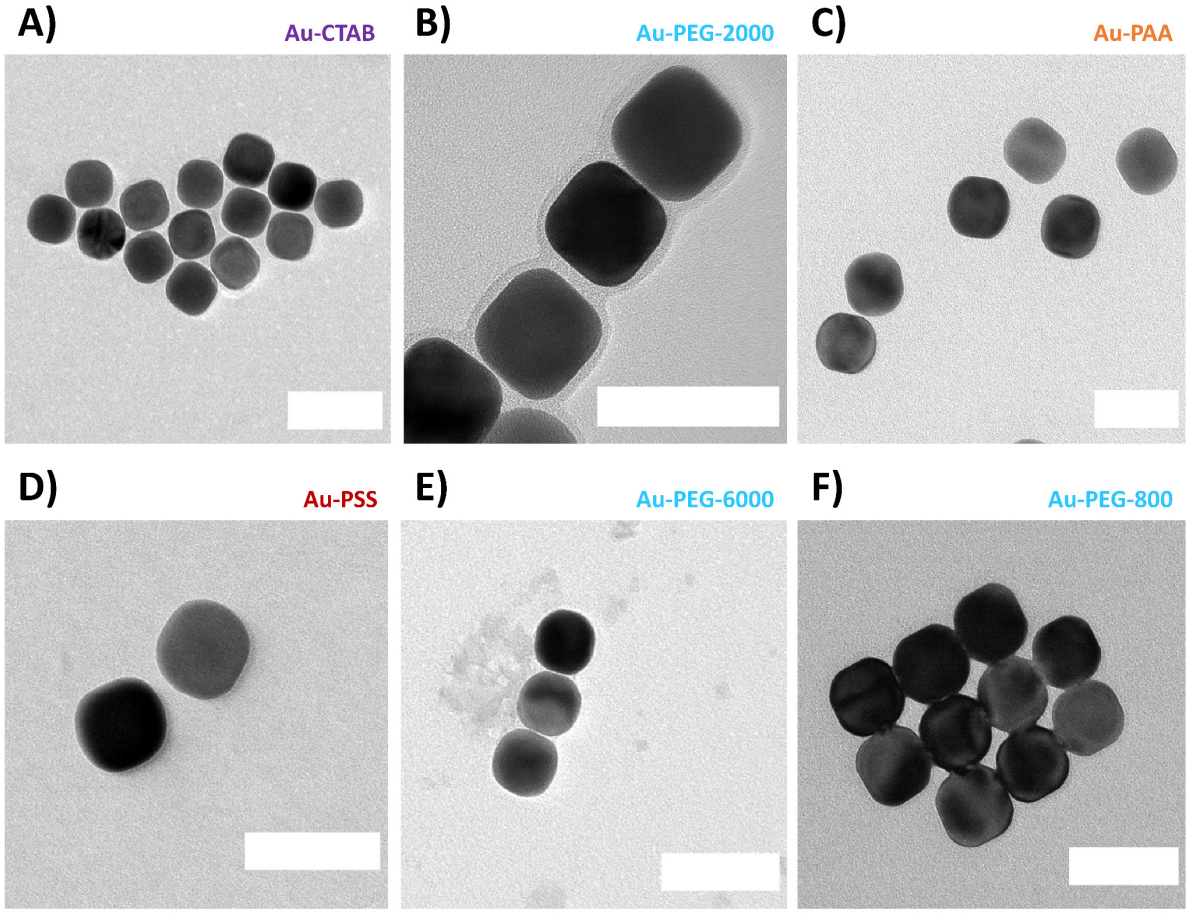

Figure A 28. HR-TEM images of functionalized gold nanocubes. The HR-TEM images of gold nanocubes functionalized with A) CTAB, B) PEG, C) PAA, D) PSS, E) PEG 6000 and F) PEG 800. The images of A-E show that the nanoparticle shape in form of truncated cuboctahedrons could be preserved during the functionalization. Image F) however, shows gold nanocubes fused into bigger aggregates as a result of the functionalization treatment. Scale bar length: 50 nm.

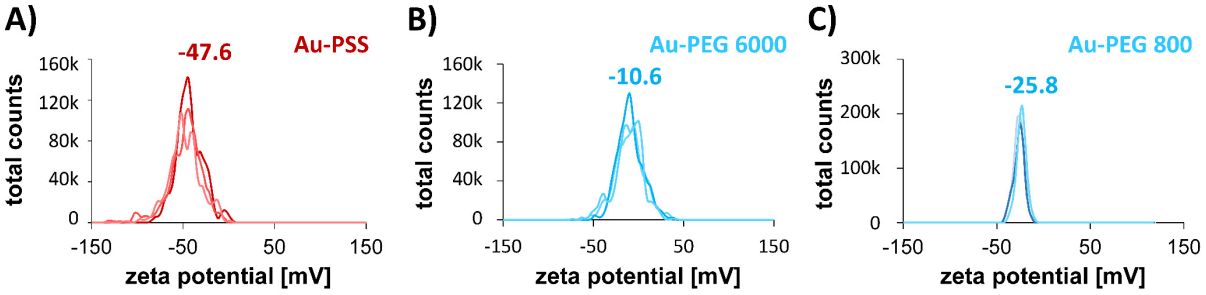

Figure A 29. Zeta potential measurements of functionalized gold nanocubes. The results show zeta potentials of A) -47.6 mV for PSS-functionalized B) -10.6 mV for PEG 6000-functionalized and C) -25.8 mV for PEG 800-functionalized gold nanocubes. The shift of the zeta potential indicates a successful ligand exchange and the variety of surface functionalizations.

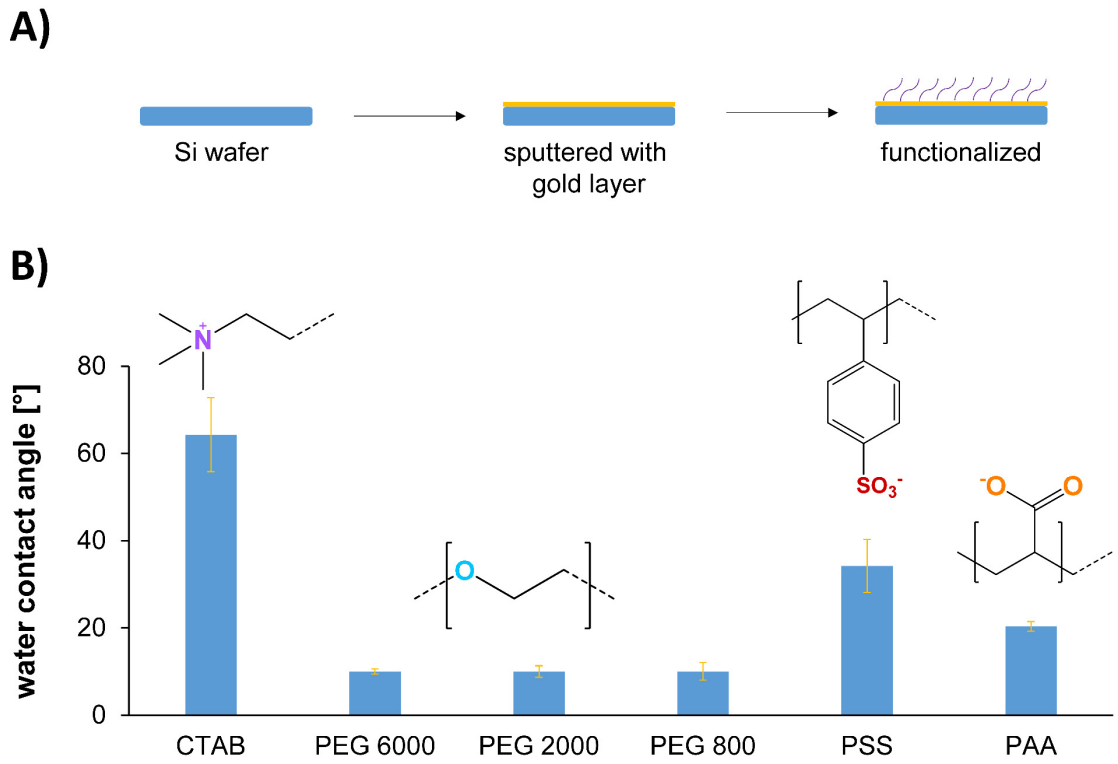

Figure A 30. Contact angle measurements of functionalized gold substrates. A) Silicon wafers were sputtered with a gold layer and functionalized with the same ligands used for the gold nanocube functionalization. B) To characterize the surface properties water contact angles were measured for the different functionalizations: CTAB, PEG (6000, 2000, 800), PSS and PAA.

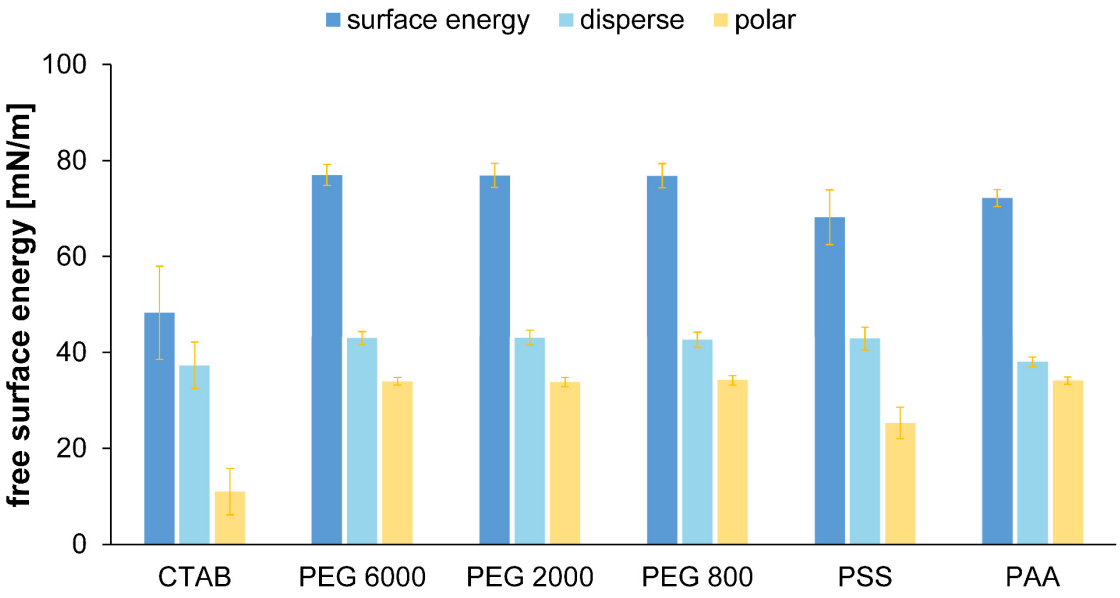

Figure A 31. Free surface energies of functionalized gold substrates. Free surface energies (blue) with their disperse (light blue) and polar (orange) parts, determined by contact angle measurements with water and diiodomethane for functionalized gold substrates. The gold substrates were functionalized with the same ligands used for the gold nanocube functionalization: CTAB, PEG (6000, 2000, 800), PSS and PAA.

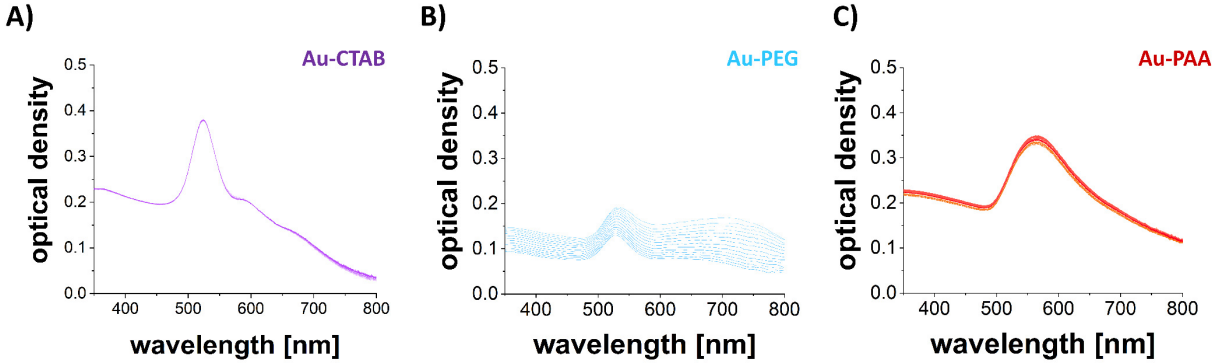

Figure A 32. Quenching of destabilized gold nanocubes dispersions. During destabilization experiments, formed aggregates and remaining single gold nanocubes could be stabilized again by adding CTAB to a concentration of 2.00 mM regardless of the functionalization of the gold nanocubes. The graphic shows UV-vis-NIR spectra of a quenched gold nanocube dispersion over a timeframe of 14 h of A) CTAB-functionalized, B) PEG-functionalized, and C) PAA-functionalized gold nanocubes. The peaks did not shift to longer wavelengths, which indicates that the gold nanocube dispersion was stabilized again in its destabilized state. The reduction of the peak intensity was caused by sedimentation of the gold nanocube aggregates. Shaking the quenched dispersion before the measurement led to a comparable peak intensity as at the time of quenching.

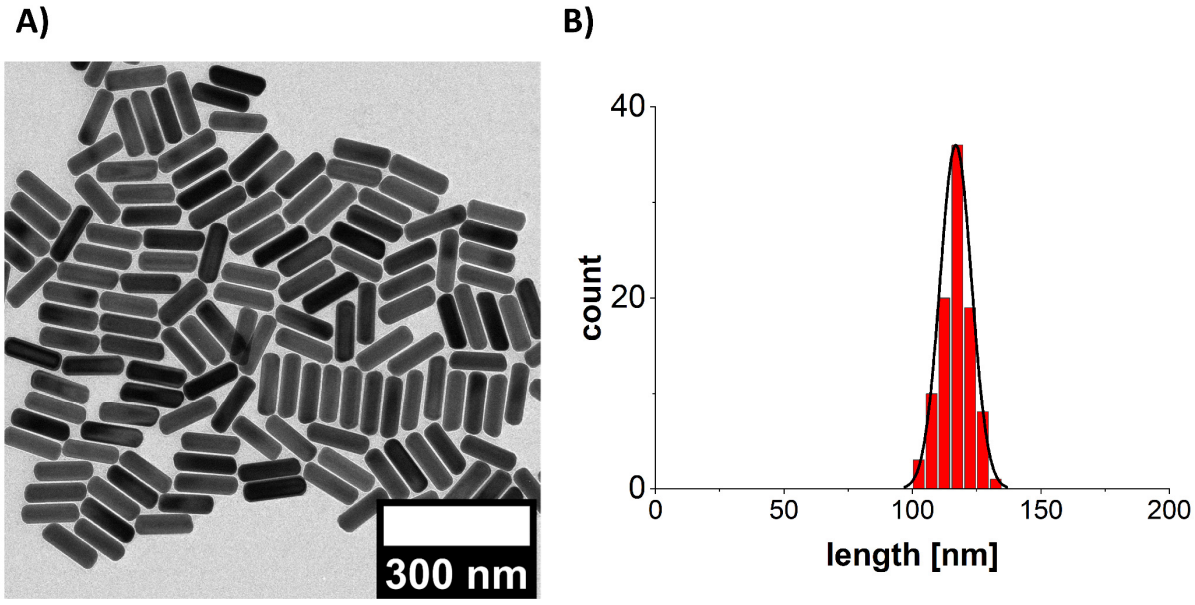

Figure A 33. CTAB gold nanorods with an aspect ratio of 3.00. A) HR-TEM image of CTAB gold nanorods with a width of approximately 40 nm. B) The histogram shows the mean length of the nanorods of 117 ± 6 nm.

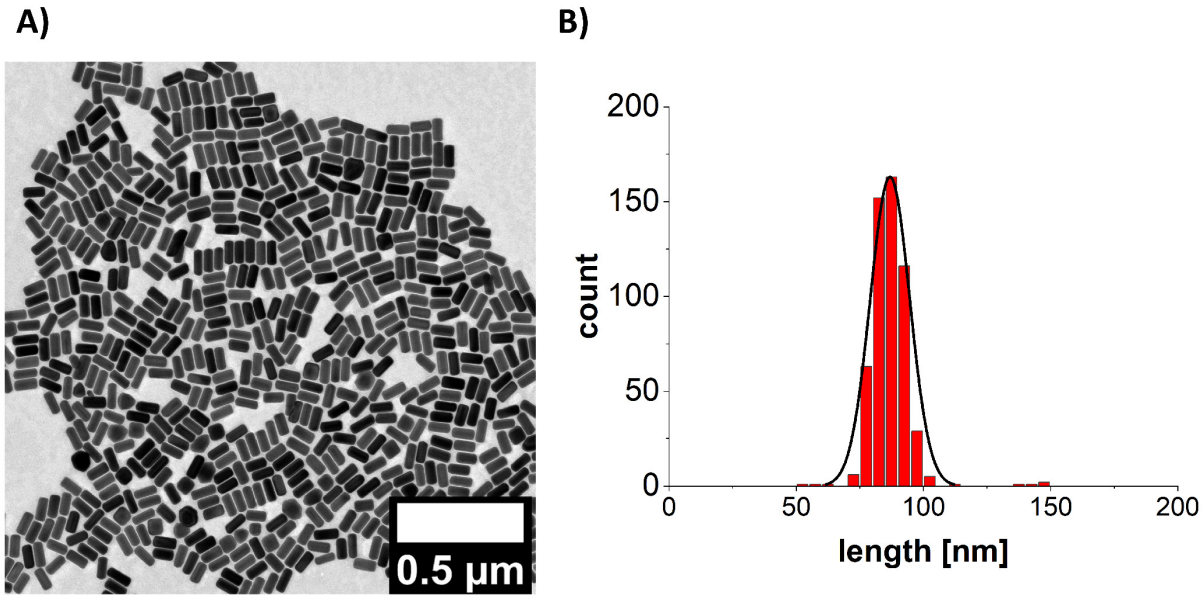

Figure A 34. CTAB gold nanorods with an aspect ratio of 2.25. A) HR-TEM image of CTAB gold nanorods with a width of approximately 40 nm. B) The histogram shows the mean length of the nanorods of 87 ± 8 nm.

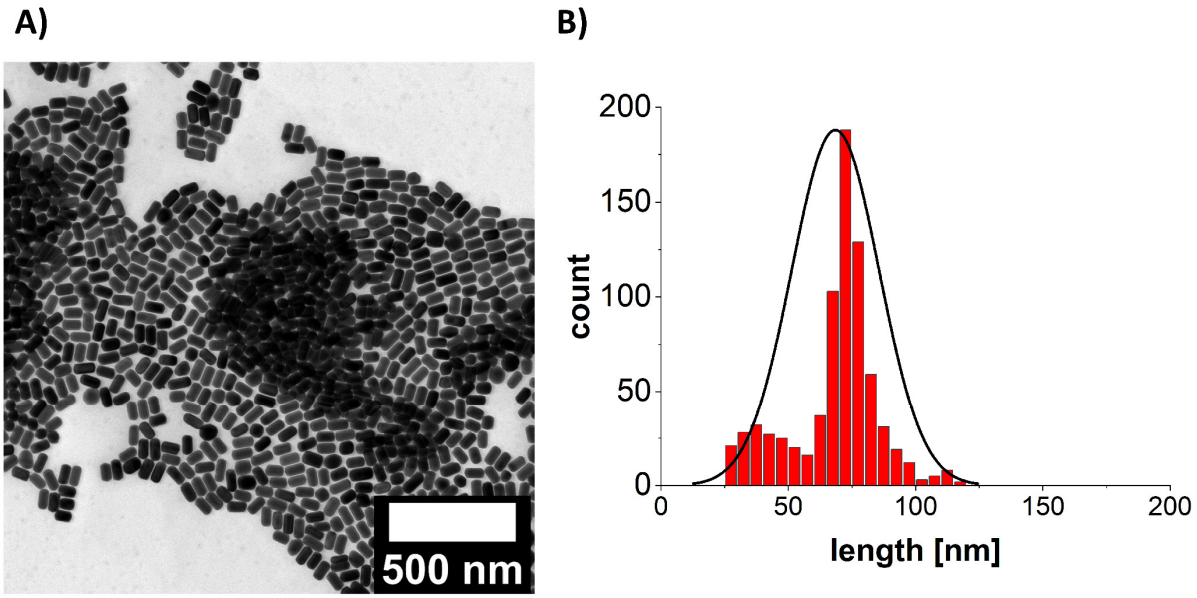

Figure A 35. CTAB gold nanorods with an aspect ratio of 1.75. A) HR-TEM image of CTAB gold nanorods with a width of approximately 40 nm. B) The histogram shows the mean length of the nanorods of 68 ± 17 nm.

4.3 Materials and Methods

4.3.1 Instruments

ATR-IR measurements were performed on a *Perkin Elmer Spectrum 100* FT-IR equipped with a universal ATR sampling accessory.

For the measurement of **contact angles** and free surface energies, the drop shape analyzer *DSA25* and the software *Advance* from *Krüss* were used. Contact angles larger than 10° were fitted with the *Ellipse (Tangent-1)* model, while contact angles smaller than 10° were fitted with the *Circle* model. The free surface energies were calculated with the contact angles from water and diiodomethane over the *Owens, Wendt, Rabel and Kaelble* (*OWRK)* model.

DLS measurements were carried out on a *Zetasizer Nano ZSP* (*Malvern Instrument*, Malvern, U.K.), using a He/Ne laser (λ = 633 nm).

TEM images were recorded on a *Zeiss Libra 120* at an accelerating voltage of 120 kV. HR-TEM images were recorded on a *JEOL JEM-2200FS* microscope at an accelerating voltage of 200 kV. The samples were applied on *Quantifoil* carbon-coated Cu 400 mesh grids.

TGA measurements were performed with a *Netzsch STA 449F3 Jupiter*. The samples were measured in a temperature range from 30 °C to 900 °C, with a heating rate of 10 K/min. The gas flow during the measurement consisted of 254 ml/min oxygen and 250 ml/min nitrogen.

The **stochastic optical reconstruction microscopy** images were taken at a *deltavision OMX*.

The **titration** experiment to monitor the opening of the succinic acid functionality was performed with an automated commercially available titration setup (*905 Titrando*) provided by *Metrohm* and operated with the custom-made software *Tiamo 2.3*. The pH measurements were recorded using a flat membrane pH electrode *Metrohm (6.0269.100)*.

UV-Vis-NIR measurements were performed with a *Varian Cary 50* spectrometer in quartz cuvettes.

Zeta potentials were measured on a *Zetasizer Nano-ZS Zen3600* from *Malvern Instruments*.

4.3.2 Materials

In all experiments, Milli-Q water (resistivity 18.2 MΩcm at 25 °C) was used. All chemicals were purchased and used without further purification.

Methanol (MeOH, ≥ 99.5%), ethanol (EtOH, ≥ 99.8%) and acetone (C_3H_6O, ≥ 99.5%) were purchased from *VWR* and sodium hydroxide pellets (NaOH, ≥ 98.0%) were purchased from *Carl Roth*. Hexane ($CH_3(CH_2)_4CH_3$, ≥ 95.0%), toluene ($C_6H_5CH_3$, ≥ 99.5%), dimethyl sulfoxide ($(CH_3)_2SO$, ≥ 99.0%), dichloromethane (CH_2Cl_2 ≥ 99.5%) and acetic acid (CH_3CO_2H, ≥ 99.7%) were purchased from *Merck*.

(3-aminopropyl)triethoxysilane for the amine functionalization was purchased from *Sigma-Aldrich*. 3-(Triethoxysilyl)propyl-succinic anhydride for the carboxyl functionalization and 3-acetoxypropyl-trimethoxysilane for the hydroxyl functionalization were purchased from *abcr*. Tetramethylammonium hydroxide solution (25 wt.-% in water) was purchased from *Merck*.

Ninhydrin (1,2,3-indantrione monohydrate), sodium bicarbonate ($NaHCO_3$), sodium carbonate (Na_2CO_3), 4-(4,6-dimethoxy-1,3,5-triazin-2-yl)-4-methyl-morpholinium chloride (DMTMM), tris(2-carboxyethyl)-phosphine hydrochloride, disodium hydrogen phosphate (Na_2HPO_4), and sodium dihydrogen phosphate (NaH_2PO_4) were purchased from *Merck*. The fluorescent dye *Alexa fluor plus 647* was purchased from *Thermo Fischer Scientific*. The c-coumarin was available in the Cölfen group synthesized by Michael Gießl derived from the publication of Shiota *et al.*.[238]

Hexadecyltrimethylammonium bromide (CTAB, ≥ 99%), 1-decanol (n-decanol, 98%), hydrogen tetrachloroaurate trihydrate ($HAuCl_4 \cdot 3H_2O$, ≥ 99.9%), silver nitrate ($AgNO_3$, ≥ 99.0%), hydroquinone (≥ 99.0%), L-ascorbic acid (≥ 99%), and sodium borohydride ($NaBH_4$, 99%) Poly(ethylene glycol) methyl ether thiol (PEG) with a M_W of 6 000 g/mol, M_W of 2 000 g/mol and M_W of 800 g/mol and Poly(sodium 4-styrenesulfonate) (PSS) with a M_W of 70 000 g/mol were purchased from *Sigma Aldrich*. (α-thiol, ω-bromo)-terminated poly(acrylic acid) (PAA) with a M_W of 8 500 g/mol was purchased from *Polymer Source™ Inc.*

4.3.3 Zinc Oxide Nanorod Functionalization

Zinc oxide nanorods stabilized by P3P were available in the Polarz and Wittmann group (provided by Sebastian Theiß and Michael Voggel). The ligand P3P of the zinc oxide nanorods was exchanged by three different silanes: (3-aminopropyl)triethoxysilane for the amine functionalization, 3-acetoxypropyl-trimethoxysilane for the hydroxyl functionalization, and 3-(triethoxysilyl)propyl-succinic anhydride for the carboxyl functionalization. To preserve the functional groups, the hydroxyl and carboxyl silanes had to be

introduced to the mica substrate with a protection group (succinic anhydride for the carboxyl group and acetyl for the hydroxyl group), followed by a deprotection step.

4.3.3.1 Ligand Exchange at High Temperature and under Protective Gas

The principle of the synthesis was adapted from Moussodia.[239] The whole synthesis was carried out under inert gas (N_2). 50 mg P3P-functionalized zinc oxide nanorods were dispersed in 10 ml toluene. 1 ml of a 0.1 M solution of the respective silane dissolved in ethanol was added to the zinc oxide nanorods under stirring. The dispersion was stirred for 5 min under RT. 1 ml of a 0.3 M solution of tetramethylammonium hydroxide in ethanol was added and the temperature was raised to 85 °C for 45 min. Afterward, the dispersion was allowed to cool down to RT and the zinc oxide nanorods were separated by centrifugation (4000 rpm, 15 min).

The zinc oxide nanorods were washed three times with toluene and afterward redispersed in water. The originally hydrophobic particles were now soluble in water. Here, they were cleaned further with precipitation-solubilization cycles. Meaning acetone was added to the water to precipitate the zinc oxide nanorods, they were separated by centrifugation (4000 rpm, 10 min) and redispersed in water. The whole procedure was repeated four times. Finally, the particles were dispersed in water.

4.3.3.2 Ligand Exchange at RT

The principle of the synthesis was adapted from De Palma.[240] 12 mg P3P-functionalized zinc oxide nanorods were dispersed in 30 ml hexane. 3 µl acetic acid and 150 µl of the respective silane were added. The dispersion was left for 72 h at RT on a shaking plate. The zinc oxide nanorods were separated by centrifugation (4000 rpm, 10 min) and washed three times with hexane. Finally, the particles were dispersed in water.

4.3.3.3 Deprotection Steps

For a functionalization with carboxyl groups, the 3-(triethoxysilyl)propyl-succinic anhydride-functionalized zinc oxide nanorods were deprotected. Therefore, the zinc oxide nanorods were given into a solution of 30 ml ethanol and 2 ml water. The mixture was heated up to 90 °C and left for 1 h. Afterward, the zinc oxide nanorods were washed with water.

For a functionalization with hydroxyl groups, the 3-acetoxypropyltrimethoxysilane-functionalized zinc oxide nanorods were deprotected. Therefore, the zinc oxide nanorods were given into a solution of dichloromethane and methanol in a ratio of 9 : 1. A solution of 2-3 N sodium hydroxide in methanol was added to reach a final solution concentration of 0.1 – 0.2 N sodium hydroxide. The mixture was shaken overnight. Subsequently, the zinc oxide nanorods were washed with water.

4.3.3.4 Coupling of Fluorescent Dyes

For the Ninhydrin test[241], a solution of 1 wt.-% ninhydrin in ethanol was prepared and added to a 10 wt.-% solution of zinc oxide nanorods in ethanol. The mixed solutions were heated up to 60 °C for 20 min. A

purple discoloration indicated the presence of amine groups for the amine-functionalized zinc oxide nanorods. While the control sample with P3P-functionalized zinc oxide nanorods did not show a discoloration.

For the coupling of the fluorescence dye *Alexa647*, amine-functionalized zinc oxide nanorods were dissolved with a concentration of 0.1 – 0.2 M in a sodium bicarbonate buffer at pH 9. A solution of 10 mg *Alexa647* in 500 µl dimethyl sulfoxide was added dropwise under stirring. The solution was left stirring overnight. The zinc oxide nanorods were separated by centrifugation (4000 rpm, 10 min) and washed six times with ethanol and four times with water. Finally, the zinc oxide nanorods were applied to a cell culture dish with a glass bottom for microscopic studies.

For the coupling of cleavable c-coumarin[238], a phosphate-buffered solution with pH 8 was prepared. 5 vol.-% dimethyl sulfoxide, 2.00 mM c-coumarin and 10 mM (4-(4,6-dimethoxy-1,3,5-triazin-2-yl)-4-methyl-morpholinium chloride) were added. 13 mg of zinc oxide nanorods were washed with water and dispersed in the phosphate-buffered solution. The mixture was left for 2 h on a shaking plate. The zinc oxide nanorods were separated by centrifugation (4000 rpm, 10 min) and redispersed in 1.5 ml methanol at 40 °C for 1 h. This washing procedure was repeated three times. Afterward, the zinc oxide nanorods were washed with 1 ml of the phosphate-buffered solution. To cleave the c-coumarin, the zinc oxide nanorods were dispersed in 1 mL phosphate-buffered solution with 4 mM tris(2-carboxyethyl)phosphine for 1 h at 40 °C. Finally, the zinc oxide nanorods were separated by centrifugation and the supernatant solvent was used for the fluorescence measurement at 420 nm.

4.3.4 Gold Nanocubes

Single crystalline gold nanocubes stabilized by CPC were available in the Cölfen group (provided by Felizitas Kirner) and synthesized in a three-step seed-mediated approach.[231]

4.3.4.1 CTAB Gold Nanocube Functionalization

The gold nanocube stabilizer CPC was exchanged with CTAB as follows. One batch of 50 ml aqueous nanoparticle dispersion, with a concentration of 0.17 mM gold nanoparticles, was centrifuged at 6000 rpm for 1 h. The supernatant was separated and the concentrated nanoparticles in the sediment were transferred to a micro test tube. The concentrated nanoparticles were washed with 2.00 mM CTAB aqueous solution and centrifuged at 6000 rpm for 20 min. The washing procedure was repeated two times. The volume of the concentrated nanoparticle sediment was determined to know the current concentration of the gold nanoparticles.

4.3.4.2 PEG Gold Nanocube Functionalization

For a functionalization with PEG, the CTAB stabilized gold nanocubes from Chapter 4.3.4.1 were used and the CTAB was exchanged with three different PEG chain lengths. All used equivalents are shown in Table A 5. For the ligand exchange, PEG was dissolved under stirring in water in a small glass vial. In a 1.5 ml micro test tube, concentrated CTAB-functionalized gold nanoparticles were dissolved in 300 µl water. Under vigorous stirring, the diluted gold nanoparticles were given dropwise into the PEG water solution. The dispersion remained deep red, indicating the stability of the gold nanoparticles. For washing, the dispersion was given into two micro test tubes and centrifuged. The supernatant was removed, the precipitate was washed with water and centrifuged. The supernatant was removed and the concentrated PEG-functionalized particles could be used for further experiments.

Table A 5. Conditions for PEG functionalization of gold nanocubes.

average molecular weight of used PEG [g/mol]	**mass PEG [mg]**	**volume water for PEG solution [ml]**	**volume concentrated particles [µl]**	**centrifugation**
6000	5.0	3	3	45 min 6000 rpm 30 min 6000 rpm
2000	10.3	1	1	20 min 6000 rpm 20 min 6000 rpm
800	24.2	1	1	20 min 2000 rpm 40 min 2000 rpm

4.3.4.3 PSS Gold Nanocube Functionalization

For a functionalization with PSS, the CTAB stabilized gold nanocubes from Chapter 4.3.4.1 were used and the CTAB was exchanged with PSS. Therefore, PSS with an average molecular weight of M_n = 70000 g/mol was used. For the ligand exchange, 0.3 g of PSS was dissolved under stirring in 100 ml water in a glass vial. In a 1.5 ml micro test tube 5 µl of concentrated CTAB-functionalized gold nanoparticles were dissolved in 125 µl water. Under vigorous stirring, the diluted gold nanoparticles were given dropwise into the PSS water solution. The dispersion remained deep red, indicating the stability of the gold nanoparticles. The dispersion was left to rest for 1 h. For washing, the dispersion was given into a micro test tube and centrifuged for 20 min at 6000 rpm. The supernatant was removed, the precipitate was washed with 1 ml water and centrifuged for 20 min at 6000 rpm. The supernatant was removed and the concentrated PSS-functionalized particles could be used for further experiments.

4.3.4.4 PAA Gold Nanocube Functionalization

For a functionalization with PAA, the CTAB stabilized gold nanocubes from Chapter 4.3.4.1 were used and the CTAB was exchanged with PAA. Therefore, (α-thiol, ω-bromo)-terminated poly(acrylic acid) (PAA) with an average molecular weight of M_n = 8500 g/mol was used. For the ligand exchange, 14.3 mg of PAA was dissolved under stirring in 1 ml water in a small glass vial. In a 1.5 ml micro test tube 1 µl of concentrated CTAB-functionalized gold nanoparticles were dissolved in 300 µl water. Under vigorous stirring, the diluted gold nanoparticles were given dropwise into the PAA water solution. The dispersion remained deep red, indicating the stability of the gold nanoparticles. For washing, the dispersion was given into a micro test tube and centrifuged for 5 min at 4000 rpm. The supernatant was removed, the precipitate was washed with 1 ml water and centrifuged for 30 min at 4000 rpm. The supernatant was removed and the concentrated PAA-functionalized particles could be used for further experiments.

4.3.5 Gold Nanorods

Gold nanorods were available in the Cölfen group (provided by Guillermo González-Rubio) and the synthesis was carried out according to a recently reported procedure.[233]

4.3.5.1 Synthesis of 1–2 nm Gold Seeds

200 µl of a 0.05 M chloroauric acid solution and 200 µl of a 0.1 M ascorbic acid solution were added to 20 ml of a 50 mM CTAB and 13.5 mM *n*-decanol solution (prepared by dissolving 9.111 g of CTAB and 1.068 g in a 500 ml glass beaker in 500 ml of warm water, ~ 60 °C, under stirring until complete dissolution). After 1–2 min, 800 µl of a freshly prepared 0.02 M sodium borohydride solution was injected under vigorous stirring (1000 rpm using a polytetrafluoroethylene plain magnetic stirring bar: 30 × 6 mm) at 25–27 °C. The seed solution was aged for 30-60 min at room temperature prior to use.

4.3.5.2 Synthesis of Small Gold Nanorods

In a typical synthesis for small gold nanorods (21 nm in length and 7.5 nm in width), 2400 µl of 0.01 M silver nitrate, 21 ml of 1 M hydrochloric acid, 3000 µl of 0.05 M chloroauric acid, and 3900 µl of 0.1 M ascorbic acid were added to 300 ml of a 50 mM CTAB and 11 mM *n*-decanol solution at exactly 25 °C (prepared by following the same procedure described for the 1–2 nm gold seeds). The growth was initiated by adding 18 ml of the seed solution under stirring. The mixture was left undisturbed at exactly 25 °C for at least 4 h. The obtained small gold nanorods, with a localized surface plasmon resonance longitudinal band located between 725–730 nm, were centrifuged at 14000–15000 rpm for 45–60 min in 2 ml tubes. The precipitate was redispersed with 4 ml of a 10 mM CTAB solution. The concentrated gold nanorods were centrifuged twice under the same conditions, and the final Au^0 concentration was fixed to 4.65 mM (Abs_{400nm}: 1, optical path: 0.1 cm).

4.3.5.3 Synthesis of Gold Nanorods with Distinct Dimensions

In a typical synthesis, a certain amount of a 0.01 M silver nitrate solution (Table A 6), 1 ml of 0.05 M chloroauric acid, 0.8 ml of a 0.1 M ascorbic acid solution (for nanorods with localized surface plasmon resonances at 730 nm and 800 nm), or 5 ml of a 0.1 M hydroquinone solution (for gold nanorods with localized surface plasmon resonances at 630 nm) were added under stirring to 100 ml of a 50 mM CTAB and 11 mM *n*-decanol (for gold nanorods with localized surface plasmon resonances at 730 nm and 800 nm) solution or a 50 mM CTAB and 5.5 mM *n*-decanol (for gold nanorods with localized surface plasmon resonances at 630 nm) solution at a 28 °C (Table A 6). A certain volume of 1 M hydrochloric acid was subsequently added under stirring, and the growth was initiated via the addition of a given amount of small gold nanorod solution (Table A 6). The mixture was left undisturbed for 4 h, and the obtained overgrown nanorods were washed by precipitation at 4000 rpm for 10 min and redispersed in 5 ml of a 1 mM CTAB solution.

Table A 6. Growth conditions for gold nanorod synthesis.

localized surface plasmon resonance [nm]	**volume silver nitrate 0.01 M solution [ml]**	**volume hydrochloric acid 1 M solution [ml]**	**volume small gold nanorod solution [µl]**
1.75	0.4	-	50
2.25	2.0	2.0	50
3.00	2.5	6.0	40

5 Characterization of Heterogeneous Nucleation

The objective of this thesis was to analyze heterogeneous nucleation using anisotropic nanoparticles as a model system, meaning the nanoparticles act like building blocks and form larger superstructures comparable to nucleation phenomena of atoms or molecules. The preliminary chapters described the development of substrate and nanoparticle systems for heterogeneous nucleation experiments. To explore the possible influences on heterogeneous nucleation of these systems, such as surface chemistry or the shape of the nanoparticle building blocks, characterization and quantification of the nucleation process is required. Therefore, the next step aimed to establish an analytical method to determine the nucleation rates and thereby open the possibility to gain thermodynamic and kinetic information of the nucleation process and to be able to compare different nucleation systems. This chapter will describe how the controlled analysis of heterogeneous nucleation events was performed and the development of a light microscope setup that allowed a facile determination of nucleation rates. Therefore, the nanoparticle systems had to be destabilized in a controlled way, nucleating heterogeneously on the defined mica substrates and allowing a continuous in situ analysis with the light microscope.

5.1 Results and Discussion

5.1.1 Controlled Heterogeneous Nucleation of Nanoparticle-based Superstructures

To study the different influences on the kinetics of heterogeneous nucleation of nanoparticle-based superstructures, an experimental procedure depicted in Figure 26 was be desirable. A stable nanoparticle dispersion with a defined concentration is crucial. Then a substrate is introduced to the nanoparticle dispersion and the system is destabilized in a controlled way by applying a trigger. If there is a preferential interaction between the nanoparticles and the introduced substrate surface, the destabilization will lead to heterogeneous nucleation of nanoparticles into superstructures on the surface. If there is no preferential interaction, heterogeneous nucleation will not occur on the surface. In addition, a strong destabilization might induce homogenous nucleation of the dispersed nanoparticles. As a first step towards a working experimental setup, a convenient trigger was crucial for the destabilization of the nanoparticle system to achieve heterogeneous nucleation on the surface. In general, destabilization can be triggered for instance by increasing the nanoparticle concentration with continuous evaporation of the solvent, by varying the supersaturation with a reduction of the temperature, or by altering the solubility of the nanoparticles in the solvent. In the following, the attempts to find a convenient trigger for a controlled nanoparticle destabilization and the accompanying development of the microscope setup are described.

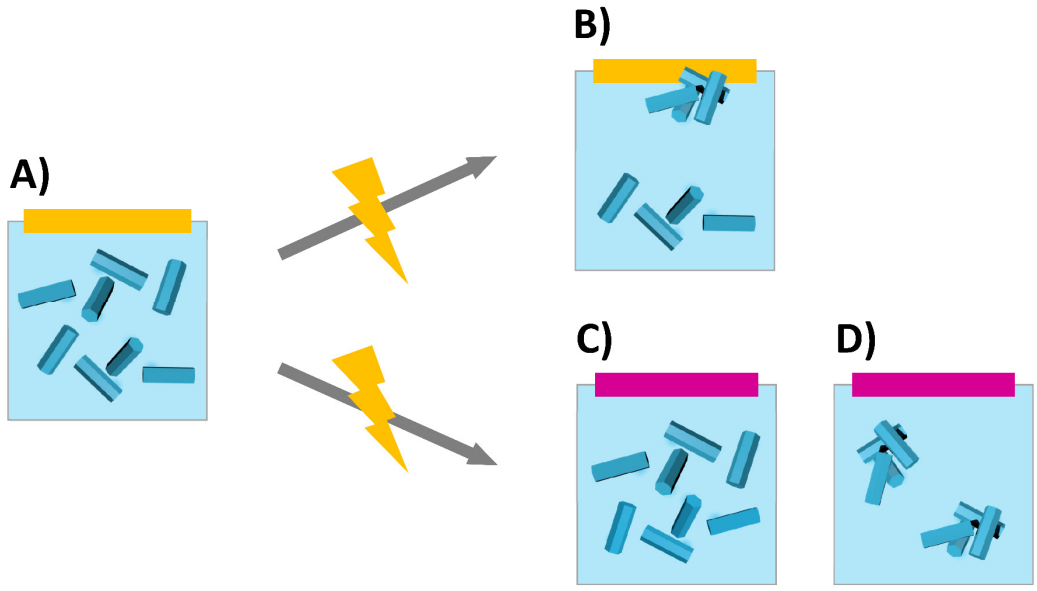

Figure 26. Experimental procedure for the analysis of heterogeneous nucleation of nanoparticle-based superstructures on defined surfaces. A) A substrate (orange) is introduced to a stable nanoparticle dispersion. The dispersion is destabilized in a controlled way. B) Due to a preferential interaction of the nanoparticles with the surface (orange), heterogeneous nucleation of nanoparticle-based superstructures occurs. C) While for an unfavorable interaction (purple), there will be no heterogeneous nucleation on the surface. D) Maybe the destabilization is high enough to induce homogeneous nucleation of the nanoparticles in the dispersion.

5.1.1.1 Concentration-Controlled Nucleation of Nanoparticle-based Superstructures

The stability of nanoparticle systems depends among other aspects on the concentration of the nanoparticles or the saturation of the system. The higher the nanoparticle concentration, the more the system is destabilized and the nanoparticles start to aggregate. This approach is used, for example, in drying-mediated self-assemblies of nanoparticles to mesocrystals.[108] Hence, a first approach tested an increase of the nanoparticle concentration as a trigger for the heterogeneous nucleation to form superstructures on mica substrates. The simplest system to start with was by putting a drop of a nanoparticle dispersion on the defined mica substrate. The nanoparticle concentration was increased by evaporation of the solvent. Because of the small volume of a drop, the evaporation rate and therefore the nanoparticle concentration varied extremely with the surrounding conditions such as temperature and humidity. Thus, the nucleation kinetics were tremendously affected.

To control the temperature and humidity during the nucleation experiments, a climate chamber was used (Figure A 36 A) which allowed adjusting both independently during light microscopy. For the improvement of the optical quality during experiments, a few optimizations were done, for example by using thinner optical glasses or a black cover to prevent scattered light (Figure A 36 A). The climate chamber has been used to keep the temperature and humidity during the experiments at a constant level. In addition, it was

also used to control the evaporation of a water drop and thereby initiate the nanoparticle destabilization for nucleation experiments (Figure A 36 B).

Experiments with a lying drop showed that aggregates formed homogeneously in dispersion sediment and could not be distinguished from heterogeneously formed structures on the substrate. This sedimentation would lead to an incorrect counted number of structures and would falsify the determined kinetic parameters. Instead, a hanging drop allowed detecting only the heterogeneously formed structures (Figure 27).

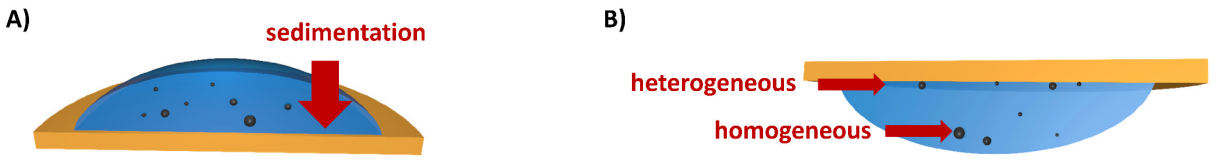

Figure 27. Schematic illustration of a lying versus a hanging drop. A) Experiments carried out with a lying drop result in sedimentation of homogeneously nucleated particles. A differentiation between heterogeneous or homogeneous nucleation is not possible. B) In contrast, a hanging drop leads to a separation of homogeneously and heterogeneously nucleated aggregates by sedimentation and makes differentiation possible.

While drying the water drop to increase the nanoparticle concentration, the coffee ring effect produced bothering effects.[242-244] Here, the evaporation of the solvent led to a nanoparticle diffusion to the solvent-air interface resulting in a concentration gradient of nanoparticles that formed a maximum at the solvent-air interface. The nanoparticles started to nucleate at this concentration maximum and it was not possible to achieve individual heterogeneous nucleation on the mica surface without contact to the solvent-air interface (Figure A 37).

An approach with evaporation of the solvent will lead in most cases to the coffee ring effect, which was not compatible with the ambition to analyze independent heterogeneous nucleation on a surface. Therefore, a closed setup without a solvent-air interface and another trigger to destabilize the nanoparticle systems were required.

5.1.1.2 Temperature-Controlled Nucleation of Nanoparticle-based Superstructures

Nucleation in general can be induced by changes in temperature, since the temperature influences the supersaturation of the system. When the temperature is lowered, the supersaturation increases and nucleation in the system is more likely. First experiments evaluated the destabilization of the different nanoparticle systems with a variation in temperature. Devices for simultaneous measurement with UV-vis-NIR spectroscopy allowed for a temperature change of 30 °C to 16 °C, while simultaneous DLS measurements allowed a temperature change from 30 °C to 5 °C. Destabilization of the different nanoparticle systems with temperature was not observed. On the one side, a precise setting of the concentration range might be important or maybe a larger temperature change is required. On the other side for the solubility of nanoparticles, the stabilizing ligand is of great importance. The solubility of CTAB,

for example, gets lower with a decrease in the temperature, which could be contradictory to the desired destabilization of the CTAB-stabilized gold nanocubes. More control might be provided with temperature switching ligands, but these were out of the scope of this thesis and not compatible with the desired variation of the nanoparticle surface chemistry which had to be analyzed in the next step.[245, 246] Hence, for the aimed system using temperature as a simple and universal trigger for nanoparticle nucleation was not suitable.

5.1.1.3 Solvent-Controlled Nucleation of Nanoparticle-based Superstructures

Besides the concentration, another factor influencing the stability of nanoparticle systems is the solvent. Depending on the stabilization of the nanoparticles, there are two approaches: destabilization by a solvent in which the nanoparticles and their stabilizers are not soluble or destabilization by a solvent in which the stabilizer of the nanoparticle is well soluble and therefore detaches itself from the nanoparticles.[232] For example a solvent-controlled destabilization of nanoparticles is used in a gas-phase diffusion approach for the synthesis of mesocrystals.[108, 109] The adaption of this approach to the aimed system in this thesis was not successful, since the nanoparticles were destabilized at the arising solvent-solvent interface and the structures were just sedimenting on the substrate (Figure A 38).

The aim was a uniform destabilization of the nanoparticle system in the entire volume. Thus, the solvent-controlled destabilization of the nanoparticle system should be achieved by a very fast addition of the destabilizing solvent and not by diffusion. CTAB stabilized gold nanocubes appeared to be a suitable test system as they can be easily destabilized by the addition of ethanol.[232] Through its adsorption on the gold surface, CTAB enables the growth of colloidal gold nanocrystals stabilized via electrostatic repulsions. When aiming at the controlled self-assembly of nanoparticles, destabilization of such electrostatic forces through the addition of water-soluble organic solvents represents the most straightforward strategy.[123, 152] As a first step towards the analysis of the heterogeneous nucleation of gold nanocubes on mica substrates, the destabilization process of gold nanocubes with a size of 23 nm in dispersion was optimized resulting in homogeneous nucleation of the nanocubes (Figure 28). First, a stock dispersion with a concentration of $3 \cdot 10^{10}$ M of gold nanocubes and 20 µM of CTAB was prepared. It was ensured that ethanol could destabilize the gold nanocubes in the desired manner, by adjusting such a low CTAB concentration, which lies 50 times below its critical micelle concentration.[247] One of the main advantages of using gold nanocubes was their ability to maintain a localized surface plasmon resonance at the interface with a surrounding dielectric medium. The nature of the plasmonic resonances depends on the presence of other particles in the vicinity, which opened access to monitoring the self-assembly process via UV-vis-NIR spectroscopy.[156, 157] Thus, we could easily monitor the process of self-assembly of gold nanocubes, destabilized by ethanol directly in dispersion, due to the changes in their extinction band (Figure 28 B). Initially, they showed a narrow plasmonic band with a maximum absorption peak at 523 nm, which then decreased during the homogeneous nucleation process. New bands corresponding to the formation of aggregates emerged at

longer wavelengths. These results indicated the suitability of using ethanol to trigger the aggregation of gold nanocubes stabilized by CTAB.

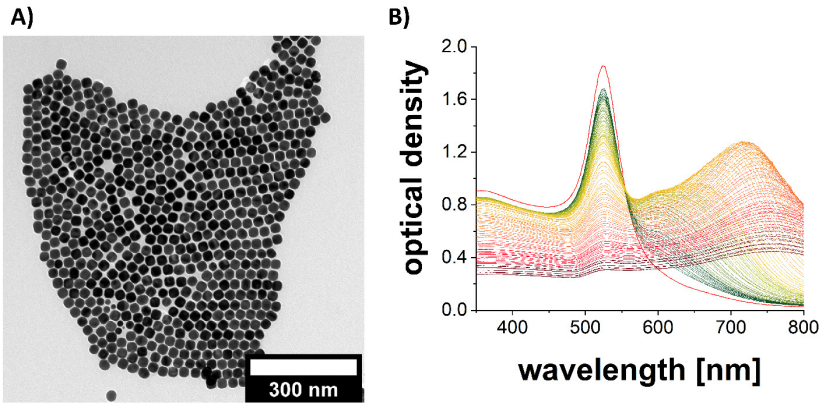

Figure 28. Homogeneous nucleation of gold nanocube-based superstructures. A) Representative TEM image of the gold nanocubes used. B) UV-vis-NIR spectra of gold nanocubes (red) and aggregates (from green to purple) formed during the self-assembly process over a timeframe of 4 h. The gold nanocubes show an absorption maximum at 523 nm, which decreases during the nucleation process. The new bands emerging at higher wavelengths can be assigned to the aggregates of the gold nanocubes.

The described solvent-controlled nucleation of the gold nanocube system seemed to be a convenient approach towards the analysis of its heterogeneous nucleation. This method enabled the controlled destabilization of the gold nanocubes inside the whole volume and did not exhibit a solvent-air or a solvent-solvent interface. As the experimental conditions for homogenous nucleation were optimized, experiments focused on the heterogeneous nucleation affected by the presence of a substrate. For this purpose, mica substrates were used, which are atomically cleavable and thereby exhibited a very smooth surface to minimize the undesired nucleation triggered by cracks or roughness. To investigate the role of a substrate in the nucleation of gold nanocube superstructures the mica substrates were functionalized with the negatively charged polystyrene sulfonate and the hydrophobic silane (heptadecafluoro-1,1,2,2-tetrahydrodecyl)triethoxysilane), respectively (Chapter 3.3.3). A gold nanoparticle stock dispersion was destabilized with ethanol (31 vol.-%). Then, the dispersion was split into several aliquots, which were introduced in micro test tubes containing the differently functionalized mica substrates. Thus, nine experiments were performed: three for each mica functionalization and three additional controls (i.e., negatively charged mica, hydrophobized mica, and the absence of a mica substrate). The self-assembly process was followed again via UV-vis-NIR spectroscopy over a timeframe of 24 h (Figure 29, Figure A 39). The results showed that the kinetics of the destabilization was slowest in the case of the fluorine mica and the control sample without mica. However, when sulfonate mica substrates were present during the self-assembly, the process was accelerated. These results can be explained by the different interactions between the gold nanocubes and the mica surfaces. On the one hand, polystyrene sulfonate is negatively charged while the gold nanocubes are positively charged, due to the CTAB functionalization. Thus, strong electrostatic interaction can drive the adsorption of the gold nanocubes on the surface, where its

concentration increases, thereby enhancing the gold nanocube self-assembly and superstructure formation.[152] On the other hand, fluorine-functionalized substrates do not allow a preferential interaction with the charged gold nanocubes, which explains why their impact on the self-assembly process is negligible and comparable to that observed in the absence of mica substrates. Analysis of both types of the mica substrates after the heterogeneous nucleation process strongly supports this idea. While the sulfonate-functionalized surfaces were covered uniformly with gold nanoparticle aggregates (Figure 29D), the fluorine-functionalized surfaces were almost empty (Figure 29C). Overall, sulfonate-functionalized substrates accelerated the destabilization of the gold nanocubes in dispersion because of an increased rate of heterogeneous nucleation on their surface. Similar results were obtained using a silicon wafer instead of mica.

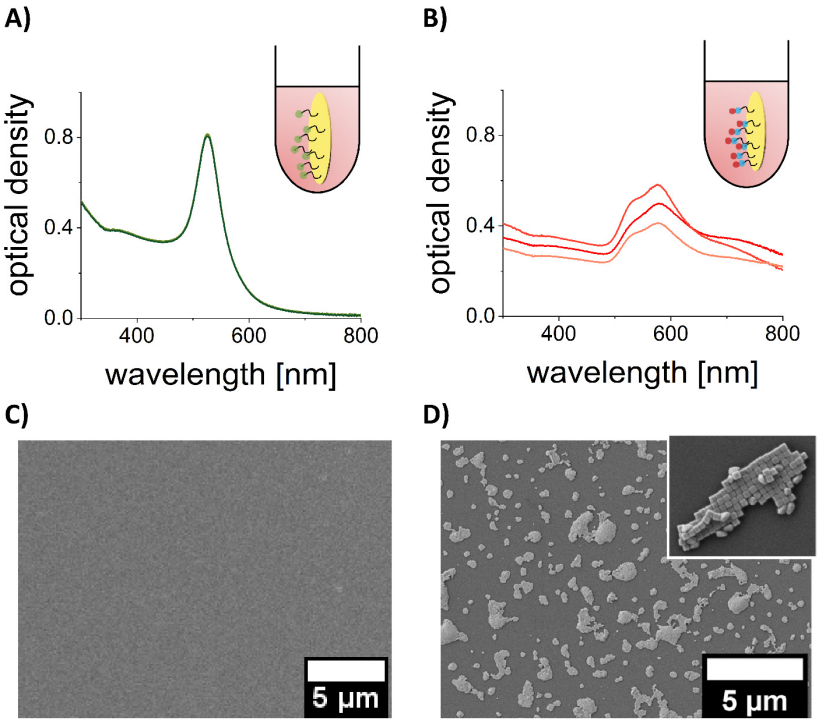

Figure 29. Heterogeneous nucleation of gold nanocube-based superstructures. Destabilization of gold nanocubes in a micro test tube in the presence of different functionalized mica substrates. A, B) Three aliquots after 15 min destabilization time are analyzed by UV-vis-NIR spectroscopy to compare the destabilization of the nanoparticle dispersion in the presence of fluorine- (A) and sulfonate-functionalized (B) substrates. C, D) SEM images of fluorine- (C) and sulfonate-functionalized (D) substrates after 24 h of destabilization time. The fluorine-functionalized surface is almost empty, while the sulfonate-functionalized surface is covered with gold nanocube-based superstructures.

To further understand the effect of surface functionalization on the heterogeneous nucleation of gold nanocube-based superstructures, the same surface functionalizations, already investigated with mica substrates, were conducted in quartz cuvettes. Thereby, the objectives were in situ investigation of the heterogeneous nucleation and gaining insights into the kinetics of the process. First, quartz cuvettes were functionalized with either fluorine or sulfonate (Figure 30A). Then a gold nanocube dispersion was

destabilized directly inside the functionalized cuvettes and the nucleation process was monitored via UV-vis-NIR spectroscopy (Figure 30B). While the gold nanocubes in contact with sulfonate-functionalized substrate destabilized extremely fast, the gold nanocubes in contact with fluorine-functionalized substrate stayed stable in dispersion. Once the process was completed, the nanocubes in suspension were removed and the spectra of gold nanocube-based superstructures, which formed on the cuvette walls, were recorded (Figure A 40). The spectra revealed a clear absorption signal of the gold nanocube-based superstructures on the sulfonate functionalized cuvette, while no signal was observed for the fluorine one. Another interesting advantage of using quartz cuvettes is the possibility of obtaining optical images via light microscopy of the gold nanocubes self-assembled on the surface (Figure 30C, D). The obtained images were in accordance with the UV-vis-NIR signals and showed almost no gold nanocube-based superstructures on fluorine-functionalized cuvettes, while sulfonate-functionalized cuvettes were covered with gold nanocube-based superstructures. These results further demonstrated the ability of sulfonate-functionalized substrate to trigger not only the homogeneous nucleation of gold nanocubes in dispersion but moreover the heterogeneous nucleation on sulfonate-functionalized surfaces.

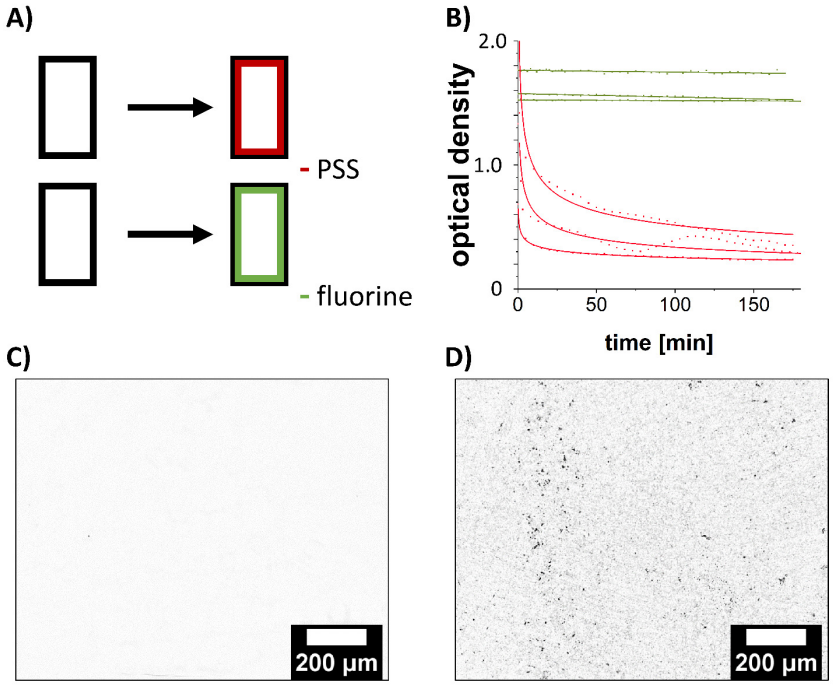

Figure 30. In situ characterization of heterogeneous nucleation of gold nanocube-based superstructures. A) Schematic representation of the functionalization of quartz cuvettes used to investigate the heterogeneous nucleation of nanocube-based superstructures in dispersion via UV-vis-NIR spectroscopy. B) The gold nanoparticle stock dispersion is destabilized in fluorine cuvettes (green) and sulfonate cuvettes (red). The heterogeneous nucleation process is observed by UV-vis-NIR spectroscopy and the optical density at 523 nm (absorption maximum of gold nanocubes) is plotted. The destabilization experiments are performed with the same nanoparticle stock dispersion and each dispersion is destabilized separately with ethanol. The plots show the relatively good reproducibility between the two different substrates. C, D) Light microscopy images of the cuvette surface after the nucleation process: (C) fluorine cuvette without gold nanoparticle-based superstructures and (D) sulfonate cuvette with gold nanoparticle-based superstructures.

Herein, it was demonstrated that the presence of a substrate could accelerate the nucleation process of gold nanocubes depending on its surface functionalization. In case of the favorable interaction between sulfonate-functionalized substrates and the CTAB stabilized gold nanocubes, even heterogeneous nucleation of nanoparticle-based superstructures on the surface could be observed. The gold nanocube system and its solvent-controlled destabilization seemed to be an appropriate foundation for the next step. Therefore, it has been used as a model system to establish a microscope setup allowing to determine nucleation rates of heterogeneous nucleation processes.

5.1.2 Microscopic Analysis of Nanoparticle-based Superstructure Formation

5.1.2.1 Microscope Setup

Despite the useful information that UV-vis-NIR spectroscopy can provide towards a better characterization of the initial stages of nucleation of gold nanocube-based superstructures, it is not possible to obtain quantitative information about the process once the nuclei reach certain dimensions. The reason is that the plasmonic properties of gold nanocubes are very sensitive to the formation of aggregates with a low number of particles like dimers, trimers, and so on.[156, 157] However, gold aggregates with a large number of particles possess similar optical properties. Therefore, it is much more complicated to distinguish between aggregates with 10 or 100 nanocubes from the analysis of their plasmon bands. To overcome this issue, the usage of light microscopy was implemented, which is more suitable for the characterization of superstructure nuclei formation once they reach a certain size. Furthermore, the light microscope gave direct information about the superstructure growth on a surface, while the UV-vis-NIR spectroscopy only provided information about the solution or dispersion in general.

As a reaction vessel for the experiments observed with the light microscope, a hydrophobized quartz cuvette was used which could be sealed with a polytetrafluoroethylene plug (Figure 31). The interaction of the gold nanocubes with the reaction vessel was minimized by using a hydrophobized cuvette, as earlier results demonstrated. Additionally, a solvent-air interface was avoided with this closed vessel, which prevented the coffee-ring effect and other evaporation-related issues experienced previously. The setup had a total volume of 4.2 ml and the contact area of the mica surface was 38.5 mm^2. Another aspect of the setup was the mica substrate, which was placed on top of the dispersion. This construction allowed observing exclusively structures formed on the surface, thereby distinguishing between heterogeneous and homogeneous nucleation and monitoring the growth of the gold nanoparticle-based superstructures on the mica surface. At the same time, UV-vis-NIR spectroscopy was used to monitor the solution or dispersion. The UV-vis-NIR spectra gave information about the self-assembly of gold nanocubes in dispersion and the concentration of gold nanocubes at any time during the experiment.

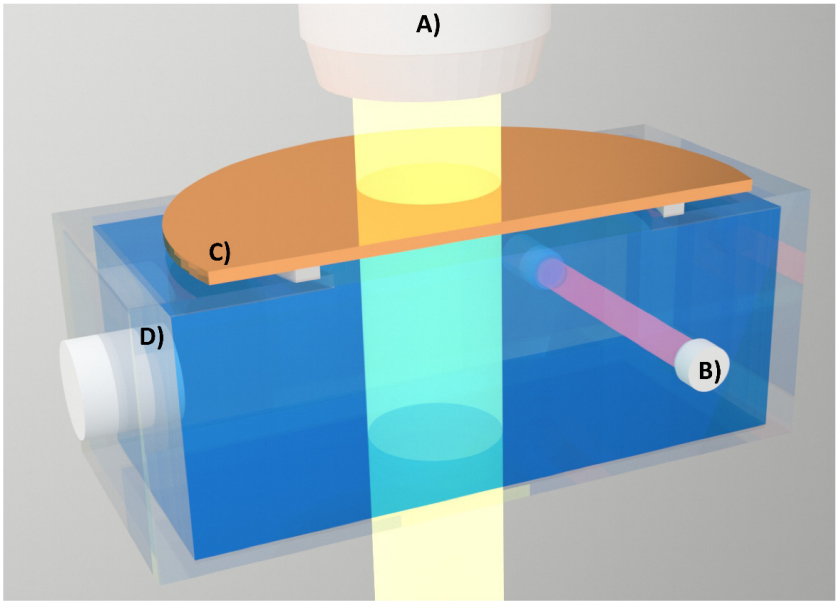

Figure 31. Setup of the nucleation experiments under the light microscope. A) With the light microscope, the growth of structures on the mica surface can be monitored in situ. B) Simultaneous analysis of the nanoparticle dispersion via UV-vis-NIR spectroscopy is possible. C) The functionalized mica substrate is glued with a hydrophobic seal spacer on top of the cuvette. Through a hole in the cuvette, the nanoparticle dispersion can get in contact with the functionalized mica surface. D) The quartz cuvette is functionalized with fluorine to prevent interaction of the gold nanocubes with the cuvette walls.

5.1.2.2 Measurement of Nucleation Rates

The setup was used to determine nucleation rates of the heterogeneous nucleation of gold nanocubes on mica. Figure 32 shows the growth of nanoparticle structures on a sulfonate-functionalized mica surface. The structures grew within a timeframe of 30 min. In order to determine the nucleation rates, the images were automatically analyzed with ImageJ, the present structures at each point in time were counted and the resulting counts were plotted against the experiment time (Figure A 41 A). The number of counted structures increased linearly with time, indicating steady-state nucleation. The slope of the linear fit for this curve gave the nucleation rate for the heterogeneous nucleation of gold nanocubes on sulfonate-functionalized mica. The ImageJ macro counted structures from a size of 0.91 µm, which corresponds to approximately 30 gold nanocubes in a row. This number reaches the range of critical crystal nuclei size or early growth species. For calcite, the number of ionic formula units in a row is calculated to 6000 ion pairs to reach a size of 0.91 µm in a rough estimate. The analysis demonstrated the advantage of nanoparticle model systems since it was able to detect the nuclei at much earlier stages of the nucleation.

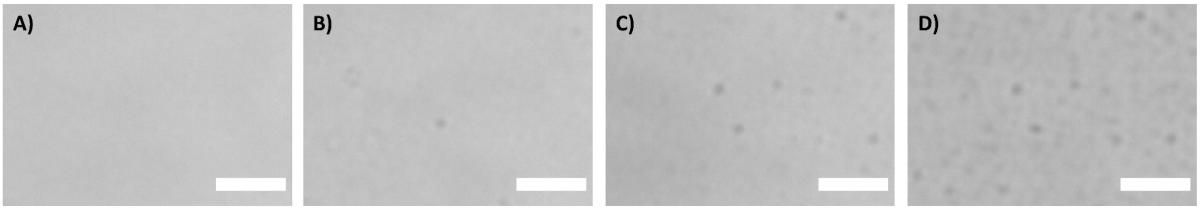

Figure 32. Gold nanoparticle-based superstructure growth. Original light microscope images of growing gold nanocube-based superstructure nuclei on a sulfonate-functionalized mica surface after A) 0, B) 11, C) 18, and D) 30 min. The scale bar is 10 µm.

To analyze the reproducibility, the experiment was repeated eight times for the nucleation of gold nanocubes on sulfonate-functionalized substrates. The combined plots (Figure A 41 B) and the summarized results (Table A 7) show the excellent reproducibility of the designed experimental approach. The nucleation not taking place of gold nanocubes on fluorine-functionalized substrates was measured five times as a reference (Table A 8). Figure 33 shows a combined plot of the number of structures against the time for both substrates. As expected, the fluorine-functionalized substrate did not promote the heterogeneous nucleation of gold nanoparticle-based superstructures and the resulting nucleation rate could be assumed as zero. For the sulfonate-functionalized substrate, a combined nucleation rate of $J_n = 2.04 \pm 1.18 \cdot 10^6$ [number/s·m²] was received, which is in the order of magnitude of nucleation rates determined for calcium carbonate on alkanethiol self-assembled monolayers by Nielsen *et al.*.[26]

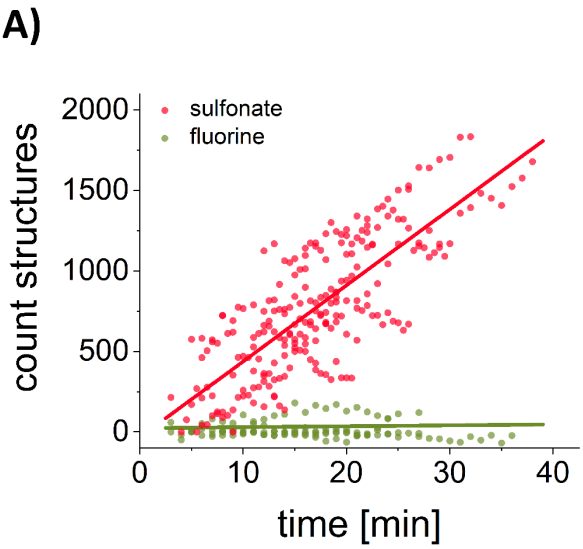

B)

functionalization	slope $[\frac{number}{min*image\ area}]$
sulfonate	47.2 ± 5.4
fluorine	-0.6 ± 0.6

Figure 33. Rate of heterogeneous nucleation determined via light microscopy. A) A plot of the time-dependent number of gold nanoparticle-based superstructures on the sulfonate- (red) and fluorine-functionalized (green) substrates. For the sulfonate-functionalized mica surfaces, eight experiments have been conducted under the same conditions. The red line shows the mean value of the fits for all eight experiments. The slope of this plot gives the averaged nucleation rate J_n for the heterogeneous nucleation of CTAB-functionalized gold nanocubes on sulfonate-functionalized mica surfaces. For the fluorine-functionalized mica surfaces, five experiments have been conducted under the same conditions. The green line shows the mean value of the fits for all five experiments. The slope of this plot gives the

averaged nucleation rate J_n for the heterogeneous nucleation of CTAB-functionalized gold nanocubes on fluorine-functionalized substrates. B) Determined mean slopes out of the plot (A) for the different substrate functionalities.

The simultaneous UV-vis-NIR spectroscopy measurements allowed analyzing the gold nanocube dispersion and gave information about the concentration and possible destabilization of the dispersion at any point in time of the experiment (Figure 34). In fact, the chosen ethanol concentration and the associated destabilization were so low that the gold nanocube dispersion stayed stable over the whole experiment time. Indicating, that the gold nanocube dispersion was in a destabilization regime there homogeneous nucleation in dispersion did not occur, while the favorable heterogeneous nucleation on the mica substrates took place.

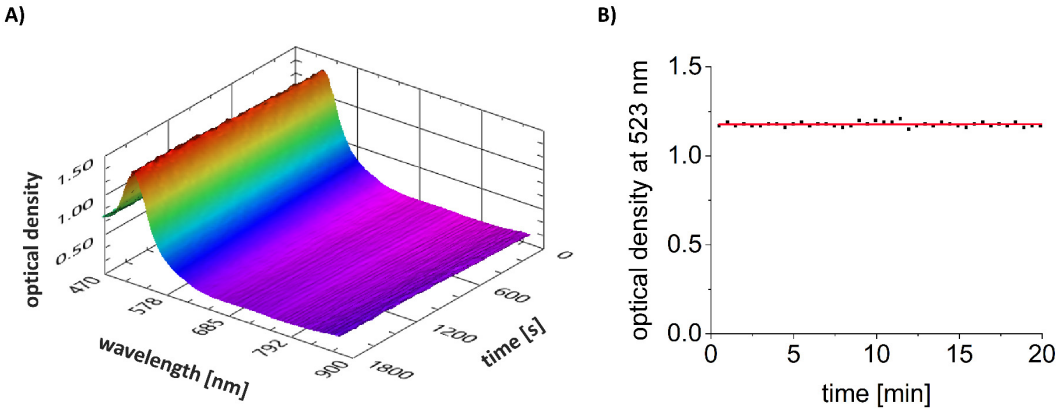

Figure 34. Simultaneous UV-vis-NIR measurement. A) UV-vis-NIR spectra measured simultaneously to the heterogeneous nucleation experiments with a sulfonate-functionalized substrate under the light microscope. The nanoparticle dispersions stays stable over the 40 min measurement time, indicating that no homogeneous nucleation in dispersion takes place. B) The intensity at 523 nm of the UV-vis-NIR measurements is plotted against the experiment time. The intensity and therewith the single gold nanocube concentration stays constant during the whole experiment.

In the approach outlined, the gold nanocube concentration stayed stable indicating that no homogeneous nucleation took place in the dispersion. This approach had the advantage that no homogeneous nucleation in dispersion interfered with the heterogeneous nucleation process. On the other side, it required a lot of experimental effort since for each nucleation rate and supersaturation one experiment had to be performed. Therefore, another experimental approach was tested choosing the destabilization that way that homogeneous nucleation in dispersion took place and thereby the gold nanoparticle concentration decreased over the experiment time. For this approach, PAA gold nanocubes in combination with amine-functionalized mica substrates were used. Here, a small destabilization regime had to be found, there homogeneous nucleation in dispersion took place, but the heterogeneous nucleation on the mica substrate was not too fast, to be observed with the light microscope setup. The absorption maxima at 523 nm decreased with ongoing experiment time, while absorption at higher wavelengths increased, indicating homogeneous nucleation of the PAA gold nanocubes in dispersion (Figure 35A). Therewith, the

supersaturation of the PAA gold nanocubes varied during the experiment. A plot of the counted structures (of PAA gold nanocubes on the mica substrate observed with light microscopy) showed that the number of structures did not grow linearly but could be fitted with a logistic function (Figure 35B). The change in the growth rate is caused by the changing supersaturation of PAA gold nanocubes during the experiment. This condition allowed determining a whole data set of nucleation rates with one single experiment. The slope of the fitted number of structures at each point in time was the nucleation rate of PAA gold nanocubes at the corresponding supersaturation. Further experiments demonstrated the good reproducibility of the results thus acquired (Figure A 42). Performing the determination of nucleation rates like this allowed receiving a whole data set of nucleation rates out of one single experiment, which was highly timesaving and gave way more data points for the evaluation. Additionally, it allowed the determination of nucleation rates at very low supersaturations. At such small supersaturations, nucleation could rarely be induced in fresh dispersions.

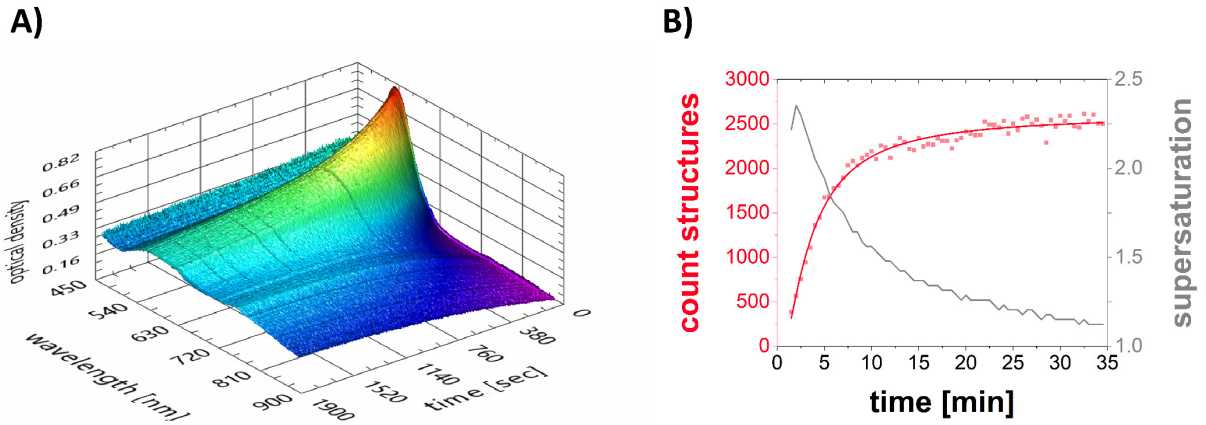

Figure 35. Determination of nucleation rates with varying gold nanocube concentration. Exemplarily the analysis of the combination of PAA gold nanocubes with amine-functionalized mica. A) Simultaneous UV-vis-NIR measurement during the heterogeneous nucleation process. The absorption maximum at 523 nm (single gold nanocubes) decreases over the experiment time and absorption at higher wavelengths increase, indicating homogeneous nucleation in dispersion simultaneously to the heterogeneous nucleation on the mica substrate observed with light microscopy. B) The supersaturation of PAA gold nanocubes (determined by UV-vis-NIR measurement) is plotted against the experiment time (grey). Thereby, the starting point of the UV-vis-NIR measurement is shifted to the point in time, where first structure growth was observed with the light microscope, to correct the offset until structures are big enough to be detected by light microscopy. Additionally, the counted structures on the mica substrate are plotted against the experiment time (red). With the decreasing concentration of PAA gold nanocubes in dispersion, the number of counted structures is not increasing linearly but can be fitted with a logistic function. The slope of this fit at each point in time is the nucleation rate for the corresponding gold nanocube supersaturation.

The used UV-vis-NIR spectroscopy represented the most suitable method for the analysis of the gold nanocube system. However, UV-vis-NIR spectroscopy is limited to the concentration measurement of light-absorbing samples and only in the concentration range where the Beer-Lambert law is valid. For a future universal application of the setup for different nanoparticle systems, one can imagine the implementation

of other optical techniques such as the very sensitive fluorescence spectroscopy (after introducing fluorescence tags to nanoparticles) or the more universal refractive-index measurement or turbidity detection.[248, 249]

Additionally to the experiments with the light microscope setup, the structure formation of gold nanocubes on sulfonate mica substrates was analyzed under the same conditions used for the determination of the nucleation rates. Figure 36 shows representative SEM images after a destabilization time of 5 to 20 min. After 5 min mainly single gold nanocubes could be observed, going further at 10 min small aggregates were dominant which increased to bigger superstructures of around 1-2 µm after 20 min destabilization time. The SEM images matched with the results of the light microscope observations, where the first structures were detected at around 10 min destabilization time.

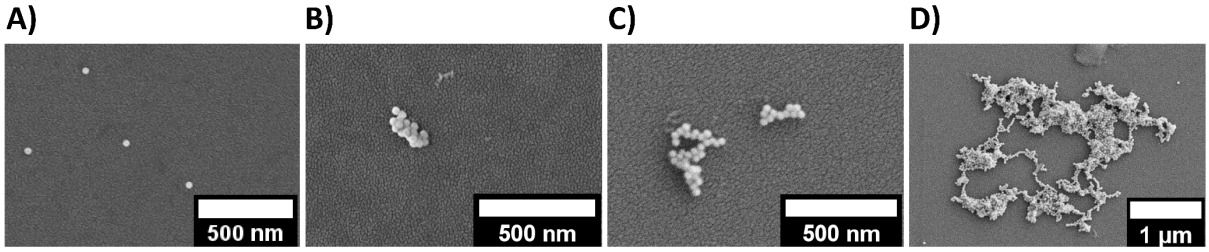

Figure 36. Structure growth under the conditions used for the analysis of heterogeneous nucleation. Exemplarily a dispersion of CTAB-functionalized gold nanocubes was destabilized with ethanol in presence of sulfonate-functionalized mica substrates. The emerging superstructures were stabilized again after A) 5 min, B) 10 min, C) 15 min, and D) 20 min and imaged by SEM. After 5 min, mainly single gold nanocubes are present on the surface and with increasing experiment time superstructures grow.

In summary, it was successful to observe heterogeneous nucleation of gold nanocubes and to determine the nucleation rate by using the microscope setup. The combination with the simultaneous UV-vis-NIR measurement was a suitable and easily accessible system to analyze heterogeneous nucleation processes in situ directly in dispersion and on a relevant statistical basis. Thereby, two approaches with a constant supersaturation and a decreasing supersaturation, which highly decreased the experimental effort, could be established. The nucleation rates thus obtained allowed the determination of important thermodynamic and kinetic information, such as the interfacial energy α and the nucleation barrier Δg_n what will be shown in the following.

5.1.2.3 Determination of the Interfacial Energy and the Nucleation Barrier

In the previous chapter, the combination of light microscopy and UV-vis-NIR spectroscopy allowed the determination of heterogeneous nucleation rates. These nucleation rates now enabled access to the calculation of further thermodynamic and kinetic parameters, as shown for the heterogeneous nucleation of calcium carbonate by Nielsen *et al.*[26] and Duffy *et al.*[250]. The calculated thermodynamic and kinetic parameters helped to analyze the heterogeneous nucleation process more detailed. Thereby, it was possible

to analyze the influence of the surface chemistry (Chapter 6) or the shape of the nanoparticles (Chapter 7) on the heterogeneous nucleation process. This chapter will first explain exemplarily the procedure to calculate thermodynamic and kinetic parameters out of the nucleation rate. While the further chapters will include a discussion of the so obtained values.

If the definition of the nucleation barrier Δg_n (equation 4, Chapter 1) is combined with the definition of the nucleation rate J_n (equation 5, Chapter 1) equation 8 results.

$$ln(J_n) = -\frac{fV_m^2}{(k_BT)^3}\alpha^3\left(\frac{1}{\sigma^2}\right) + ln\left(A * e^{-\frac{E_A}{k_BT}}\right) \tag{8}$$

Having a closer look at equation (8), one can see that it is possible to plot the logarithm of the nucleation rate $ln(J_n)$ against the inverse square of the supersaturation $1/\sigma^2$ which should result in a straight line. Now the slope of the straight line is the equation part preceding $1/\sigma^2$. By determining the slope out of the graph, it was thus possible to calculate the effective interfacial energy α. While the second part of the sum in equation 8 constitutes the y-intercept. To get access to these calculations, the nucleation rates J_n for the heterogeneous nucleation of CTAB gold nanocubes on sulfonate-functionalized mica were determined at different supersaturations (Figure A 43, Table A 9). Thereby, the nucleation rates increased with increasing gold nanocube concentration. The upper limit for the measurements became apparent at a concentration of $5.21 \cdot 10^{-7}$ mol/l (2.3 optical density at 523 nm) since the nucleation process above this concentration started too fast to be observed with the light microscope in time and the absorption of the gold nanocube dispersion got too strong impacting the image quality. Going to smaller concentrations the lower limit appeared at $1.50 \cdot 10^{-7}$ mol/l (0.7 optical density at 523 nm), since in experiments with lower concentrations heterogeneous nucleation was observed only in very few cases and with negligible small nucleation rates. In general, the nucleation processes at higher concentrations started earlier and proceeded faster.

Before calculating the effective interfacial energy α and the nucleation barrier Δg_n, the logarithm of the nucleation rates J_n had to be plotted against the inverse square of the supersaturations σ like described in equation 8 (Figure 37). At this point, care had to be taken to give the supersaturations as concentration of gold nanocubes and not as concentration of gold atoms since the building blocks in our nucleation system were the gold nanocubes (Chapter 5.3.5).

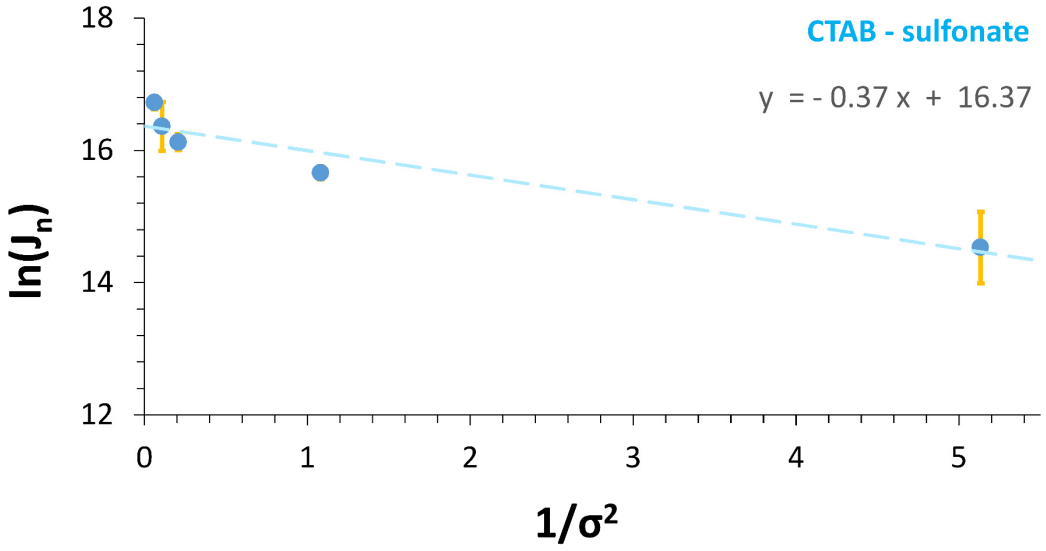

Figure 37. Plot of nucleation rates against supersaturations. The experimental data for the combination of CTAB gold nanocubes and sulfonate-functionalized mica for different supersaturations. The natural logarithm of the nucleation rates is plotted against the inverse square of the supersaturation according to equation 8 and a straight fit is performed for the data.

The plot of the nucleation rates (Figure 37) resulted in an excellent linear relationship and was fitted with a straight line. From equation 8, the slope s of the straight line enabled to calculate the effective interfacial energy α over equation 9.

$$s = -\frac{f V_m^2}{(k_B T)^3}\alpha^3 \tag{9}$$

To be able to calculate the interfacial energy α, the parameters V_m and f had to be defined. The Boltzmann constant k_B and the temperature T were known. V_m is the volume per molecule of the solid phase. For the gold nanocube system, V_m = 1.22·10^{-23} m^3 as the volume of one gold nanocube with an edge length of 23 nm was used. f is a numerical factor depending on the geometry of the nucleus. Generally, a spherical nucleus is assumed but for the analysis of heterogeneous nucleation, a spherical nucleus attached to a substrate was considered (Figure A 44). The geometry of this spherical nucleus on a substrate was defined by its contact angle Θ and in dependence, the form factor f was calculated according to equation 10.

$$f = \frac{1}{4}\left(2 - 3\cos(\Theta) + cos^3(\Theta)\right)\frac{16}{3}\,\Pi \tag{10}$$

To give a possible range for the interfacial energies, these energies were calculated for contact angles of 60°, 90°, and 120° and amount to 5.23 – 9.12·10^{-6} J/m^2 (Table A 10). Knowing the effective interfacial energy, it was possible to calculate the nucleation barriers Δg_n according to equation 4 (Chapter 1). Figure 38 shows

the resulting nucleation barriers dependent on the supersaturation. For the analyzed supersaturations, the nucleation barrier amounted to 0.18 – 2.17 k_BT. For higher nucleation barriers, heterogeneous nucleation was observed only in very few cases and with negligible nucleation rates.

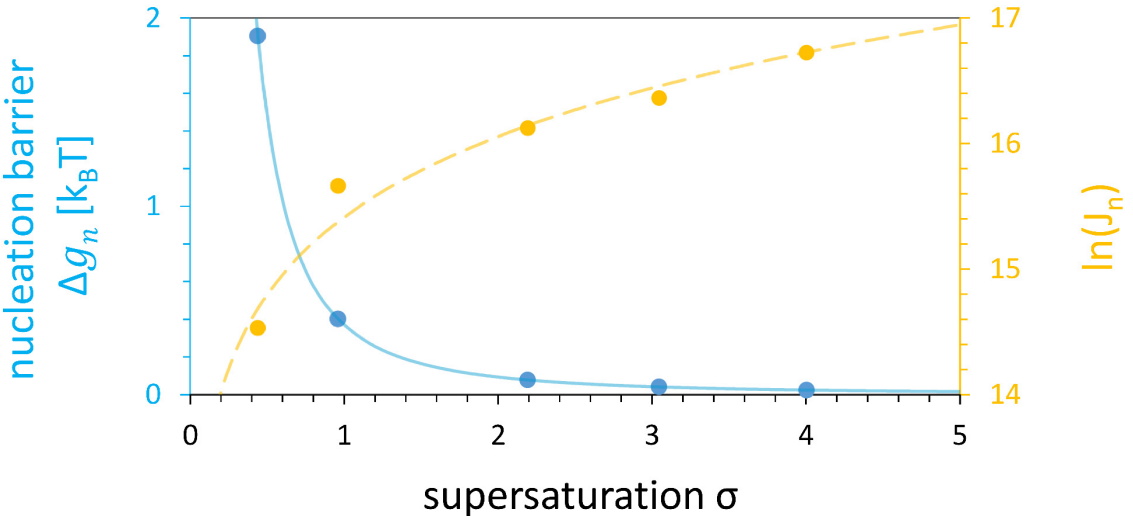

Figure 38. Nucleation barrier dependent on supersaturation. Plotted in blue is the nucleation barrier for the combination of CTAB gold nanocubes with sulfonate-functionalized substrates dependent on the supersaturation of gold nanocubes. Plotted in yellow is the logarithm of nucleation rates determined experimentally for the different supersaturations.

Next to the effective interfacial energy and the nucleation barrier, which could be calculated from the slope of the plot (Figure 37), it was possible to receive the kinetic term from the y-intercept, which amounted to 16.73 (Table 3). This kinetic term includes the effective activation barrier E_A, which describes the kinetic barriers to the nucleation reaction for example the attachment of the forming nucleus and structural rearrangements.[26] Further analysis of this term and the calculation of the effective activation barrier E_A were not possible with the available data, since the parameter A is unknown. This parameter is a „complicated function of the molecular-level parameters. Its exact type strongly depends on features of the accepted model, which are difficult to verify experimentally"[47]. The parameter A could be determined by temperature-dependent measurements under the same conditions, but this was far beyond the scope of this thesis. But for comparison and characterization of the heterogeneous nucleation experiments in the following chapters, comparing the order of magnitude of the kinetic term with the thermodynamic term was useful. For the combination of CTAB gold nanocubes on sulfonate-functionalized mica the thermodynamic term amounted to 0.18 – 2.17 for the analyzed concentration regime (Table 3).

Table 3. Thermodynamic and kinetic term for the combination of CTAB gold nanocubes with sulfonate-functionalized mica.

thermodynamic term $fV_m^2(k_BT)^{-3} * \alpha^3 * \sigma^{-2}$	kinetic term $ln(A * \exp(-E_A/k_BT))$
0.18 – 2.17	16.73

Concluding, it was achieved to establish a suitable and easily accessible system to analyze heterogeneous nucleation processes in situ directly in dispersion and on a relevant statistical basis, by combining light microscopy with simultaneous UV-vis-NIR spectroscopy measurements. Therefore, the controlled destabilization of the nanoparticle systems was examined by increasing the nanoparticle concentration with continuous evaporation of the solvent, by varying the supersaturation with reduction of the temperature, or by altering the solubility of the nanoparticles in the solvent. With altering solubility as a trigger, a suitable and controlled destabilization of gold nanocubes by the addition of ethanol was established. Thereby, it was possible to analyze successfully the homogeneous nucleation of CTAB stabilized gold nanocubes in dispersion, the acceleration of the process by the presence of a favorable surface (sulfonate-functionalized substrates), and the heterogeneous nucleation of the gold nanocubes on these surfaces resulting in nanoparticle-based superstructures. Time-resolved light microscopy and UV-vis-NIR spectroscopy allowed for the determination of nucleation rates as well as the nanoparticle concentration in solution at each time. The UV-vis-NIR spectra allowed for a quantitative evaluation of the nucleation process by showing the time-dependent aggregation of the nanocubes via spectral shifts of the nanocube plasmonic band to longer wavelengths. This approach opened the possibility to calculate the effective interfacial energy and the nucleation barrier and to characterize the heterogeneous nucleation process more precisely. Therewith, this method provided the possibility to analyze and characterize the heterogeneous nucleation of nanoparticles on substrates. This approach could be used in the next steps to analyze the influence of surface chemistry and particle shape on heterogeneous nucleation by allowing a comparison of the variations in the nucleation systems.

5.2 Appendix

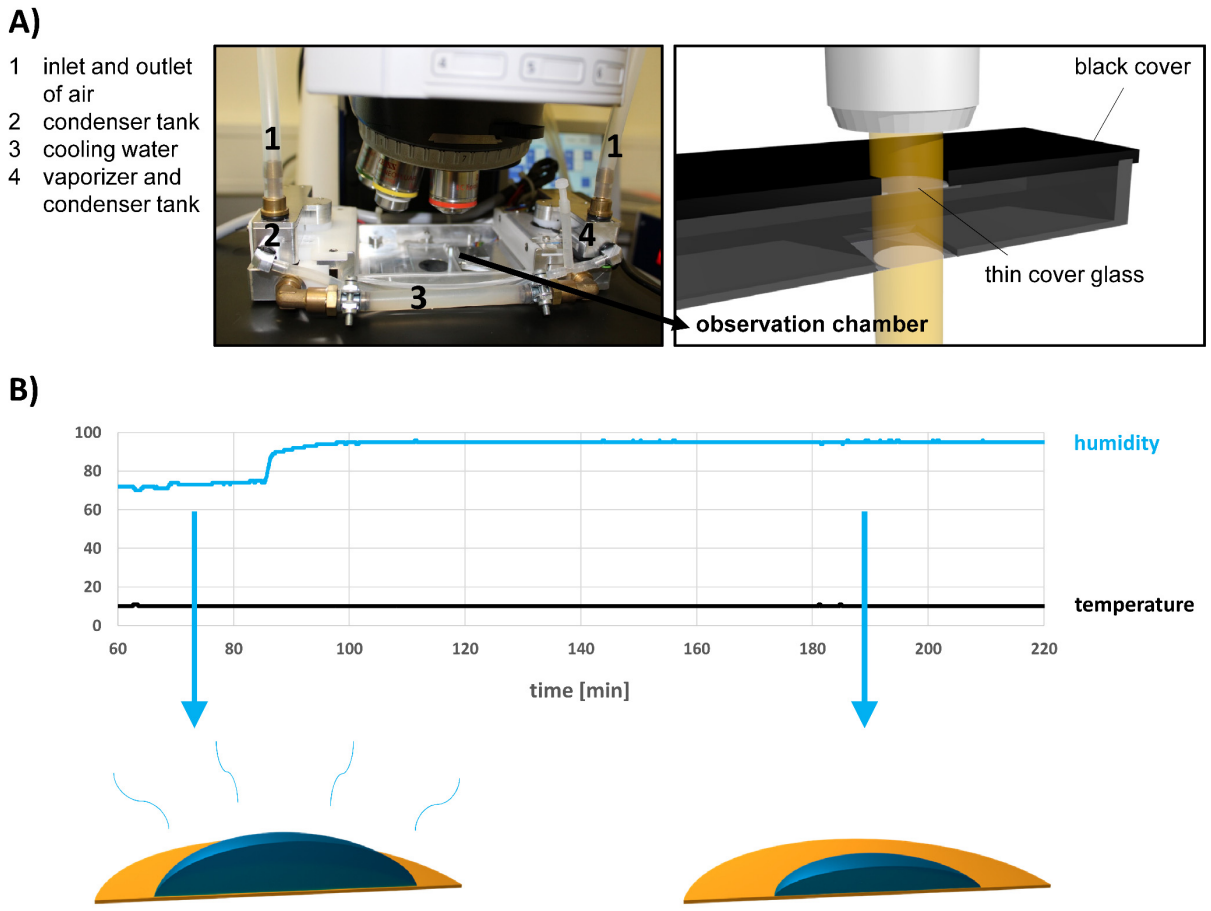

Figure A 36. Climate chamber. A) The setup of the climate chamber to control the temperature and humidity (left) and its optic improvements (right). B) Possible control over the particle concentration by adjusting the humidity during nucleation experiments. Low humidity allows the fast evaporation of the water drop at the beginning of the experiment and thereby increases the nanoparticle concentration. Afterward the humidity is raised and the evaporation of the water drop is decelerated. At these steady-like conditions, the nucleation of nanoparticle-based superstructures can be analyzed.

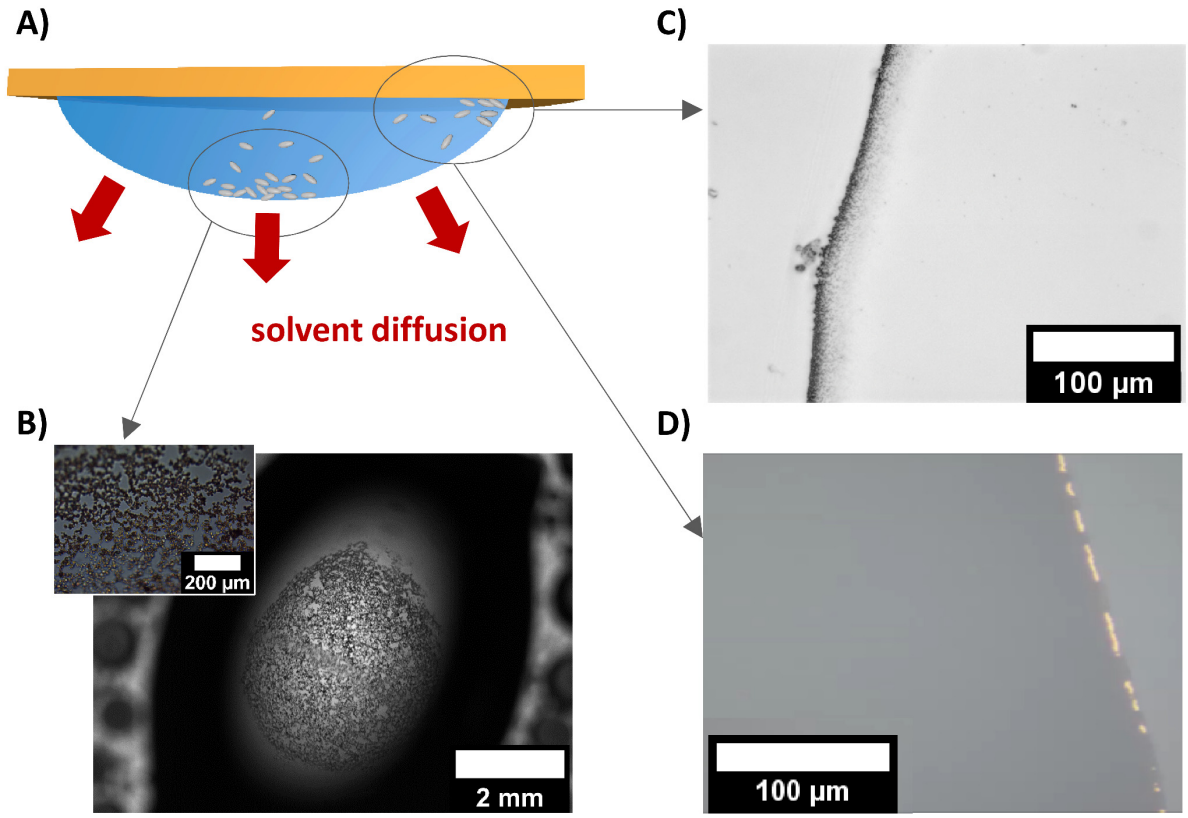

Figure A 37. Nucleation at solvent-air interface. A) The scheme shows the setup of a hanging drop. The evaporation of solvent leads to a diffusion of solvent and nanoparticles to the solvent-air interface. The nanoparticle concentration maxima at the solvent-air interface induces nucleation. B) A TEM image of the lower part of a hanging drop. Hydroxyl-functionalized zinc oxide nanorods nucleate at the solvent-air interface. The inset shows a zoom on the nucleated structures. C) TEM image of the border of a hanging drop. Hydroxyl-functionalized zinc oxide nanorods nucleate at the solvent-air interface and are deposited as a coffee ring on the substrate. D) Reflection polarization light microscope image of the border of a hanging drop. CTAB-functionalized gold nanocubes nucleate at the solvent-air interface and are deposited as a coffee ring on the substrate.

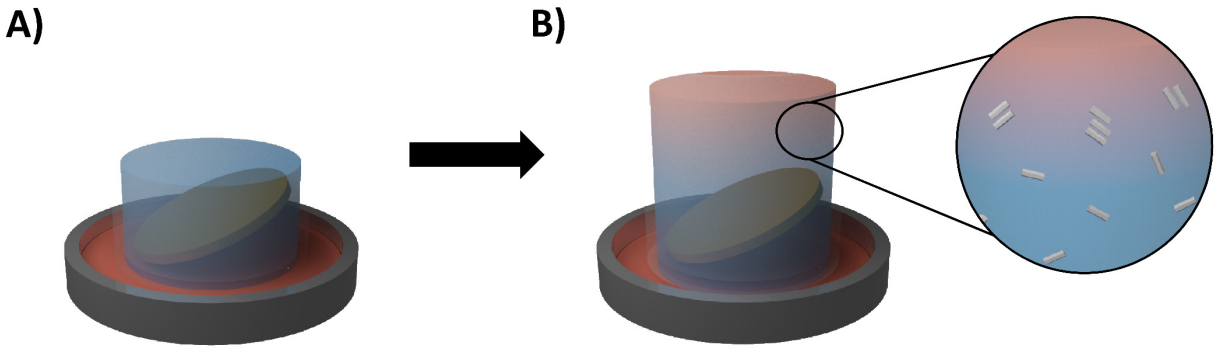

Figure A 38. Gas-phase diffusion approach. A) A mica substrate is placed in a vessel and an aqueous nanoparticle dispersion (blue) is given into the vessel. Outside ethanol (red) is given into a reservoir and the whole system is closed (which is not shown in the sketch). B) Over time, more and more ethanol diffuses into the water forming a solvent gradient. As the nanoparticles are destabilized by ethanol, they start to

aggregate at the solvent-solvent interface resulting in bigger aggregates sedimenting down on the mica surface.

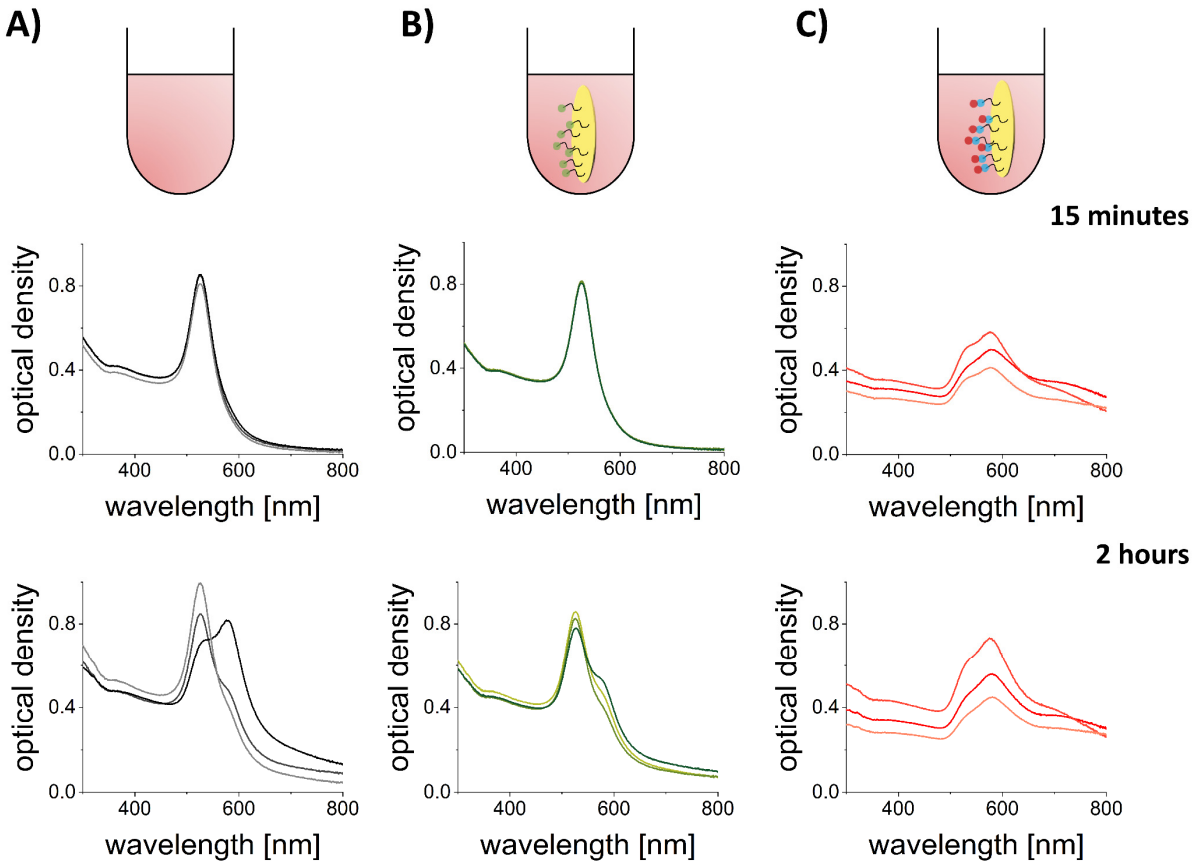

Figure A 39. Influence of a present substrate on the nucleation of gold nanocubes. A gold nanocube dispersion was destabilized with ethanol in a micro test tube without and with the presence of different functionalized mica substrates. Aliquots at different points in time are analyzed by UV-vis-NIR spectroscopy to compare the destabilization of the nanoparticle dispersion. A) Shows the destabilization of the gold nanoparticle dispersion without the presence of an additional substrate after 15 min (upper row) and after 2 h (bottom row). The gold nanocubes start to aggregate slowly, which is indicated by the arising peaks at higher wavelengths. B) shows the destabilization with the presence of a fluorine-functionalized substrate after 15 min (upper row) and after 2 h (bottom row). The dispersion behaves comparably to the dispersion without an additional substrate. This finding indicates that the gold nanocubes are not interacting with the fluorine-functionalized substrate. C) shows the destabilization with the presence of a sulfonate-functionalized substrate after 15 min (upper row) and after 2 h (lower row). The gold nanocubes destabilize much faster in the presence of the sulfonate-functionalized substrate. This observation indicates a favorable interaction of the gold nanocubes with the sulfonate-functionalized substrate.

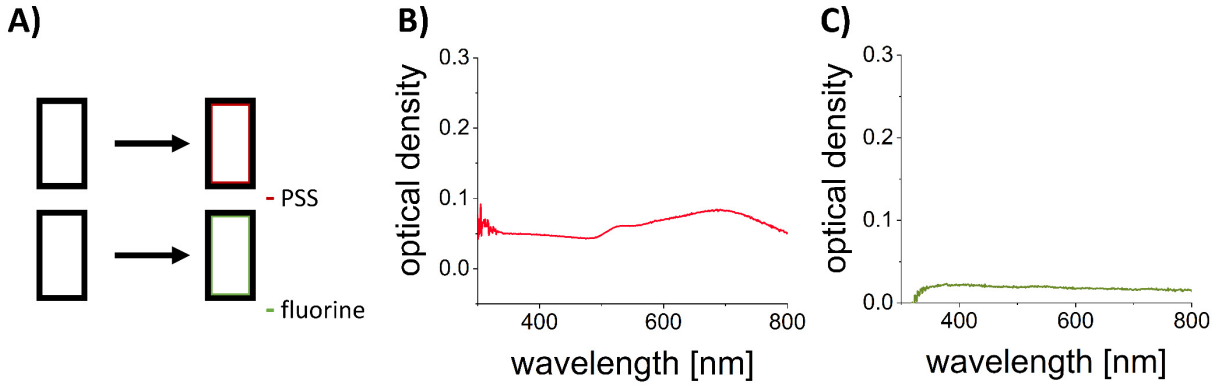

Figure A 40. Characterization of heterogeneous nucleation of gold nanocube-based superstructures with different functionalized quartz cuvettes. A) A schematic representation of the functionalization of quartz cuvettes used to investigate the heterogeneous nucleation of nanocube-based superstructures in dispersion by UV-Vis-NIR spectroscopy. B) The UV-vis-NIR spectrum of the gold nanoparticle-based superstructures formed on the sulfonate-functionalized surface. C) The UV-vis-NIR spectrum for the fluorine-functionalized surface, where no gold nanoparticle-based superstructures formed.

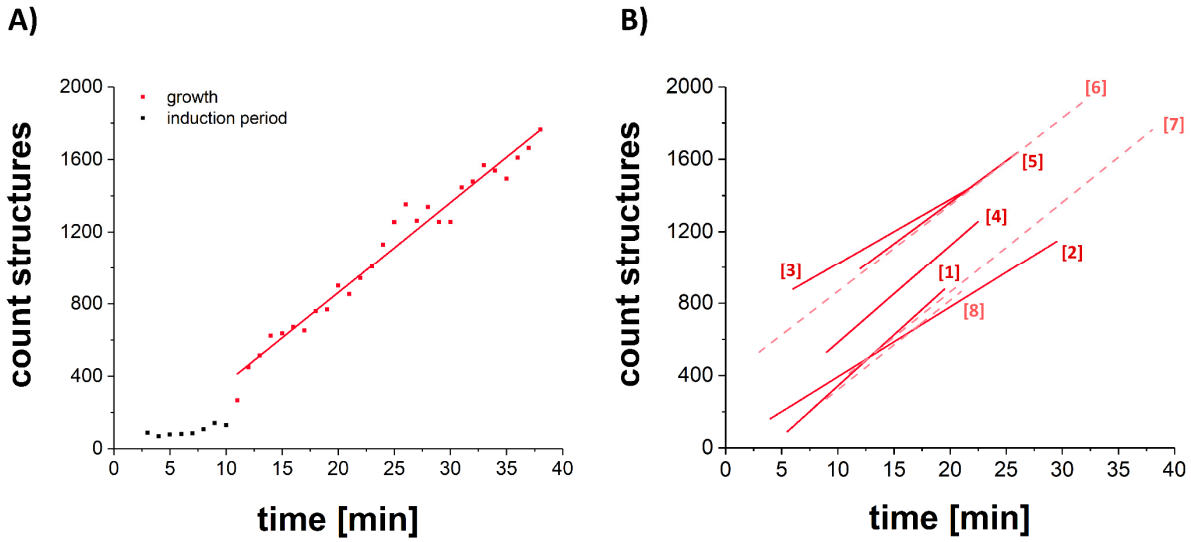

Figure A 41. Determination of nucleation rates. Plots of the counted structures obtained from the ImageJ analysis against the experiment time for the nucleation of CTAB gold nanocubes on a sulfonate-functionalized mica substrate. A) It is possible to detect the first nuclei growth after 10 min of induction time. After around 40 min no more nuclei appear. For further analysis, only the growth period in the plot is used. The slope of the growth period corresponds to the nucleation rate J_n. B) The experiment was repeated three times with the same gold nanocube dispersion (light red dashed lines) and five times under the same conditions but with different batches of gold nanocubes (red lines) to test the reproducibility of the experiment.

Table A 7. Determined nucleation rates for the nucleation of CTAB gold nanocubes on a sulfonate-functionalized mica surface. The experiment numbers correspond to the shown plots in Figure A 41 B.

experiment sulfonate	**R^2 of the fitted straight line**	**J_n** $[\frac{number}{min * image\ area}]$	**ln (J_n)** $[\frac{number}{s * m^2}]$
1	0.95	56.30 ± 2.58	16.30
2	0.77	38.59 ± 3.21	15.92
3	0.79	35.68 ± 3.53	15.84
4	0.82	53.87 ± 4.91	16.25
5	0.77	45.96 ± 4.78	16.09
6	0.95	48.08 ± 2.22	16.14
7	0.97	49.98 ± 1.74	16.18
8	0.75	49.31 ± 8.49	16.16
mean	**0.85**	**47.22 ± 5.36**	**16.12**

Table A 8. Determined nucleation rates for the nucleation of CTAB gold nanocubes on a fluorine-functionalized mica surface.

experiment fluorine	**R^2 of the fitted straight line**	**Jn** $[\frac{number}{min * image\ area}]$	**ln (Jn)** $[\frac{number}{s * m^2}]$
1	0.31	-1.38 ± 0.36	-
2	0.06	-1.17 ± 1.04	-

3	0.01	0.31 ± 0.66	-
4	0.00	-0.02 ± 0.15	-
5	0.13	-0.59 ± 0.34	-
mean	**0.10**	**-0.57 ± 0.57**	**-**

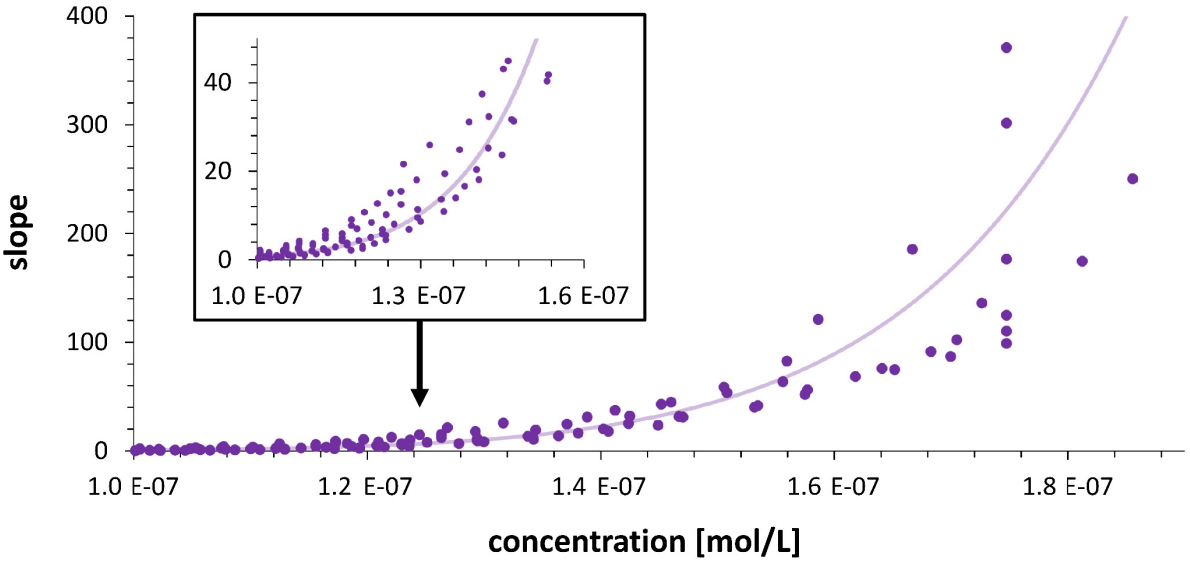

Figure A 42. Determined slopes for calculation of nucleation rates with varying supersaturation. The graph shows determined slopes of the plot of the number of counted structures against the experiment time dependent on the concentration of PAA gold nanocubes for the combination with amine-functionalized mica substrates. The results of several experiments under the same conditions are combined.

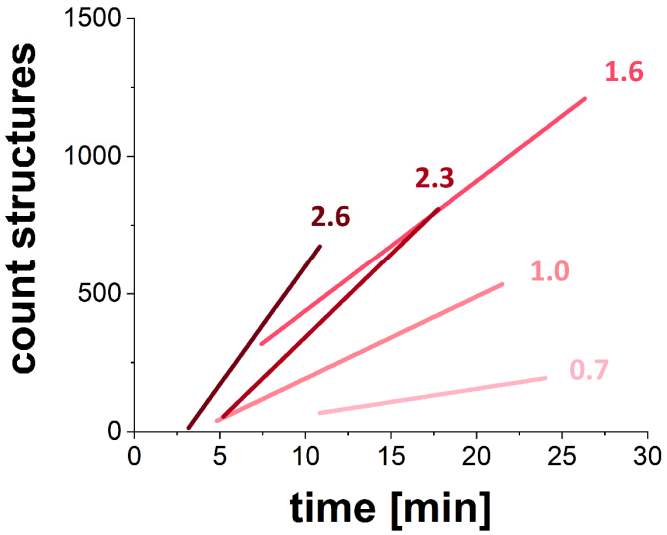

Figure A 43. Determination of nucleation rates at different supersaturations. Shown are the plots of the determined mean nucleation rates (counted structures against experiment time) for each supersaturation of the combination of CTAB gold nanocubes on sulfonate-functionalized mica. The number at each plot gives the maximum absorption at 523 nm (absorption peak of single gold nanocubes). The mean start and duration of the observation of structure formation have been incorporated in the straight fits.

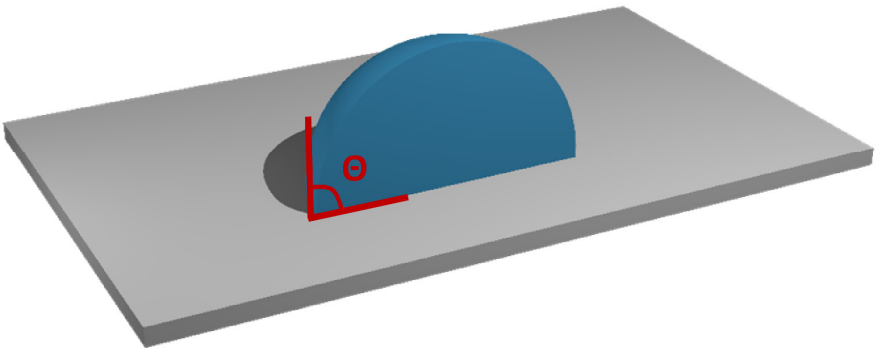

Figure A 44. Assumed spherical nucleus on a substrate. For the analysis of heterogeneous nucleation processes, a spherical nucleus on a substrate was assumed. The geometry of the nucleus can be defined by its contact angle Θ.

Table A 9. Determined nucleation rates. Summarized results for the determined nucleation rates dependent on the gold nanocube supersaturation. The corresponding mean R^2 value for the straight fit to the curve of counted structures (used to determine the nucleation rates) and the optical density at 523 nm are given as well.

combination	optical density at 523 nm	supersaturation gold nanocubes	R^2	J_n [germs/s·m²]
CTAB - sulfonate	0.7	0.44	0.81	$2.04 \cdot 10^6 \pm 1.18 \cdot 10^6$
	1.0	0.96	0.95	$6.03 \cdot 10^6 \pm 0.62 \cdot 10^6$
	1.6	2.19	0.85	$1.00 \cdot 10^7 \pm 0.01 \cdot 10^6$
	2.0	3.05	0.99	$1.28 \cdot 10^7 \pm 0.45 \cdot 10^7$
	2.3	4.00	0.99	$1.83 \cdot 10^7 \pm 0.18 \cdot 10^7$

Table A 10. Calculation of the form factors f and the resulting effective interfacial energy α for different contact angles.

contact angle Θ [°]	form factor f	effective interfacial energy α [J/m²]
60	2.62	$3.99 \cdot 10^{-6}$
90	8.38	$2.71 \cdot 10^{-6}$
120	14.14	$2.27 \cdot 10^{-6}$

5.3 Materials and Methods

5.3.1 Instruments

Light microscopy images were recorded with an *AxioImager* from *Zeiss* with an LD Epiplan 50x/0.50 HD DIC objective using transmitted light, bright field illumination, a condenser numerical aperture at 0.9, an Axiocam 506 bw as an imaging device, and an exposure time of 10 ms.

SEM images were recorded with a *Gemini500* by *Zeiss* operating at 3 kV equipped with an Inlens and a secondary electron detector for secondary and backscattered electrons. Samples were coated with a 2.5 nm platinum layer, mounted on aluminum stubs, and attached by carbon conductive layers.

TEM images were recorded on a *Zeiss Libra 120* microscope at an accelerating voltage of 120 kV. The samples were applied on *Quantifoil* carbon-coated Cu 400 mesh grids.

UV-vis-NIR measurements were performed with a *Varian Cary 50* spectrometer in quartz cuvettes. The UV-vis-NIR measurements carried out simultaneously with light microscopy measurements were performed with a modular *USB2000+* spectrometer from *Ocean Optics* equipped with a *USB-DT* miniature deuterium tungsten halogen lamp.

5.3.2 Materials

In all experiments, Milli-Q water (resistivity 18.2 MΩcm at 25 °C) was used. Hexadecyltrimethylammonium bromide (CTAB ≥ 99%) was purchased from *Sigma-Aldrich*. Ethanol was purchased from *VWR*.

5.3.3 Nucleation Experiments

5.3.3.1 Preparation of Gold Nanoparticle Dispersions

For destabilization experiments, a stock dispersion of the gold nanocubes from Chapter 4 was prepared. One batch of 50 ml aqueous nanoparticle dispersion, with a concentration of 0.17 mM gold nanocubes, was centrifuged at 6000 rpm for 1 h. The supernatant was removed and the concentrated gold nanocubes in the sediment were transferred to a micro test tube. The concentrated gold nanocubes were washed with a 2.00 mM CTAB aqueous solution, centrifuged at 6000 rpm for 20 min, and the supernatant was removed. The washing procedure was repeated two times. The volume of the concentrated nanoparticle sediment was determined to know the current concentration of the gold nanocubes. A solution of 0.02 mM CTAB in water was prepared. The concentrated gold nanocubes were added to the CTAB solution to reach a concentration of 0.5 mM of gold nanocubes. Before using the stock dispersion of gold nanocubes in experiments, the stability of the gold nanocubes was checked with UV-vis-NIR spectroscopy.

5.3.3.2 Destabilization of Nanoparticle Dispersions

To destabilize the stock dispersion of gold nanocubes ethanol was added to an amount of 12 to 38 vol.-%. The conditions during the different destabilization experiments are summarized in Table 4.

Table 4. Summary of the nucleation experiments with gold nanocubes and the experimental conditions.

experiment	reaction vessel	surface	surface functionali-zation	ethanol content [vol.-%]	surface/ volume ratio [1/cm]
homogeneous nucleation	cuvette	-	-	38	-
introducing mica substrate	micro test tube	mica	sulfonate	31	0.39
			fluorine	31	0.39
		-	-	31	-
kinetics	cuvette	cuvette	sulfonate	15	2.45
	cuvette	cuvette	fluorine	15	2.45
light microscopy	hydropho-bized cuvette	mica	sulfonate	12	0.09
		mica	fluorine	12	0.09

5.3.3.3 Quenching the Destabilized Nanoparticle Dispersions

During or after the destabilization experiments, the formed aggregates and remaining single particles were stabilized again. This approach allowed freezing and analyzing aliquots at their actual destabilization stage. Therefore, a CTAB solution was added to adjust the amount of CTAB to 2.00 mM. To analyze the structures formed on mica surfaces, the mica platelets were washed thoroughly with water and dried with a nitrogen stream at RT.

5.3.4 Image Analysis

During the experiments, light microscope images were taken every 60 respectively 30 s and processed with ImageJ. After separating the timespan with nuclei growth, a *trainable weka segmentation* was applied, differentiating between nuclei on the surface, background, and moving aggregates in dispersion. The classifier results were displayed either as probabilities and the canal for the nuclei was used to count their number or the classifier results were given out as results and the number of nuclei species was counted. Therefore, a threshold (*MaxEntropy*) was applied and the number of nuclei was counted by using the *analyze particles* function (size = 10 – infinity pixel). The number of counted species of the first image (only background, structure growth did not start yet) was subtracted from all following results.

5.3.5 Calculation of Gold Nanocube Supersaturation

For the determination of the gold nanocube concentrations, the optical density at 400 nm from UV-vis-NIR spectra was used. After Hendel *et al.*, an extinction coefficient of 2.685 l/mol·cm could be assumed for the 23 nm gold nanocubes.[251] With the Beer-Lambert law (equation 11) the Au(0) concentration c could be calculated since the extinction E_λ is known from the UV-vis-NIR measurements and the depth of the used cuvette d.[252]

$$E_\lambda = \varepsilon_\lambda \cdot c \cdot d \tag{11}$$

However, in the system, the concentration of monomers is not the concentration of gold atoms but gold nanocubes. Therefore, the gold nanocube concentration had to be estimated from the Au(0) concentration. It was known that one gold nanocube had an edge length of 23 nm. With this edge length, the volume of one gold nanocube was calculated resulting in 12176 nm^3. Gold only forms a face-centered cubic package with a lattice parameter of 0.4078 nm resulting in the volume of the unit cell of 0.07 nm^3.[253] Therewith, the number of gold unit cells fitting into one gold nanocube was 179408. One gold unit cell contains 4 atoms[254] of gold which gave the amount of 717632 gold atoms in one gold nanocube. With this quantity, the Au(0) concentration could be converted into a gold nanocube concentration.

To calculate the supersaturation σ, the concentration of gold nanocubes in a saturated dispersion x^* was determined separately for each particle surface system. Therefore, the Au(0) concentration after the destabilization of the nanocubes (when a steady state was reached) was measured with UV-vis-NIR spectroscopy and the corresponding gold nanocube concentration was calculated. The resulting supersaturation for each destabilization experiment at a gold nanocube concentration x was calculated with equation 12.

$$\sigma = \frac{x}{x^*} \tag{12}$$

6 Influence of Surface Chemistry on Heterogeneous Nucleation

So far, the presented work laid the foundation to analyze heterogeneous nucleation with the model system of anisotropic nanoparticles. In Chapter 1, suitable substrates for heterogeneous nucleation with varying surface chemistry were prepared and in Chapter 4, three different anisotropic nanoparticle systems were provided, differing either in their surface chemistry or in their aspect ratio. Furthermore, in Chapter 5 different methods for the analysis of the heterogeneous nucleation of the anisotropic nanoparticles on the substrates were tested and a light microscope setup with simultaneous UV-vis-NIR spectroscopy was developed. Beyond, the evaluation of the so received kinetic data could be established. Based on this, the following chapter will analyze the impact of surface chemistry on heterogeneous nucleation. Therefore, the zinc oxide nanorods and gold nanocubes varying in their surface chemistry are combined with the differently functionalized substrates. The influence of these combinations on the heterogeneous nucleation and the resulting superstructures are analyzed using the methods introduced in Chapter 5.

6.1 Results and Discussion

6.1.1 Formation of Zinc Oxide Nanorod-based Superstructures in dependence of Surface Chemistry

In Chapter 4 among gold nanoparticle systems, zinc oxide nanorods were functionalized with amine, hydroxyl, and carboxyl groups to be able to analyze the influence of their surface chemistry on the heterogeneous nucleation into larger superstructures. Following this, Chapter 5 aimed for an approach on how to perform and analyze heterogeneous nucleation of the nanoparticle systems. Here, a controlled destabilization of the gold nanoparticle systems was established successfully by altering the solvent properties and thereby avoiding any solvent-air or solvent-solvent interfaces, which simplified the reproducible analysis of the heterogeneous nucleation. For the zinc oxide nanorods, a similarly controlled destabilization could not be established. Hence, the subsequent analysis of heterogeneous nucleation in Chapter 6 and Chapter 7 focused on the gold nanoparticle systems. Nevertheless, first results on the influence of the surface chemistry on heterogeneous nucleation could also be obtained for the zinc oxide nanorods.

Functionalized mica substrates were placed at an angle of 45° in a vessel containing amine zinc oxide nanorod dispersions (Figure A 45). The solvent was evaporated and thus, the concentration of zinc oxide nanorods increased and zinc oxide nanorod-based superstructures formed on the mica substrates. Thereby, the structure of the zinc oxide nanorod-based superstructures differed depending on the functionalization of the mica substrates (Figure 39, Table A 11). The amine-functionalized zinc oxide nanorods seemed to

have a favorable interaction with the carboxyl functionalized mica substrates and formed widely disturbed layers with a large contact area to the substrate. This finding can be explained by the coulomb interaction between the positively charged amine group on the nanoparticles and the negatively charged carboxyl group on the substrate. Accordingly, the amine zinc oxide nanorods appear to have an unfavorable interaction with the also positively charged amine substrate. Here, the nanorods formed larger superstructures with less contact area to the substrate. Similar results were obtained for the hydrophobic fluorine functionalized mica substrate. The hydrophilic amine zinc oxide nanorods seemed to avoid the interaction with the substrate and formed even larger superstructures compared to the amine-functionalized substrate. As a result, this simple experiment showed that depending on the interaction of the nanoparticle surface with the substrate surface structures could be varied from layer-like to three-dimensional superstructures.

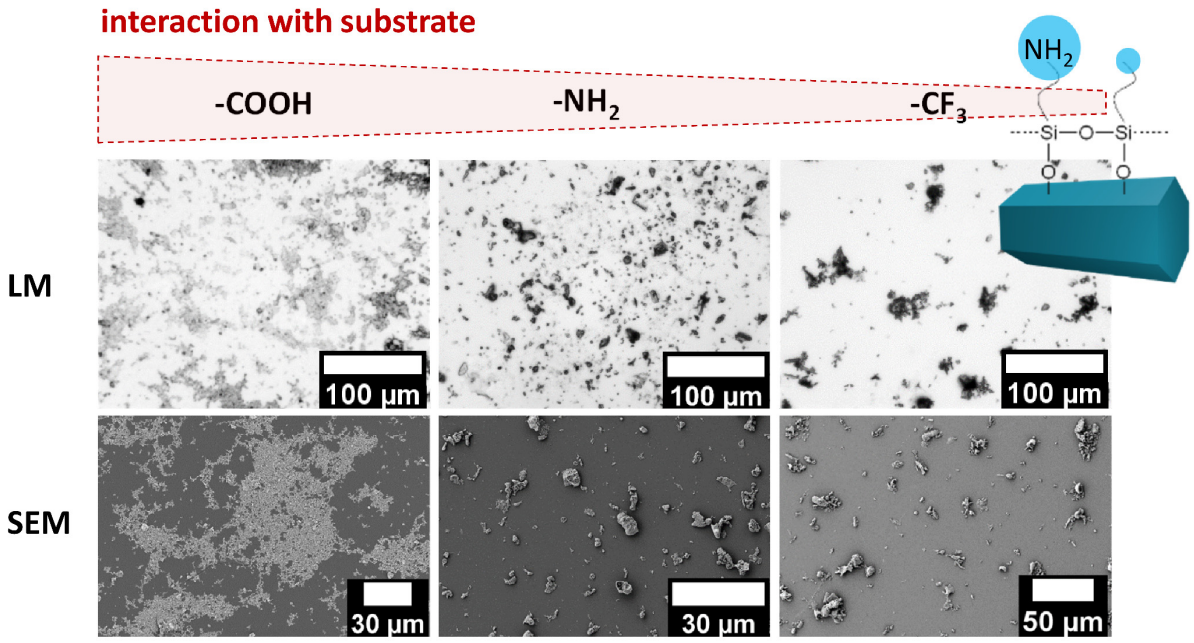

Figure 39. Zinc oxide nanorod-based superstructures on differently functionalized mica substrates. Amine-functionalized zinc oxide nanorod dispersions were dried and the zinc oxide nanorods built into larger superstructures on mica substrates placed in the vessel. The mica substrates have been functionalized with either a negatively charged carboxyl group (left column), a positively charged amine group (middle column), or a fluorine group (right column). The upper row shows light microscope images while the bottom row shows SEM images of the superstructures on the substrates.

6.1.2 Influence of Surface Chemistry on the Nucleation of Gold Nanocube-based Superstructures

The investigation on zinc oxide nanorods revealed an influence of the substrate surface chemistry on the superstructure formation of the nanorods. After this first insight, the aim was to study the impact of surface chemistry on nucleation in more detail. Therefore, the gold nanocubes introduced in Chapter 4 were used. These gold nanocubes were functionalized with positively charged CTAB ($-N^+(CH_3)_3$), negatively charged

PAA (-COO-), and hydrophilic PEG (-O-), thereby represent a variety in surface chemistry and additionally are still able to be dispersed in water (Figure 40). While CTAB provides stabilization over electrostatic repulsion, PAA and PEG provide electrostatic and steric stabilization. In contrast to the zinc oxide nanorods, for the gold nanocubes, a controlled destabilization was established by altering the solvent properties. Furthermore, in Chapter 1 several substrates for heterogeneous nucleation have been tuned in their surface chemistry by introducing silanes with different functionalities such as acid (-COOH, -SO_3H), basic (-NH_2), polar (-OH), and nonpolar (-CH_3, -CF_3) groups (Figure 40). As a result, it was now possible to combine the differently functionalized substrates with the gold nanocubes and to analyze the impact on the nucleation of the gold nanocubes into larger superstructures. The six different substrate functionalities and three different gold nanocube functionalities resulted in 18 possible combinations. Thereby, not only the influence of the substrate surface chemistry but additionally the influence of the nanoparticle surface chemistry could be studied.

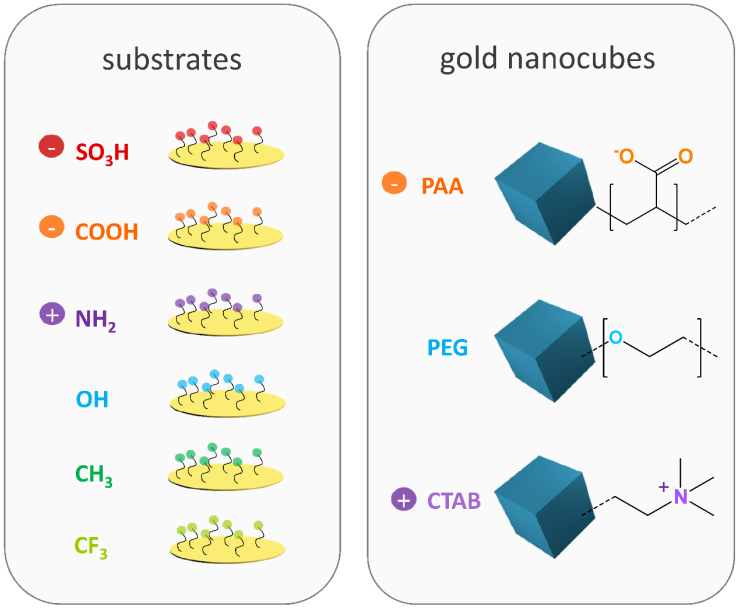

Figure 40. Combinations of differently functionalized mica substrates and gold nanocubes. The left side shows the variety in surface chemistry of substrates with different functional groups introduced via siloxane chemistry: sulfonate (SO_3H), carboxyl (COOH), amine (NH_2), hydroxyl (OH), carbonyl (CH_3), and fluorine (CF_3). The groups are varying from positively to negatively charged, respectively to the pH value and from hydrophilic to hydrophobic properties. The right side shows the three differently functionalized gold nanocubes: PAA (negatively charged), PEG (hydrophilic), and CTAB (positively charged).

To analyze the influence of surface chemistry on nucleation, the methods established in Chapter 5 were used. Mainly, the destabilization kinetics of gold nanocube dispersions in contact with functionalized mica substrates and functionalized quartz cuvettes were examined analogous to Chapter 5.1.1.3. Here, the mica substrates or the walls of quartz cuvettes have been functionalized with the functional groups depicted in Figure 40. Gold nanocube dispersions were destabilized and added to these mica substrates or quartz

cuvettes. With the quartz cuvettes, it was further possible to monitor the destabilization kinetics by UV-vis-NIR spectroscopy in situ. First, the results for the CTAB gold nanocubes are elucidated followed by the results with PAA and PEG gold nanocubes.

6.1.2.1 CTAB Gold Nanocubes

As Chapter 4 demonstrated, the positively charged CTAB gold nanocubes could be destabilized in a controlled manner by the addition of ethanol. The detailed experimental conditions for the following experiments are described in Chapter 7.3.3 and Table 10. In the first step, the impact of a functionalized mica substrate present during the destabilization of CTAB gold nanocubes was analyzed (analogous to Chapter 5.1.1.3. Aliquots for each functionalization after 15 min destabilization time were analyzed by UV-vis-NIR spectroscopy (Figure A 46). It was observed that, after 15 min destabilization time, the negatively charged mica functionalizations (sulfonate and carboxyl) already destabilized the CTAB gold nanocube dispersions. Probably, the favorable strong electrostatic interaction of the negatively charged substrates and the positively charged CTAB gold nanocubes led to the enhanced destabilization of the system, while the dispersions in contact with the other four functionalizations were still stable. Figure 41 shows UV-vis-NIR spectra of the aliquots for each functionalization after 24 h destabilization time.

Here an additional destabilization by the hydroxyl and alkyl functionalization was detected, while CTAB gold nanocubes in contact with the fluorine and positively charged amine functionalization were stable over the whole 24 h experiment time. This finding could be explained by the missing interaction of the substrates with the CTAB gold nanocubes. While the hydrophilic particles did not show a favorable interaction with the hydrophobic fluorine functionalization, the positively charged amine functionalization led to a strong electrostatic repulsion to the as well positively charged CTAB gold nanocubes.

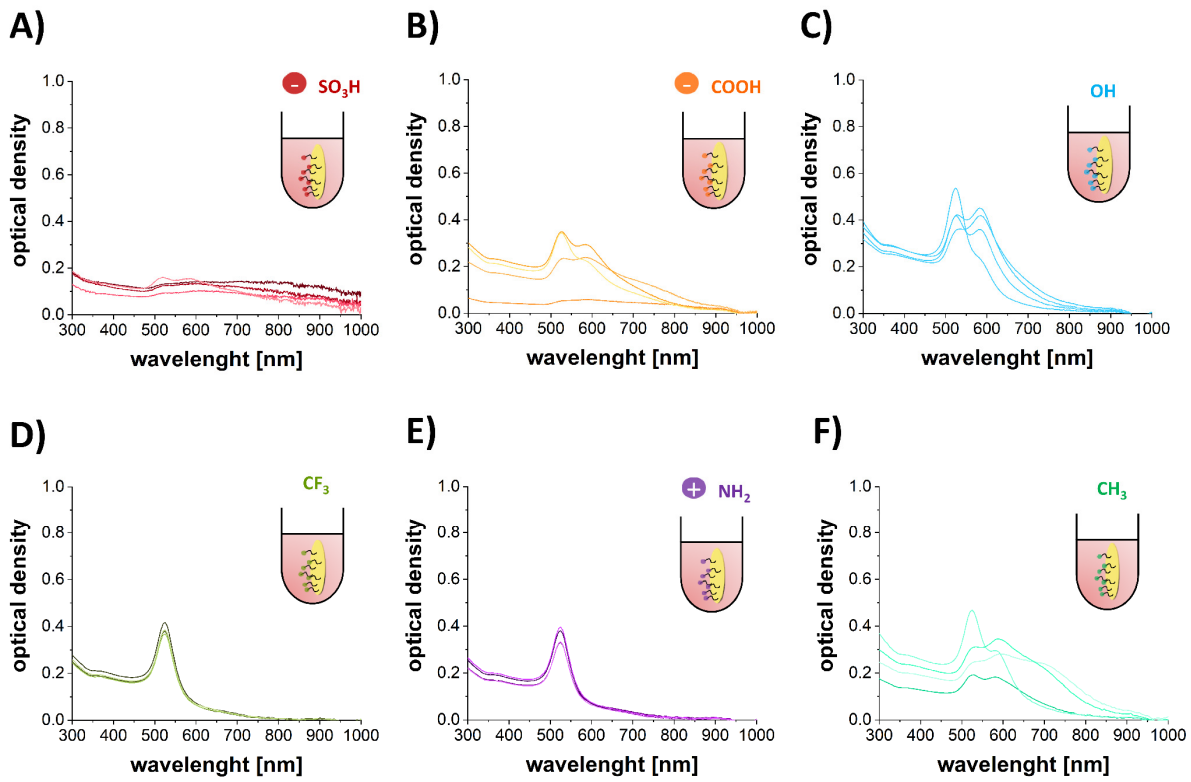

Figure 41. Destabilization in presence of functionalized mica substrates after 24 h. CTAB gold nanocube dispersions are destabilized with ethanol in presence of different functionalized mica substrates. UV-vis-NIR spectra of the dispersions are measured after 24 h of each three samples per functionalization: A) sulfonate, B) carboxyl, C) hydroxyl, D) fluorine, E) amine, and F) alkyl.

To gain more information about the impact of the substrates' surface chemistry on the destabilization kinetics, the destabilization of CTAB gold nanocube dispersions was monitored in situ by UV-vis-NIR spectroscopy. As mentioned above the cuvette walls have been functionalized and destabilized particle solutions are monitored in these functionalized cuvettes Figure 30. Figure 42 shows the development over the experiment time of the optical density at the absorption maxima at 523 nm corresponding to single gold nanocubes. The results were consistent with the outcome of the first experiments with functionalized mica in contact with destabilizing CTAB gold nanocube dispersions (Figure 41). In addition, the results of several control experiments were well reproducible. The optical density for amine and fluorine-functionalized cuvettes stayed constant over the experiment time of 24 h indicating that the CTAB gold nanocube dispersions in contact with these functionalizations did not destabilize. In contrast, the negatively charged carboxyl and sulfonate-functionalized cuvettes strongly enhanced the destabilization of the CTAB gold nanocubes. In between these two significant influences of no destabilization and fast destabilization due to electrostatic interaction, a slight destabilization for hydroxyl and alkyl-functionalized cuvettes was detected. The hydrophilic CTAB gold nanocubes seemed to interact with these functionalizations as well. The slightly stronger destabilization by the alkyl compared to the hydroxyl functionalization might be explained by a comparison of the free surface energies determined by contact angle measurements (Figure A 47). The free

surface energy of the CTAB gold nanocubes with their disperse and polar parts is closer to that of the alkyl functionalization. The better the total free surface energy and its disperse and polar parts fit each other, the more favorable is the interaction.

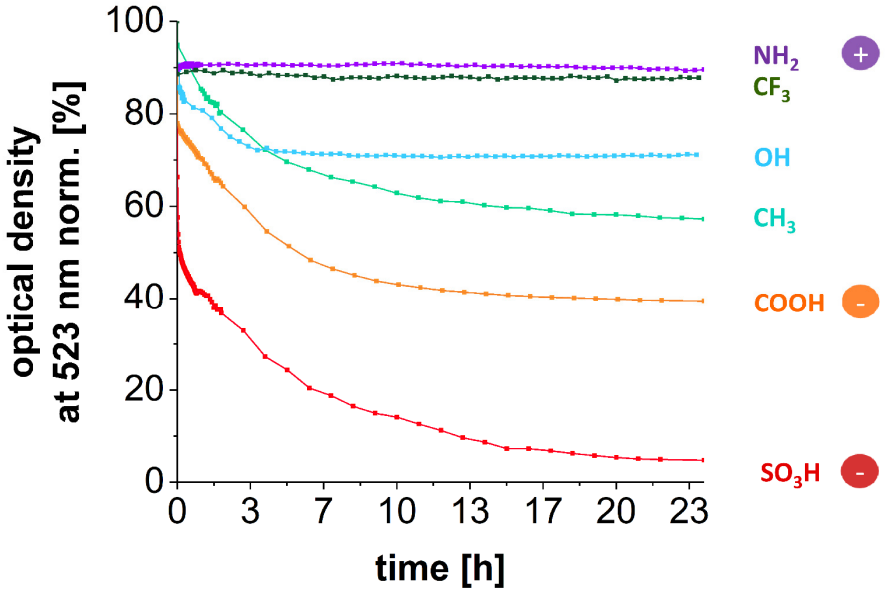

Figure 42. Destabilization kinetics of CTAB gold nanocubes dependent on the surface functionality. Dispersions of CTAB-functionalized gold nanocubes are destabilized with ethanol in functionalized quartz cuvettes. The maximum of the single gold nanocube absorption at 523 nm is plotted against the destabilization time. The optical density of 100 % corresponds to the gold nanocube absorption before dilution through the addition of ethanol.

Having a closer look at the kinetics of the destabilization process, it was determined that all four destabilizations (hydroxyl, alkyl, carboxyl, and sulfonate) proceeded as a second-order reaction (Table A 12). A second-order suggests a mechanism based on bimolecular collisions. The corresponding rate constants for the destabilization of the CTAB gold nanocubes could be determined as shown in Table 5. Whereby the combination of CTAB gold nanocubes with sulfonate-functionalized mica stands out with a significant high rate constant of 99304 l/mol∗min compared to the other rate constants in a range of 2000 to 6000 l/mol∗min.

Table 5. Rate constants for the destabilization of CTAB gold nanocubes. Rate constants determined for the destabilization of CTAB gold nanocubes in functionalized cuvettes. A reaction of second order is assumed.

	sulfonate	**carboxyl**	**hydroxyl**	**alkyl**
rate constant [l/min·mol]	99 302	2 139	3 754	5 628

With these two experiments (functionalized quartz cuvettes and mica substrates), the influence of different functionalized substrates on the destabilization of CTAB gold nanocubes in solution was analyzed successfully. The destabilization of the CTAB gold nanocubes in solution did not seem to follow exclusively a homogeneous nucleation pathway. The enhancement of the destabilization in solution with the presence of a favorable substrate can be explained by an interaction of gold nanocubes with these functionalized substrates. Maybe small aggregates of gold nanocubes formed on the substrate, then reattach off the substrate into solution and promote the destabilization in the solution. Thereby, the influence of the different functionalizations on the destabilization process corresponds very well to the expectations of the interaction between the nanoparticle surface and the functionalization of the substrate. While some functional groups did not influence the destabilization of CTAB gold nanocubes (fluorine and amine), especially the negatively charged groups significantly enhanced the destabilization (carboxyl and sulfonate). Thereby, the findings of the different experiments fit together well and can be explained by the interaction of the positively charged CTAB gold nanocube surface with the respective functional group on the substrate.

6.1.2.2 PAA Gold Nanocubes

Until now, the destabilization kinetics of positively charged CTAB gold nanocubes in contact with differently functionalized substrates were analyzed. In the next step, similar experiments were performed with negatively charged PAA gold nanocubes. In Chapter 4, the controlled destabilization of PAA gold nanocubes could be established with the addition of calcium chloride. The experimental conditions for the following experiments with the PAA gold nanocubes are described in detail in Chapter 7.3.3 and are summarized in Table 11. PAA gold nanocube dispersions were destabilized in functionalized quartz cuvettes and the destabilization kinetics were monitored with UV-vis-NIR spectroscopy. Figure 43 shows the development of the optical density at the absorption maxima at 523 nm corresponding to single gold nanocubes. During the experiment time of 120 min, all optical densities decreased indicating a destabilization of the PAA gold nanocube dispersions. However, similar to the CTAB gold nanocubes, the destabilization kinetics of the PAA gold nanocubes varied dependent on the surface functionalization. The PAA gold nanocubes in contact with the fluorine-functionalized quartz cuvettes destabilized slowest indicating an unfavorable interaction between the hydrophilic PAA gold nanocubes and the hydrophobic fluorine functionalization. The PAA gold nanocubes in the alkyl, carboxyl, sulfonate, and hydroxyl-functionalized quartz cuvettes destabilized with a comparable speed. Here, it should be presumed that the interaction with the negatively charged surfaces (carboxyl and sulfonate) is more unfavorable. Nevertheless, the destabilization with calcium chloride has to be considered which might lead to a different level of shielding of the charged groups. On the other hand, the differences in the destabilization kinetics in contact with the four groups may only become apparent if the destabilization of the PAA gold nanocubes is even lower. As expected, the positively charged amine group destabilized the negatively charged PAA gold nanoparticles the most and led to significantly enhanced destabilization kinetics.

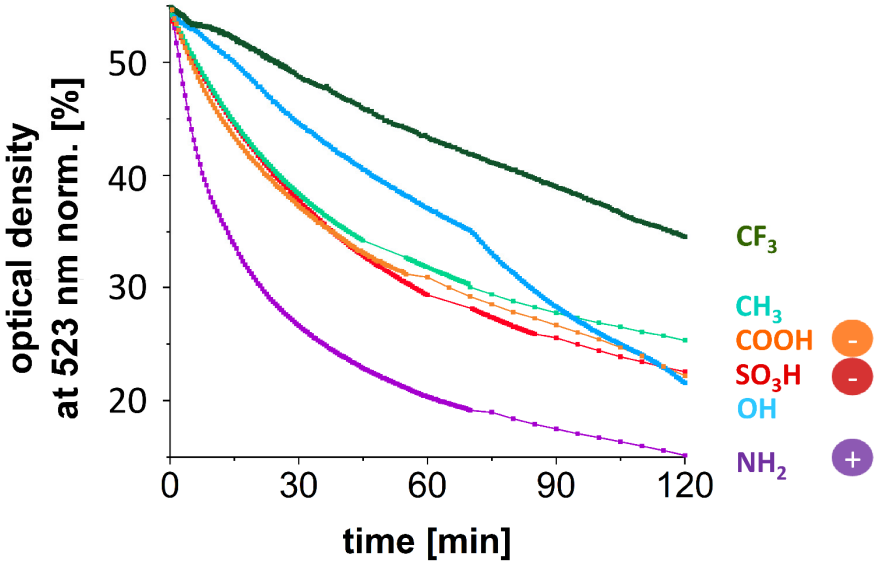

Figure 43. Destabilization kinetics of PAA gold nanocubes dependent on the surface functionality. Dispersions of PAA-functionalized gold nanocubes are destabilized with ethanol in functionalized quartz cuvettes. The maximum of the single gold nanocube absorption at 523 nm is plotted against the destabilization time. The optical density of 100 % corresponds to the gold nanocube absorption before dilution through the addition of calcium chloride.

The PAA gold nanocube destabilization mainly proceeded as a second-order reaction (Table A 13). However, the difference between second-order and first-order was not as significant as for the CTAB gold nanocubes and for the sulfonate- and fluorine-functionalized substrates even a first-order was determined. The calculated rate constants are summarized in Table 6. Above all, the amine functionalization stands out with the highest rate constant of 25165 l/min∗mol. In conclusion, also the destabilization of PAA gold nanocubes was influenced by the substrates surface functionalization and the combination with positively charged amine groups has greatly accelerated the destabilization kinetics.

Table 6. Rate constants for the destabilization of PAA gold nanocubes. Rate constants determined for the destabilization of PAA gold nanocubes in functionalized cuvettes. A reaction of second order is assumed.

	sulfonate	**carboxyl**	**amine**	**hydroxyl**	**alkyl**	**fluorine**
rate constant [l/min·mol]	2 032	6 122	25 165	1 811	2 777	1 037

6.1.2.3 PEG Gold Nanocubes

So far, positively charged CTAB and negatively charged PSS gold nanocubes have been analyzed. To complete the picture, the destabilization kinetics of hydrophilic PEG gold nanocubes dependent on the substrates' surface functionalization were examined. PEG gold nanocubes could be destabilized in a controlled manner through the addition of hydrochloric acid and the resulting decrease of the pH value (Chapter 4.1.2). However, to achieve a destabilization of the PEG gold nanocubes, a pH value of less than 0 was necessary. In combination with the functionalized substrates, such a low pH value would dissolve the silane bondings of the substrates' functionalizations. Therefore, the behavior of the PEG gold nanocubes in combination with carboxyl-functionalized substrates was analyzed for different pH values from 4 to 0 (Figure A 48). UV-vis-NIR measurements detected a decrease in the absorption maxima with decreasing pH value, indicating a loss of PEG gold nanocubes from the dispersion (Figure A 48 A). Nevertheless, a destabilization of PEG gold nanocubes indicated by the arising of absorption at larger wavelengths was not detected. The optical control of the carboxyl-functionalized mica substrates revealed red to purple substrates for the experiments with a pH value from 3 to 0. While the mica substrate for a pH value of 4 appeared unchanged in color (Figure A 48 B). This optical control suggested PEG gold nanocubes on the substrates' surface that could explain the loss of PEG gold nanocubes in dispersion detected with UV-vis-NIR spectroscopy. Further measurements with SEM confirmed the presence of PEG gold nanocube superstructures on the mica substrates for experiments performed with pH values from 3 to 0. With these findings, the destabilization kinetics were examined at a pH value of 3 assuring the stability of the silane bondings from the substrates functionalizations but still allowing heterogeneous nucleation of the PEG gold nanocubes. The detailed experimental conditions are described in Chapter 7.3.3 and Table 12.

With a pH of 3, the PEG gold nanocubes stayed stable in dispersion, but with contact to a substrate, heterogeneous nucleation and structure growth on the substrate was induced. The loss of PEG gold nanocubes in solution - due to the structure growth on the substrate - became apparent in the UV-vis-NIR spectra of the solution by a decrease of the maximum absorption peak at 523 nm (Figure A 48). Therewith, it was possible to plot the kinetics of the process for the PEG gold nanocubes dependent on the substrates' functionalization (Figure 44). PEG gold nanocubes in contact with negatively charged sulfonate-functionalized substrates destabilized very fast. The carboxyl-functionalized substrates with a $pK_{s1} = 4.16$ and $pK_{s2} = 5.61$ should be protonated at the pH of 3.[216] Nevertheless, they comparably destabilized the PEG gold nanocubes to sulfonate-functionalized substrates and as well as the hydroxyl- and carbonyl-functionalized substrates. PEG gold nanocubes appeared to have a good interaction with these four functionalizations ($-SO_3H$, -COOH, -OH, $-CH_3$). In comparison, the structure growth on fluorine-functionalized substrates proceeded slower, which could be explained by the more unfavorable interaction of the hydrophilic PEG gold nanocubes with the fluorine-functionalized substrates. However, amine-functionalized substrates influenced the PEG gold nanocube system fewest of all. This result was not expected, due to the negative zeta potential of PEG gold nanocubes, which should result in a favorable

interaction with the positively charged amine functionalization. But a zeta potential measurement at pH 3 demonstrated, that with the decreasing pH value the zeta potential of the PEG gold nanocubes shifted from -25 eV to +44 eV, which could explain well the unfavorable interaction with the positively charged amine-functionalized surface (Figure A 49). Probably, at this pH value, PEG adsorbs protons and therefore gets positively charged.

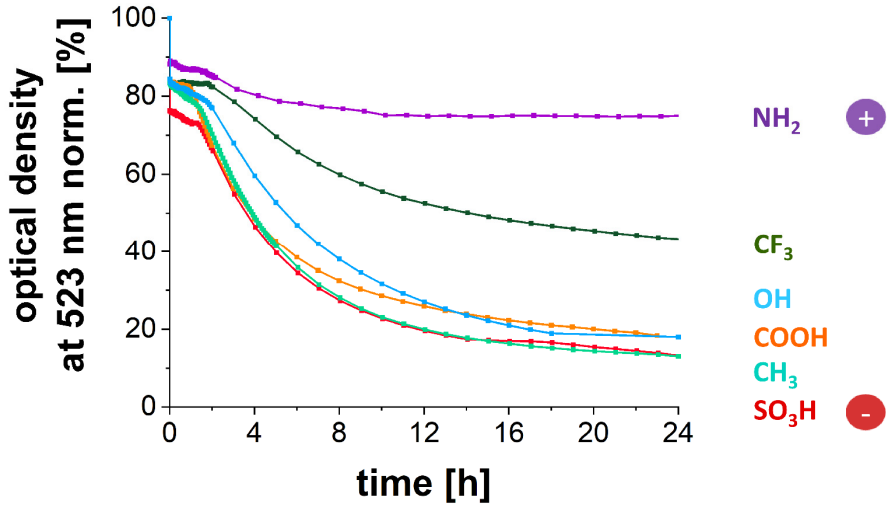

Figure 44. Destabilization kinetics of PEG gold nanocubes dependent on surface functionality. PEG gold nanocubes are destabilized in functionalized quartz cuvettes by adjusting the pH to 3 with hydrochloric acid. The maximum of the single gold nanocube absorption at 523 nm is plotted against the destabilization time. The optical density of 100 % corresponds to the gold nanocube absorption before dilution through the addition of hydrochloric acid.

All destabilizations of the PEG gold nanocubes proceeded as a reaction of second-order (Table A 14), like the previous gold nanocubes, and the rate constants were determined (Table 7).

Table 7. Rate constants for the destabilization of PEG gold nanocubes. Rate constants determined for the destabilization of PEG gold nanocubes in functionalized cuvettes. A reaction of second order is assumed.

	sulfonate	carboxyl	amine	hydroxyl	alkyl	fluorine
rate constant [l/min·mol]	3 696	2 641	387	3 926	3 362	1 512

The determined kinetics for CTAB and PAA gold nanocubes included the possible structure growth on the substrates and the destabilization of gold nanocubes in solution meaning heterogeneous and homogeneous nucleation. In contrast, for the PEG gold nanocubes, it was possible to monitor only the kinetics of structure growth of the gold nanocubes without a destabilization in solution. However, similar to the two systems before, the kinetics for PEG gold nanocubes were dependent on the substrates' surface functionalization.

While the PEG gold nanocubes seemed to have a favorable interaction with numerous functionalizations, again the interaction with fluorine was not favorable. Furthermore, the unfavorable interaction with positively charged amine-functionalized substrates could be explained by the shifted zeta potential of the PEG gold nanocubes at a pH value of 3. Thereby, the determined interactions of the gold nanocube functionalizations with the substrates' functionalizations fit well the expected interactions for all three systems. After the analysis of the kinetics in dispersion, in the following, the superstructures that have grown on the substrates should be analyzed.

6.1.3 Influence of Surface Chemistry on the Superstructure Formation of Gold Nanocubes on Substrates

After determining the influence of substrate and particle surface chemistry on the kinetics of the destabilization of gold nanocubes in dispersion, analysis went one step further. The structure formation of gold nanocubes on the substrates was examined dependent on the surface functionalization. Therefore, the substrates from the experiments before could be used: first the structures formed on the functionalized cuvette walls were analyzed by UV-vis-NIR spectroscopy and second the structures formed on the mica substrates were analyzed by SEM as described in Chapter 5.1.1.3.

6.1.3.1 CTAB Gold Nanocubes

For CTAB gold nanocubes, large gold nanocube-based superstructures were observed for sulfonate- (Figure 45 A) and carboxyl-functionalized (Figure A 50 A) substrates that became apparent in the SEM images and peaks at higher wavelengths in UV-vis-NIR spectra. This finding fits the earlier results, which indicated a favorable interaction of the positively charged CTAB gold nanocubes and the negatively charged substrates (Figure 42). The size of the CTAB gold nanocube-based superstructures, obtained by the SEM images, mainly ranged between 0.5 and 3 µm. The superstructures were disordered, which could be explained by the short nucleation time. The aliquots (Figure A 46) taken after 15 min destabilization time showed already a heavily destabilized system. In contrast to the big CTAB gold nanocube-based superstructures for the favorable interaction, no structure formation was observed for fluorine- and amine-functionalized substrates (Figure A 50 C, D). While no gold nanocubes could be observed in the SEM, the UV-vis-NIR spectra of the cuvette wall did not show a signal either. Since the interaction of the positively charged CTAB gold nanocubes was not favorable with these two functionalizations, no gold nanocubes attached to the substrates. Again, the hydroxyl (Figure 45 B) and carbonyl (Figure A 50 B) functionalized substrates lay between the two scenarios of a favorable interaction and no interaction with the substrate. For these two functionalizations, mainly single particles and small aggregates of two to four CTAB gold nanocubes were observed in the SEM images. This result agreed with the UV-vis-NIR spectra of the cuvette walls. Here a signal for single CTAB gold nanocubes or very small aggregates was observed. With the obtained results in mind, the question arose if it is possible to achieve larger superstructures on the hydroxyl or carbonyl-functionalized substrates. A stronger destabilization by adding a larger amount of ethanol and a longer

destabilization time (one week instead of 24 h) were therefore tested. Both cases came to the same results as before (single nanoparticles and small aggregates on the substrates) and did not result in larger superstructures.

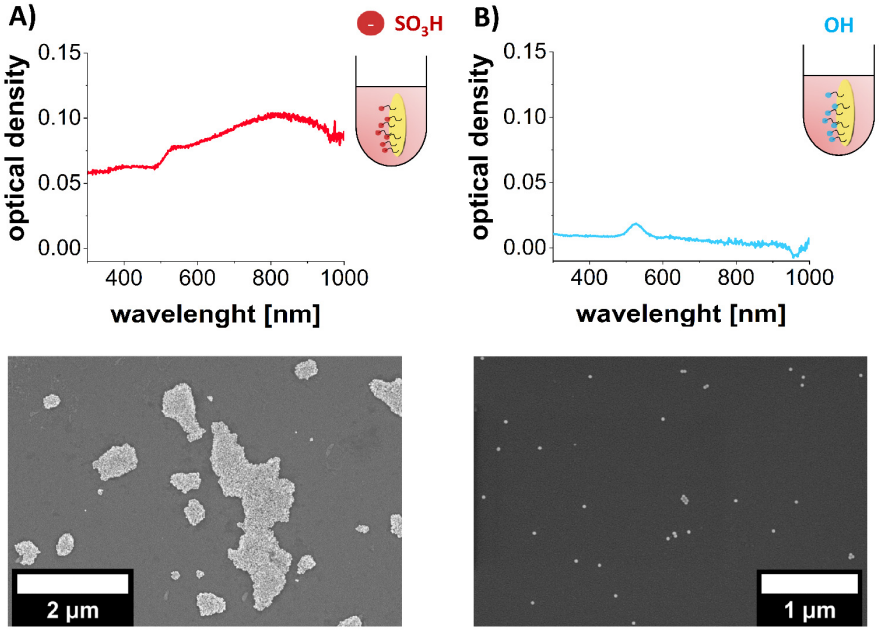

Figure 45. CTAB gold nanocube superstructures. The upper row shows UV-vis-NIR spectra of CTAB gold nanocube-based superstructures that formed on A) sulfonate- and B) hydroxyl-functionalized quartz cuvettes. The bottom row shows SEM images of the CTAB gold nanocubes on the corresponding functionalized mica substrates.

In summary, the influence of the six different substrate functionalizations on the destabilization of CTAB gold nanocubes in dispersion corresponded very well to the structure analysis on these substrates. Negatively charged substrates not only enhanced the destabilization of CTAB gold nanocubes in dispersion significantly but additionally led to a superstructure growth of the nanoparticles on the substrates. In contrast, fluorine and positively charged substrates did not influence the destabilization of CTAB gold nanocubes in dispersion. Samples here behaved like the control samples without the addition of a substrate. Consequently, no nanoparticles were observed on these substrates. In between lay the more polar hydroxyl and carbonyl functionalizations. These enhanced the destabilization of CTAB gold nanocubes slightly and led to single CTAB gold nanocubes and small aggregates on the substrates.

6.1.3.2 PAA Gold Nanocubes

Like for the CTAB gold nanocubes, the superstructure formation of the PAA gold nanocubes was dependent on the substrates' surface chemistry. The unfavorable combination with fluorine-functionalized substrates revealed no signal in the UV-vis-NIR spectra of the functionalized quartz cuvettes and only a few single gold nanocubes on the substrates in the SEM images (Figure A 51 D). These findings supported the result of the slowest destabilization kinetics in Chapter 6.1.2.2. PAA gold nanocubes seemed to have little

interaction with the fluorine-functionalized substrates and therefore the destabilization kinetics in dispersion was not enhanced by the substrates. The UV-vis-NIR spectra for hydroxyl- (Figure 46 B), alkyl-, carboxyl-, and sulfonate-functionalized (Figure A 51 A-C) quartz cuvettes showed signals for single gold nanocubes. While the SEM images of alkyl-functionalized substrates revealed various single gold nanocubes and aggregates, the SEM images of hydroxyl-, carboxyl-, and sulfonate-functionalized substrates showed fewer single gold nanocubes and small aggregates (Figure 46 B, Figure A 51 A-C). The comparable results for these four functionalizations fit the kinetics data where they performed with similar speed and course. The positively charged amine functionalization enhanced the destabilization of PAA gold nanocubes significantly, indicating a favorable interaction. This result is supported by the superstructure analysis. For amine-functionalized substrates, huge gold nanocube-based superstructures were observed in the SEM images (Figure 46 A). These superstructures were disordered and similar to the large superstructures obtained for CTAB gold nanocubes but reaching larger sizes of up to 20 µm. The UV-vis-NIR spectra for amine-functionalized quartz cuvettes predominantly showed the signal for single gold nanocubes. Maybe, because the superstructures obtained are too large to give an absorption signal in this wavelength range.

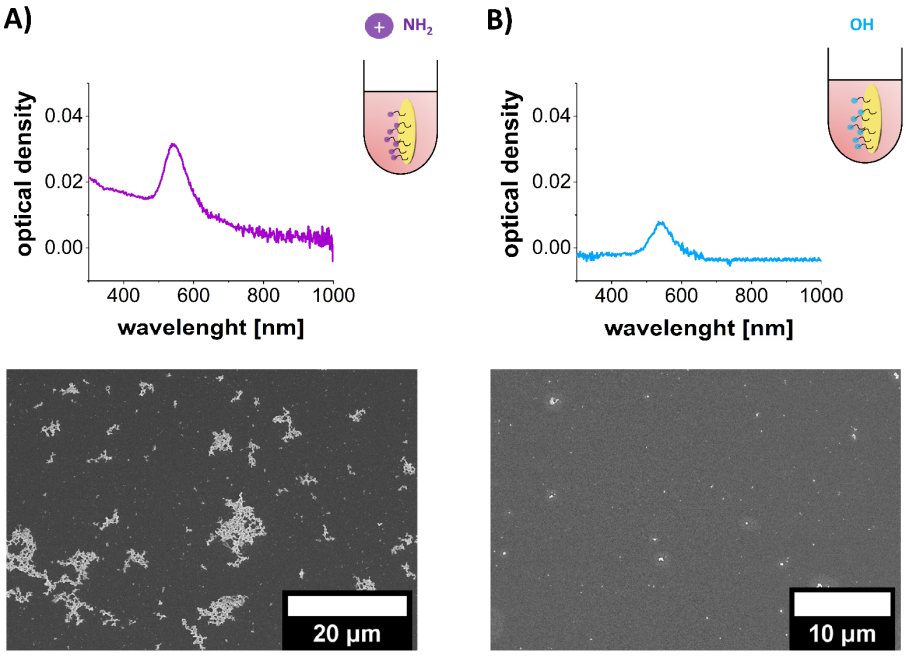

Figure 46. PAA gold nanocube-based superstructures. The upper row shows UV-vis-NIR spectra of PAA gold nanocube-based superstructures that formed on A) amine and B) hydroxyl-functionalized quartz cuvettes. The bottom row shows SEM images of the PAA gold nanocubes on the corresponding functionalized mica substrates.

Thereby, the analysis of the superstructure formation of PAA gold nanocubes on different functionalized substrates indicated a dependence on the substrates' surface chemistry as well. The results obtained fit well the results of the kinetics determined in Chapter 6.1.2.2 and large superstructures were obtained for the favorable interaction of negatively charged PAA gold nanocubes with positively charged amine substrates.

6.1.3.3 PEG Gold Nanocubes

Further, the superstructures formed on substrates by the PEG gold nanocubes were analyzed by SEM measurements (Figure 47). On positively charged amine substrates, few single gold nanocubes and few small aggregates were observed, while fluorine-functionalized substrates exhibited mainly single gold nanocubes. In contrast, on the other four functionalized substrates (-SO_3H, -COOH, -OH, -CH_3), large gold nanocube-based superstructures were obtained covering the whole substrates. The superstructures for these four functionalizations were similar and all four exhibited different characteristics reaching from small island structures (Figure 47 C) to huge continuous particle networks (Figure 47 F). These insights fit well with the aforementioned kinetic results obtained with UV-vis-NIR measurements in dispersion where the four functionalized substrates showed the fastest progress (Chapter 6.1.2.3).

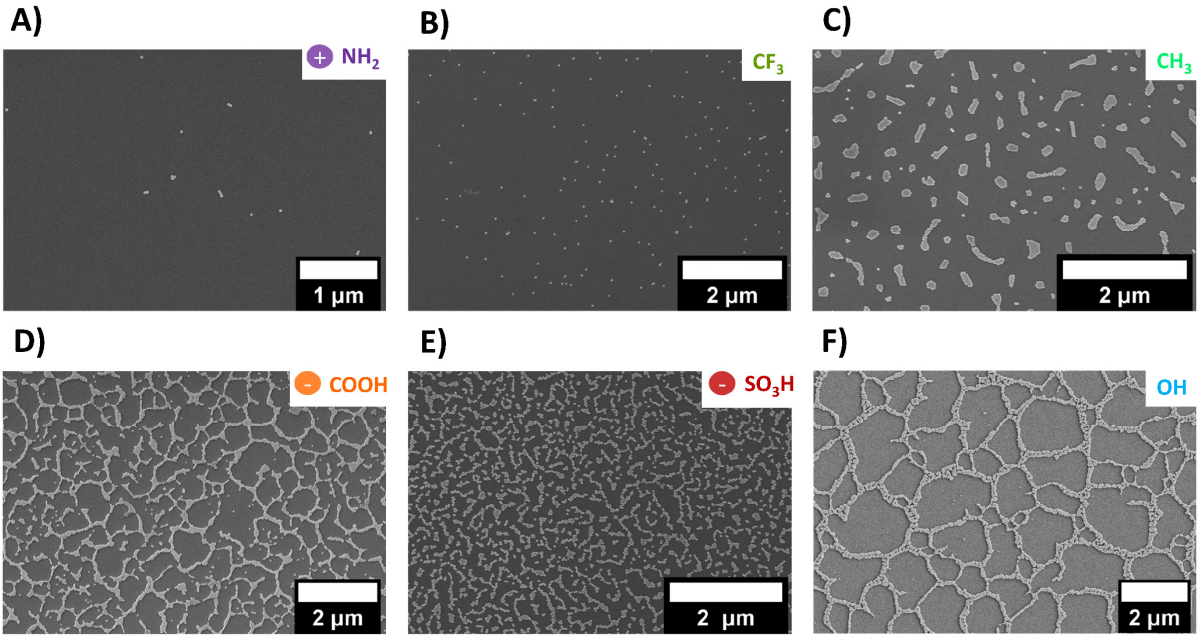

Figure 47. PEG gold nanocube-based superstructures. PEG-functionalized gold nanocube dispersions were destabilized in presence of different functionalized mica substrates: A) amine, B) fluorine, C) alkyl, D) carboxyl, E) sulfonate, and F) hydroxyl-functionalized. The images were taken by SEM and show the corresponding substrate surfaces.

The superstructures obtained for PEG gold nanocubes differed from the superstructures out of CTAB or PAA gold nanocubes. These showed huge disordered superstructures with few layers of gold nanocubes and forms that are more tattered. However, the PEG gold nanocubes formed more defined island structures or huge networks with a one-dimensional layer.

6.1.4 Microscopic Analysis of the Influence of Surface Chemistry on the Heterogeneous Nucleation of Gold Nanocube-based Superstructures

Up to now, the influence of substrate and nanoparticle surface chemistry were studied not only for the destabilization of the gold nanocubes in dispersion but further for the structure growth of the gold nanocubes on the substrates. These studies revealed a significant influence of surface chemistry in both cases. At this point, the kinetics of the heterogeneous nucleation of gold nanocubes with favorable substrates should be analyzed in situ by the combination of light microscopy and UV-vis-NIR spectroscopy. The experimental setup and the analysis of the resulting kinetic data were already described in Chapter 5.1.2 and the following will focus on the obtained results.

6.1.4.1 CTAB Gold Nanocubes

So far, six different combinations of CTAB gold nanocubes with differently functionalized substrates were analyzed (Figure 40) resulting in the identification of two favorable interactions of the CTAB gold nanocubes with the sulfonate- and carboxyl-functionalized substrates. Analyzing the heterogeneous nucleation of CTAB gold nanocubes on these favorable substrates was of interest. Therefore, the nucleation rates for this process were determined for varying supersaturations of the CTAB gold nanocubes (Figure A 52, Table A 15) and the resulting nucleation rates were plotted against the supersaturations in order to be able to calculate the kinetic parameters of the heterogeneous nucleation process (Figure 48). As expected, the nucleation rates increased with increasing particle supersaturations for both substrate combinations. In general, the nucleation processes at higher supersaturations started earlier and proceeded faster. The carboxyl-functionalized substrates showed lower nucleation rates and a lower increase of the nucleation rates with increasing supersaturation. Further, a smaller supersaturation range could be analyzed, as the optical density of the gold nanocube dispersion defines the upper detection limit for observation with the light microscope, which was reached earlier for carboxyl-functionalized substrates. In comparison, the sulfonate-functionalized substrates showed higher nucleation rates and a greater increase of these nucleation rates with increasing supersaturation. Furthermore, the carboxyl-functionalized substrates allowed for the analysis of a wider supersaturation regime. These results fit well with the findings from the kinetic studies made with the same particle substrate combinations in functionalized quartz cuvettes (Figure 42) where the carboxyl-functionalized substrates enhanced the destabilization of CTAB gold nanocubes the most.

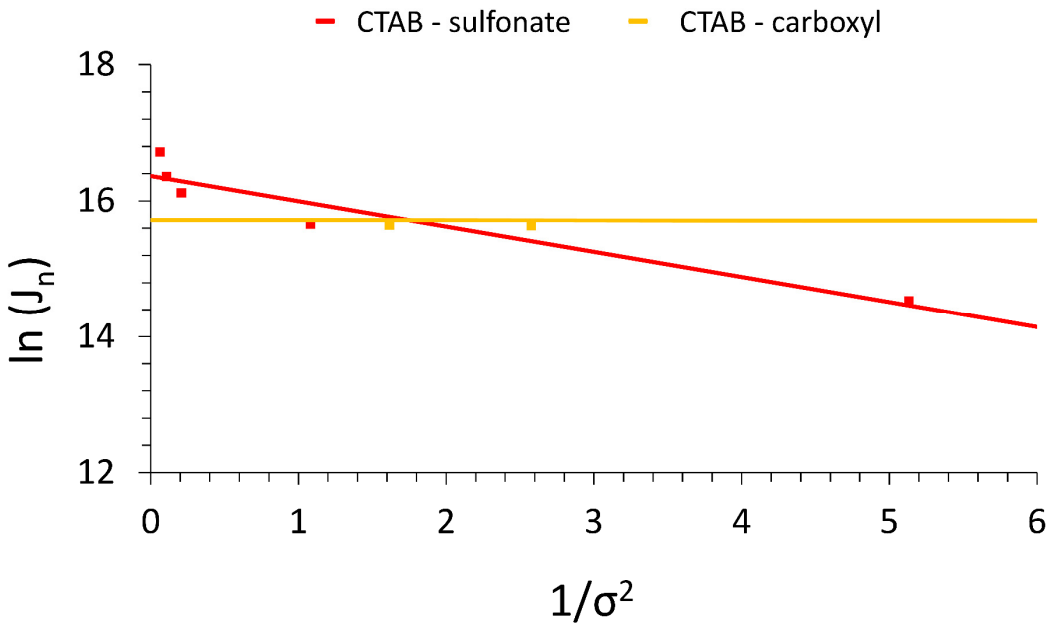

Figure 48. Plot of nucleation rates against supersaturations. The natural logarithm of the nucleation rates is plotted against the inverse square of the supersaturation for each particle substrate combination: CTAB gold nanocubes with sulfonate-functionalized mica (red) and carboxyl-functionalized mica (orange). Only two data points for the CTAB-carboxyl combination are shown as the y-axis is zoomed in. A straight fit is performed for the data, linear equation: (red) y = -4.50 x + 16.73 (R^2 = 0.97) and (yellow) -0.57 + 15.86 (R^2 = 0.54).

A linear relationship is supposed for the plots of the nucleation rates (Figure 48). The fit with a straight line allowed calculating the effective interfacial energy α over its slope. The calculation of the interfacial energy α depends on the form factor and thus on the approximated contact angle of the nucleus on the substrate. Table A 16 lists the results for different contact angles while Table 8 summarizes the results. The interfacial energies amounted to 5.23 - 9.17 · 10^{-6} J/m² (CTAB - sulfonate) and 2.62 - 4.59 · 10^{-6} J/m² (CTAB - carboxyl). The values for CTAB gold nanocubes on sulfonate- and carboxyl-functionalized mica were directly comparable since only the substrate functionalization differed in the experiments. Here, the combination with a carboxyl-functionalized substrate resulted in smaller interfacial energy and therewith a beneficial interaction. As a comparison, Nielsen *et al.* determined effective interfacial energies for the nucleation of calcium carbonate on different self-assembled monolayers between 7.2 and 9.5 · 10^{-2} J/m². Other publications for calcium carbonate systems are in the same size range, which are in a larger order of magnitude than the determined values for gold nanocubes.[26, 250, 255-257] This smaller order of magnitude of the interfacial energy for the gold nanocubes could be explained by the much smaller supersaturations needed for the nucleation of the gold nanocubes in comparison to an atomic system like calcium carbonate. Further, a nanoparticle exhibits a larger surface compared to an ion. The nanoparticle therefore carries a higher number of surface charges which would be beneficial for the interfacial energy compared to the single charge of an ion.

Table 8. Calculated kinetic and thermodynamic parameters. The effective interfacial energy range for contact angles of 60° to 90°, the nucleation barrier, and the kinetic and thermodynamic term are given for the combinations of CTAB gold nanocubes with sulfonate- and carboxyl-functionalized mica. Since the thermodynamic term is dependent on the supersaturation σ, it was determined for supersaturations of 1.0 to 2.0.

particle substrate combination	**effective interfacial energy α** $[\frac{J}{m^2}]$	**nucleation barrier Δg_n** $[k_BT]$	**thermodynamic term** $\frac{fV_m^2}{(k_BT)^3}\alpha^3\left(\frac{1}{\sigma^2}\right)$	**kinetic term** $\ln\left(A * e^{-\frac{E_A}{k_BT}}\right)$
CTAB - sulfonate	5.23 – 9.17 · 10^{-6}	0.18 – 2.17	1.13 - 4.51	16.72
CTAB - carboxyl	2.62 – 4.59 · 10^{-6}	0.17 – 0.50	0.14 - 0.57	15.86

By knowing the effective interfacial energies for the particle substrate combinations, it was possible to calculate the nucleation barriers Δg_n. A comparison of the two nucleation barriers is shown in Figure 49 and the values are summarized in Table 8. The analysis revealed nucleation barriers of 0.18 – 2.17 k_BT (CTAB - sulfonate) and 0.17 – 0.50 k_BT (CTAB – carboxyl) within the experimental supersaturation regime. While the combination of CTAB gold nanocubes with carboxyl-functionalized mica exhibited a very small nucleation barrier, the combination with sulfonate-functionalized mica exhibited a distinct nucleation barrier approaching the supersaturation of 1. Compared to Nielsen *et al.* who determined nucleation barriers of 19 to 27 k_BT for their calcium carbonate systems, the obtained values for the gold nanocubes lie below.[26] Thereby, the determined nucleation barriers for the nucleation of gold nanocube-based superstructures were low compared to the thermal energy. This result is not surprising if the opposite charges of particles and substrates are taken into account and fits the classical nucleation theory in contrast to some ionic or molecular systems exhibiting unrealistic high nucleation barriers.[34]

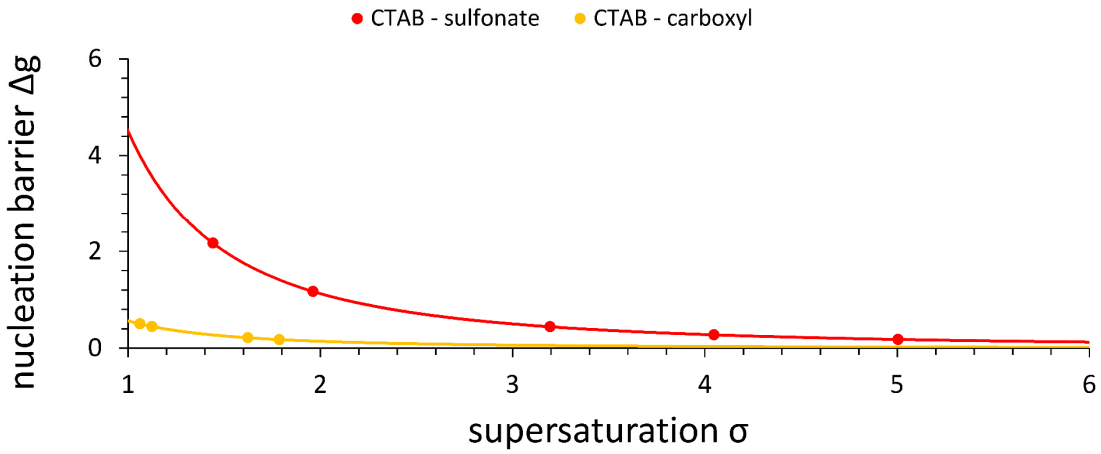

Figure 49. Nucleation barriers. The resulting nucleation barriers for the two analyzed combinations: CTAB gold nanocubes with sulfonate-functionalized mica (red) and carboxyl-functionalized mica (orange). A fit is performed for the data, (red) $4.51 \cdot x^2$ (R^2=1.00) and (yellow) $0.57 \cdot x^2$ (R^2=1.00).

Next to the effective interfacial energy and the nucleation barrier, it was possible to determine the kinetic and thermodynamic terms for the heterogeneous nucleation of the CTAB gold nanocubes. The results are summarized in Table 8 and Figure 50 visualizes the comparison of the kinetic and thermodynamic terms. The magnitude of the thermodynamic term related to the nucleation barrier depends on the supersaturation σ and was determined for supersaturations of 1.0 to 2.0 (Table 8). The combination of CTAB gold nanocubes on sulfonate-functionalized substrates exhibited a thermodynamic term of 1.13 – 5.51 and a dominating kinetic term of 16.72. Similar values were obtained for the combination with carboxyl-functionalized substrates with a thermodynamic term of 0.14 – 0.57 and a kinetic term of 15.86. It was surprising, that the kinetic term was larger than the thermodynamic term since for most analyzed nucleation systems the thermodynamic term predominates strongly. One explanation could be diffusion. The diffusion of nanoparticles is more restricted than that of ions or molecules and leads to a more limited supply of building units to the nucleation side as compared to small ions or molecules. For the nucleation of ions or molecules, the interfacial energy and therefore the nucleation barrier determines the nucleation rate. While for the nucleation of the gold nanocubes, the amount of the kinetic term increased due to the stronger restriction in diffusion and results in a larger kinetic hindrance for the nucleation of the gold nanocubes.

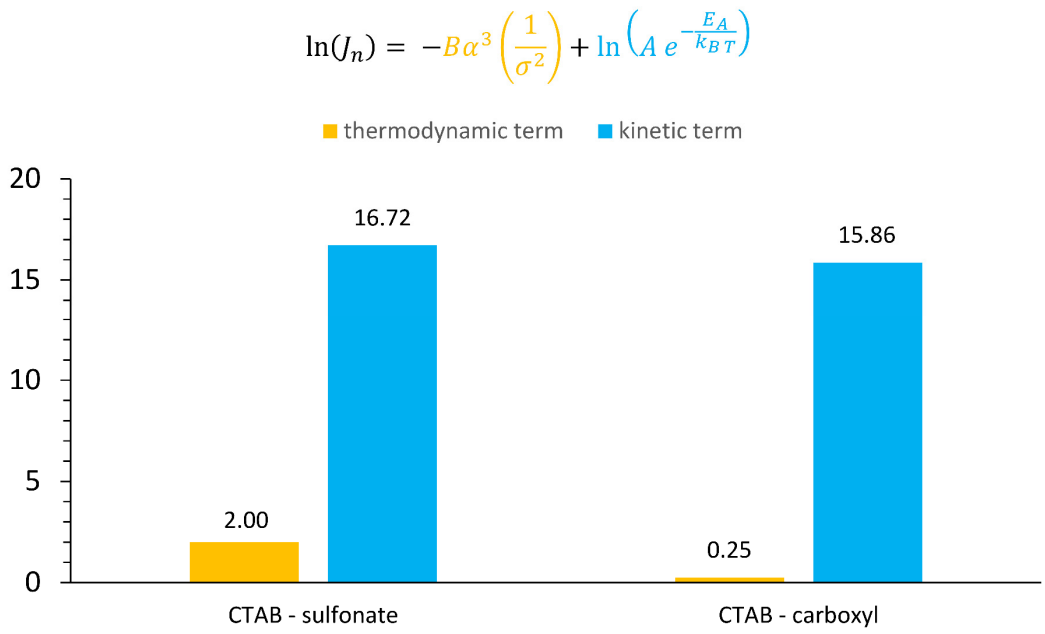

Figure 50. Kinetic versus thermodynamic term. Comparison of the share of the kinetic (blue) and the thermodynamic (orange) term of the nucleation rates for the combinations of CTAB gold nanocubes with sulfonate- and carboxyl-functionalized substrates. The thermodynamic terms are calculated for a supersaturation of 1.5.

Conclusively, the heterogeneous nucleation of CTAB gold nanocubes on sulfonate- and carboxyl-functionalized substrates could be successfully analyzed in situ by the combination of light microscopy and UV-vis-NIR spectroscopy. The experimental approach allowed determining the nucleation rates and further calculating the effective interfacial energies, the nucleation barriers, and the thermodynamic and kinetic terms. The so obtained values show a more favorable interaction between the CTAB gold nanocubes with the sulfonate-functionalized substrate compared to the carboxyl-functionalized substrate. This result fits well the observations made with kinetic experiments in functionalized quartz cuvettes (Chapter 6.1.2.1) and the superstructure formation observed with SEM (Chapter 6.1.3.1). In addition, differences between the nanoparticle system to ionic or molecular systems were discovered, especially the dominating kinetic term and the so resulting kinetic hindrance of the heterogeneous nucleation of nanoparticles. This finding could be explained by the slower diffusion of nanoparticles compared to ions or molecules, making the diffusion a more relevant parameter for their nucleation into superstructures.

6.1.4.2 PAA Gold Nanocubes

Similar to the CTAB gold nanocubes, the kinetics of the heterogeneous nucleation of the PAA gold nanocubes were analyzed by light microscopy in combination with UV-vis-NIR spectroscopy. For the negatively charged PAA gold nanocubes, a favorable interaction was revealed with the positively charged amine-functionalized substrates leading to superstructures with sizes of up to 20 µm (Figure 40). With these huge PAA gold nanocube-based superstructures, an analysis by light microscopy was possible. According

to the method described in Chapter 5.1.2, the nucleation rates for the controlled destabilization of PAA gold nanocubes with the addition of calcium chloride were determined (Figure A 53). Here the supersaturation of the PAA gold nanocubes could be adjusted to receive a controlled destabilization of the gold nanocubes in solution parallel to the superstructure growth on the substrates. This destabilization in solution was slow enough to detect the superstructure growth on the substrates but led to a decrease of the supersaturation during the experiment, which allowed to measure nucleation rates at different supersaturations in one single experiment. The experimental approach and the analysis of the so obtained data were already described in Chapter 5.1.2. This analysis revealed in principle the same data as seen for the CTAB gold nanocubes above with the difference that it was possible to measure considerably more data points. Figure 51 shows a plot of the nucleation rates against the corresponding supersaturation, which was used for the further calculation. The plot resulted in a higher slope and y-intercept compared to the fit of the CTAB gold nanocubes in combination with sulfonate-functionalized substrates. However, the results cannot be compared quantitatively since the destabilization of the two gold nanoparticle systems differed. Likewise, the further values are only to be compared qualitatively.

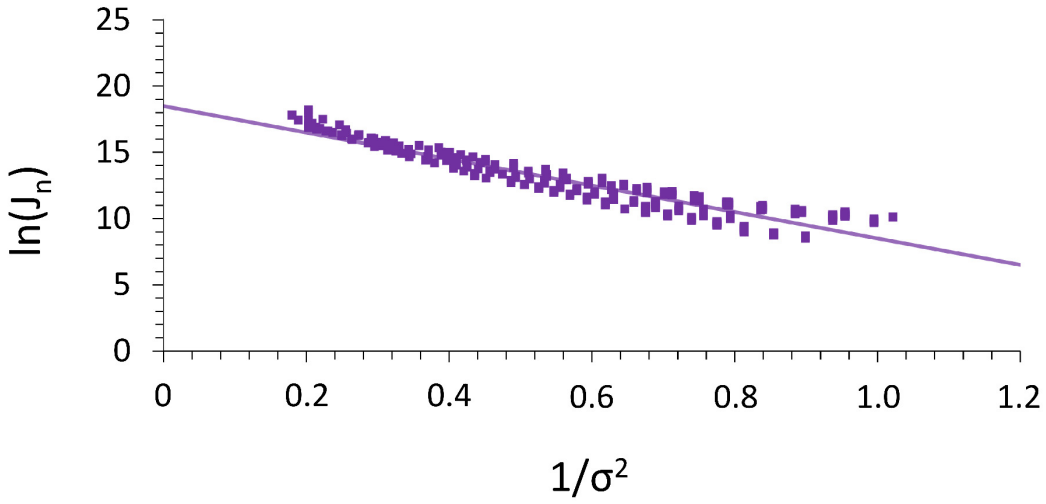

Figure 51. Plot of nucleation rates against supersaturations. The natural logarithm of the nucleation rates is plotted against the inverse square of the supersaturations for the analyzed combination: PAA gold nanocubes with amine-functionalized mica. A straight fit is performed for the data, linear equation: $y = -9.98\ x + 18.49$ ($R^2 = 0.89$).

From the slope of the plot in Figure 51 the effective interfacial energy was calculated to be $6.81 – 11.95 \cdot 10^{-6}$ J/m². The single values for the different assumed form factors are given in Table A 17 and summarized in Table 9. The effective interfacial energy for the PAA gold nanocubes was therewith higher compared to the energies of the CTAB gold nanocube systems. The higher effective interfacial energy indicated a more favorable interaction which fit the larger superstructures obtained for PAA gold nanocubes. Nevertheless, all determined effective interfacial energies were of the same order of magnitude.

Table 9. Calculated kinetic and thermodynamic parameters. The effective interfacial energy range for contact angles of 60° to 90°, the nucleation barrier, and the kinetic and thermodynamic term are given for the combination of PAA gold nanocubes with amine-functionalized mica. Since the thermodynamic term is dependent on the supersaturation σ, it was determined for supersaturations of 1.0 to 2.0.

particle substrate combination	effective interfacial energy α $[\frac{J}{m^2}]$	nucleation barrier Δg_n $[k_BT]$	thermodynamic term $\frac{fV_m^2}{(k_BT)^3}\alpha^3\left(\frac{1}{\sigma^2}\right)$	kinetic term $\ln\left(A * e^{-\frac{E_A}{k_BT}}\right)$
PAA - amine	6.81 – 11.95 · 10^{-6}	1.80 – 10.20	2.50 – 9.98	18.49

In the next step, the nucleation barriers of the system were calculated to an amount of 1.80 – 10.20 k_BT within the experimental supersaturations. The values are shown in Figure 52 and summarized in Table 9. The obtained nucleation barriers for supersaturations smaller than 1.5 are higher than the ones obtained for the CTAB gold nanocubes. One explanation might be the difference in the data acquisition. For the PAA gold nanocubes, it was possible to obtain many data points near the supersaturation of 1.0, which were determined at the end of the experiment times. While for the CTAB gold nanocubes individual experiments had to be performed for each supersaturation.

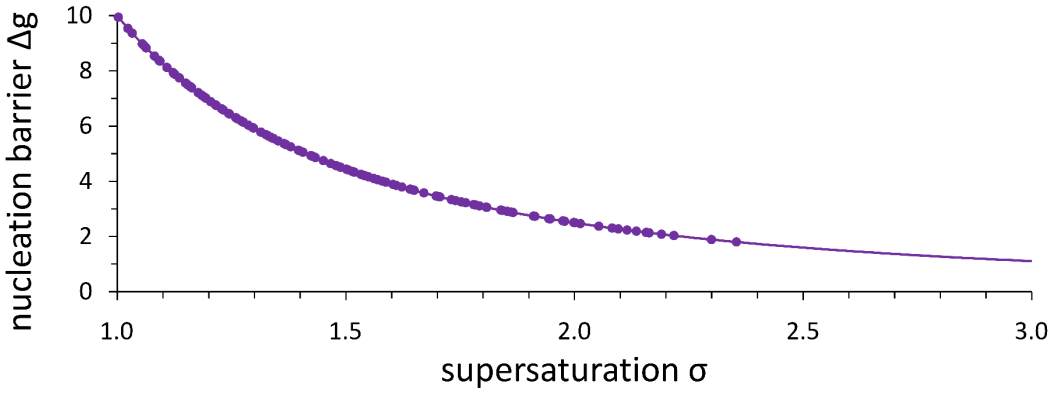

Figure 52. Nucleation barriers. The resulting nucleation barriers for the analyzed combination: PAA gold nanocubes with amine-functionalized mica. A fit was performed for the data, 9.99 · x^2 (R^2=1.00)

Beyond, the thermodynamic and kinetic terms were calculated for the heterogeneous nucleation of the PAA gold nanocubes (Table 9) and are depicted in Figure 53. The combination of PAA gold nanocubes with amine-functionalized substrates showed a thermodynamic term of 2.50 – 9.98 and a kinetic term of 18.49. The thermodynamic term had a higher proportion compared to the CTAB gold nanocube systems.

Nevertheless, the kinetic term still dominated the system and led to a kinetic hindrance of the heterogeneous nucleation of PAA gold nanocubes.

$$\ln(J_n) = -B\alpha^3\left(\frac{1}{\sigma^2}\right) + \ln\left(A\, e^{-\frac{E_A}{k_B T}}\right)$$

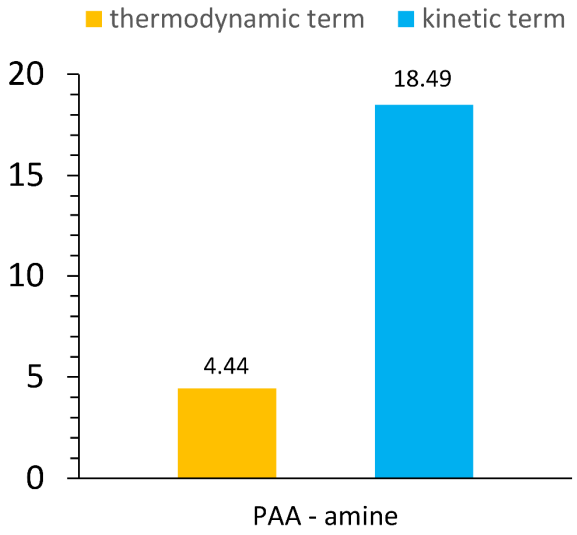

Figure 53. Kinetic versus thermodynamic term. Comparison of the share of the kinetic (blue) and the thermodynamic (orange) term of the nucleation rates for the combination of PAA gold nanocubes with amine-functionalized substrates. The thermodynamic term is calculated for a supersaturation of 1.5.

In summary, the heterogeneous nucleation of PAA gold nanocubes on amine-functionalized substrates was successfully analyzed in situ by light microscopy in combination with UV-vis-NIR spectroscopy. The adjustment of the gold nanocube supersaturation allowed a determination of nucleation rates at different supersaturations in one single experiment reducing the experimental effort tremendously. The so obtained data could be verified in additional experiments and allowed to calculate the nucleation rates, the effective interfacial energies, the nucleation barriers, and the thermodynamic and kinetic term. The determined values were comparable to the values obtained for CTAB gold nanocubes and showed the same dominating kinetic term.

6.1.4.3 PEG Gold Nanocubes

The analysis of the heterogeneous nucleation of PEG gold nanocubes so far revealed four interesting combinations resulting in superstructures, namely with alkyl-, hydroxyl-, carboxyl- and sulfonate-functionalized substrates (Figure 47). All observed superstructures of the four different substrates showed small island structures or huge networks. Nevertheless, the sizes of the island structures were small, barely reaching 1 µm, and the thickness of the network structures constituted only a few gold nanocubes. The majority of these small structure sizes were below the detection limit of around 0.9 µm of the light

microscope setup. Admittedly, it was possible detecting the upcoming superstructures as very fine noise in the microscopic images. However, the automated analysis of the number of structures revealed different trends depending on the sensitivity of the model and the optical density of the differently concentrated nanoparticle solutions, which even changed the sign of the straight-line slope (Figure A 54). Therefore, a more detailed analysis of the heterogeneous nucleation of PEG gold nanocubes with the light microscope setup was not possible.

Concluding this chapter, the impact of surface chemistry on heterogeneous nucleation could be successfully analyzed using the model system of nanoparticles as building blocks. The simple experiments with zinc oxide nanorods showed that depending on the interaction of the nanoparticle surface with the substrates' surface, structures could be varied from layer-like to three-dimensional superstructures.
In the following, the impact of surface chemistry was analyzed in more detail with the system of gold nanocubes where 18 different surface chemistry combinations could be studied. First, the impact of the substrates' surface chemistry on the destabilization kinetics of the gold nanocubes in solution was analyzed by UV-vis-NIR spectroscopy. The destabilization of the gold nanocubes in solution did not seem to follow exclusively a homogeneous nucleation pathway. Here, the studies revealed a huge enhancement of the destabilization kinetics for a favorable interaction of the gold nanocubes with the substrates. While unfavorable interactions did not influence the destabilization kinetics. The analysis of the destabilization kinetics indicated that the gold nanocube destabilization proceeded as a second-order reaction and the rate constants for the 18 different surface combinations could be determined. Second, the superstructures formed on the substrates were analyzed. The results fit well the kinetic studies and favorable interactions resulted not only in the enhancement of the destabilization kinetics but also in huge superstructures on the substrate's surface.
The favorable interaction of CTAB gold nanocubes with sulfonate- and carboxyl-functionalized substrates and of PAA gold nanocubes with amine-functionalized substrates allowed a quantitative analysis of the heterogeneous nucleation process using time-resolved light microscopy and simultaneous UV-vis-NIR spectroscopy. Therewith, the nucleation rates could be determined successfully and allowed further the calculation of the interfacial energies, the nucleation barriers, and the thermodynamic and kinetic terms. The results fit well the previous insights. Further, for all three systems, a noticeable dominating kinetic term was observed revealing the differences of nanoparticles as building blocks showing a slow diffusion compared to faster diffusing ions or molecules.

6.2 Appendix

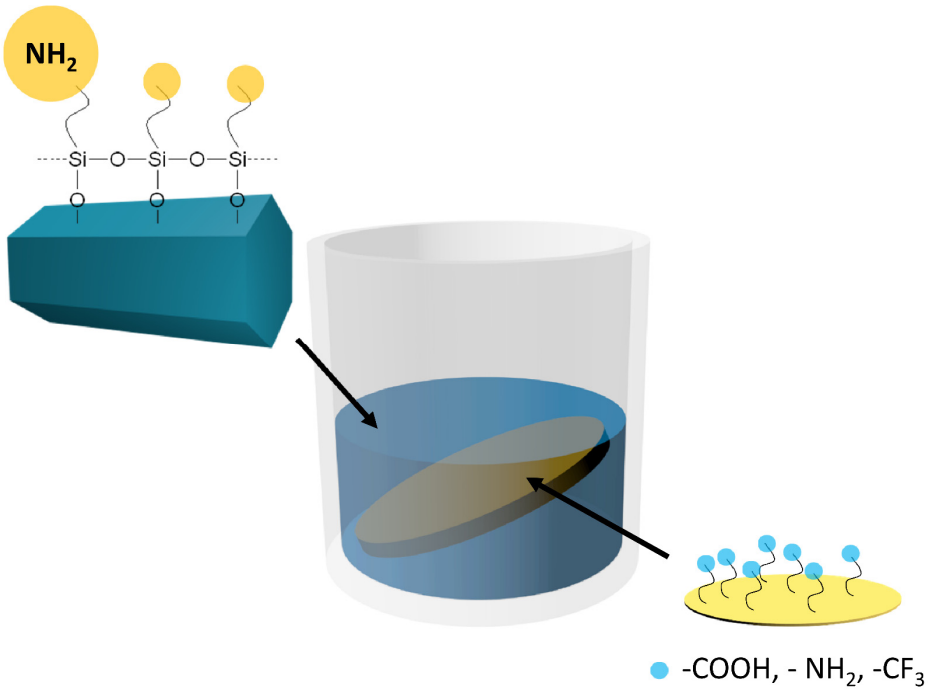

Figure A 45. Illustration of the experimental setup for the formation of zinc oxide nanorod-based superstructures. An amine-functionalized zinc oxide nanorod dispersion is evaporated. The zinc oxide nanorods assemble at a mica substrate, which is placed at an angle in the vessel. The mica substrate was functionalized respectively with carboxyl (-COOH), amine ($-NH_2$), or fluorine ($-CF_3$) groups.

Table A 11. Counted zinc oxide nanorod superstructures. The superstructures formed by zinc oxide nanorods on differently functionalized substrates were analyzed by light microscopy and the percentage of the analyzed substrate surface covered with superstructures and the average size of superstructures are given.

substrate functionality	% area	average size [µm²]
COOH	43.09	331.87
NH_2	9.39	42.95
CF_3	9.10	90.77

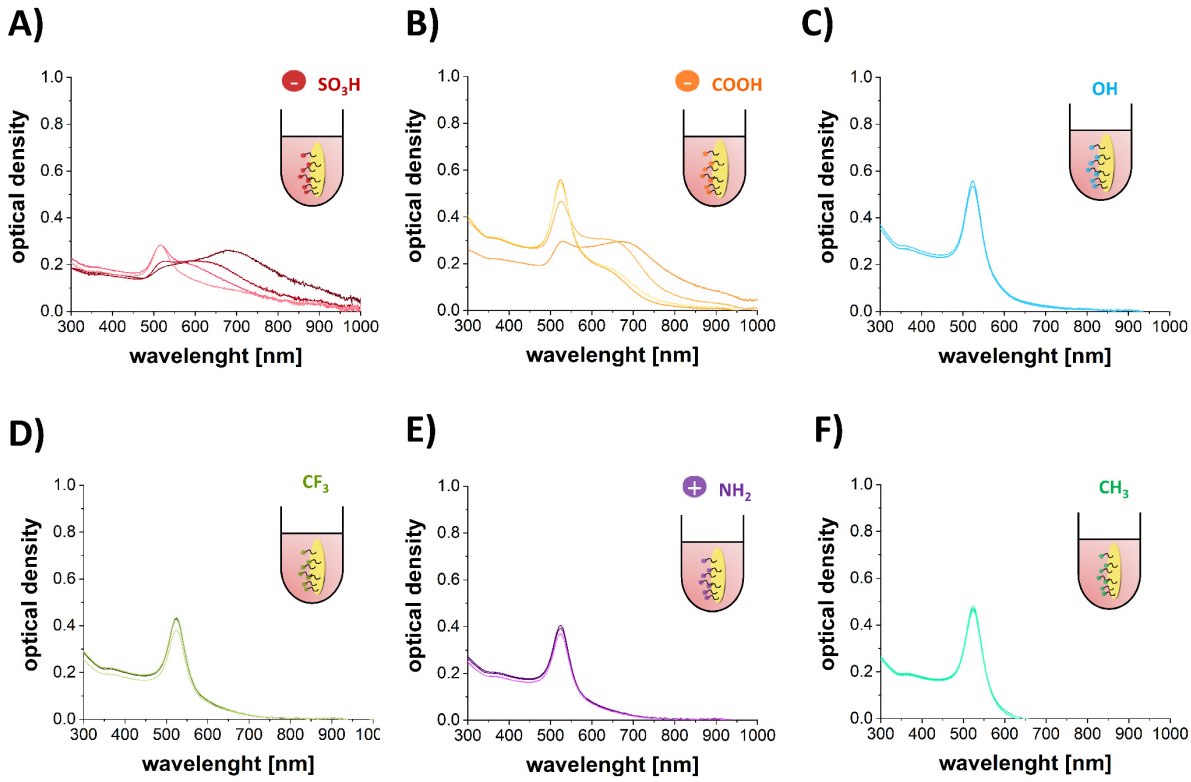

Figure A 46. Destabilization in presence of functionalized mica substrates after 15 min. CTAB gold nanocube dispersions were destabilized with ethanol in presence of different functionalized mica substrates. UV-vis-NIR spectra of the dispersions were measured after 15 min of each three samples per functionalization: A) sulfonate, B) carboxyl, C) hydroxyl, D) fluorine, E) amine, and F) alkyl.

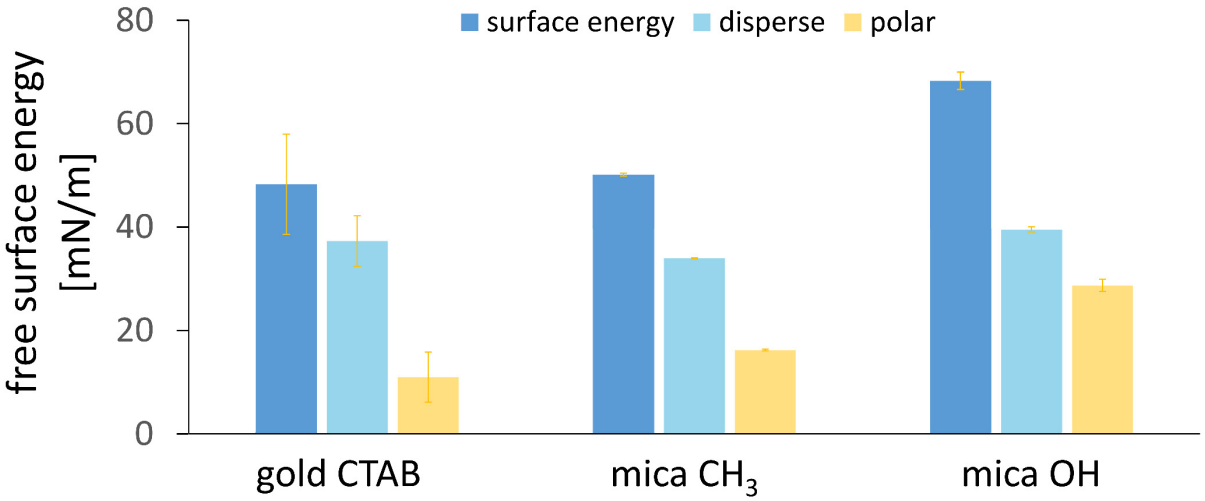

Figure A 47. Comparison of free surface energies for understanding the interaction of gold nanocubes and substrates. The graph shows the free surface energy and its' disperse and polar parts of CTAB-functionalized gold (Chapter 4.1.2) compared to mica substrates functionalized with hydroxyl (OH) or carbonyl (CH_3) groups. For a favorable interaction, not only the total value of the free surface energy should be similar in size but also the disperse and polar parts have to be comparable. The comparison of the three surface energies indicates that gold functionalized with CTAB is more

comparable with the carbonyl (CH_3) functionalization than with the hydroxyl (OH) functionalization of substrates. This may explain why the carbonyl (CH_3) functionalization destabilized CTAB-functionalized gold nanocubes faster, than the hydroxyl (OH) functionalization does.

Table A 12. Determination of the reaction order (CTAB gold nanocubes). Determination of the reaction order for the nucleation of CTAB gold nanocube superstructures on sulfonate-, carboxyl-, hydroxyl-, and alkyl-functionalized substrates. The optical density at the respective absorption maxima is plotted linearly against the experiment time dependent on the assumed reaction order. The R^2 values, which describe the quality of the linear fit, are given.

assumed reaction order	plot	sulfonate	carboxyl	hydroxyl	alkyl
0. order	Abs → t	0.84	0.94	0.83	0.92
1. order	ln(Abs) → t	0.96	0.95	0.85	0.94
2. order	1/Abs → t	0.98	0.96	0.88	0.96

Table A 13. Determination of the reaction order (PAA gold nanocubes). Determination of the reaction order for the nucleation of PAA gold nanocube superstructures on amine-, sulfonate-, carboxyl-, hydroxyl-, alkyl- and fluorine-functionalized substrates. The optical density at the respective absorption maxima is plotted linearly against the experiment time dependent on the assumed reaction order. The R^2 values, which describe the quality of the linear fit, are given.

assumed reaction order	plot	amine	sulfonate	carboxyl	hydroxyl	alkyl	fluorine
0. order	Abs → t	0.80	0.79	0.89	0.85	0.93	0.89
1. order	ln(Abs) → t	0.90	0.96	0.94	0.93	0.96	0.99
2. order	1/Abs → t	0.96	0.95	0.98	0.98	0.99	0.96

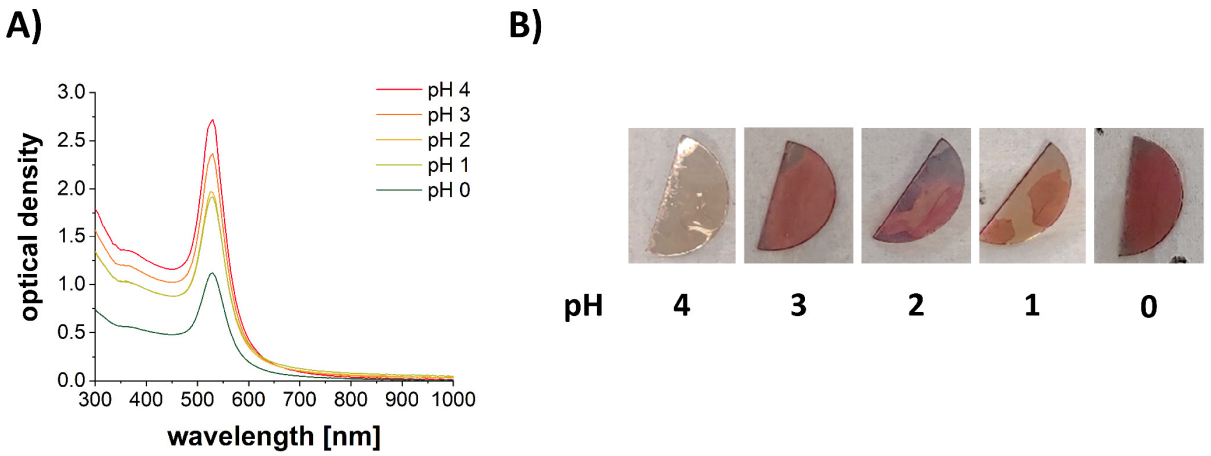

Figure A 48. Destabilization of PEG gold nanocubes dependent on the pH value. Hydrochloric acid was added to PEG gold nanocube dispersions to reach pH values of 4, 3, 2, 1, and 0 in the presence of carboxyl-functionalized mica substrates. A) The optical density of the PEG gold nanocube dispersions is measured by UV-vis-NIR spectroscopy after 36 h. The spectra show only the plasmon absorption band of single gold nanocubes at 523 nm and no absorption of larger gold nanocube-based superstructures. However, the intensity of the absorption band decreases with decreasing pH value indicating a loss of PEG gold nanocubes. B) Photographs of the carboxyl-functionalized substrates after 36 h. The mica substrate placed in the dispersion at pH 4 shows no change and is still colorless. In contrast, the mica substrates placed in the dispersions at pH values of 3 and less show red to purple colors indicating PEG gold nanocubes on the substrates.

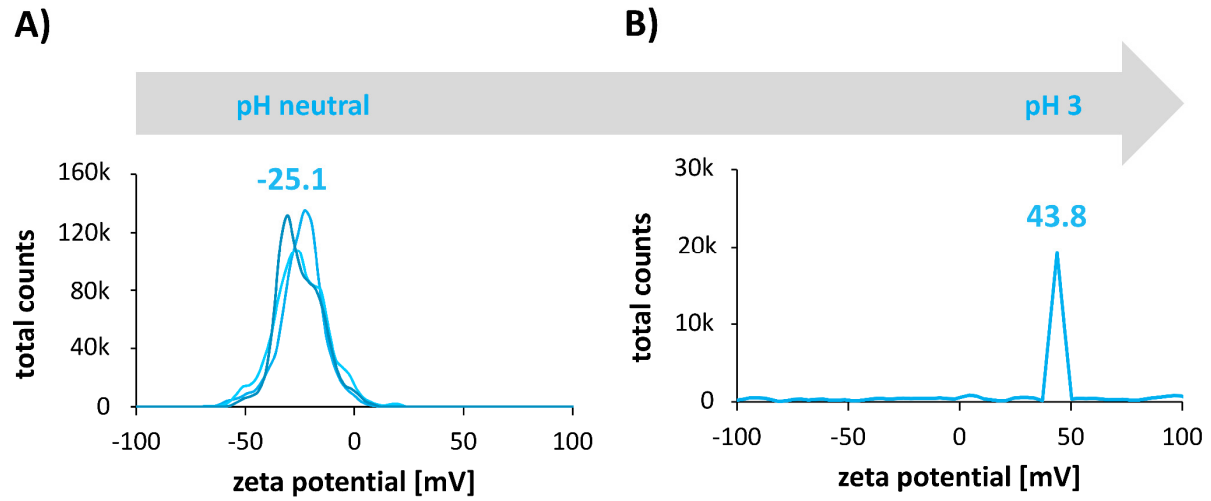

Figure A 49. Zeta potential measurements of PEG gold nanocube dispersions dependent on the pH value. For PEG gold nanocube dispersions, a negative zeta potential of -25.1 mV is determined for a solution with neutral pH. With the addition of hydrochloric acid to reach a pH value of 3, the zeta potential of the PEG gold nanocube dispersion increases to 43.8 mV.

Table A 14. Determination of the reaction order (PEG gold nanocubes). Determination of the reaction order for the nucleation of PEG gold nanocube superstructures on amine-, sulfonate-, carboxyl-, hydroxyl-, alkyl- and fluorine-functionalized substrates. The optical density at the respective absorption maxima is plotted linearly against the experiment time dependent on the assumed reaction order. The R^2 values, which describe the quality of the linear fit, are given.

assumed reaction order	plot	amine	sulfonate	carboxyl	hydroxyl	alkyl	fluorine
0. order	Abs → t	0.80	0.79	0.88	0.91	0.82	0.92
1. order	ln(Abs) → t	0.86	0.91	0.95	0.96	0.95	0.96
2. order	1/Abs → t	0.97	0.99	0.99	0.99	0.99	0.99

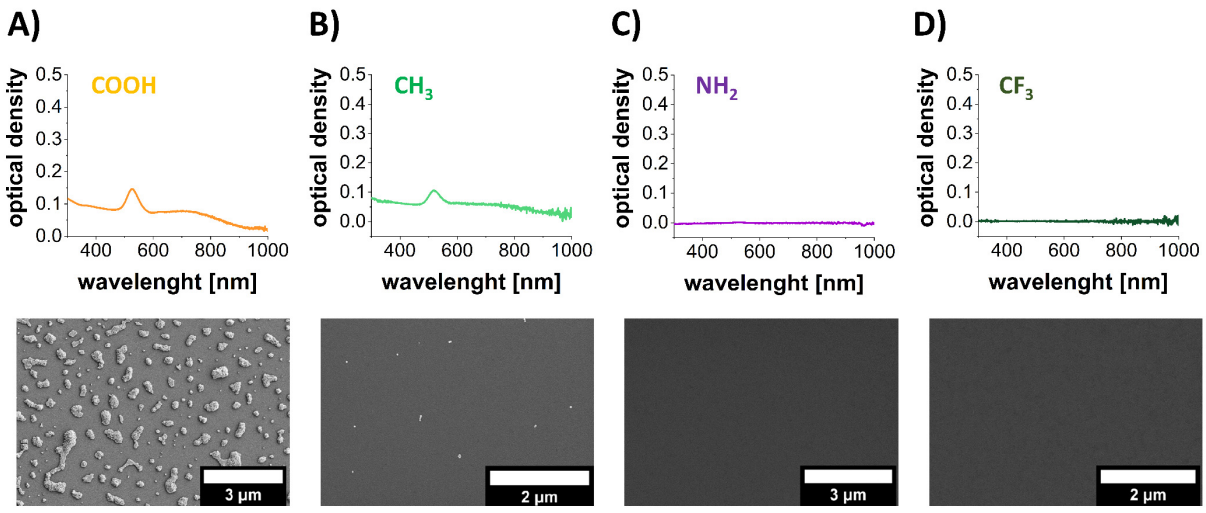

Figure A 50. CTAB gold nanocube-based superstructures. CTAB gold nanocubes were destabilized in presence of different functionalized substrates: A) carboxyl, B) alkyl, C) amine, and D) fluorine. The upper row shows UV-vis-NIR spectra of functionalized quartz cuvettes after the destabilization experiments. The bottom row shows SEM images of respectively functionalized mica substrates after the destabilization experiments

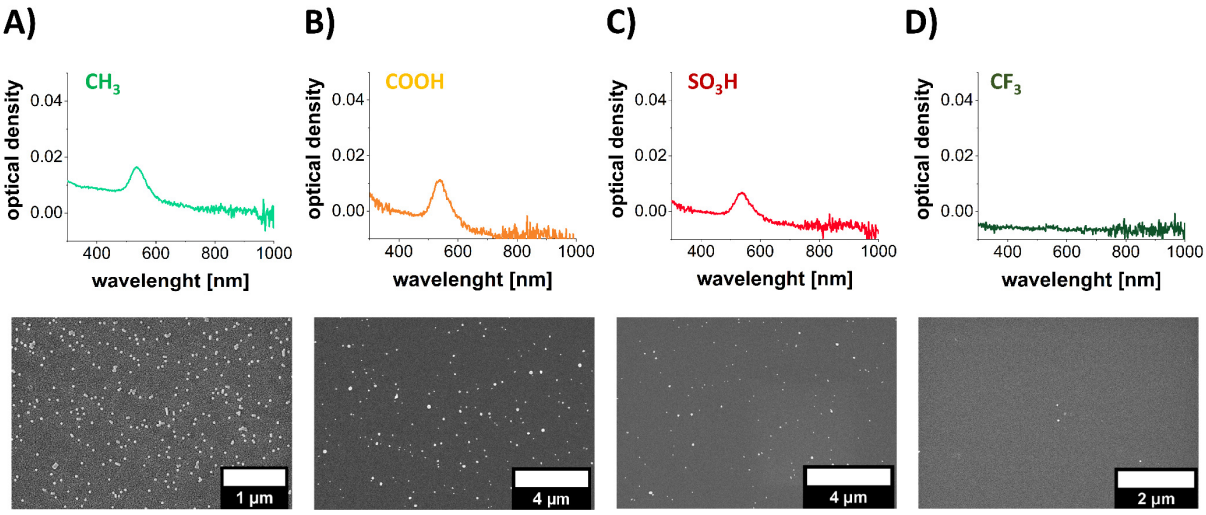

Figure A 51. PAA gold nanocube-based superstructures. PAA-functionalized gold nanocubes were destabilized in presence of different functionalized substrates: A) alkyl, B) carboxyl, C) sulfonate, and D) fluorine. The upper row shows UV-vis-NIR spectra of functionalized quartz cuvettes after the destabilization experiments. The bottom row shows SEM images of respectively functionalized mica substrates after the destabilization experiments.

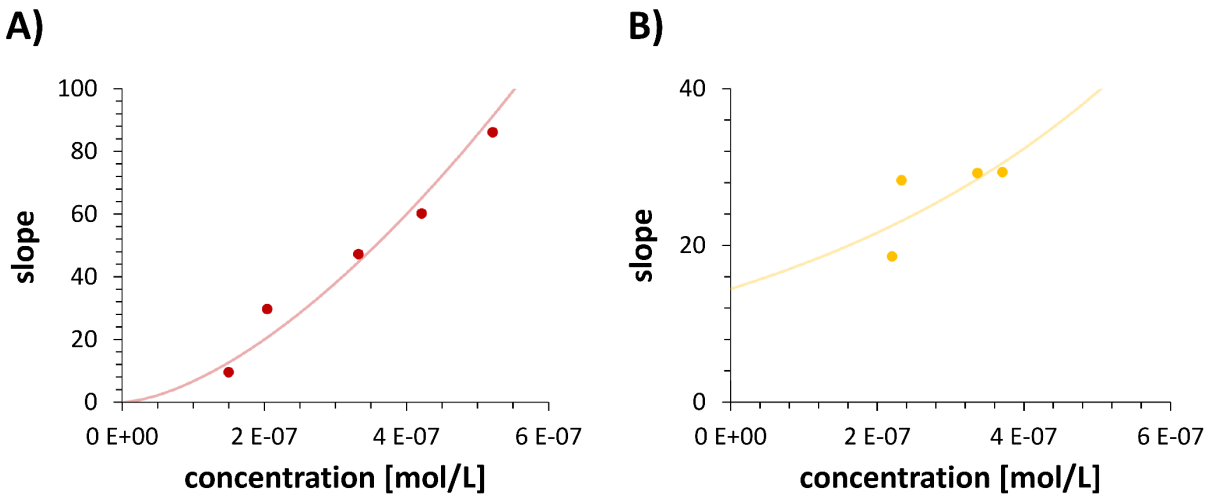

Figure A 52. Determined slopes for the calculation of nucleation rates (CTAB gold nanocubes). The graphs show determined slopes for the plots of the number of counted structures against the experiment time dependent on the concentration of CTAB gold nanocubes: for the combination with A) sulfonate- and B) carboxyl-functionalized mica substrates.

Table A 15. Determined nucleation rates for CTAB gold nanocubes. Summarized results for the nucleation rates of the different particle substrate combinations dependent on the CTAB gold nanocube

concentration. The mean R^2 value for the straight lines fitted to the plot of counted structures (used to determine the nucleation rates) is given as well.

combination	concentration gold nanocubes [mol/ L]	R^2	J_n [germs/s·m²]
CTAB - sulfonate	$1.50 \cdot 10^{-07}$	0.81	$2.04 \cdot 10^6 \pm 1.18 \cdot 10^6$
	$2.04 \cdot 10^{-07}$	0.95	$6.03 \cdot 10^6 \pm 0.62 \cdot 10^6$
	$3.33 \cdot 10^{-07}$	0.85	$1.00 \cdot 10^6 \pm 0.01 \cdot 10^7$
	$4.22 \cdot 10^{-07}$	0.99	$1.28 \cdot 10^7 \pm 0.45 \cdot 10^7$
	$5.21 \cdot 10^{-07}$	0.99	$1.83 \cdot 10^7 \pm 0.18 \cdot 10^7$
CTAB - carboxyl	$2.20 \cdot 10^{-07}$	0.92	$3.95 \cdot 10^6 \pm 3.45 \cdot 10^6$
	$2.33 \cdot 10^{-07}$	0.94	$7.17 \cdot 10^6 \pm 3.74 \cdot 10^6$
	$3.37 \cdot 10^{-07}$	0.77	$6.21 \cdot 10^6 \pm 2.66 \cdot 10^6$
	$3.71 \cdot 10^{-07}$	0.84	$6.23 \cdot 10^6 \pm 2.31 \cdot 10^6$

Table A 16. Calculation of the effective interfacial energy α for different form factors for CTAB gold nanocubes.

particle substrate combination	form factor *f*	effective interfacial energy α
CTAB - sulfonate	2.62 (60°)	$9.17 \cdot 10^{-6}$ J/m²
	8.38 (90°)	$6.22 \cdot 10^{-6}$ J/m²
	14.14 (120°)	$5.23 \cdot 10^{-6}$ J/m²

CTAB - carboxyl	2.62 (60°)	$4.59 \cdot 10^{-6}$ J/m²
	8.38 (90°)	$3.12 \cdot 10^{-6}$ J/m²
	14.14 (120°)	$2.62 \cdot 10^{-6}$ J/m²

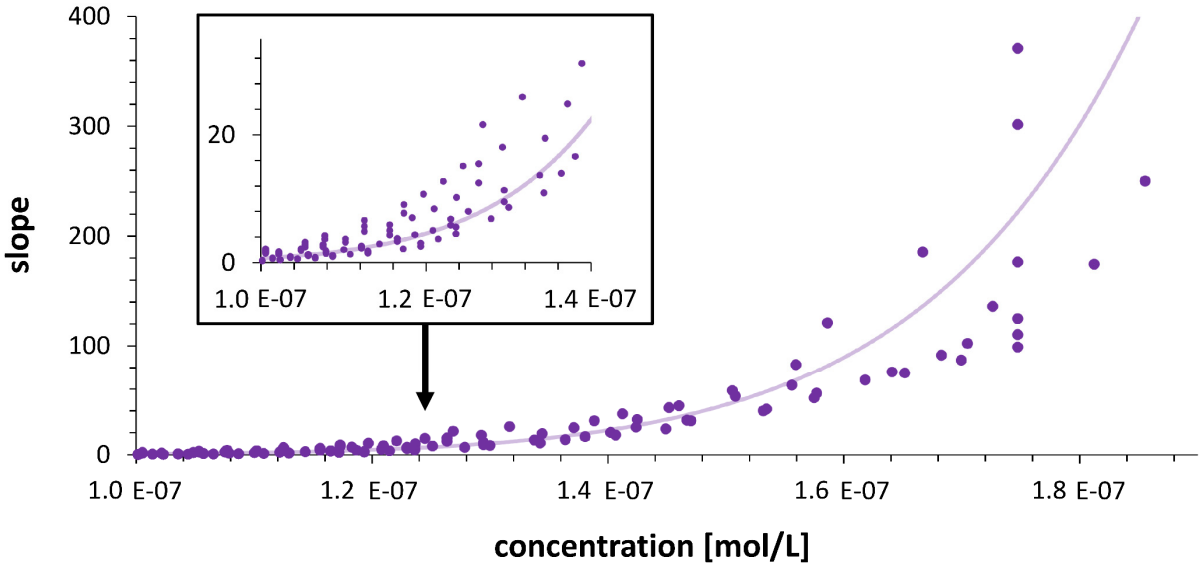

Figure A 53. Determined slopes for the calculation of nucleation rates (PAA gold nanocubes). The graph shows determined slopes for the plots of the number of counted structures against the experiment time dependent on the concentration of PAA gold nanocubes: for the combination with amine-functionalized mica substrates. A fit is performed for the data: $1 \cdot 10^{72} \cdot x^{10.33}$ ($R^2 = 0.92$).

Table A 17. Calculation of the effective interfacial energy α for different form factors for PAA gold nanocubes.

particle substrate combination	form factor *f*	effective interfacial energy α
PAA - amine	2.62 (60°)	$11.95 \cdot 10^{-6}$ J/m²
	8.38 (90°)	$8.11 \cdot 10^{-6}$ J/m²
	14.14 (120°)	$6.81 \cdot 10^{-6}$ J/m²

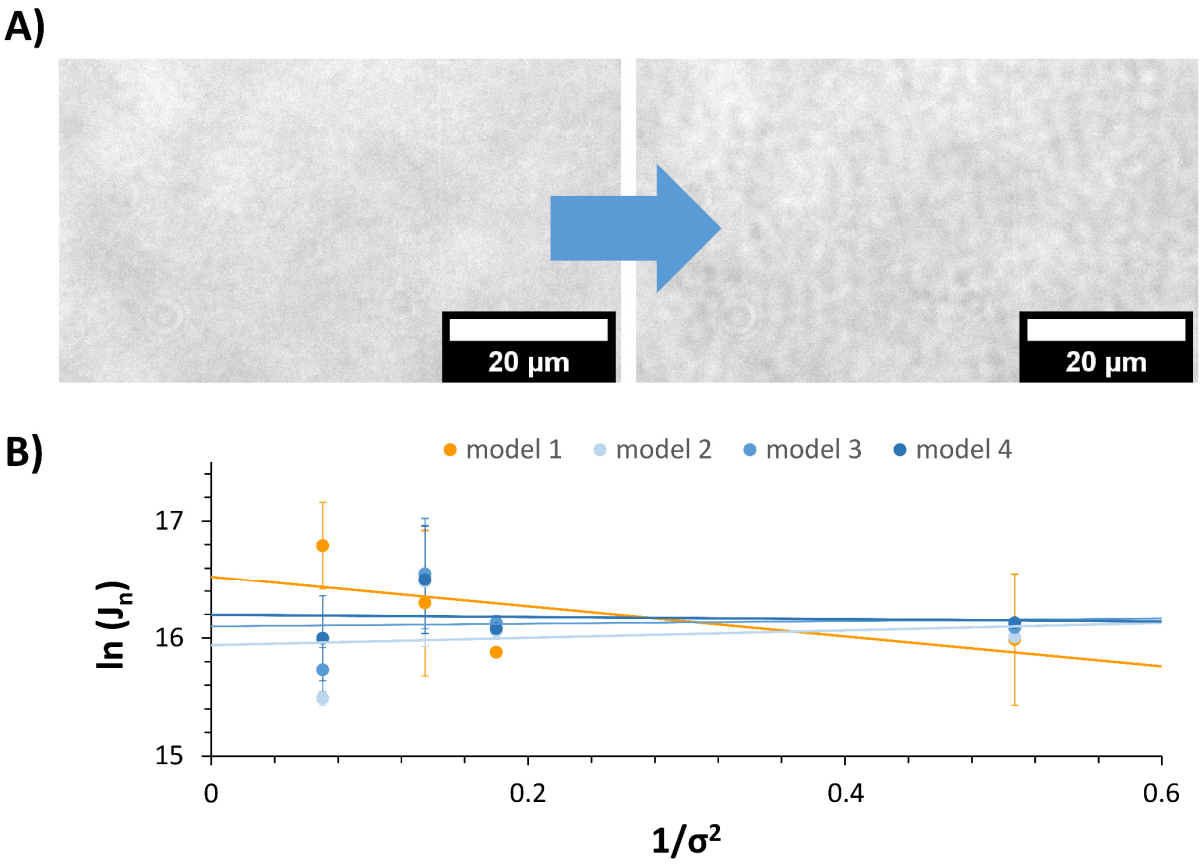

Figure A 54. Microscopic analysis of the heterogeneous nucleation of PEG gold nanocube superstructures on carboxyl-functionalized substrates. A) Light microscope images before (left) and after (right) the heterogeneous nucleation process. The resulting superstructures are below the resolution limit and are only visible through the noise of the image. B) Plot of the logarithm of counted nucleation rates against the inverse square of the supersaturations. The analysis via different sensitive models shows that the number of structures cannot be calculated properly through the noise of the image and the straight fits vary dramatically with the sensitivity of the respective model.

6.3 Materials and Methods

6.3.1 Instruments

For **contact angle** and free surface energy measurements, the drop shape analyzer *DSA25* and the software *Advance* from *Krüss* were used. Contact angles larger than 10° were fitted with the *Ellipse (Tangent-1)* model, while contact angles smaller than 10° were fitted with the *Circle* model. The free surface energies were calculated with the contact angles from water and diiodomethane over the *Owens, Wendt, Rabel and Kaelble* (*OWRK)* model.

Light microscopy images were recorded with an *AxioImager* from *Zeiss* with an LD Epiplan 50x/0.50 HD DIC objective using transmitted light, bright field illumination, a condenser numerical aperture at 0.9, an Axiocam 506 bw as an imaging device, and an exposure time of 10 ms.

SEM images were recorded with a *Gemini500* by *Zeiss* operating at 3 kV equipped with an Inlens and a secondary electron detector for secondary and backscattered electrons. Samples were coated with a 2.5 nm platinum layer, mounted on aluminum stubs, and attached by carbon conductive layers.

UV-vis-NIR measurements were performed with a *Varian Cary 50* spectrometer in quartz cuvettes. The UV-vis-NIR measurements carried out simultaneously with light microscopy measurements were performed with a modular *USB2000+* spectrometer from *Ocean Optics* equipped with a *USB-DT* miniature deuterium tungsten halogen lamp.

6.3.2 Methods

Table 10. Summary of the experimental conditions for the nucleation experiments with CTAB-functionalized gold nanocubes.

experiment	reaction vessel	surface	ethanol content [vol.-%]	surface/ volume ratio [1/cm]	absorption at 523 nm [a.u.]
introducing substrate	micro test tube	mica functionalized	31	0.39	1.5 - 1.7
kinetics	quartz cuvette	cuvette wall functionalized	15	2.45	1.5 - 1.7
light microscopy	hydropho-bized cuvette	mica functionalized	12	0.09	0.7 - 2.3

Table 11. Summary of the experimental conditions for the nucleation experiments with PAA-functionalized gold nanocubes.

experiment	reaction vessel	surface	calcium chloride content [vol.-%]	surface/ volume ratio [1/cm]	absorption at 523 nm [a.u.]
introducing substrate	micro test tube	mica functionalized	36 10 mM $CaCl_2$	0.87	1.5 – 1.7
kinetics	quartz cuvette	cuvette wall functionalized	36 10 mM $CaCl_2$	2.45	1.5 – 1.7
light microscopy	hydropho-bized cuvette	mica functionalized	37 10 mM $CaCl_2$	0.09	1.5 – 1.7

Table 12. Summary of the experimental conditions for the nucleation experiments with PEG-functionalized gold nanocubes.

experiment	reaction vessel	surface	hydrochloric acid content [vol.-%]	surface/ volume ratio [1/cm]	absorption at 523 nm [a.u.]
introducing substrate	micro test tube	mica functionalized	1 0.1 M HCl	0.87	1.5 – 1.7
kinetics	quartz cuvette	cuvette wall functionalized	1 0.1 M HCl	2.45	1.5 – 1.7
light microscopy	hydropho-bized cuvette	mica functionalized	1 0.1 M HCl	0.09	1.5 – 1.7

7 Influence of Particle Anisotropy on Heterogeneous Nucleation

After Chapter 6 explained the influence of surface chemistry on the heterogeneous nucleation with gold nanocubes, this chapter is going to deal with the influence of particle anisotropy on heterogeneous nucleation. Therefore, the three gold nanorods introduced in Chapter 5 were utilized exhibiting a similar structure and surface chemistry but differed only in their aspect ratios. By comparing the heterogeneous nucleation of the three gold nanorods with different aspect ratios under the same conditions, the influence of the aspect ratio on the nucleation process could be determined. Herein again, the analysis of the heterogeneous nucleation and the calculation of corresponding nucleation parameters were performed in combination with light microscopy and UV-vis-NIR spectroscopy and the methods introduced in Chapter 5.

7.1 Results and Discussion

7.1.1 Microscopic Analysis of Heterogeneous Nucleation

In Chapter 4.1.3, gold nanorods were introduced with different aspect ratios (3.00, 2.25, and 1.75). As these gold nanorods were stabilized with CTAB, a controlled destabilization was successfully conducted by the addition of ethanol (Figure 25). Analysis of the destabilization kinetics showed that the reactions proceeded as a second-order reaction similar to the destabilization of the gold nanocubes in Chapter 6.1.2 (Table A 18). These findings suggested a mechanism based on bimolecular collisions. After a methodology for the controlled destabilization of gold nanorods was established, the next step aimed to accomplish heterogeneous nucleation and growth of the gold nanorod-based superstructures triggered by substrates. Chapter 6 found out that the interaction between positively charged CTAB gold nanocubes and negatively charged sulfonate-functionalized substrates is the most preferred amongst the analyzed substrate functionalizations. The interaction of the gold nanorods with the sulfonate-functionalized mica substrates was evaluated by destabilizing gold nanorods with ethanol in the presence of these substrates via UV-vis-NIR spectroscopy. After that, the self-assembly kinetics were compared with that of samples destabilized in the absence of substrates (Figure A 55). The experiments showed that sulfonate-functionalized substrates successfully enhanced the destabilization of the gold nanorod dispersions, due to the favorable interaction. Thus, the combination with sulfonate-functionalized substrates was chosen for the heterogeneous nucleation experiments to ensure a gold nanorod-based superstructure growth on the substrates.

In the next step, the heterogeneous nucleation of gold nanorod-based superstructures on sulfonate-functionalized mica substrates was analyzed with light microscopy and simultaneous UV-vis-NIR spectroscopy. The experimental approach and the evaluation of the resulting data were described in detail in Chapter 5 and the experimental conditions for the gold nanorods are described in chapter 7.3.3. The gold

nanorod dispersions were destabilized in a controlled manner with 20 vol.-% ethanol to ensure the colloidal stability of the gold nanorods in dispersion while enabling the superstructure growth on the substrates (Figure A 56). Figure 54 shows a detailed comparison of the results obtained from the different investigated nanorod aspect ratios. The number of superstructures detected on the substrate via light microscopy, their formation speed and with it the slope correlate with the anisotropy degree of the gold nanorods. For instance, gold nanorods with a high aspect ratio (3.00) tended to form fewer superstructures and exhibited lower nucleation rates. Whereas, those gold nanorods with a lower aspect ratio (1.75) nucleated faster and formed a higher number of superstructures.

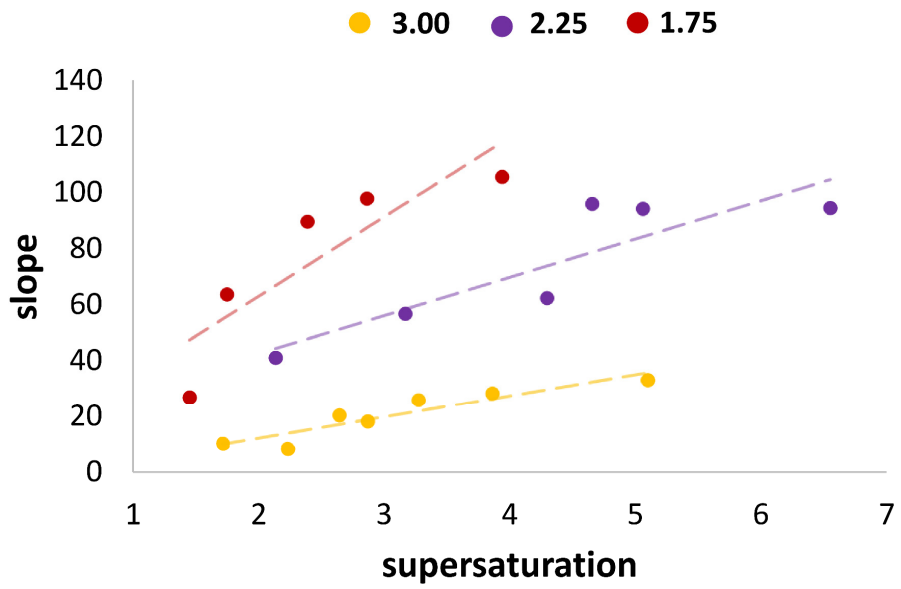

Figure 54. Slopes of superstructure growth dependent on the aspect ratio. The determined slopes are the number of counted superstructures against the experiment time, which is equivalent to the unnormalized nucleation rate. These slopes are plotted against the supersaturation for gold nanorods with varying aspect ratios: 3.00 (yellow), 2.25 (purple), and 1.75 (red).

A logarithmic plot of the nucleation rates J_n against the inverse square of the supersaturations σ (Figure 55) allowed determining the interfacial energies for the heterogeneous nucleation process as described in Chapter 5.1.2.3. The calculated interfacial energies are summarized in Table A 19. Herein, the interfacial energies increased with decreasing gold nanorod aspect ratio.

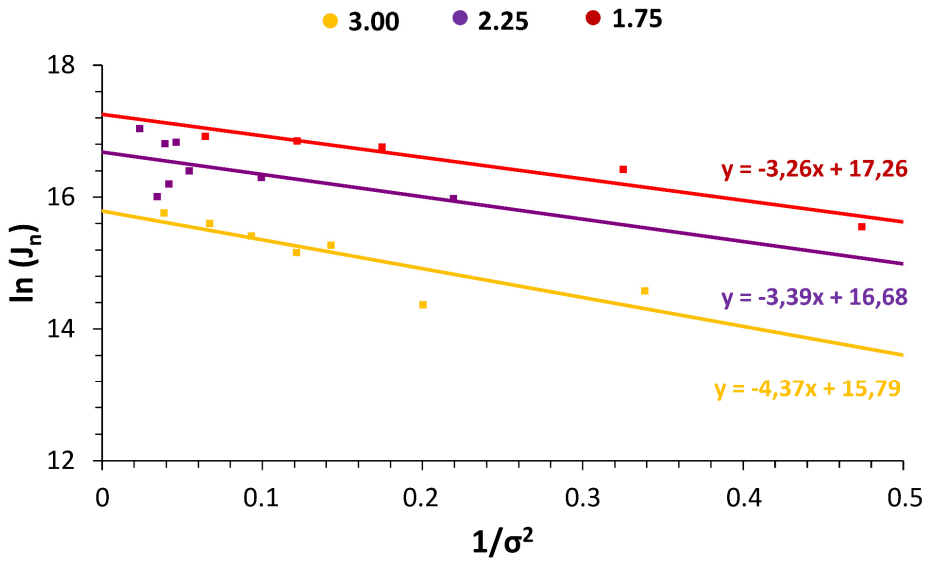

Figure 55. Nucleation rates versus supersaturations. The logarithms of the determined nucleation rates are plotted against the inverse square of the supersaturation for gold nanorods with aspect ratios of 3.00 (yellow), 2.25 (purple), and 1.75 (red). The nucleation rates correlate with the aspect ratio of the gold nanorods.

Further on, the nucleation barrier for the heterogeneous nucleation of the gold nanorods on sulfonate-functionalized mica were calculated as described in Chapter 5.1.2.3. Figure 56 shows the nucleation barriers obtained for different gold nanorod supersaturations. In general, the obtained nucleation barriers were low compared to the thermal energy, thereby favoring nucleation without thermodynamic barrier at $\sigma > 2$ for all analyzed aspect ratios. This result is not surprising if the opposite charges of particles and substrates are considered. Furthermore, the nucleation barriers augmented with increasing aspect ratio: gold nanorods with an aspect ratio of 3.00 exhibited the highest nucleation barriers (1.09 k_BT for $\sigma = 2$), while those of 2.25 and 1.75 differed hardly in terms of their magnitude (0.85 k_BT and 0.82 k_BT, respectively for $\sigma = 2$).

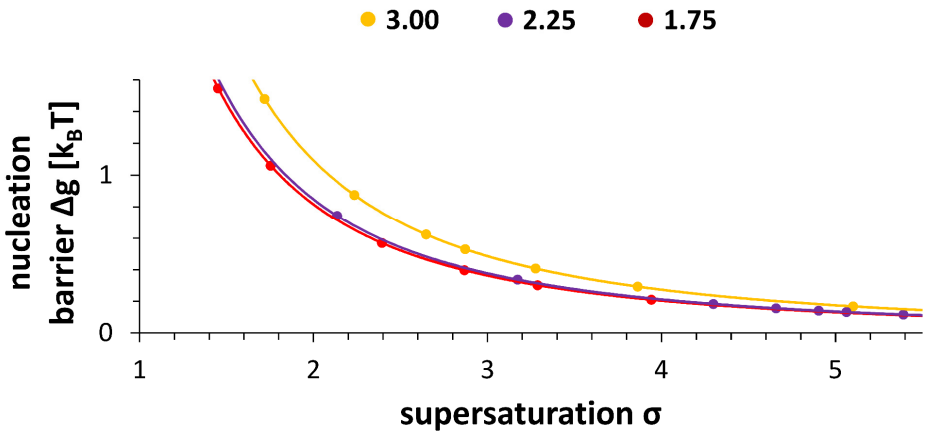

Figure 56. Nucleation Barrier. The nucleation barrier determined for the heterogeneous nucleation of gold nanorods is plotted against the supersaturation. The gold nanorods differ in their aspect ratio: 3.00 (yellow), 2.25 (purple), and 1.75 (red).

Finally, the kinetic and thermodynamic terms for the heterogeneous nucleation of the invested gold nanorod superstructures were calculated (Table 13). A low correlation was observed between the magnitude of the kinetic terms and the nanorod anisotropy. For instance, the kinetic term increased when lowering the aspect ratios, indicating a decrease of E_A consistent with the higher nucleation rates depicted in Figure 54. However, the obtained values hardly differed and were of the same magnitude. The magnitude of the thermodynamic term related to the nucleation barrier depends on the supersaturation σ and was determined for supersaturations of 1.0 and two typical supersaturations from the experiments: 1.5 and 2.0 (Table 13). The thermodynamic terms were decreasing in absolute numbers with decreasing aspect ratio indicating a decreasing nucleation barrier, which makes nucleation with a high aspect ratio thermodynamically less favorable than nucleation with a low aspect ratio. In general, the values of the kinetic terms are dominating even for the lowest supersaturation of 1.0. This order of magnitude of thermodynamic and kinetic terms was also obtained in Chapter 6 for the nucleation of gold nanocubes and stands in contrast to molecular or ionic systems, for example, the nucleation of calcium carbonate on organothiol self-assembled monolayers.[26] At a rough estimate from the published graph, these examined systems showed thermodynamic terms of about -550, for a supersaturation σ of 1.0, which were significantly larger than the kinetic terms of around 40. The difference between the nanoparticle systems to ionic and molecular systems could be explained by a higher impact of diffusion for the nucleation of larger nanoparticles compared to small ions or molecules. This impact would make diffusion a crucial aspect for the heterogeneous nucleation of nanoparticles due to the more limited supply of building units to the nucleation site as compared to fast diffusing ions or atoms. The increasing kinetic term with decreasing aspect ratios could support this idea (Table 13). Furthermore, a stronger diffusion is observed for the rods with a lower aspect ratio compared to those with a larger aspect ratio due to the larger hydrodynamic radii and the larger volume of the latter. In addition, these findings are supported by the results obtained in Chapter 6 for CTAB gold nanocubes nucleating on sulfonate-functionalized mica through a destabilization with ethanol. In principle, the CTAB functionalization, the destabilization with ethanol, and the sulfonate-functionalized substrate were the same compared to the experiments with gold nanorods. Further, the gold nanocubes can be considered as gold nanorods with an aspect ratio of 1.00. Very rapid nucleation was observed for the gold nanocubes, which fits well into the series of the decreasing aspect ratios obtained here for the gold nanorods. Though, the exact values of the two systems cannot be compared since the gold nanocubes were destabilized with 12.36 vol.-% ethanol and the gold nanorods with 20 vol.-%. Additionally, performing the experiments for the gold nanocubes with a higher ethanol concentration was not possible since the nucleation proceeded too fast to be monitored. However, in summary, the rapid nucleation for CTAB gold nanocubes is consistent with the results obtained for the gold nanorods with different aspect ratios.

Table 13. Kinetic and thermodynamic term. The kinetic and thermodynamic terms determined for the heterogeneous nucleation of gold nanorod-based superstructures on sulfonate-functionalized mica substrates. Since the thermodynamic term is dependent on the supersaturation σ, it is determined for supersaturations of 1.0, 1.5, and 2.0.

	3.00	**2.25**	**1.75**
kinetic term	15.79	16.68	17.26
thermodynamic term with σ = 1.0	-4.37	-3.39	-3.26
thermodynamic term with σ = 1.5	-1.94	-1.51	-1.45
thermodynamic term with σ = 2.0	-1.09	-0.85	-0.82

7.1.2 Superstructure Formation on Substrates dependent

After the investigation of the heterogeneous nucleation kinetics of gold nanorods with varying aspect ratios, the gold nanorod-based superstructures formed on the substrates were analyzed. Therefore, the approaches described in Chapter 5.1.1.3 were used. The upper rows of Figure 57 show SEM images of the gold nanorod-based superstructures formed on sulfonate-functionalized substrates. Here, the rods form randomly organized assemblies, which is not surprising given the short building time of 40 min. The rods with an aspect ratio of 3.00 formed superstructures up to a size of around 5 μm, which tended to be elongated and tattered and grew mostly in one spatial direction. However, lower aspect ratios (2.25 and 1.75) lead to more and denser-packed gold nanorod superstructures with larger dimensions in two spatial directions of up to 10 μm for the aspect ratio of 1.75 (Table A 20, Figure A 57). These findings are consistent with the obtained higher nucleation rates for smaller aspect ratios.

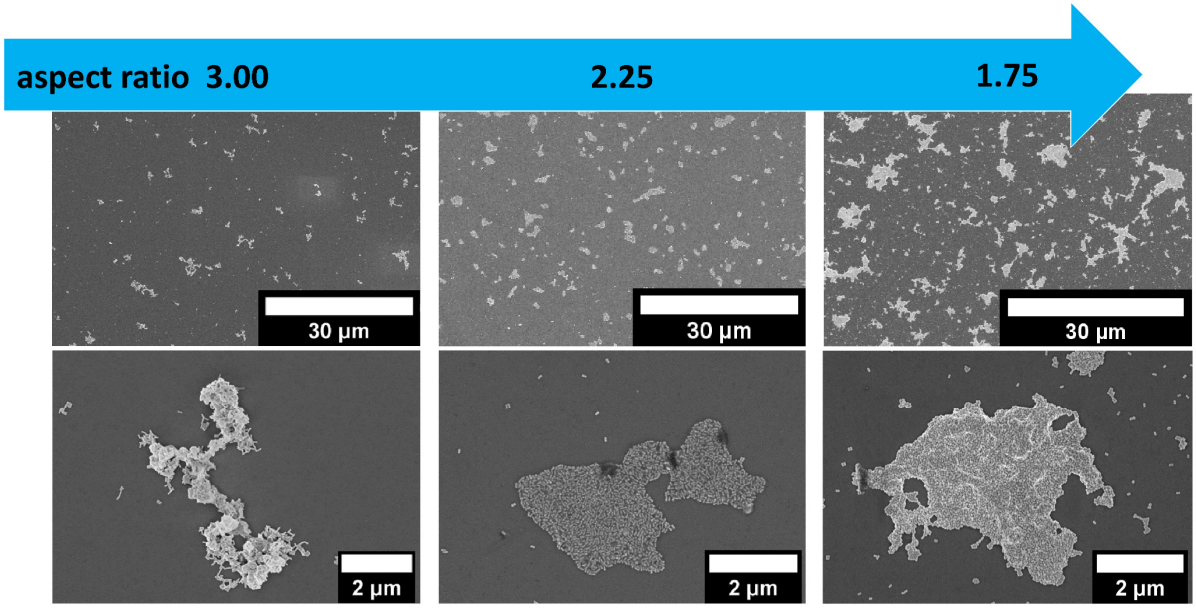

Figure 57. Gold nanorod-based superstructures. SEM images of gold nanorod-based superstructures on sulfonate-functionalized substrates. The gold nanorods are varying in their aspect ratio: 3.00 (left row), 2.25 (middle row), and 1.75 (right row).

In summary, it was possible to quantitatively investigate the heterogeneous nucleation phenomenon of superstructures based on anisotropic nanoparticles using a set of gold nanorods with different aspect ratios as a model system. Time-resolved light microscopy and UV-vis-NIR spectroscopy allowed for the determination of nucleation rates as well as the nanoparticle concentration in dispersion at each time. The shape of nanoparticles was found to strongly influence the heterogeneous nucleation rate of superstructures from anisotropic building blocks, as faster nucleation was noticed for nanorods with lower aspect ratios. In addition, evaluation of the nucleation rates in dependence of the supersaturation revealed a much larger kinetic nucleation barrier than the thermodynamic one. This dominating kinetic term is in agreement with the results obtained for the gold nanocubes (Chapter 6.1.4) and is in opposite of the situation reported for ionic or molecular systems. The reason might be the much faster diffusion of ions than the nanorods and, therefore, a larger kinetic hindrance for the nucleation of the nanorod building units. On the other hand, the thermodynamic barrier did not practically exist for the investigated nanorods, as it was found to be $< 1\ k_BT$ already for supersaturations > 2 and only reached a few k_BT at its' maximum at supersaturations approaching 1.0. The reason could be the electrostatic attraction between the negatively charged mica substrates and the positively charged nanorods, which almost eliminates the thermodynamic barrier, while the kinetic one is still significant.

Overall, the obtained data set on heterogeneous nucleation of monodisperse nanorods with different anisotropy degrees into superstructures provides important insight into the formation of superstructures from anisotropic nanoparticles. Moreover, the reported experiments can also serve as experimental data for theoretical descriptions of nucleation using non-spherical building units.

7.2 Appendix

Table A 18. Determination of the reaction order. Determination of the reaction order for the nucleation of gold nanorods in solution with aspect ratios of 3.00, 2.25, and 1.75 (Figure 25). The optical density at the respective absorption maxima is plotted linearly against the experiment time dependent on the assumed reaction order. The R^2 values, which describe the quality of the linear fit, are given.

assumed reaction order	plot	3.00	2.25	1.75
0. order	Abs → t	0.58	0.81	0.73
1. order	ln(Abs) → t	0.69	0.89	0.89
2. order	1/Abs → t	0.79	0.93	0.93

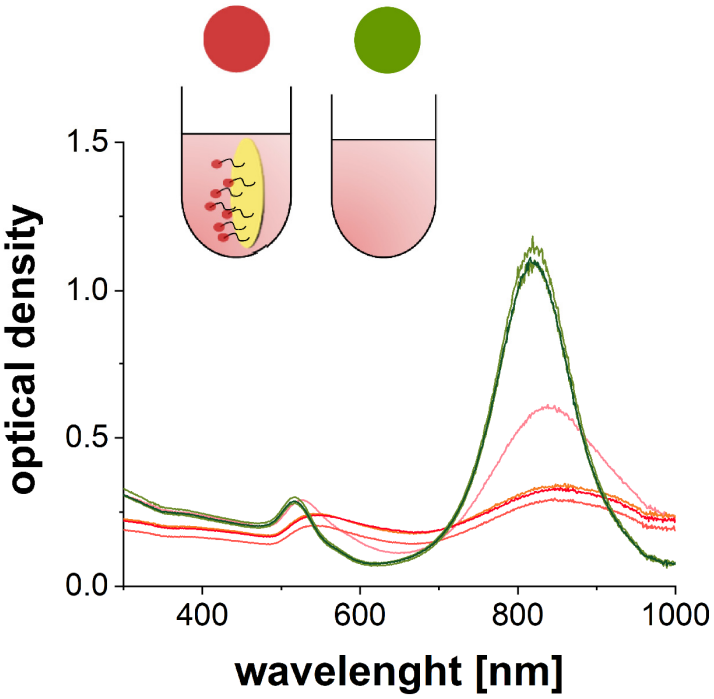

Figure A 55. Effect of sulfonate-functionalized substrates on the nucleation process. Gold nanorod dispersions with an aspect ratio of 3.00 were destabilized by adding ethanol in the presence of mica substrates functionalized with sulfonate. Two hours after adding ethanol, the UV-vis-NIR spectra of the investigated gold nanorod dispersions show that sulfonate-functionalized mica can trigger the nucleation of gold nanorod-based superstructures (red), while in their absence such processes do not occur (green). The experiment was repeated four times.

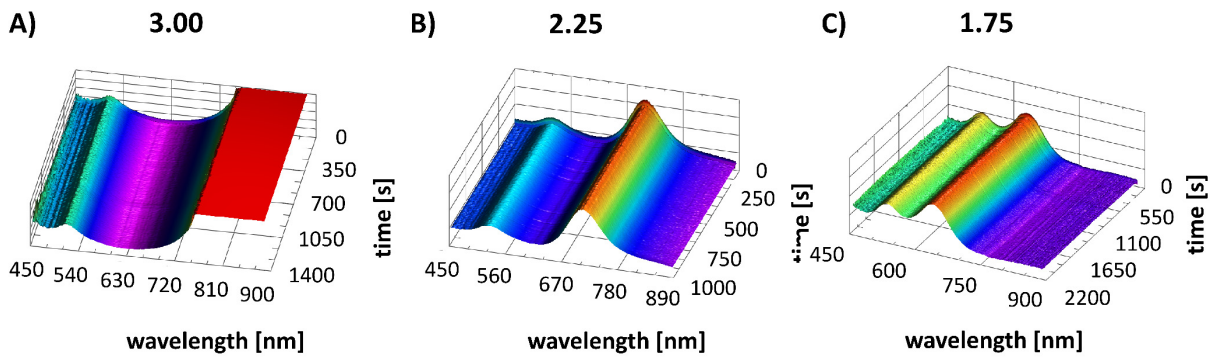

Figure A 56. Simultaneous UV-vis-NIR measurement. UV-vis-NIR spectra of gold nanorod dispersions with aspect ratios of A) 3.00, B) 2.25, and C) 1.75. The respective absorption maxima remain constant throughout the experiment time, indicating that the gold nanorod dispersions are stable, and the particles are not aggregating in dispersion. The absorption at 830 nm of the gold nanorods with an aspect ratio of 3.00 was out of the detection limit. With the same concentration, bigger nanorods have a greater extinction cross-section that leads to a higher absorption.

Table A 19. Interfacial Energies. Interfacial energies determined for the heterogeneous nucleation of gold nanorods on sulfonate-functionalized mica substrates. A contact angle of 60 to 120° is assumed.

	3.00	**2.25**	**1.75**
interfacial energy [J/m²]	$3.83 – 6.72 \cdot 10^{-07}$	$4.27 – 7.48 \cdot 10^{-07}$	$4.98 – 8.74 \cdot 10^{-07}$

Table A 20. Counted gold nanorod superstructures. The superstructures formed by gold nanorods with different aspect ratios were analyzed by SEM and the percentage of the analyzed substrate surface covered with superstructures, the average size of superstructures from sizes of 1 µm² and bigger, and the size of the biggest superstructure are given.

aspect ratio	**% area**	**average size [µm²]**	**biggest superstructure [µm²]**
3.00	1.85	2.18	4
2.25	6.76	2.21	15
1.75	11.62	3.62	23

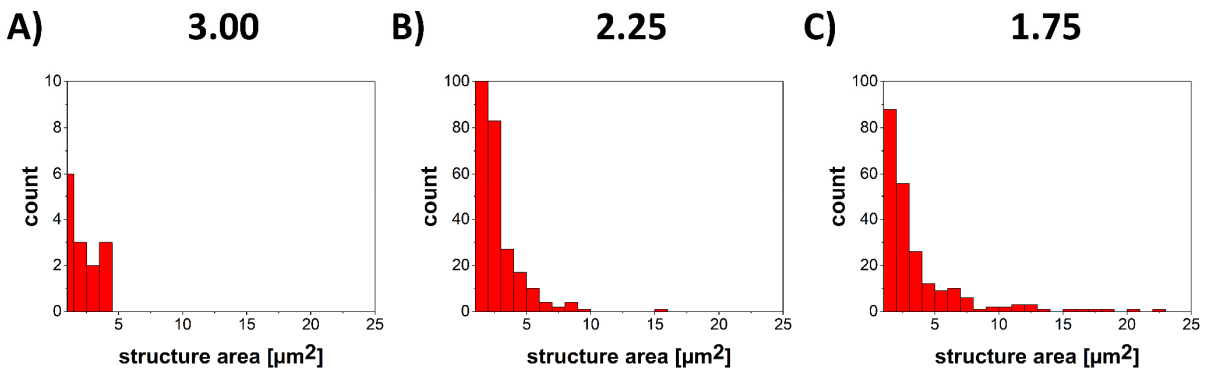

Figure A 57. Structure area dependent on the nanoparticle anisotropy. Superstructures of gold nanorods formed on sulfonate-functionalized substrates with different aspect ratios of A) 3.00, B) 2.25, C) 1.75 were analyzed by SEM. The structure area of the counted superstructures is plotted in histograms.

7.3 Materials and Methods

7.3.1 Instruments

Light microscopy images were recorded with an *AxioImager* from *Zeiss* with an *LD Epiplan* 50x/0.50 HD DIC objective using transmitted light, bright field illumination, a condenser numerical aperture at 0.9, an *Axiocam* 506 bw as an imaging device, and an exposure time of 10 ms.

SEM images were recorded with a *Gemini500* by *Zeiss* operating at 3 kV equipped with an Inlens and a secondary electron detector for secondary and backscattered electrons. Samples were coated with a 2.5 nm platinum layer, mounted on aluminum stubs, and attached by carbon conductive layers.

UV-Vis-NIR measurements were performed with a *Varian Cary* 50 spectrometer in quartz cuvettes. The UV-vis-NIR measurements carried out simultaneously with light microscopy measurements were performed with a modular *USB2000+* spectrometer from *Ocean Optics* equipped with a *USB-DT* miniature deuterium tungsten halogen lamp.

7.3.2 Materials

All the starting materials were obtained from commercial suppliers and used without further purification. Hexadecyltrimethylammonium bromide (CTAB, ≥ 99%) was purchased from *Aldrich* and ethanol (EtOH, ≥ 99.8%) was purchased from *VWR*.

7.3.3 Methods

7.3.3.1 Preparations of Gold Nanorod Dispersions

The concentrated gold nanorods from Chapter 4.3.5 were washed with a 2.00 mM CTAB aqueous solution, centrifuged at 6000 rpm for 20 min, and the supernatant was removed. The washing procedure was repeated two times. A solution of 0.02 mM CTAB in water was prepared. The concentrated gold nanorods were added to the CTAB solution to reach the desired optical density. Before using the dispersion of gold nanorods in experiments, the stability of the gold nanorods was checked with UV-vis-NIR spectroscopy.

7.3.3.2 Destabilization of Gold Nanorods

To destabilize the dispersion of gold nanorods ethanol was added to an amount of 20 vol.-% (for the microscopic analysis). During or after the destabilization experiments, the formed aggregates and remaining single particles were stabilized using an excess of CTAB. This approach allowed freezing and analyzing aliquots at their actual destabilization stage. Therefore, a CTAB solution was added to adjust the amount of CTAB to 2.00 mM. To analyze the structures formed on mica surfaces, the mica platelets were washed thoroughly with water and dried with a nitrogen stream at RT.

7.3.3.3 Image Analysis

During the experiments light microscope images were taken every 30 s and processed with *ImageJ*. A *trainable weka segmentation* was applied, differentiating between nuclei on the surface, background and moving aggregates in solution. The classifier results were given out as results and the number of nuclei species was counted. Therefore, a threshold (*MaxEntropy*) was applied and the number of nuclei was counted by using the *analyse particles* function (size = 10 – infinity pixel). The number of counted species of the first image (only background, structure growth did not start yet) was subtracted from all following results.

7.3.3.4 Determination of Supersaturation

For the determination of the gold nanorods concentrations, the optical density at 400 nm was taken from UV-vis-NIR spectra. After Hendel *et al.*[251], we assumed an extinction coefficient of 2.685 l/mol·cm for our gold nanorods. With the Beer-Lambert law (equation 11) the Au(0) concentration c could be calculated, since the extinction E_λ from the UV-vis-NIR measurements and the depth of the used cuvette d are known.[252]

$$E_\lambda = \varepsilon_\lambda \cdot c \cdot d \tag{13}$$

With this connectivity, the Au(0) concentration of the solution was known. However, in the system the monomer was not the gold atom but the gold nanorods. Therefore, the gold nanorod concentration had to be calculated from the Au(0) concentration. The volume for each gold nanorod aspect ratio was calculated: $6.02 \cdot 10^{-22}$ m^3 (3.00), $4.52 \cdot 10^{-22}$ m^3 (2.25), and $3.52 \cdot 10^{-22}$ m^3 (1.75). Gold only forms a face-centered cubic package with lattice parameter of 0.4078 nm resulting in the volume of the unit cell of 0.07 nm^3.[213] Therewith, the number of gold unit cells fitting into one gold nanorod were calculated. One gold unit cell contains 4 atoms of gold which gave us the number of gold atoms in one gold nanorod: $3.56 \cdot 10^7$ (3.00), $2.67 \cdot 10^7$ (2.25), and $2.08 \cdot 10^7$ (1.75).[214] With this quantity, we converted the Au(0) concentration into a gold nanorod concentration.

To calculate the supersaturation σ, the concentration of gold nanorods in a saturated solution x* was determined for each particle surface system. Therefore, the Au (0) concentration after the destabilization of the nanorods (when a steady state was reached) was determined with UV-vis-NIR spectroscopy and the corresponding gold nanorod concentration was calculated. Finally, the resulting supersaturation for each destabilization experiment at a gold nanorod concentration x was calculated with equation 14.

$$\sigma = \frac{x}{x^*} \tag{14}$$

8 Summary, Conclusion and Outlook of the Thesis

Nucleation processes play a significant role throughout nature, science, and industry, as they constitute the first step in the spontaneous formation of distinct thermodynamic phases and structures. They often occur around us, with the formation of clouds through the condensation of water vapor into liquid droplets being among the most elegant examples. In industry, the quality and properties of pharmaceutical drugs can depend on the nucleation conditions used during their production. Further, an unwanted aspect of nucleation constitutes the precipitation of calcium carbonate minerals in pipes for water conduction. These examples show how gaining insight into nucleation can help to understand countless processes occurring in nature and industry. Furthermore, this understanding should help to manipulate systems in a targeted manner to eventually deliver optimized methods for desired applications or functional materials with tailor-made properties. Despite the importance of nucleation processes in nature and technology, the complex system still poses many unanswered questions. This fact can be partially explained by a lack of analytical methods with sufficient spatial and temporal resolution to characterize the nucleation of critical germs, which possess dimensions in the nanometer range.

This thesis used anisotropic nanoparticles as a model system to study heterogeneous nucleation. Nanoparticles as model system means that instead of atoms or molecules nucleating into larger structures, nanoparticles were used as building blocks and assembled into larger superstructures in a process comparable to the nucleation of atomic, ionic or molecular systems. This approach brought the system to a larger scale and thus simplified the analysis of nucleation processes. Herein, the thesis dealt explicitly with heterogeneous nucleation as this is the most common form compared to homogeneous nucleation. Moreover, the thesis worked with anisotropic particles, since anisotropic building blocks are omnipresent in nature and technology, unlike isotropic particles commonly utilized for nucleation experiments. With the model system of anisotropic particles, the thesis analyzed the impact of surface chemistry and particle shape on the nucleation of the nanoparticles into superstructures to gain insight into the complex phenomenon of heterogeneous nucleation. To study the effects of these parameters, the thesis first focused on substrates where the heterogeneous nucleation of the nanoparticles took place (Chapter 3), then on the nanoparticles used as building blocks for the nucleation (Chapter 4), and finally, on analytical methods, which allowed observing the nucleation process and measuring its kinetic behavior (Chapter 5).

Accordingly, Chapter 3 was dedicated to investigate the substrates used for heterogeneous nucleation experiments. Here, mica was identified as a promising substrate for the analysis of heterogeneous nucleation due to its smooth atomically surface. A variety of surface chemistry properties were introduced, by varying their hydrophilicity and surface charge, while preserving the smooth substrate's surface, the prerequisite for the investigation of heterogeneous nucleation events. The applied functionalization reactions using silanes only depended on free hydroxyl groups on the substrate's surface. Thus, not only mica but additionally silicon and quartz could be functionalized in the same way. Having three different substrates was

advantageous to investigate and characterize nucleation of nanoparticle superstructures. For instance, mica substrates were employed for optical microscope analysis and SEM experiments and the surface of quartz cuvettes to analyze kinetics in situ via UV-vis-NIR spectroscopy.

Chapter 4 focused on the nature of the colloidal nanoparticle systems used as building blocks for heterogeneous nucleation experiments. Here, three different anisotropic nanoparticle systems were successfully prepared and their nucleation and assembly into larger superstructures was investigated: zinc oxide nanorods, gold nanocubes, and gold nanorods. Zinc oxide nanorods were functionalized via ligand exchange with siloxanes carrying three different polar groups (-NH_2, -OH, -COOH). Furthermore, gold nanocubes were functionalized with four different polar groups (-NH_2, -OH, -SO_3H, -COOH). With these two nanoparticle systems, it was possible to analyze the influence of the surface chemistry on heterogeneous nucleation by using the same nanoparticle, which only differs in its surface chemistry, as a building block for heterogeneous nucleation (Chapter 6). To further study the influence of the nanoparticle shape (Chapter 7), three sets of gold nanorods with distinct aspect ratios (3.00, 2.25, and 1.75) were investigated.

However, to properly examine the nucleation behavior of nanoparticle-based superstructures, it also was necessary to design an appropriate experimental setup that allowed to observe and quantify the heterogeneous nucleation in situ (Chapter 5). For this reason, a suitable and easily accessible system was designed and implemented based on the combination of light microscopy with simultaneous UV-vis-NIR spectroscopy measurements. With this setup, it was possible to analyze heterogeneous nucleation processes in situ, directly in dispersion, and on a relevant statistical basis. Therefore, the controlled destabilization of the nanoparticle systems was established by altering the solubility of the nanoparticles in the solvent through the addition of ethanol. Thereby, it was possible to successfully analyze the homogeneous nucleation of CTAB stabilized gold nanocubes in dispersion, the acceleration of the process by the presence of a favorable surface (sulfonate-functionalized substrates), and the heterogeneous nucleation of the gold nanocubes on these surfaces resulting in nanoparticle-based superstructures. The plasmon resonance of the gold nanocubes gave valuable information about the early nucleation of the particles and their concentration in solution via UV-vis-NIR spectroscopy. The combination with a light microscope enabled the simultaneous detection of nucleated species on the substrates and opened the possibility to analyze the kinetics of the heterogeneous nucleation process. This approach opened the possibility to calculate the effective interfacial energy and the nucleation barrier and to characterize the heterogeneous nucleation process more precisely. Thereby, it could be demonstrated that the combination of light microscopy and UV-vis-NIR spectroscopy is a suitable and easy to handle system to analyze heterogeneous nucleation processes in situ directly in solution on a relevant statistical basis with simple and commonly available equipment. Hence, this approach was used in the next steps to analyze the influence of surface chemistry and particle shape on heterogeneous nucleation by allowing a comparison of the variations in the nucleation systems.

In Chapter 6, the impact of surface chemistry on heterogeneous nucleation could be successfully analyzed using the presented model system of nanoparticles as building blocks. The simple experiments with zinc

oxide nanorods showed that depending on the interaction of the nanoparticle surface with the substrate surface, structures could be varied from layer-like to three-dimensional superstructures. In the following, the impact of surface chemistry was analyzed in more detail with the system of gold nanocubes, wherein 18 different surface chemistry combinations could be studied. First, the impact of the substrate's surface chemistry on the destabilization kinetics of the gold nanocubes in solution was analyzed by UV-vis-NIR spectroscopy. Here, the destabilization of the gold nanocubes in solution did not seem to follow exclusively a homogeneous nucleation pathway. Electrostatic interactions between substrates and nanoparticles with opposite charges were crucial for enhancing the nucleation rates and decreasing the nucleation barrier of superstructure formation. Unfavorable interactions between nanoparticles and substrates did not influence the destabilization kinetics at all. Second, the superstructures formed on the substrates were analyzed. The results fit well the kinetic studies, and favorable interactions resulted not only in the enhancement of the destabilization kinetics but also in huge superstructures on the substrate's surface. The favorable interaction of CTAB gold nanocubes with sulfonate- and carboxyl-functionalized substrates and of PAA gold nanocubes with amine-functionalized substrates allowed a quantitative analysis of the heterogeneous nucleation process using time-resolved light microscopy and simultaneous UV-vis-NIR spectroscopy. Thereby, the nucleation rates could be determined successfully and allowed further the calculation of the interfacial energies, the nucleation barriers, and the thermodynamic and kinetic terms. The results suggested that the interfacial energies and the nucleation barriers of the investigated nanoparticle systems are significantly lower than that of atoms and molecules. Moreover, the kinetic component plays a more significant role than the thermodynamic one, most probably due to the lower diffusion constants of nanoparticles in comparison to atoms or molecules.

Next to the influence of surface chemistry on heterogeneous nucleation, Chapter 7 analyzed the influence of particle anisotropy in terms of the aspect ratio. It was possible to quantitatively investigate the heterogeneous nucleation phenomenon of superstructures based on anisotropic nanoparticles using a set of gold nanorods with different aspect ratios as a model system. Time-resolved light microscopy and UV-vis-NIR spectroscopy made it possible to determine the nucleation rates as well as the nanoparticle concentration in dispersion at each time. The studies consistently exhibited an influence of the aspect ratio on the nucleation behavior resulting in faster nucleation of superstructures as the aspect ratio decreased. In addition, evaluation of the nucleation rates in dependence of the supersaturation revealed a much larger kinetic nucleation barrier than the thermodynamic one. This dominating kinetic term is in agreement with the results obtained for the gold nanocubes (Chapter 6) and is in opposition to the situation reported for ionic or molecular systems. The cause might be the much faster diffusion of ions and molecules than of nanorods and, therefore, a larger kinetic hindrance for the nucleation of the nanorod building units. On the other hand, the thermodynamic barrier did effectively not exist for the investigated nanorods as it was found to be smaller than 1 k_BT already for supersaturations higher than 2 and only reached a few k_BT at its' maximum for supersaturations approaching 1. The reason could be the electrostatic attraction between the

negatively charged mica substrates and the positively charged nanorods, which almost eliminated the thermodynamic barrier, while the kinetic one was still significant. Overall, the obtained data set on heterogeneous nucleation of monodisperse nanorods with different anisotropy degrees into superstructures provided important insights into the formation of superstructures from anisotropic nanoparticles. Moreover, the reported experiments can also serve as experimental data for theoretical descriptions of nucleation using non-spherical building units. That a theory describing nucleation with anisotropic building units is important can already be seen from the fact that molecules are rarely spherical and commonly exhibit anisotropy. Therefore, understanding their nucleation and crystallization better could be truly beneficial for several applications ranging from nanoparticle superstructures like mesocrystals via macromolecular crystals in protein crystallization to the crystallization of small molecules in pharmacy.

In summary, with the combination of widely available techniques such as UV-vis-NIR spectroscopy and light microscopy, this thesis established a straightforward method to analyze heterogeneous nucleation processes on the model system of nanoparticles. With this approach, it was possible to qualitatively and quantitatively investigate the heterogeneous nucleation phenomenon of superstructures based on anisotropic gold nanoparticles. Thereby, the influence of the surface chemistry, as well as particle anisotropy, were studied successfully. This fact demonstrates the potential of using nanoparticle systems with different physicochemical features to investigate heterogeneous nucleation phenomena, a strategy that should eventually serve to study and unveil the mechanism behind complex nucleation processes observed in nature and industry. This potential opens the possibility to explore many more aspects of heterogeneous nucleation. Subsequent to this thesis, it would be interesting, for example, to extend the analytical setup. UV-vis-NIR spectroscopy is limited to the concentration measurement of light-absorbing samples and only in the concentration range where the Lambert-Beer law is valid. One can imagine the implementation of other optical techniques such as the very sensitive fluorescence spectroscopy after the introduction of fluorescence tags to the nanoparticles. A more universal approach would be a refractive-index measurement or turbidity detection. The latter would be possible already with the UV-vis-NIR spectroscopy setup and could take advantage of dynamic sensitivity in multiwavelength detection since light scattering intensity is proportional to the inverse light wavelength to the power of four.[248] The turbidity τ of the nanoparticle dispersion is related to the nanoparticle number concentration c (particles/ml) via equation 15.[249]

$$\tau = \frac{\pi}{4} K d^2 c \tag{15}$$

Here, d is the nanoparticle diameter and K the scattering coefficient being a function of nanoparticle size, light wavelength, and the refractive index difference of nanoparticles and medium. This dependence means that the nanoparticle size and scattering coefficient need to be determined in advance and that very small particles with negligible light scattering cannot be investigated anymore. But on the other hand, this concentration detection method is universal and opens the possibility to analyze various nanoparticle systems. Next to the extension of the analytical setup, further studies on the role of the substrates in

heterogeneous nucleation would be of interest. Here, one could imagine functionalizing patterned substrates with different surface chemistries. Another possibility would be to use other nanoparticles or small aggregates instead of a macroscopic substrate and to analyze the heterogeneous nucleation on the surface of these particles. Moreover, the reported experiments can also serve as experimental data for theoretical descriptions of nucleation using non-spherical building units. A combination of experimental data and simulations would be promising. The first results for the particle anisotropy presented here are limited, but a more systematic future investigation using the established experimental methodology can potentially yield larger data sets to systematically reveal the influence of the building units' shape on nucleation processes.

There are still countless mysteries and fascinating aspects in the field of nucleation and probably every question that has been solved raises numerous new ones. However, every small finding allows more control over existing processes, the production of materials with improved properties and thereby takes us one step further.

9 Zusammenfassung, Schlussfolgerung und Ausblick der Arbeit

Nukleationsprozesse spielen überall in der Natur, der Wissenschaft und der Industrie eine bedeutende Rolle, denn sie sind der erste Schritt in der spontanen Bildung definierter thermodynamischer Phasen und Strukturen. Damit umgeben uns Nukleationsprozesse oft im Alltag, wobei die Bildung von Wolken durch die Kondensation von Wasserdampf zu flüssigen Tröpfchen eines der anschaulichsten Beispiele darstellt. Weiterhin können in der Industrie oft Qualität und Eigenschaften pharmazeutischer Wirkstoffe von den Nukleationsbedingungen während ihrer Produktion abhängen. Ungewollte Aspekte der Nukleation sind zum Beispiel die Verkalkung von Wasserleitungen. Diese Beispiele veranschaulichen, dass ein Einblick in Nukleationsprozesse dabei helfen kann, unzählige natürliche und industrielle Vorgänge zu verstehen. Weiterhin kann dieses Verständnis helfen, Systeme gezielt zu beeinflussen, um eventuell Methoden für gewünschte Anwendungen zu optimieren oder funktionelle Materialien mit maßgeschneiderten Eigenschaften zu kreieren. Obwohl Nukleationsprozesse in der Natur und Technologie von großer Bedeutung sind, sind immer noch viele Vorgänge rätselhaft und Fragen unbeantwortet. Dies liegt teilweise daran, dass analytische Methoden mit ausreichender räumlicher und zeitlicher Auflösung fehlen, um die Nukleation kritischer Keime im Nanometerbereich zu untersuchen.

Diese Dissertation verwendet anisotrope Nanopartikel als Modellsystem, um heterogene Nukleationsprozesse zu untersuchen. Nanopartikel als Modellsystem bedeutet, dass anstelle von Atomen oder Molekülen, die zu größeren Strukturen nukleieren, Nanopartikel als Bausteine verwendet und zu größeren Überstrukturen zusammengesetzt werden. Dieser Assemblierungsprozess, der vergleichbar ist mit der Nukleation und dem Wachstum von Atomen, Ionen oder molekularen Systemen, hat das System auf eine höhere Größenskala gebracht und damit die Analyse des Nukleationsprozesses enorm vereinfacht. Dabei stand explizit die heterogene Nukleation im Fokus, da sie die meist verbreitete Form im Vergleich zur homogenen Nukleation ist. Außerdem wurde mit anisotropen Partikeln gearbeitet, da diese allgegenwärtig in der Natur und Technologie sind, im Gegensatz zu isotropen Partikeln, die gewöhnlich für Nukleationsexperimente verwendet werden. Mit dem Modellsystem der anisotropen Partikeln wurde der Einfluss der Oberflächenchemie und Partikelform auf die Nukleation der Nanopartikel in Überstrukturen analysiert, was einen Einblick in das komplexe Phänomen der heterogenen Nukleation ermöglichte. Um den Einfluss dieser Parameter zu bestimmen, standen zunächst die Substrate im Zentrum, auf denen später die Nukleation stattfand (Kapitel 3) dann die Nanopartikel, die als Bausteine für die Nukleation verwendet wurden (Kapitel 4) und letztendlich die analytischen Methoden, mit denen es gelang, die Nukleationsprozesse zu beobachten und ihre Kinetik zu messen (Kapitel 5).

In Kapitel 3 wurden die Substrate für die Experimente zur heterogenen Nukleation untersucht. Aufgrund seiner atomar glatten Oberfläche fiel die Wahl auf Mica als vielversprechendes Substrat für die Untersuchung heterogener Nukleation. Durch die Funktionalisierung mit Siloxanen konnten die Oberflächeneigenschaften des Micas auf vielfältige Weise variiert werden, wobei Hydrophilie und Oberflächenladung angepasst wurden. Dabei gelang es, die glatte Oberfläche des Substrates zu erhalten, was die Voraussetzung für die Untersuchung heterogener Nukleationsevents darstellte. Das Aufbringen der Siloxane war dabei nur abhängig von den freien Hydroxylgruppen auf der Oberfläche des Substrates. Daher konnten neben Mica auch Silizium und Quarz auf dieselbe Weise funktionalisiert werden. Die Auswahl zwischen drei unterschiedlichen Substraten war bei der Untersuchung und Charakterisierung der Nukleation von Nanopartikelüberstrukturen vorteilhaft. Beispielsweise wurde Mica für die Analyse mit dem Lichtmikroskop und dem SEM verwendet, während die Oberfläche von Quarz-Küvetten genutzt wurde, um die Kinetik mittels UV-vis-NIR-Spektroskopie zu untersuchen.

Kapitel 4 konzentriert sich auf die Natur der kolloidalen Nanopartikelsysteme, die als Bausteine für die heterogenen Nukleationsexperimente verwendet wurden. Hier wurden drei unterschiedliche anisotrope Nanopartikelsysteme erfolgreich hergestellt und ihre Nukleation und Assemblierung in größere Überstrukturen untersucht: Zinkoxidnanostäbchen, Goldnanowürfel und Goldnanostäbchen. Zinkoxidnanostäbchen wurden über einen Ligandenaustausch mit drei verschiedenen polaren Siloxanen funktionalisiert (-NH_2, -OH, -COOH). Außerdem wurden Goldnanowürfel mit vier unterschiedlichen polaren Gruppen funktionalisiert (-NH_2, -OH, -SO_3H, -COOH). Mit diesen zwei Nanopartikelsystemen war es möglich, den Einfluss der Oberflächenchemie auf ihre heterogene Nukleation in Überstrukturen zu untersuchen, indem die gleichen Nanopartikel mit variierender Oberflächenchemie als Bausteine verwendet wurden (Kapitel 6). Um im Folgenden auch den Einfluss der Nanopartikelform zu analysieren (Kapitel 7), wurden drei Sets an Goldnanostäbchen mit definiertem Kantenlängenverhältnis untersucht (3.00, 2.25, 1.75).

Um das Nukleationsverhalten von nanopartikel-basierten Überstrukturen tatsächlich untersuchen zu können, war es notwendig, einen geeigneten experimentellen Aufbau zu designen, der es erlaubte, den heterogenen Nukleationsprozess in situ beobachten und quantifizieren zu können (Kapitel 5). Daher wurde ein passendes und leicht zugängliches System konstruiert und etabliert, basierend auf der Kombination von Lichtmikroskopie und simultaner UV-vis-NIR-Spektroskopie. Mit diesem Aufbau war es möglich, heterogene Nukleationsprozesse in situ, direkt in Dispersion und mit einer relevanten statistischen Anzahl untersuchen zu können. Dafür wurde die kontrollierte Destabilisierung der Nanopartikelsysteme etabliert: eine Veränderung der Löslichkeit der Nanopartikel in ihrem Medium durch das Hinzugeben von Ethanol. Dadurch war es möglich, die homogene Nukleation von CTAB-stabilisierten Goldnanowürfeln in Dispersion, die Beschleunigung des Prozesses aufgrund der Anwesenheit einer favorisierten Oberfläche (sulfonat-funktionalisiertes Substrat) und die heterogene Nukleation der Goldnanowürfel auf den Substraten in Überstrukturen erfolgreich zu analysieren. Die Plasmonenresonanz der Goldnanowürfel gab

mittels UV-vis-NIR-Spektroskopie wertvolle Informationen über deren frühe Nukleation und ihre Konzentration in Lösung. Die Kombination mit einem Lichtmikroskop erlaubte die simultane Detektion von nukleierten Spezies auf dem Substrat und eröffnete die Möglichkeit, die Kinetik des heterogenen Nukleationsprozesses zu analysieren. Dieser Ansatz erlaubte es, die effektive Grenzflächenenergie und die Nukleationsbarriere zu berechnen und damit den Nukleationsprozess genauer zu charakterisieren. Dabei konnte demonstriert werden, dass die Kombination von Lichtmikroskopie und UV-vis-NIR-Spektroskopie ein geeignetes und leicht zu handhabendes System ist, um heterogene Nukleationsprozesse in situ direkt in Lösung mit einer relevanten statistischen Anzahl und einfachem und allgemein zugänglichem Equipment zu untersuchen. Dieser Ansatz erlaubte es, Variationen im Nukleationssystem zu detektieren und zu vergleichen; er wurde daher im nächsten Schritt verwendet, um den Einfluss der Oberflächenchemie und der Partikelform auf die heterogene Nukleation zu analysieren.

In Kapitel 6 konnte der Einfluss der Oberflächenchemie auf die heterogene Nukleation erfolgreich analysiert werden, indem das dargestellte Modellsystem von Nanopartikeln als Baustein verwendet wurde. Die einfachen Experimente mit Zinkoxidnanostäbchen zeigten, dass abhängig von der Interaktion der Nanopartikeloberfläche mit der Substratoberfläche schichtartige oder dreidimensionale Strukturen erzeugt werden konnten. Im Folgenden wurde der Einfluss der Oberflächenchemie mit dem Goldnanowürfelsystem detaillierter untersucht, wobei 18 unterschiedliche Oberflächenchemiekombinationen analysiert werden konnten. Zuerst wurde der Einfluss der Substratoberflächenchemie auf die Destabilisierungskinetik der Goldnanowürfel in Lösung mittels UV-vis-NIR-Spektroskopie untersucht. Hier schien die Destabilisierung der Goldnanowürfel nicht ausschließlich einem homogenen Nukleationspfad zu folgen. Die elektrostatische Interaktion zwischen den Substraten und Nanopartikeln mit gegensätzlicher Ladung beschleunigte die Nukleationsraten enorm und senkte die Nukleationsbarriere zur Bildung von Überstrukturen. Unvorteilhafte Interaktionen zwischen den Nanopartikeln und den Substraten hat die Destabilisierungskinetik dagegen nicht beeinflusst. Im nächsten Schritt wurden die gebildeten Überstrukturen untersucht. Die Resultate passen gut zu den kinetischen Untersuchungen und vorteilhafte Interaktionen führen nicht nur zu einer Beschleunigung der Destabilisierungskinetik, sondern auch zu großen Überstrukturen auf der Oberfläche des Substrates. Die favorisierte Interaktion von CTAB-Goldnanowürfeln mit sulfonat- und carboxylfunktionalisierten Substraten und von PAA-Goldnanowürfeln mit amin-funktionalisierten Substraten erlaubte eine quantitative Analyse des heterogenen Nukleationsprozesses mittels zeitaufgelöster Lichtmikroskopie und simultaner UV-vis-NIR-Spektroskopie. Damit konnten die Nukleationsraten erfolgreich bestimmt werden und erlaubten im nächsten Schritt die Berechnung der Grenzflächenenergien, der Nukleationsbarrieren sowie des thermodynamischen und kinetischen Terms. Die Resultate legten nahe, dass die Grenzflächenenergien und Nukleationsbarrieren der untersuchten Nanopartikelsysteme signifikant geringer sind als die von atomaren oder molekularen Systemen. Zusätzlich scheint die kinetische Komponente eine wichtigere Rolle zu spielen als die

thermodynamische, möglicherweise aufgrund der geringeren Diffusionskonstante von Nanopartikeln im Vergleich zu Atomen oder Molekülen.

Neben dem Einfluss der Oberflächenchemie auf die heterogene Nukleation untersucht Kapitel 7 den Einfluss der Partikelanisotropie, genauer gesagt des Kantenlängenverhältnisses. Dabei war es möglich, quantitativ die heterogene Nukleation von Superstrukturen basierend auf anisotropen Nanopartikeln zu untersuchen, indem ein Set von Goldnanostäbchen mit unterschiedlichem Kantenlängenverhältnis als Modellsystem verwendet wurde. Zeitaufgelöste Lichtmikroskopie und UV-vis-NIR-Spektroskopie ermöglichten zu jedem Zeitpunkt die Bestimmung der Nukleationsraten sowie der Nanopartikelkonzentration in Dispersion. Die Studien zeigten durchgehend einen Einfluss des Kantenlängenverhältnisses auf das Nukleationsverhalten, wobei ein sinkendes Kantenlängenverhältnis zu schnellerer Nukleation der Superstrukturen führte. Zusätzlich offenbarte die Auswertung der Nukleationsraten in Abhängigkeit von der Übersättigung eine viel größere kinetische als thermodynamische Nukleationsbarriere. Dieser dominierende kinetische Term stimmt mit den Resultaten der Goldnanowürfel (Kapitel 6) überein und verhält sich gegensätzlich zu Ergebnissen, die zu ionischen oder molekularen Systeme bekannt sind. Die Erklärung könnte wiederum eine viel schnellere Diffusion von Ionen und Molekülen im Vergleich zu den Nanostäbchen und damit eine größere kinetische Hemmnis für die Nukleation der Nanostäbchenbausteine sein. Andererseits hat die thermodynamische Barriere für die untersuchten Nanostäbchen effektiv nicht existiert, da sie schon für größere Übersättigungen als 2 kleiner als 1 k_BT war und nur wenige k_BT bei einer maximalen Übersättigung gegen 1 erreicht hat. Grund dafür könnte die elektrostatische Anziehung zwischen dem negativ geladenen Mica-Substrat und den positiv geladenen Nanostäbchen sein, die die thermodynamische Barriere nahezu eliminiert haben könnte, während die kinetische verblieb und signifikant wurde. Insgesamt gesehen haben die erhaltenen Daten über die heterogene Nukleation von monodispersen Nanostäbchen mit unterschiedlichem Kantenlängenverhältnis wichtige Einblicke in die Bildung von Superstrukturen aus anisotropen Nanopartikeln ermöglicht. Zudem können die beschriebenen Experimente auch als experimenteller Datensatz für die theoretische Beschreibung der Nukleation nicht sphärischer Bausteine dienen. Dass eine Theorie, die die Nukleation anisotroper Bausteine beschreibt, von großer Bedeutung ist, zeigt schon der Fakt, dass Moleküle selten sphärisch sind und üblicherweise Anisotropie vorweisen. Daher könnte es durchaus vorteilhaft sein, ihre Nukleation und Kristallisation besser zu verstehen, um verschiedenste Anwendungen von Nanopartikelüberstrukturen, wie Mesokristallen, und makromolekularen Kristallen beispielsweise von Proteinen oder kleinen Molekülen in der Pharmazie besser zu verstehen.

Zusammenfassend hat diese Dissertation mit der Kombination aus weitverbreiteten Techniken wie der UV-vis-NIR-Spektroskopie und der Lichtmikroskopie eine unkomplizierte Methode etabliert, heterogene Nukleationsprozesse am Modellsystem von Nanopartikeln zu analysieren. Mit diesem Ansatz war es möglich, qualitativ und quantitativ die heterogene Nukleation von Superstrukturen basierend auf anisotropen Goldnanopartikeln zu untersuchen. Dabei wurden der Einfluss der Oberflächenchemie sowie

der Partikelanisotropie erfolgreich untersucht. Diese Anwendung demonstriert das Potenzial, Nanopartikelsysteme mit unterschiedlichen physikalisch-chemischen Eigenschaften zu verwenden, um heterogene Nukleationsphänomene zu untersuchen. Diese Strategie könnte eventuell dazu verwendet werden, den Mechanismus hinter komplexen Nukleationsprozessen aus der Natur oder der Industrie zu untersuchen und aufzudecken. Dieses Potenzial eröffnet auch die Möglichkeit, viele weitere Aspekte der heterogenen Nukleation zu erforschen.

Anschließend an diese Dissertation wäre es interessant, beispielsweise den analytischen Versuchsaufbau zu erweitern. UV-vis-NIR-Spektroskopie ist limitiert auf die Konzentrationsmessung lichtabsorbierender Proben und nur in dem Konzentrationsbereich anwendbar, wo das Lambert-Beersche Gesetz gültig ist. Die Implementierung anderer optischer Techniken wäre vorstellbar, wie zum Beispiel die sehr sensitive Fluoreszenzspektroskopie nach dem Aufbringen von Fluoreszenzmarkern. Ein universellerer Ansatz wäre die Brechungsindexmessung oder Trübungsdetektion. Letzteres wäre direkt mit dem UV-vis-NIR-Spektroskopie-Aufbau möglich und wäre vorteilhaft aufgrund der dynamischen Sensitivität der Multiwellenlängendetektion, da die Lichtstreuungsintensität proportional zur inversen Lichtwellenlänge hoch fünf ist. Die Trübung τ der Nanopartikel Dispersion ist über Gleichung 15 verknüpft mit der Nanopartikel Konzentration c (Partikel / ml).

$$\tau = \frac{\pi}{4} K d^2 c \tag{15}$$

Hier ist d der Nanopartikeldurchmesser und K der Streuungskoeffizient, der eine Funktion aus der Nanopartikelgröße, der Wellenlänge des Lichts und der Brechungsindexdifferenz zwischen den Nanopartikeln und dem Medium bildet. Diese Abhängigkeit bedeutet, dass die Nanopartikelgröße und der Streuungskoeffizient im Vorhinein bestimmt werden müssen und sehr kleine Partikel mit vernachlässigbarer Lichtstreuung nicht mehr untersucht werden können. Andererseits ist diese Konzentrationsdetektionsmethode universell und ermöglicht, verschiedenste Nanopartikelsysteme zu untersuchen. Neben dem Ausbau des analytischen Aufbaus wären weiterführende Studien zur Rolle des Substrates in der heterogenen Nukleation von Interesse. Dabei wäre es denkbar, Substrate strukturiert mit verschiedener Oberflächenchemie zu funktionalisieren. Ein weiterer Ansatz könnte sein, andere Partikel oder kleine Partikelaggregate anstelle von makroskopischen Substraten zu verwenden, um die heterogene Nukleation auf der Oberfläche dieser Partikel zu analysieren. Darüber hinaus können die gezeigten Experimente als experimenteller Datensatz für die theoretische Beschreibung der Nukleation nicht sphärischer Bauteile dienen. Eine Kombination von experimentellen Daten und Simulationen wäre in diesem Bereich vielversprechend. Die ersten hier präsentierten Resultate der Partikelanisotropie mögen limitiert sein, aber ein systematischerer Ansatz mit der etablierten experimentellen Methode könnte in der Zukunft größere Datensätze produzieren, um systematisch den Einfluss der Form der Bausteine auf den Nukleationsprozess zu enthüllen.

Es gibt immer noch unzählige Rätsel und faszinierende Aspekte im Feld der Nukleation und möglicherweise wirft jede gelöste Frage zahlreiche neue auf. Doch jede kleine Erkenntnis erlaubt möglicherweise mehr Kontrolle über existierende Prozesse, die Produktion von Materialien mit verbesserten Eigenschaften und bringt uns damit einen Schritt voran.

10 Bibliography

[1] *Gedichte, Gesammelte Werke*. Suhrkamp: Frankfurt am Main, 1987; Vol. 1.

[2] Peukert, W., Wie durch Nukleation Partikel „aus dem Nichts“ entstehen. **2014,** https://www.fau.de/2014/06/news/veranstaltungen/wie-durch-nukleation-partikel-aus-dem-nichts-entstehen/.

[3] Göppert, A.-K.; González-Rubio, G.; Cölfen, H., Microscopic Analysis of Heterogeneous Nucleation of Nanoparticle Superstructures. *The Journal of Physical Chemistry A* **2020**.

[4] Göppert, A.-K.; González-Rubio, G.; Cölfen, H., Influence of anisotropy on heterogeneous nucleation of gold nanorod assemblies. *Faraday Discussions* **2022**.

[5] Nielsen, M. H.; Li, D. S.; Zhang, H. Z.; Aloni, S.; Han, T. Y. J.; Frandsen, C.; Seto, J.; Banfield, J. F.; Cölfen, H.; De Yoreo, J. J., Investigating Processes of Nanocrystal Formation and Transformation via Liquid Cell TEM. *Microscopy and Microanalysis* **2014,** *20* (2), 425-436.

[6] Liu, X., Heterogeneous nucleation or homogeneous nucleation? *The Journal of Chemical Physics* **2000,** *112* (22), 9949-9955.

[7] Sear, R. P., Nucleation: theory and applications to protein solutions and colloidal suspensions. *Journal of Physics: Condensed Matter* **2007,** *19* (3), 033101.

[8] Oxtoby, D. W., Homogeneous nucleation: theory and experiment. *Journal of Physics: Condensed Matter* **1992,** *4* (38), 7627.

[9] Sear, R. P., Quantitative studies of crystal nucleation at constant supersaturation: experimental data and models. *CrystEngComm* **2014,** *16* (29), 6506-6522.

[10] Schmelzer, J.; Röpke, G.; Priezzhev, V. B., *Nucleation theory and applications*. Wiley Online Library: 2005; Vol. 76.

[11] Volmer, M.; Weber, A., Keimbildung in übersättigten Lösungen. *Z. Phys. Chem.* **1926,** *119*, 277.

[12] Farkas, L., Keimbildungsgeschwindigkeit in übersättigten Dämpfen. *Z. phys. Chem* **1927,** *125* (1), 236-242.

[13] Frenkel, Y. I., Kinetic theory of liquids. **1955**.

[14] Gibbs, J. W., ART. LII.--On the Equilibrium of Heterogeneous Substances. *American Journal of Science and Arts (1820-1879)* **1878,** *16* (96), 441.

[15] Wagner, C., Kinetik Der Phasenbildung. *Angew. Chem.* **1939,** *52* (30), 503-504.

[16] Stranski, I.; Kaischew, R., The theory of the linear rate of crystallisation. *Z. Phys. Chem. A* **1934,** *170*, 295-299.

[17] Lutsko, J. F., How crystals form: A theory of nucleation pathways. *Science advances* **2019,** *5* (4), eaav7399.

[18] De Yoreo, J. J.; Vekilov, P. G., Principles of crystal nucleation and growth. *Reviews in mineralogy and geochemistry* **2003,** *54* (1), 57-93.

[19] Wegst, U. G. K.; Bai, H.; Saiz, E.; Tomsia, A. P.; Ritchie, R. O., Bioinspired structural materials. *Nature Materials* **2015,** *14* (1), 23-36.

[20] Seto, J.; Ma, Y.; Davis, S. A.; Meldrum, F.; Gourrier, A.; Kim, Y.-Y.; Schilde, U.; Sztucki, M.; Burghammer, M.; Maltsev, S.; Jäger, C.; Cölfen, H., Structure-property relationships of a biological mesocrystal in the adult sea urchin spine. *P. Natl. Acad. Sci. USA* **2012,** *109* (10), 3699-3704.

[21] Haberkorn, H.; Franke, D.; Frechen, T.; Goesele, W.; Rieger, J., Early stages of particle formation in precipitation reactions—quinacridone and boehmite as generic examples. *Journal of colloid and interface science* **2003,** *259* (1), 112-126.

[22] Floquet, N.; Vielzeuf, D., Ordered misorientations and preferential directions of growth in mesocrystalline red coral sclerites. *Crystal growth & design* **2012,** *12* (10), 4805-4820.

[23] Oaki, Y.; Kotachi, A.; Miura, T.; Imai, H., Bridged Nanocrystals in Biominerals and Their Biomimetics: Classical Yet Modern Crystal Growth on the Nanoscale. *Adv. Funct. Mater.* **2006,** *16* (12), 1633-1639.

[24] Glotzer, S.; Solomon, M.; Kotov, N. A., Self-assembly: From nanoscale to microscale colloids. *AIChE Journal* **2004,** *50* (12), 2978-2985.

[25] Sangwal, K., *Nucleation and Crystal Growth: Metastability of Solutions and Melts.* 2018.

[26] Nielsen, M. H.; Lee, J. R. I.; Hu, Q. N.; Han, T. Y. J.; De Yoreo, J. J., Structural evolution, formation pathways and energetic controls during template-directed nucleation of $CaCO_3$. *Faraday Discussions* **2012,** *159*, 105-121.

[27] Reimer, N., Klimaprognosen, jetzt alle falsch? © Karen Bleier/AFP/Getty Images. *Zeit online* **2016,** https://www.zeit.de/wissen/2016-05/wolken-atmosphaere-aerosol-erderwaermung-meteorologie-wolkenbildung?utm_referrer=https%3A%2F%2Fwww.google.com%2F (accessed 23.05.2021).

[28] Aomorikuma, Blick auf die aus Perlmutt bestehende Innenfläche der Schale eines Seeohrs (Haliotis). **2008,** https://de.wikipedia.org/wiki/Perlmutt#/media/Datei:Shell_of_Haliotis.JPG (accessed 13.02.2022).

[29] Waschmaschine entkalken. *Heimhelden © Nomad_Soul / Shutterstock* **2016,** https://www.heimhelden.de/waschmaschine-entkalken (accessed 23.05.2021).

[30] Vesselinov, M. I., *Crystal growth for beginners: fundamentals of nucleation, crystal growth and epitaxy*. World scientific: **2016**.

[31] Volmer, M., Kinetik der Phasenbildung. **1939**.

[32] Becker, R.; Döring, W., Kinetische Behandlung der Keimbildung in übersättigten Dämpfen. *Annalen der Physik* **1935,** *416* (8), 719-752.

[33] Gránásy, L. In *Comparison of modern theories of vapor condensation*, AIP Conference Proceedings, American Institute of Physics: **2000**; pp 209-212.

[34] Kashchiev, D., Toward a better description of the nucleation rate of crystals and crystalline monolayers. *The Journal of chemical physics* **2008,** *129* (16), 164701.

[35] Vekilov, P. G., The two-step mechanism of nucleation of crystals in solution. *Nanoscale* **2010,** *2* (11), 2346-2357.

[36] Gebauer, D.; Kellermeier, M.; Gale, J. D.; Bergström, L.; Cölfen, H., Pre-nucleation clusters as solute precursors in crystallisation. *Chemical Society Reviews* **2014,** *43* (7), 2348-2371.

[37] Cho, A., Connecting the dots to custom catalysts. *Science* **2003,** *299* (5613), 1684-1685.

[38] Borel, P.; Buffat, J., Size effect on the melting temperature of gold particles. *Phys. Rev. A* **1976,** *13*, 2287-2298.

[39] Klokkenburg, M.; Vonk, C.; Claesson, E. M.; Meeldijk, J. D.; Erné, B. H.; Philipse, A. P., Direct imaging of zero-field dipolar structures in colloidal dispersions of synthetic magnetite. *Journal of the American Chemical Society* **2004,** *126* (51), 16706-16707.

[40] Xu, Z.; Hou, Y.; Sun, S., Magnetic core/shell Fe3O4/Au and Fe3O4/Au/Ag nanoparticles with tunable plasmonic properties. *Journal of the American Chemical Society* **2007,** *129* (28), 8698-8699.

[41] Ekimov, A. I.; Efros, A. L.; Onushchenko, A. A., Quantum size effect in semiconductor microcrystals. *Solid State Communications* **1985,** *56* (11), 921-924.

[42] Brus, L. E., Electron–electron and electron-hole interactions in small semiconductor crystallites: The size dependence of the lowest excited electronic state. *The Journal of chemical physics* **1984,** *80* (9), 4403-4409.

[43] Dillmann, A.; Meier, G., Homogeneous nucleation of supersaturated vapors. *Chemical physics letters* **1989,** *160* (1), 71-74.

[44] Dillmann, A.; Meier, G., A refined droplet approach to the problem of homogeneous nucleation from the vapor phase. *The Journal of chemical physics* **1991,** *94* (5), 3872-3884.

[45] Ford, I.; Laaksonen, A.; Kulmala, M., Modification of the Dillmann–Meier theory of homogeneous nucleation. *The Journal of chemical physics* **1993,** *99* (1), 764-765.

[46] Zhang, H.; Banfield, J. F., Energy calculations predict nanoparticle attachment orientations and asymmetric crystal formation. *The Journal of Physical Chemistry Letters* **2012,** *3* (19), 2882-2886.

[47] Galkin, O.; Vekilov, P. G., Direct determination of the nucleation rates of protein crystals. *Journal of Physical Chemistry B* **1999,** *103* (49), 10965-10971.

[48] Gasser, U., Crystallization in three- and two-dimensional colloidal suspensions. *Journal of Physics-Condensed Matter* **2009,** *21* (20).

[49] Nielsen, A. E., *Kinetics of precipitation*. Pergamon: **1964**; Vol. 18.

[50] Abraham, F. F., *Homogeneous nucleation theory*. Elsevier: **1974**; Vol. 263.

[51] Picker, A. Influence of Polymers on Nucleation and Assembly of Calcium Silicate Hydrates. *Universität Konstanz*, Konstanzer Online-Publikations-System, **2013**.

[52] Aizenberg, J.; Black, A. J.; Whitesides, G. M., Oriented growth of calcite controlled by self-assembled monolayers of functionalized alkanethiols supported on gold and silver. *Journal of the American Chemical Society* **1999,** *121* (18), 4500-4509.

[53] Aizenberg, J.; Black, A. J.; Whitesides, G. M., Control of crystal nucleation by patterned self-assembled monolayers. *Nature* **1999,** *398* (6727), 495-498.

[54] Travaille, A. M.; Donners, J. J.; Gerritsen, J. W.; Sommerdijk, N. A.; Nolte, R. J.; van Kempen, H., Aligned growth of calcite crystals on a self-assembled monolayer. *Advanced Materials* **2002,** *14* (7), 492-495.

[55] Modern, A. C., Crystallography III, Crystal Growth. *Springer Ser Solid State* **1984,** *36*.

[56] Mullin, J., Crystallization 3rd edn, Ch. 5 and 6. Butterworth–Heinemann: **1992**.

[57] Robinson, V.; Robins, J., Nucleation kinetics of gold deposition onto UHV cleaved surfaces of KCl and NaF. *Thin Solid Films* **1970,** *5* (5-6), 313-327.

[58] Robinson, V.; Robins, J., Nucleation kinetics of gold deposited onto UHV cleaved surfaces of NaCl and KBr. *Thin Solid Films* **1974,** *20* (1), 155-175.

[59] Paunov, M.; Harsdorff, M., Untersuchungen zur Keimbildung von Gold auf Kohlenstoffschichten/Investigations to the Nucleation of Gold on Carbon Layers. *Zeitschrift für Naturforschung A* **1974,** *29* (9), 1311-1318.

[60] S., T.; I., M., *Ber. Bunsenges. Phys. Chem.* **1969,** *73*, 184.

[61] Wu, S.; Li, M.; Sun, Y., In Situ Synchrotron X-ray Characterization Shining Light on the Nucleation and Growth Kinetics of Colloidal Nanoparticles. *Angewandte Chemie International Edition* **2019,** *58* (27), 8987-8995.

[62] Tanaka, T.; Ohyama, J.; Teramura, K.; Hitomi, Y., Formation mechanism of metal nanoparticles studied by XAFS spectroscopy and effective synthesis of small metal nanoparticles. *Catalysis today* **2012,** *183* (1), 108-118.

[63] Saha, D.; Bøjesen, E. D.; Jensen, K. M.; Dippel, A.-C.; Iversen, B. B., Formation mechanisms of Pt and Pt3Gd nanoparticles under solvothermal conditions: an in situ total X-ray scattering study. *The Journal of Physical Chemistry C* **2015,** *119* (23), 13357-13362.

[64] Hao, X.; Chen, M.; Wang, L.; Cao, Z.; Li, Y.; Han, S.; Zhang, M.; Yu, K.; Zeng, J., In situ SAXS probing the evolution of the precursors and onset of nucleation of ZnSe colloidal semiconductor quantum dots. *Chemical Communications* **2020,** *56* (13), 2031-2034.

[65] Pong, B.-K.; Elim, H. I.; Chong, J.-X.; Ji, W.; Trout, B. L.; Lee, J.-Y., New Insights on the Nanoparticle Growth Mechanism in the Citrate Reduction of Gold(III) Salt: Formation of the Au Nanowire Intermediate and Its Nonlinear Optical Properties. *The Journal of Physical Chemistry C* **2007,** *111* (17), 6281-6287.

[66] Schiener, A.; Magerl, A.; Krach, A.; Seifert, S.; Steinrück, H.-G.; Zagorac, J.; Zahn, D.; Weihrich, R., In situ investigation of two-step nucleation and growth of CdS nanoparticles from solution. *Nanoscale* **2015,** *7* (26), 11328-11333.

[67] Cölfen, H.; Pauck, T., Determination of particle size distributions with angström resolution. *Colloid and Polymer Science* **1997,** *275* (2), 175-180.

[68] Gebauer, D.; Volkel, A.; Colfen, H., Stable Prenucleation Calcium Carbonate Clusters. *Science* **2008,** *322* (5909), 1819-1822.

[69] Zeng, C.; Vitale-Sullivan, C.; Ma, X., In situ atomic force microscopy studies on nucleation and self-assembly of biogenic and bio-inspired materials. *Minerals* **2017,** *7* (9), 158.

[70] Li, M.; Wang, L.; Putnis, C. V., Atomic force microscopy imaging of classical and nonclassical surface growth dynamics of calcium orthophosphates. *CrystEngComm* **2018,** *20* (21), 2886-2896.

[71] Tao, J.; Nielsen, M. H.; De Yoreo, J. J., Nucleation and phase transformation pathways in electrolyte solutions investigated by in situ microscopy techniques. *Current Opinion in Colloid & Interface Science* **2018,** *34*, 74-88.

[72] Asakawa, H.; Holmström, E.; Foster, A. S.; Kamimura, S.; Ohno, T.; Fukuma, T., Direct imaging of atomic-scale surface structures of brookite TiO2 nanoparticles by frequency modulation atomic force microscopy in liquid. *The Journal of Physical Chemistry C* **2018,** *122* (42), 24085-24093.

[73] Tracey, J.; Miyazawa, K.; Spijker, P.; Miyata, K.; Reischl, B.; Canova, F. F.; Rohl, A. L.; Fukuma, T.; Foster, A. S., Understanding 2D atomic resolution imaging of the calcite surface in water by frequency modulation atomic force microscopy. *Nanotechnology* **2016,** *27* (41), 415709.

[74] Miyata, K.; Kawagoe, Y.; Tracey, J.; Miyazawa, K.; Foster, A. S.; Fukuma, T., Variations in Atomic-Scale Step Edge Structures and Dynamics of Dissolving Calcite in Water Revealed by High-Speed Frequency Modulation Atomic Force Microscopy. *The Journal of Physical Chemistry C* **2019,** *123* (32), 19786-19793.

[75] Ito, F.; Kobayashi, K.; Spijker, P.; Zivanovic, L.; Umeda, K.; Nurmi, T.; Holmberg, N.; Laasonen, K.; Foster, A. S.; Yamada, H., Molecular resolution of the water interface at an alkali halide with terraces and steps. *The Journal of Physical Chemistry C* **2016,** *120* (35), 19714-19722.

[76] Radisic, A.; Ross, F.; Searson, P., In situ study of the growth kinetics of individual island electrodeposition of copper. *The Journal of Physical Chemistry B* **2006,** *110* (15), 7862-7868.

[77] Radisic, A.; Vereecken, P. M.; Hannon, J. B.; Searson, P. C.; Ross, F. M., Quantifying electrochemical nucleation and growth of nanoscale clusters using real-time kinetic data. *Nano Letters* **2006,** *6* (2), 238-242.

[78] Li, D.; Nielsen, M. H.; Lee, J. R.; Frandsen, C.; Banfield, J. F.; De Yoreo, J. J., Direction-specific interactions control crystal growth by oriented attachment. *Science* **2012,** *336* (6084), 1014-1018.

[79] Liao, H.-G.; Cui, L.; Whitelam, S.; Zheng, H., Real-time imaging of Pt_3Fe nanorod growth in solution. *Science* **2012,** *336* (6084), 1011-1014.

[80] De Yoreo, J. J.; Gilbert, P. U. P. A.; Sommerdijk, N. A. J. M.; Penn, R. L.; Whitelam, S.; Joester, D.; Zhang, H. Z.; Rimer, J. D.; Navrotsky, A.; Banfield, J. F.; Wallace, A. F.; Michel, F. M.; Meldrum, F. C.; Colfen, H.; Dove, P. M., Crystallization by particle attachment in synthetic, biogenic, and geologic environments. *Science* **2015,** *349* (6247).

[81] Assoud, L.; Ebert, F.; Keim, P.; Messina, R.; Maret, G.; Löwen, H., Crystal nuclei and structural correlations in two-dimensional colloidal mixtures: experiment versus simulation. *Journal of Physics: Condensed Matter* **2009,** *21* (46), 464114.

[82] Schöpe, H. J.; Palberg, T., A study on the homogeneous nucleation kinetics of model charged sphere suspensions. *Journal of Physics: Condensed Matter* **2002,** *14* (45), 11573.

[83] de Villeneuve, V.; Verboekend, D.; Dullens, R.; Aarts, D.; Kegel, W.; Lekkerkerker, H., Hard sphere crystal nucleation and growth near large spherical impurities. *Journal of Physics: Condensed Matter* **2005,** *17* (45), S3371.

[84] Auer, S.; Frenkel, D., Numerical simulation of crystal nucleation in colloids. In *Advanced Computer Simulation*, Springer: **2005**; pp 149-208.

[85] Society, A. M., Glossary of Meteorology. *American Meteorological Society* **2012,** https://glossary.ametsoc.org/wiki/Particle (accessed 06.02.2022).

[86] Coulter, W. H., What is a particle? **2016,** http://perc.ufl.edu/particle.asp.

[87] Goesmann, H.; Feldmann, C., Nanoparticulate Functional Materials. *Angewandte Chemie-International Edition* **2010,** *49* (8), 1362-1395.

[88] Rao, C. N. R.; Müller, A.; Cheetham, A. K., *The chemistry of nanomaterials: synthesis, properties and applications*. John Wiley & Sons: **2006**.

[89] Thomas, J. M.; Raja, R., The advantages and future potential of single-site heterogeneous catalysts. *Topics in catalysis* **2006,** *40* (1-4), 3-17.

[90] Shiju, N. R.; Guliants, V. V., Recent developments in catalysis using nanostructured materials. *Applied Catalysis A: General* **2009,** *356* (1), 1-17.

[91] Zhou, L.; O'Brien, P., Mesocrystals — Properties and Applications. *The Journal of Physical Chemistry Letters* **2012,** *3* (5), 620-628.

[92] Frey, N. A.; Peng, S.; Cheng, K.; Sun, S., Magnetic nanoparticles: synthesis, functionalization, and applications in bioimaging and magnetic energy storage. *Chemical Society Reviews* **2009,** *38* (9), 2532-2542.

[93] Park, J.; An, K.; Hwang, Y.; Park, J.-G.; Noh, H.-J.; Kim, J.-Y.; Park, J.-H.; Hwang, N.-M.; Hyeon, T., Ultra-large-scale syntheses of monodisperse nanocrystals. *Nature materials* **2004,** *3* (12), 891-895.

[94] Faure, B.; Wetterskog, E.; Gunnarsson, K.; Josten, E.; Hermann, R. P.; Brückel, T.; Andreasen, J. W.; Meneau, F.; Meyer, M.; Lyubartsev, A., 2D to 3D crossover of the magnetic properties in ordered arrays of iron oxide nanocrystals. *Nanoscale* **2013,** *5* (3), 953-960.

[95] Zhang, J. Z.; Noguez, C., Plasmonic optical properties and applications of metal nanostructures. *Plasmonics* **2008,** *3* (4), 127-150.

[96] Ajdari, N.; Vyas, C.; Bogan, S. L.; Lwaleed, B. A.; Cousins, B. G., Gold nanoparticle interactions in human blood: a model evaluation. *Nanomedicine: Nanotechnology, Biology and Medicine* **2017,** *13* (4), 1531-1542.

[97] Link, S.; El-Sayed, M. A., Optical Properties and Ultrafast Dynamics of Metallic Nanocrystals. *Annual Review of Physical Chemistry* **2003,** *54* (1), 331-366.

[98] Murphy, C.; Jana, N.; Gearheart, L.; Obare, S.; Caswell, K.; Mann, S.; Johnson, C.; Davis, S.; Dujardin, E.; Edler, K., Synthesis, assembly and reactivity of metallic nanorods. *The Chemistry of Nanomaterials: Synthesis, Properties and Applications* **2004**, 285-307.

[99] García, M. A., Surface plasmons in metallic nanoparticles: fundamentals and applications. *Journal of Physics D: Applied Physics* **2011,** *44* (28), 283001.

[100] Hövel, H.; Fritz, S.; Hilger, A.; Kreibig, U.; Vollmer, M., Width of cluster plasmon resonances: bulk dielectric functions and chemical interface damping. *Physical Review B* **1993,** *48* (24), 18178.

[101] Lin, S.-Y.; Chen, N.-T.; Sum, S.-P.; Lo, L.-W.; Yang, C.-S., Ligand exchanged photoluminescent gold quantum dots functionalized with leading peptides for nuclear targeting and intracellular imaging. *Chemical communications* **2008,** (39), 4762-4764.

[102] Hutter, E.; Fendler, J. H., Exploitation of localized surface plasmon resonance. *Advanced materials* **2004,** *16* (19), 1685-1706.

[103] Eustis, S.; El-Sayed, M. A., Why gold nanoparticles are more precious than pretty gold: Noble metal surface plasmon resonance and its enhancement of the radiative and nonradiative properties of nanocrystals of different shapes. *Chemical Society Reviews* **2006,** *35* (3), 209-217.

[104] Auer, S.; Frenkel, D., Suppression of crystal nucleation in polydisperse colloids due to increase of the surface free energy. *Nature* **2001,** *413* (6857), 711-713.

[105] Cacciuto, A.; Auer, S.; Frenkel, D., Onset of heterogeneous crystal nucleation in colloidal suspensions. *Nature* **2004,** *428* (6981), 404-406.

[106] Niederberger, M.; Cölfen, H., Oriented attachment and mesocrystals: non-classical crystallization mechanisms based on nanoparticle assembly. *Physical Chemistry Chemical Physics* **2006,** *8* (28), 3271-3287.

[107] Cölfen, H.; Antonietti, M., Mesocrystals: inorganic superstructures made by highly parallel crystallization and controlled alignment. *Angewandte Chemie International Edition* **2005,** *44* (35), 5576-5591.

[108] Sturm, E. V.; Cölfen, H., Mesocrystals: past, presence, future. *Crystals* **2017,** *7* (7), 207.

[109] Sturm, E. V.; Cölfen, H., Mesocrystals: structural and morphogenetic aspects. *Chemical Society Reviews* **2016,** *45* (21), 5821-5833.

[110] Moureaux, C.; Perez-Huerta, A.; Compère, P.; Zhu, W.; Leloup, T.; Cusack, M.; Dubois, P., Structure, composition and mechanical relations to function in sea urchin spine. *Journal of structural biology* **2010,** *170* (1), 41-49.

[111] Perrin, J.; Vielzeuf, D.; Ricolleau, A.; Dallaporta, H.; Valton, S.; Floquet, N., Block-by-block and layer-by-layer growth modes in coral skeletons. *American Mineralogist* **2015,** *100* (4), 681-695.

[112] Vielzeuf, D.; Floquet, N.; Chatain, D.; Bonneté, F.; Ferry, D.; Garrabou, J.; Stolper, E. M., Multilevel modular mesocrystalline organization in red coral. *Am. Mineral.* **2010,** *95* (2-3), 242-248.

[113] Cölfen, H.; Antonietti, M., *Mesocrystals and nonclassical crystallization*. John Wiley & Sons: **2008**.

[114] Bergström, L.; Sturm, E. V.; Salazar-Alvarez, G.; Cölfen, H., Mesocrystals in Biominerals and Colloidal Arrays. *Accounts Chem. Res.* **2015,** *48* (5), 1391-1402.

[115] Debus, C.; Wu, B.; Kollmann, T.; Duchstein, P.; Siglreitmeier, M.; Herrera, S.; Benke, D.; Kisailus, D.; Schwahn, D.; Pipich, V., Bioinspired multifunctional layered magnetic hybrid materials. *Bioinspired, Biomimetic and Nanobiomaterials* **2019,** *8* (1), 28-46.

[116] Farhadi-Khouzani, M.; Schutz, C.; Durak, G. M.; Fornell, J.; Sort, J.; Salazar-Alvarez, G.; Bergstrom, L.; Gebauer, D., A CaCO3/nanocellulose-based bioinspired nacre-like material. *J Mater Chem A* **2017,** *5* (31), 16128-16133.

[117] Yamagishi, K.; Onuma, K.; Suzuki, T.; Okada, F.; Tagami, J.; Otsuki, M.; Senawangse, P., A synthetic enamel for rapid tooth repair. *Nature* **2005,** *433* (7028), 819-819.

[118] Pieranski, P., Colloidal Crystals. *Contemporary Physics* **1983,** *24* (1), 25-73.

[119] Dinsmore, A. D.; Crocker, J. C.; Yodh, A. G., Self-assembly of colloidal crystals. *Current opinion in colloid & interface science* **1998,** *3* (1), 5-11.

[120] Soukoulis, C. M., *Photonic crystals and light localization in the 21st century*. Springer Science & Business Media: **2012**; Vol. 563.

[121] Hynninen, A.-P.; Thijssen, J. H.; Vermolen, E. C.; Dijkstra, M.; Van Blaaderen, A., Self-assembly route for photonic crystals with a bandgap in the visible region. *Nature materials* **2007,** *6* (3), 202-205.

[122] Park, S. H.; Xia, Y., Assembly of mesoscale particles over large areas and its application in fabricating tunable optical filters. *Langmuir* **1999,** *15* (1), 266-273.

[123] Boles, M. A.; Engel, M.; Talapin, D. V., Self-assembly of colloidal nanocrystals: From intricate structures to functional materials. *Chemical reviews* **2016,** *116* (18), 11220-11289.

[124] Pinheiro, A. V.; Han, D. R.; Shih, W. M.; Yan, H., Challenges and opportunities for structural DNA nanotechnology. *Nature Nanotechnology* **2011,** *6* (12), 763-772.

[125] Dill, K. A.; MacCallum, J. L., The Protein-Folding Problem, 50 Years On. *Science* **2012,** *338* (6110), 1042-1046.

[126] Chen, I. A.; Walde, P., From Self-Assembled Vesicles to Protocells. *Cold Spring Harbor Perspectives in Biology* **2010,** *2* (7).

[127] Bates, F. S.; Hillmyer, M. A.; Lodge, T. P.; Bates, C. M.; Delaney, K. T.; Fredrickson, G. H., Multiblock Polymers: Panacea or Pandora's Box? *Science* **2012,** *336* (6080), 434-440.

[128] Aizenberg, J.; Hanson, J.; Koetzle, T. F.; Weiner, S.; Addadi, L., Control of Macromolecule Distribution within Synthetic and Biogenic Single Calcite Crystals. *Journal of the American Chemical Society* **1997,** *119* (5), 881-886.

[129] Fang, J.; Ding, B.; Gleiter, H., Mesocrystals: Syntheses in metals and applications. *Chemical Society Reviews* **2011,** *40* (11), 5347-5360.

[130] Tachikawa, T.; Majima, T., Metal oxide mesocrystals with tailored structures and properties for energy conversion and storage applications. *NPG Asia Materials* **2014,** *6* (5), e100-e100.

[131] Uchaker, E.; Cao, G., Mesocrystals as electrode materials for lithium-ion batteries. *Nano Today* **2014,** *9* (4), 499-524.

[132] Ma, M.-G.; Cölfen, H., Mesocrystals—Applications and potential. *Current opinion in colloid & interface science* **2014,** *19* (2), 56-65.

[133] Zhou, L.; O'Brien, P., Mesocrystals: Properties and Applications. *The Journal of Physical Chemistry Letters* **2012,** *3* (5), 620-628.

[134] Bahrig, L.; Hickey, S. G.; Eychmüller, A., Mesocrystalline materials and the involvement of oriented attachment–a review. *CrystEngComm* **2014,** *16* (40), 9408-9424.

[135] Ngo, A.-T.; Richardi, J.; Pileni, M. P., Crack patterns in superlattices made of maghemite nanocrystals. *Physical Chemistry Chemical Physics* **2013,** *15* (26), 10666-10672.

[136] Leung, K.-t.; Néda, Z., Pattern formation and selection in quasistatic fracture. *Physical review letters* **2000,** *85* (3), 662.

[137] Groisman, A.; Kaplan, E., An experimental study of cracking induced by desiccation. *EPL (Europhysics Letters)* **1994,** *25* (6), 415.

[138] Rupich, S. M.; Shevchenko, E. V.; Bodnarchuk, M. I.; Lee, B.; Talapin, D. V., Size-dependent multiple twinning in nanocrystal superlattices. *Journal of the American Chemical Society* **2010,** *132* (1), 289-296.

[139] Anderson, V. J.; Lekkerkerker, H. N. W., Insights into phase transition kinetics from colloid science. *Nature* **2002,** *416* (6883), 811-815.

[140] Yethiraj, A., Tunable colloids: control of colloidal phase transitions with tunable interactions. *Soft Matter* **2007,** *3* (9), 1099-1115.

[141] Gasser, U.; Weeks, E. R.; Schofield, A.; Pusey, P. N.; Weitz, D. A., Real-Space Imaging of Nucleation and Growth in Colloidal Crystallization. *Science* **2001,** *292* (5515), 258-262.

[142] Wang, Z.; Wang, F.; Peng, Y.; Zheng, Z.; Han, Y., Imaging the homogeneous nucleation during the melting of superheated colloidal crystals. *Science* **2012,** *338* (6103), 87-90.

[143] Iyer, A. S. J.; Lyon, L. A., Self-Healing Colloidal Crystals. *Angewandte Chemie* **2009,** *121* (25), 4632-4636.

[144] Zhang, K.-Q.; Liu, X. Y., In situ observation of colloidal monolayer nucleation driven by an alternating electric field. *Nature* **2004,** *429* (6993), 739-743.

[145] Savage, J.; Blair, D.; Levine, A.; Guyer, R.; Dinsmore, A., Imaging the sublimation dynamics of colloidal crystallites. *Science* **2006,** *314* (5800), 795-798.

[146] Agthe, M.; Wetterskog, E.; Mouzon, J.; Salazar-Alvarez, G.; Bergström, L., Dynamic growth modes of ordered arrays and mesocrystals during drop-casting of iron oxide nanocubes. *Crystengcomm* **2014,** *16* (8), 1443-1450.

[147] Agthe, M.; Wetterskog, E.; Bergström, L., Following the Assembly of Iron Oxide Nanocubes by Video Microscopy and Quartz Crystal Microbalance with Dissipation Monitoring. *Langmuir* **2017,** *33* (1), 303-310.

[148] Kapuscinski, M.; Agthe, M.; Bergström, L., Time-resolved viscoelastic properties of self-assembling iron oxide nanocube superlattices probed by quartz crystal microbalance with dissipation monitoring. *Journal of Colloid and Interface Science* **2018,** *522*, 104-110.

[149] Lapointe, C. P.; Mason, T. G.; Smalyukh, I. I., Shape-controlled colloidal interactions in nematic liquid crystals. *Science* **2009,** *326* (5956), 1083-1086.

[150] Jenkins, I. C.; Crocker, J. C.; Sinno, T., Interaction heterogeneity can favorably impact colloidal crystal nucleation. *Physical Review Letters* **2017,** *119* (17), 178002.

[151] Hueckel, T.; Hocky, G. M.; Palacci, J.; Sacanna, S., Ionic solids from common colloids. *Nature* **2020,** *580* (7804), 487-490.

[152] Grzelczak, M.; Vermant, J.; Furst, E. M.; Liz-Marzán, L. M., Directed self-assembly of nanoparticles. *ACS Nano* **2010,** *4* (7), 3591-3605.

[153] Lin, H.; Lee, S.; Sun, L.; Spellings, M.; Engel, M.; Glotzer, S. C.; Mirkin, C. A., Clathrate colloidal crystals. *Science* **2017,** *355* (6328), 931-935.

[154] Auer, S.; Frenkel, D., Prediction of absolute crystal-nucleation rate in hard-sphere colloids. *Nature* **2001,** *409* (6823), 1020-1023.

[155] Schöpe, H. J.; Bryant, G.; van Megen, W., Small changes in particle-size distribution dramatically delay and enhance nucleation in hard sphere colloidal suspensions. *Physical Review E* **2006,** *74* (6), 060401.

[156] Liz-Marzán, L. M., Tailoring surface plasmons through the morphology and assembly of metal nanoparticles. *Langmuir* **2006,** *22* (1), 32-41.

[157] Haran, G.; Chuntonov, L., Artificial plasmonic molecules and their interaction with real molecules. *Chemical reviews* **2018,** *118* (11), 5539-5580.

[158] Brunner, J.; Maier, B.; Rosenberg, R.; Sturm, S.; Cölfen, H.; Sturm, E. V., Nonclassical Recrystallization. *Chemistry – A European Journal* **2020,** *26* (66), 15242-15248.

[159] Alder, B. J.; Wainwright, T. E., Phase Transition for a Hard Sphere System. *The Journal of Chemical Physics* **1957,** *27* (5), 1208-1209.

[160] Wood, W. W.; Jacobson, J. D., Preliminary Results from a Recalculation of the Monte Carlo Equation of State of Hard Spheres. *The Journal of Chemical Physics* **1957,** *27* (5), 1207-1208.

[161] Pusey, P. N.; Van Megen, W., Phase behaviour of concentrated suspensions of nearly hard colloidal spheres. *Nature* **1986,** *320* (6060), 340-342.

[162] Antl, L.; Goodwin, J.; Hill, R.; Ottewill, R. H.; Owens, S.; Papworth, S.; Waters, J., The preparation of poly (methyl methacrylate) latices in non-aqueous media. *Colloids and Surfaces* **1986,** *17* (1), 67-78.

[163] Phan, S.-E.; Russel, W. B.; Cheng, Z.; Zhu, J.; Chaikin, P. M.; Dunsmuir, J. H.; Ottewill, R. H., Phase transition, equation of state, and limiting shear viscosities of hard sphere dispersions. *Physical Review E* **1996,** *54* (6), 6633-6645.

[164] Jardine, R. S.; Bartlett, P., Synthesis of non-aqueous fluorescent hard-sphere polymer colloids. *Colloids and Surfaces A: Physicochemical and Engineering Aspects* **2002,** *211* (2-3), 127-132.

[165] Savage, J. R.; Dinsmore, A. D., Experimental Evidence for Two-Step Nucleation in Colloidal Crystallization. *Physical Review Letters* **2009,** *102* (19), 198302.

[166] Nonat, A., The structure and stoichiometry of C-S-H. *Cement and Concrete Research* **2004,** *34* (9), 1521-1528.

[167] Nadeau, P., The physical dimensions of fundamental clay particles. *Clay Minerals* **1985,** *20* (4), 499-514.

[168] Soroka, I., Setting and hardening. In *Portland Cement Paste and Concrete*, Springer: **1979**; pp 28-45.

[169] Holcomb, J.; Spellmon, N.; Zhang, Y.; Doughan, M.; Li, C.; Yang, Z., Protein crystallization: Eluding the bottleneck of X-ray crystallography. *AIMS biophysics* **2017,** *4* (4), 557-575.

[170] Lizandara-Pueyo, C.; Siroky, S.; Wagner, M. R.; Hoffmann, A.; Reparaz, J. S.; Lehmann, M.; Polarz, S., Shape Anisotropy Influencing Functional Properties: Trigonal Prismatic ZnO Nanoparticles as an Example. *Advanced Functional Materials* **2011,** *21* (2), 295-304.

[171] Kang, Y.; Li, M.; Cai, Y.; Cargnello, M.; Diaz, R. E.; Gordon, T. R.; Wieder, N. L.; Adzic, R. R.; Gorte, R. J.; Stach, E. A., Heterogeneous catalysts need not be so "heterogeneous": Monodisperse Pt nanocrystals by combining shape-controlled synthesis and purification by colloidal recrystallization. *Journal of the American Chemical Society* **2013,** *135* (7), 2741-2747.

[172] Aslam, M.; Bhobe, R.; Alem, N.; Donthu, S.; Dravid, V., Controlled large-scale synthesis and magnetic properties of single-crystal cobalt nanorods. *Journal of applied physics* **2005,** *98* (7), 074311.

[173] Darques, M.; Piraux, L.; Encinas, A., P. BayleGuillem aud, A. Popa, U. Ebels. *Appl. Phys. Lett* **2005,** *86*, 072508-072511.

[174] Polarz, S., Shape Matters: Anisotropy of the Morphology of Inorganic Colloidal Particles - Synthesis and Function. *Advanced Functional Materials* **2011,** *21* (17), 3214-3230.

[175] Burrows, N. D.; Vartanian, A. M.; Abadeer, N. S.; Grzincic, E. M.; Jacob, L. M.; Lin, W.; Li, J.; Dennison, J. M.; Hinman, J. G.; Murphy, C. J., Anisotropic nanoparticles and anisotropic surface chemistry. *The journal of physical chemistry letters* **2016,** *7* (4), 632-641.

[176] Link, S.; El-Sayed, M. A., Spectral properties and relaxation dynamics of surface plasmon electronic oscillations in gold and silver nanodots and nanorods. ACS Publications: **1999**; Vol. 103, pp 8410-8426.

[177] Link, S.; Mohamed, M. B.; El-Sayed, M., Simulation of the optical absorption spectra of gold nanorods as a function of their aspect ratio and the effect of the medium dielectric constant. *The Journal of Physical Chemistry B* **1999,** *103* (16), 3073-3077.

[178] Guerrero-Martínez, A.; Barbosa, S.; Pastoriza-Santos, I.; Liz-Marzán, L. M., Nanostars Shine Bright for You: Colloidal Synthesis, Properties and Applications of Branched Metallic Nanoparticles. In *Colloidal Synthesis of Plasmonic Nanometals*, Jenny Stanford Publishing: **2020**; pp 285-320.

[179] Kharisov, B. I., A review for synthesis of nanoflowers. *Recent patents on nanotechnology* **2008,** *2* (3), 190-200.

[180] Chen, D.; Hou, X.; Li, T.; Yin, L.; Fan, B.; Wang, H.; Li, X.; Xu, H.; Lu, H.; Zhang, R., Effects of morphologies on acetone-sensing properties of tungsten trioxide nanocrystals. *Sensors and Actuators B: Chemical* **2011,** *153* (2), 373-381.

[181] Hsu, S.-W.; On, K.; Tao, A. R., Localized surface plasmon resonances of anisotropic semiconductor nanocrystals. *Journal of the American Chemical Society* **2011,** *133* (47), 19072-19075.

[182] Jiang, R.; Li, B.; Fang, C.; Wang, J., Metal/semiconductor hybrid nanostructures for plasmon-enhanced applications. *Advanced materials* **2014,** *26* (31), 5274-5309.

[183] Huang, X.; El-Sayed, I. H.; Qian, W.; El-Sayed, M. A., Cancer cell imaging and photothermal therapy in the near-infrared region by using gold nanorods. *Journal of the American Chemical Society* **2006,** *128* (6), 2115-2120.

[184] Banholzer, M. J.; Millstone, J. E.; Qin, L.; Mirkin, C. A., Rationally designed nanostructures for surface-enhanced Raman spectroscopy. *Chemical Society Reviews* **2008,** *37* (5), 885-897.

[185] Norman, R. S.; Stone, J. W.; Gole, A.; Murphy, C. J.; Sabo-Attwood, T. L., Targeted photothermal lysis of the pathogenic bacteria, Pseudomonas aeruginosa, with gold nanorods. *Nano letters* **2008,** *8* (1), 302-306.

[186] Jiang, S.; Chen, Q.; Tripathy, M.; Luijten, E.; Schweizer, K. S.; Granick, S., Janus particle synthesis and assembly. *Advanced materials* **2010,** *22* (10), 1060-1071.

[187] Talapin, D. V., Nanocrystal solids: A modular approach to materials design. *MRS bulletin* **2012,** *37* (1), 63.

[188] Quan, Z. W.; Fang, J. Y., Superlattices with non-spherical building blocks. *Nano Today* **2010,** *5* (5), 390-411.

[189] Zhang, S. Y.; Regulacio, M. D.; Han, M. Y., Self-assembly of colloidal one-dimensional nanocrystals. *Chemical Society Reviews* **2014,** *43* (7), 2301-2323.

[190] Schlotheuber né Brunner, J.; Maier, B.; Thomä, S. L. J.; Kirner, F.; Baburin, I. A.; Lapkin, D.; Rosenberg, R.; Sturm, S.; Assalauova, D.; Carnis, J.; Kim, Y. Y.; Ren, Z.; Westermeier, F.; Theiss, S.; Borrmann, H.; Polarz, S.; Eychmüller, A.; Lubk, A.; Vartanyants, I. A.; Cölfen, H.; Zobel, M.; Sturm, E. V., Morphogenesis of Magnetite Mesocrystals: Interplay between Nanoparticle Morphology and Solvation Shell. *Chemistry of Materials* **2021,** *33* (23), 9119-9130.

[191] Russel, W.; Saville, D.; Schowalter, W., Colloidal Dispersions Press Cambridge: Cambridge Univ, **1989**.

[192] Luedtke, W. D.; Landman, U., Structure, dynamics, and thermodynamics of passivated gold nanocrystallites and their assemblies. *Journal of Physical Chemistry* **1996,** *100* (32), 13323-13329.

[193] Jiang, L.; Chen, X. D.; Lu, N.; Chi, L. F., Spatially Confined Assembly of Nanoparticles. *Accounts of Chemical Research* **2014,** *47* (10), 3009-3017.

[194] Zhou, Y.; Zhou, X. Z.; Park, D. J.; Torabi, K.; Brown, K. A.; Jones, M. R.; Zhang, C.; Schatz, G. C.; Mirkin, C. A., Shape-Selective Deposition and Assembly of Anisotropic Nanoparticles. *Nano Letters* **2014,** *14* (4), 2157-2161.

[195] Cui, Y.; Bjork, M. T.; Liddle, J. A.; Sonnichsen, C.; Boussert, B.; Alivisatos, A. P., Integration of colloidal nanocrystals into lithographically patterned devices. *Nano Letters* **2004,** *4* (6), 1093-1098.

[196] Hanske, C.; Hill, E. H.; Vila-Liarte, D.; González-Rubio, G.; Matricardi, C.; Mihi, A.; Liz-Marzán, L. M., Solvent-Assisted Self-Assembly of Gold Nanorods into Hierarchically Organized Plasmonic Mesostructures. *ACS Applied Materials & Interfaces* **2019,** *11* (12), 11763-11771.

[197] Wang, X.; Feng, J.; Bai, Y.; Zhang, Q.; Yin, Y., Synthesis, Properties, and Applications of Hollow Micro-/Nanostructures. *Chemical Reviews* **2016,** *116* (18), 10983-11060.

[198] Dinsmore, A. D.; Hsu, M. F.; Nikolaides, M. G.; Marquez, M.; Bausch, A. R.; Weitz, D. A., Colloidosomes: Selectively permeable capsules composed of colloidal particles. *Science* **2002,** *298* (5595), 1006-1009.

[199] Lin, Y.; Boker, A.; Skaff, H.; Cookson, D.; Dinsmore, A. D.; Emrick, T.; Russell, T. P., Nanoparticle assembly at fluid interfaces: Structure and dynamics. *Langmuir* **2005,** *21* (1), 191-194.

[200] He, J.; Zhang, Q.; Gupta, S.; Emrick, T.; Russell, T. R.; Thiyagarajan, P., Drying droplets: A window into the behavior of nanorods at interfaces. *Small* **2007,** *3* (7), 1214-1217.

[201] Delmas, T.; Roberts, M. M.; Heng, J. Y., Nucleation and crystallization of lysozyme: Role of substrate surface chemistry and topography. *Journal of adhesion science and technology* **2011,** *25* (4-5), 357-366.

[202] Jun, Y.-S.; Kim, D.; Neil, C. W., Heterogeneous Nucleation and Growth of Nanoparticles at Environmental Interfaces. *Accounts of Chemical Research* **2016,** *49* (9), 1681-1690.

[203] Goncalves, G.; Marques, P. A.; Granadeiro, C. M.; Nogueira, H. I.; Singh, M.; Gracio, J., Surface modification of graphene nanosheets with gold nanoparticles: the role of oxygen moieties at graphene surface on gold nucleation and growth. *Chemistry of Materials* **2009,** *21* (20), 4796-4802.

[204] Jin, Y.; Kang, X.; Song, Y.; Zhang, B.; Cheng, G.; Dong, S., Controlled nucleation and growth of surface-confined gold nanoparticles on a (3-aminopropyl) trimethoxysilane-modified glass slide: a strategy for SPR substrates. *Analytical chemistry* **2001,** *73* (13), 2843-2849.

[205] Musino, D.; Rivard, C.; Landrot, G.; Novales, B.; Rabilloud, T.; Capron, I., Hydroxyl groups on cellulose nanocrystal surfaces form nucleation points for silver nanoparticles of varying shapes and sizes. *Journal of Colloid and Interface Science* **2021,** *584*, 360-371.

[206] Lee, Y. H.; Shi, W.; Lee, H. K.; Jiang, R.; Phang, I. Y.; Cui, Y.; Isa, L.; Yang, Y.; Wang, J.; Li, S., Nanoscale surface chemistry directs the tunable assembly of silver octahedra into three two-dimensional plasmonic superlattices. *Nature communications* **2015,** *6* (1), 1-7.

[207] Corricelli, M.; Depalo, N.; Fanizza, E.; Altamura, D.; Giannini, C.; Siliqi, D.; Di Mundo, R.; Palumbo, F.; Kravets, V. G.; Grigorenko, A. N., Two-dimensional plasmonic superlattice based on Au nanoparticles self-assembling onto a functionalized substrate. *The Journal of Physical Chemistry C* **2014,** *118* (14), 7579-7590.

[208] Rorvik, P. M.; Almli, A.; van Helvoort, A. T. J.; Holmestad, R.; Tybell, T.; Grande, T.; Einarsrud, M. A., $PbTiO_3$ nanorod arrays grown by self-assembly of nanocrystals. *Nanotechnology* **2008,** *19* (22).

[209] Zhuravlev, L., Concentration of hydroxyl groups on the surface of amorphous silicas. *Langmuir* **1987,** *3* (3), 316-318.

[210] Crampton, N.; Bonass, W. A.; Kirkham, J.; Thomson, N. H., Formation of Aminosilane-Functionalized Mica for Atomic Force Microscopy Imaging of DNA. *Langmuir* **2005,** *21* (17), 7884-7891.

[211] Lyubchenko, Y. L.; Gall, A. A.; Shlyakhtenko, L. S.; Harrington, R. E.; Jacobs, B. L.; Oden, P. I.; Lindsay, S. M., Atomic Force Microscopy Imaging of Double Stranded DNA and RNA. *Journal of Biomolecular Structure and Dynamics* **1992,** *10* (3), 589-606.

[212] Onclin, S.; Ravoo, B. J.; Reinhoudt, D. N., Engineering Silicon Oxide Surfaces Using Self-Assembled Monolayers. *Angewandte Chemie International Edition* **2005,** *44* (39), 6282-6304.

[213] Mirabella, F. M., *Internal reflection spectroscopy: theory and applications*. CRC Press: **1992**; Vol. 15.

[214] Fowkes, F. M., Attractive forces at interfaces. *Industrial & Engineering Chemistry* **1964,** *56* (12), 40-52.

[215] Wasserman, S. R.; Tao, Y. T.; Whitesides, G. M., Structure and reactivity of alkylsiloxane monolayers formed by reaction of alkyltrichlorosilanes on silicon substrates. *Langmuir* **1989,** *5* (4), 1074-1087.

[216] Rappoport, Z.; Frankel, M., *CRC handbook of tables for organic compound identification*. Boca Raton, Fla. : CRC Press: **1984**.

[217] Lide, R. D., *CRC Handbook of Chemistry and Physics*. 79. Aufl. ed.; CRC Press: Boca Raton, Boston, London, New York, Washington DC, **1998**.

[218] King, J., *Acidity. Sulphonic Acids, Esters and their Derivatives.* Wiley: Chichester, **1991**; p 249-259.

[219] Emoto, K.; Harris, J. M.; Van Alstine, J. M., Grafting poly (ethylene glycol) epoxide to amino-derivatized quartz: effect of temperature and pH on grafting density. *Analytical chemistry* **1996,** *68* (21), 3751-3757.

[220] Anderson, J.; Chris, G. V. d. W., Fundamentals of zinc oxide as a semiconductor. *Rep. Prog. Phys* **2009,** *72* (12), 126501.

[221] Look, D. C.; Claflin, B., P-type doping and devices based on ZnO. *physica status solidi (b)* **2004,** *241* (3), 624-630.

[222] Meyer, B.; Alves, H; Hofmann, D.; Kriegseis, W.; Forster, D.; Bertram, F.; Christen, J.; Hoffmann, A.; Straßburg, M.; Dworzak, M., Bound exciton and donor–acceptor pair recombinations in ZnO. *physica status solidi (b)* **2004,** *241* (2), 231-260.

[223] Look, D. C.; Reynolds, D.; Litton, C.; Jones, R.; Eason, D.; Cantwell, G., Characterization of homoepitaxial p-type ZnO grown by molecular beam epitaxy. *Applied physics letters* **2002,** *81* (10), 1830-1832.

[224] Monroy, E.; Omnès, F.; Calle, F., Wide-bandgap semiconductor ultraviolet photodetectors. *Semiconductor science and technology* **2003,** *18* (4), R33.

[225] Lin, H.; Tzeng, S.; Hsiau, P.; Tsai, W., *Nanostruct. Mater.* **1998**.

[226] Bauer, T.; Voggenreiter, M.; Xu, T.; Wähler, T.; Agel, F.; Pohako-Esko, K.; Schulz, P.; Döpper, T.; Görling, A.; Polarz, S., ZnO Nanoparticle Formation from the Molecular Precursor $[MeZnOtBu]_4$ by Ozone Treatment in Ionic Liquids: in-situ Vibrational Spectroscopy in an Ultrahigh Vacuum Environment. *Zeitschrift für anorganische und allgemeine Chemie* **2017,** *643* (1), 31-40.

[227] Tian, Z. R.; Voigt, J. A.; Liu, J.; Mckenzie, B.; Mcdermott, M. J.; Rodriguez, M. A.; Konishi, H.; Xu, H., Complex and oriented ZnO nanostructures. *Nature materials* **2003,** *2* (12), 821-826.

[228] Gerigk, M.; Bahner, J.; Kollek, T.; Helfrich, S.; Rosenberg, R.; Cölfen, H.; Polarz, S., Order and Defects in Ceramic Semiconductor Nanoparticle Superstructures as a Function of Polydispersity and Aspect Ratio. *Particle & Particle Systems Characterization* **2016**, n/a-n/a.

[229] Xia, Y.; Gilroy, K. D.; Peng, H. C.; Xia, X., Seed-mediated growth of colloidal metal nanocrystals. *Angewandte Chemie International Edition* **2017,** *56* (1), 60-95.

[230] O'Brien, M. N.; Jones, M. R.; Brown, K. A.; Mirkin, C. A., Universal noble metal nanoparticle seeds realized through iterative reductive growth and oxidative dissolution reactions. *Journal of the American Chemical Society* **2014,** *136* (21), 7603-7606.

[231] Kirner, F.; Potapov, P.; Schultz, J.; Geppert, J.; Muller, M.; Gonzalez-Rubio, G.; Sturm, S.; Lubk, A.; Sturm, E., Additive-controlled synthesis of monodisperse single crystalline gold nanoparticles: interplay of shape and surface plasmon resonance. *Journal of Materials Chemistry C* **2020,** *8* (31), 10844-10851.

[232] Liao, J.; Zhang, Y.; Yu, W.; Xu, L.; Ge, C.; Liu, J.; Gu, N., Linear aggregation of gold nanoparticles in ethanol. *Colloids and Surfaces A: Physicochemical and Engineering Aspects* **2003,** *223* (1-3), 177-183.

[233] Gonzalez-Rubio, G.; Kumar, V.; Llombart, P.; Diaz-Nunez, P.; Bladt, E.; Altantzis, T.; Bals, S.; Pena-Rodriguez, O.; Noya, E. G.; MacDowell, L. G.; Guerrero-Martinez, A.; Liz-Marzan, L. M., Disconnecting Symmetry Breaking from Seeded Growth for the Reproducible Synthesis of High Quality Gold Nanorods. *Acs Nano* **2019,** *13* (4), 4424-4435.

[234] Yu, R.; Liz-Marzán, L. M.; de Abajo, F. J. G., Universal analytical modeling of plasmonic nanoparticles. *Chemical Society Reviews* **2017,** *46* (22), 6710-6724.

[235] Myroshnychenko, V.; Rodríguez-Fernández, J.; Pastoriza-Santos, I.; Funston, A. M.; Novo, C.; Mulvaney, P.; Liz-Marzán, L. M.; De Abajo, F. J. G., Modelling the optical response of gold nanoparticles. *Chemical Society Reviews* **2008,** *37* (9), 1792-1805.

[236] González-Rubio, G.; González-Izquierdo, J.; Bañares, L.; Tardajos, G.; Rivera, A.; Altantzis, T.; Bals, S.; Peña-Rodríguez, O.; Guerrero-Martínez, A.; Liz-Marzán, L. M., Femtosecond laser-controlled tip-to-tip assembly and welding of gold nanorods. *Nano letters* **2015,** *15* (12), 8282-8288.

[237] Schupp, D. J.; Angst, J.; Schaefer, E. A.; Schupp, S. M.; Cölfen, H., Controlling Oriented Attachment of Gold Nanoparticles by Size and Shape. *The Journal of Physical Chemistry C* **2021,** *125* (37), 20343-20350.

[238] Shiota, S.; Yamamoto, S.; Shimomura, A.; Ojida, A.; Nishino, T.; Maruyama, T., Quantification of Amino Groups on Solid Surfaces Using Cleavable Fluorescent Compounds. *Langmuir* **2015,** *31* (32), 8824-8829.

[239] Moussodia, R.-O.; Balan, L.; Merlin, C.; Mustin, C.; Schneider, R., Biocompatible and stable ZnO quantum dots generated by functionalization with siloxane-core PAMAM dendrons. *Journal of Materials Chemistry* **2010,** *20* (6), 1147-1155.

[240] De Palma, R.; Peeters, S.; Van Bael, M. J.; Van den Rul, H.; Bonroy, K.; Laureyn, W.; Mullens, J.; Borghs, G.; Maes, G., Silane Ligand Exchange to Make Hydrophobic Superparamagnetic Nanoparticles Water-Dispersible. *Chemistry of Materials* **2007,** *19* (7), 1821-1831.

[241] Kockmann, A.; Hesselbach, J.; Zellmer, S.; Kwade, A.; Garnweitner, G., Facile surface tailoring of metal oxide nanoparticles via a two-step modification approach. *RSC Advances* **2015,** *5* (75), 60993-60999.

[242] Deegan, R. D.; Bakajin, O.; Dupont, T. F.; Huber, G.; Nagel, S. R.; Witten, T. A., Capillary flow as the cause of ring stains from dried liquid drops. *Nature* **1997,** *389* (6653), 827.

[243] Denkov, N. D.; Velev, O.; Kralchevsky, P.; Ivanov, I.; Yoshimura, H.; Nagayama, K., Two-dimensional crystallization. *Nature* **1993,** *361* (6407), 26.

[244] Hu, H.; Larson, R. G., Evaporation of a sessile droplet on a substrate. *The Journal of Physical Chemistry B* **2002,** *106* (6), 1334-1344.

[245] Mirkin, C. A.; Letsinger, R. L.; Mucic, R. C.; Storhoff, J. J., A DNA-based method for rationally assembling nanoparticles into macroscopic materials. *Nature* **1996,** *382* (6592), 607.

[246] Grzelczak, M.; Liz-Marzán, L. M.; Klajn, R., Stimuli-responsive self-assembly of nanoparticles. *Chemical Society Reviews* **2019,** *48* (5), 1342-1361.

[247] Li, W.; Han, Y.-C.; Zhang, J.-L.; Wang, B.-G., Effect of ethanol on the aggregation properties of cetyltrimethylammonium bromide surfactant. *Colloid Journal* **2005,** *67* (2), 159-163.

[248] Walter, J.; Peukert, W., Dynamic range multiwavelength particle characterization using analytical ultracentrifugation. *Nanoscale* **2016,** *8* (14), 7484-7495.

[249] Irache, J.; Durrer, C.; Ponchel, G.; Duchêne, D., Determination of particle concentration in latexes by turbidimetry. *International journal of pharmaceutics* **1993,** *90* (3), R9-R12.

[250] Duffy, D. M.; Travaille, A. M.; van Kempen, H.; Harding, J. H., Effect of bicarbonate ions on the crystallization of calcite on self-assembled monolayers. *The Journal of Physical Chemistry B* **2005,** *109* (12), 5713-5718.

[251] Hendel, T.; Wuithschick, M.; Kettemann, F.; Birnbaum, A.; Rademann, K.; Polte, J. r., In situ determination of colloidal gold concentrations with UV–Vis spectroscopy: limitations and perspectives. *Analytical chemistry* **2014,** *86* (22), 11115-11124.

[252] Beer, A., Bestimmung der Absorption des rothen Lichts in farbigen Flüssigkeiten. *Ann. Physik* **1852,** *162*, 78-88.

[253] Wyckoff, R., Crystal structures. 2. Auflage. Band 1. *John Wiley & Sons, New York/London, Sydney* **1963,** *1*, S. 3 (im Anhang).

[254] Strunz, H.; Nickel, E. H., Strunz Mineralogical Tables. Chemical-structural mineral classification system. 9. Auflage. Schweizerbart'sche Verlagsbuchhandlung (Nägele u. Obermiller), Stuttgart: **2001**; p 34.

[255] Söhnel, O.; Mullin, J., A method for the determination of precipitation induction periods. *Journal of Crystal Growth* **1978,** *44* (4), 377-382.

[256] Söhnel, O., Electrolyte crystal-aqueous solution interfacial tensions from crystallization data. *Journal of Crystal Growth* **1982,** *57* (1), 101-108.

[257] Söhnel, O.; Mullin, J., Precipitation of calcium carbonate. *Journal of Crystal Growth* **1982,** *60* (2), 239-250.